Occurrence and Energy Dissipation of Breaking Surface Waves in the Nearshore Studied with Coherent Marine Radar

Dissertation

zur Erlangung des Doktorgrades

der Mathematisch-Naturwissenschaftlichen Fakultät

der Christian-Albrechts-Universität zu Kiel

vorgelegt von

Michael Streßer

aus Lebach

Kiel, 2020

Erster Gutachter:	Prof. Dr. Burkard Baschek
Zweiter Gutachter:	Dr. Grant Deane

Tag der mündlichen Prüfung: 26. März, 2020

Abstract

Wave breaking influences air-sea interactions, wave induced forces on coastal structures, sediment transport and associated coastline changes. A good understanding of the process and a proper incorporation of wave breaking into earth system models is crucial for a solid assessment of the impacts of climate change and human influences on coastal dynamics. However, many aspects are still poorly understood which can be attributed to the fact that wave breaking is difficult to observe and study because it occurs randomly and involves multiple spatial and temporal scales.

Within this doctoral work, a nearshore field experiment was planned and conducted on the island of Sylt in the North Sea to investigate the dynamics of wave breaking. The study combines in-situ observations, numerical simulations and remote sensing using shore-based coherent marine radar. The field measurements are used to investigate the coherent microwave backscatter from shoaling and breaking waves. Three major developments result from the study. The first one is a forward model to compute the backscatter intensity and Doppler velocity from known wave kinematics. The second development is a new classification algorithm to identify dominant breakers, whitecaps and radar imaging artifacts within the radar raw data. The algorithm is used to infer the fraction of breaking waves over a sub- and an inter-tidal sandbar as well as whitecap statistics and results are compared to different parameterizations available in literature. The third development is a new method to deduce the energy of the surface roller from the Doppler velocity measured by the radar. The roller energy is related to the dissipation of roller energy by the stress acting at the surface under the roller. From the spatial gradient of roller energy, the transformation of the significant wave height is computed along the entire cross-shore transect. Comparisons to in-situ measurements of the significant wave height from two bottom mounted pressure gauges and a wave rider buoy show a total root-mean-square-error of 0.20 m and a bias of -0.02 m.

It is the first time that measurements of the spatio-temporal variation of the bulk wave energy dissipation together with the fraction of breaking waves are achieved in storm conditions over such a large distance of more than one kilometer. The largest dissipation rates (> 300 W/m^2) take place on a short distance of less than one wave length (≈ 50 m) at the inter-tidal sandbar. However, during storm conditions 50 % of the incoming wave energy flux is already dissipated at the sub-tidal sandbar. The simultaneous measurements of the occurrence frequency and the energy dissipation facilitate an assessment of the bulk dissipation of individual breaking waves. For the spilling-type breakers in this area, the observed dissipation rate is about 30 % smaller than the dissipation rate according to the generally used bore analogy. This must be considered within nearshore wave models if accurate predictions of the breaking probability are required.

Zusammenfassung

Brechende Meereswellen beinflussen die Wechselwirkung zwischen Ozean und Atmosphäre, verursachen hohe Belastungen auf Bauwerke und mobilisieren Sedimente im Küstenraum. Eine verlässliche Analyse der durch den Klimawandel verursachten Veränderungen der Küstendynamik erfordert daher ein gutes Verständnis des Prozesses. Wellenbrechen ist jedoch nur schwer zu untersuchen, denn der Prozess spielt sich auf unterschiedlichen räumlichen und zeitlichen Skalen ab und behinhaltet von Natur aus ein hohes Maß an Zufälligkeit.

Um die Dynamik des küstennahen Wellenbrechens näher zu untersuchen, wurde im Rahmen dieser Doktorarbeit ein Feldexperiment auf der Nordseeinsel Sylt geplant und durchgeführt. Die Studie umfasst In-Situ Messungen, numerische Modellierung und Fernerkundung unter Verwendung eines landgestützen, marinen Dopplerradars. Drei neue Entwicklungen gehen aus den Untersuchungen hervor. Erstens wird ein Vorwärtsmodell zur Berechnung der Rückstreuintensität und Dopplergeschwindigkeit von einer bekannten Form der Meeresoberfläche vorgestellt. Die zweite Entwicklung ist ein Algorithmus zur Erkennung der Signaturen dominanter Brecher, kleinerer Ereignisse (Schaumkronen) und unerwünschter Abbildungsartefakte innerhalb der kohärenten Radarrrohdaten. Die entwickelte Methodik wird dann angewandt, um die Auftretenswahrscheinlichkeit von brechenden Wellen entlang eines Riff-Rinne Profiles normal zur Küste zu untersuchen. Die dritte Errungenschaft ist eine neue Methode, um aus der Dopplergeschwindigkeit die innerhalb der turbulenten Walze am Kamm einer brechenden Welle gespeicherte Energie zu bestimmen. Diese kann wiederum zur Dissipation der Seegangsenergie in Verbindung gesetzt werden. Auf diese Weise kann die Transformation der signifikanten Wellenhöhe auf einer Distanz von über einem Kilometer entlang des Strandprofils bestimmt werden. Ein Vergleich zu In-Situ Messungen von zwei strandnah platzierten Druckdosen und einer Wellenboje ergibt einen mittleren quadratischen Fehler von 0.20 m mit einem Bias von -0.02 m.

Durch die entwickelten Methoden können erstmals die räumlich und zeitlich veränderliche Wahrscheinlichkeit des Wellenbrechens gleichzeitig mit der damit verbundenen Dissipation der Seegangsenergie über eine große Distanz von mehr als einem Kilometer im Feld bestimmt werden. Die größten Dissipationsraten werden hierbei innerhalb der Brecherzone am inneren Sandriff auf einer relativ kurzen Strecke von weniger als einer Wellenlänge festgestellt. Bei Sturmbedingungen jedoch wird die Hälfte des ankommenden Seegangsenergieflusses bereits am äußeren Riff dissipiert. Die neuen Messmethoden erlauben weiterhin eine Untersuchung der zur Abschätzung der Dissipation häufig genutzten "Borenanalogie". Die Messungen zeigen ungefähr 30 % geringere Dissipationsraten für die untersuchten Schwallbrecher. Dieser Umstand muss bei der Modellierung des küstennahen Seegangs beachtet werden, wenn die Brecherwahrscheinlichkeit korrekt vorhergesagt werden soll.

Contents

List of Figures

List of Tables

Chapter 1

Introduction

1.1 Motivation

More than 600 million people (around 10 percent of the world's population) live in coastal areas that are less than 10 meters above sea level. Nearly 2.4 billion people (about 40 percent of the world's population) live within 100 km (60 miles) from the coast[1]. Historically, the main reason for the popularity of coastal areas is the availability of food that is supplied by fisheries and a prospering agriculture borne by the nutrient-rich soils. Seaborne trade, both in the past and today, is an essential cornerstone of the global economy. The coastal zone also takes a prime role for tourism because of its high recreational value. At the same time, it is increasingly facing heavy human impacts and a rapidly changing climate. Despite the special value of coastal regions for society, our knowledge about the key processes that influence the coastal environment is still limited in many aspects. A better understanding of the mechanisms that govern the coastal environment and their mutual interdependencies is therefore of crucial importance for a sustainable development of coastal regions worldwide. The demand for progress in the field of coastal research requires an integrated research approach enclosing multiple research disciplines (geophysics, biogeochemistry, civil engineering and socioeconomics) and research tools (field observations, remote sensing and numerical simulations).

[1] Numbers are taken from the UN Ocean fact sheet, `https://www.un.org/sustainabledevelopment/wp-content/uploads/2017/05/Ocean-fact-sheet-package.pdf`, accessed on November 26, 2018

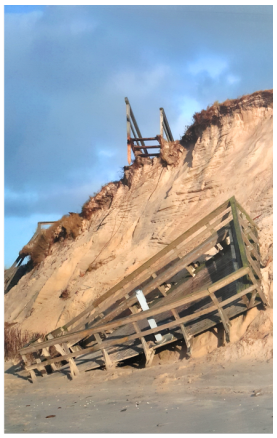

Figure 1.1: Left: Northward view along the approximately 30-m tall sea cliff at North Explanade beach in Pacifica, California in 1997. Source: U.S. Geological Survey, `http://pubs.usgs.gov/pp/pp1693`. **Right:** Visitors platform damaged by erosion of the dune face at the Southwest coast of the island Sylt, Germany in 2015. Credit: Jochen Horstmann.

Coastal dynamics

The coast forms the boundary between the part of the earth's surface above sea level and the ocean. The location of the world's coastlines is continuously changing. A loss of soil material to the sea along with a landward movement of the coastline is called *coastal erosion*. Whereas other parts of the coastline may also gain material (which is called accretion), erosion can be a problem in areas where people live close to shore. Figure 1.1 shows two examples of human developments threatened or damaged by coastal erosion. Coastline changes depend on the geological conditions in the area of interest and can have different reasons. Rain drainage, heat and cold are causes of erosion on the part of the land, while inundated parts are more affected by the water motions, i.e. *coastal hydrodynamics*. The latter are subject of the present study.

Causes of water motion - waves and tides

On the open ocean, the circulation is mostly driven by temperature and density gradients as well as the effect of Earth's rotation. In contrast to that, *nearshore hydrodynamics*, i.e. water motions the direct vicinity of the coastline (up to a water depth of approx. 20 m), are governed by the influence of waves and tides. Tides are excited by the periodic influence of the gravity of the moon and the sun and cause sea level gradients that generate *tidal currents*. The second important driver of coastal water motions

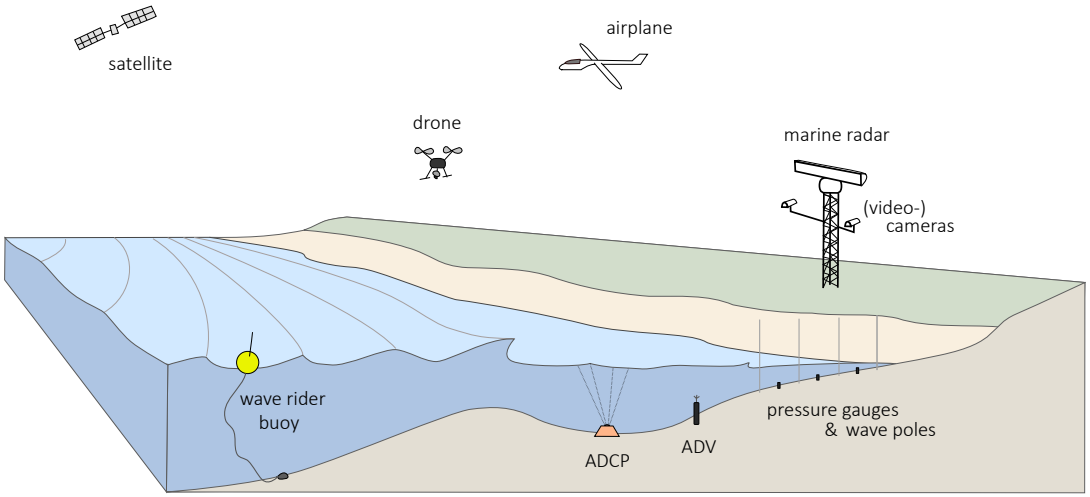

Figure 1.2: Sketch illustrating the complex interaction of the nearshore wave field with the sea floor. The incoming waves refract, steepen and break over a sandbar. This generates turbulence and currents which suspend and transport sediments. Nearshore hydrodynamics may be observed using multiple techniques covering in situ measurements and remote sensing from satellites, airplanes or shore based instruments.

are *surface waves*. Waves start to grow from initially small disturbances at the water surface under the influence of the wind that blows over the water surface. Waves can also be generated by other mechanisms such as earthquakes, landslides, strong variations in atmospheric pressure or ships. Once generated, the wave field travels across the ocean and transports mechanical energy. In the vicinity of the coast, shallower water depths slow down the propagation speed of the wave crests. This aligns the wave crests with the shoreline (refraction) and steepens the waves (shoaling) until they eventually break. Figure 1.2 shows a sketch of the wave field breaking over a sand bar and a compilation of available tools to observe waves in the nearshore.

The role of wave breaking

For any person watching the sea, wave breaking is probably the most notable and fascinating process. A portion of the water at the crest of the wave gets accelerated forward and crashes on the underlying water body. Water droplets are generated and the wave collapses. This produces a thundering noise that can be heard from a relatively large distance as the sound of the sea. Surfers are generally aware of the extreme forces a breaking wave can produce and utilize the dynamics of the wave to gain and maintain

speed. For swimmers, or other beach users, breaking waves and related hazards can become dangerous. The water that is pushed towards the beach by the breaking waves can cause strong offshore directed *rip currents* which are the reason of many deadly drowning accidents, year after year. Wave breaking also links the incoming wave energy to the production of turbulence and currents. It mixes the water body and is a key process for the mobilization and transport of sediments. The process is therefore of great scientific importance, but still far from being completely understood.

Impediments to studying the process

Wave breaking is a highly dynamic process that occurs rapidly and naturally includes a certain randomness. The flow field of breaking waves covers a wide range of scales starting from wave groups (several minutes and hundreds of meters) down to the scales at which turbulent motions are dissipated into heat (sub-millimeter). This makes it inherently complicated to study the process. *Numerical studies* of the breaking process require an enormously high grid resolution in order to resolve wave breaking turbulence. This is computationally expensive hence unfeasible for real world applications. Wave breaking is therefore still highly simplified and empirically parameterized in recent wave prediction models. The observation of breaking waves in natural conditions is a difficult task because the deployment and maintenance of *field instrumentation* placed in a breaking wave environment is challenging. Instruments can get quickly covered by sand, misplaced or damaged by the wave loads. For this reason most of the available datasets stem from *hydraulic experiments* in the laboratory. Controlled conditions in a laboratory can indeed help to separate the different contributions of single parameters under specific circumstances but they cannot perfectly imitate the actual situation in the field.

Prospects for progress

Wave breaking directly influences the nearshore the wave height and thus the highest water level during storms (surge and wave runup). Facing an expected change in the climatology of storms, a reduction of uncertainties within the model parameterizations for depth induced wave breaking will facilitate more meaningful predictions of the impacts of storms on the coast. In order to improve the breaking parameterizations, more observations are needed with a good coverage and a high resolution in space and

time. As mentioned earlier, this is difficult to realize in the nearshore using in-situ instruments.

Remote sensing of the nearshore is an advantageous addition to in-situ measurements, because the instruments can be placed outside the harsh ocean environment. They are therefore much easier to install and maintain. *Satellites* or *airplanes* equipped with cameras or radar are often used for large scale remote sensing studies. However, they overfly a specific area very fast and the return period for a the next overflight is often long (in the order of hours for planes and days for satellites). This narrows the usability of such air- and space-borne instruments for the study of nearshore of wave breaking. *Unmanned aerial vehicles* (UAV) may help to overcome this restriction, but their usage is restricted to short time windows due to limited battery capacity and the possible payloads are still to small for many instruments. Moreover, most drones cannot be flown in high wind conditions. Shore-based instruments are therefore beneficial observations in space and time are required. *Coastal video* camera systems have become very popular within the last decade for studying wave breaking dynamics in the nearshore. However, a sophisticated calibration procedure is required for every new installation and calibration coefficients can change throughout the day due to temperature differences. Cameras obviously are restricted to daylight use and the quality of visible light imagery is strongly degraded by the presence of fog.

Marine radar remote sensing is instead not restricted to daylight. Compared to visible light video, which is a passive electromagnetic technique, marine radar records the backscatter of actively sent microwave radiation. Doppler radar systems additionally provide information about the velocities of the scattering objects at the sea surface. These benefits together with the ability of marine radar to probe the ocean with high resolution in space and time over large distances makes it a perfect tool for studying wave propagation and wave breaking in the nearshore.

1.2 Scope and Structure

Within this work, I present three new scientific developments based on a nearshore field study that combines remote sensing, in-situ measurements and numerical modelling. The first development is a forward model to simulate the intensity and Doppler velocity of coherent marine radar backscatter from shoaling and breaking waves. The second development is a new approach to remotely observe the occurrence of dominant breaking waves as well as smaller breakers (whitecaps). The third development is a new methodology to remotely observe the spatial distribution of the amount of dissipated wave energy due to breaking. The dissipation rate estimates are then used to compute the transformation of wave energy along a shore normal transect. This was not possible yet with existing marine radar based wave measurement techniques. The concurrent measurement of breaking probability and dissipation is a milestone for the development of a more physical representation of nearshore wave breaking within wave models. This will help to improve the prediction and understanding of wave driven nearshore circulation and related hazards. It will also augment the prediction and understanding of coastal sediment transport and associated morphological changes (erosion and sedimentation) of the coastline under the pressure of human influence and a changing climate. A brief review of the basic theory for the description ocean surface waves in finite depth conditions is given in chapter 2. Forthermore, typical means of wave measurements in the nearshore are outlined and pros and cons of their application are evaluated. Other reported nearshore field studies that focus on wave breaking are reviewed. Because coherent marine radar is the main instrument used within the present study, the microwave scattering theory is introduced in a dedicated section. This is followed by a review of different types of numerical wave models with a subjective evaluation of the respective parameterization of wave breaking. In chapter 3, the "WaveDiss2016" field experiment is described, which was designed and conducted as part of the present work. The study area, environmental conditions as well as the instrumentation and methodology that was used to collect and analyze the field data is outlined. Moreover, the different numerical wave model setups that were applied within this study are described. Chapter 4 contains a study of coherent marine radar backscatter from shoaling and breaking waves during a medium severe storm event. The results are used to develop a new forward model to estimate the backscatter intensity and Doppler velocity from known wave kinematics, which for the present work are estimated using a phase-resolving non-linear wave model. Based on these findings,

a new algorithm to detect wave breaking in coherent marine radar backscatter is developed and described within chapter 5. The algorithm is then utilized to compute the probability of dominant, depth induced wave breaking as well as whitecap statistics and the results are compared to commonly used parameterizations. In chapter 6, a new technique is introduced to derive wave energy dissipation from an instantaneous spatial increase of the Doppler velocity. A physical explanation is given based on the concept of the surface roller. The newly developed techniques are used to quantify the probability of wave breaking (ch. 5) and the surface wave energy dissipation rateire (ch. 6) along a $\approx$ 1.5 km long cross-shore transect covering a sub-tidal and an inter-tidal sandbar. Chapter 7 discusses implications of the findings of the previous chapters for geophysical processes such as nearshore hydrodynamics or sediment transport, which are both affected by breaking.

Chapter 2

Nearshore Surface Waves - Theory, Measurement and Numerical Models

The present study combines in situ observations, radar remote sensing and numerical models to analyze the transformation of surface wave energy in the nearshore. This requires basic knowledge in *wave theory*, *means of wave measurement*, *microwave scattering theory* and *numerical modelling* of waves. This chapter contains a compilation of the basic theory needed within the later parts of the thesis and lists relevant literature. Moreover, the state of the art in measurement and simulation of breaking waves is described.

In section 2.1, the theory of surface waves in coastal waters is briefly outlined. Terms and definitions used within the later parts of this thesis are introduced. Section 2.2 reviews the state of the art with respect to the measurement of waves in nearshore environments. This is possible using in-situ instrumentation or remote sensing, respectively. The main instrument utilized in this study is a coherent marine (microwave) radar. The theory of microwave backscatter from the ocean surface, which is needed for a utilization of marine radar for wave measurements, is therefore outlined distinctly within section 2.3. Finally, section 2.4 gives an overview of available numerical models for the simulation of nearshore waves. Model types are in particular discussed with respect to their ability to simulate wave breaking.

2.1 Physics of Nearshore Surface Gravity Waves

The goal of this section is to provide the reader with the basic theoretical background of wave hydrodynamics in coastal waters and to introduce important terms and definitions used throughout the rest of this thesis. Within sec. 2.1.1, a basic overview about the description of wave motions in coastal waters is given. The widely used linear wave theory (or Airy wave theory) is introduced in section 2.1.2. The sea state, i.e. the superposition of individual wave components, is described in section 2.1.3. Finally, 2.1.4 elaborates on wave breaking, which is the most dynamic and non-linear process related to surface waves.

2.1.1 Description of Waves

The interface between the atmosphere and the water mass in the ocean is characterized by random motions usually referred to as *ocean surface waves*. A single wave is typically defined by two length scales and one time scale. The the first length scale, the wave height H, defines the distance between the highest and the lowest water elevation within the wave. The second length scale is the wave length L. Probably the most widely used convention is to define the wave length as the distance between two successive wave crests, whereas other wave definitions are also possible (e.g. trough to trough or level up- or down-crossing). The time scale of a wave is called the wave period T and is defined as the time between the passing of two consecutive waves at a given location. Figure 2.1 illustrates the characterizing measures for the description of a wave. Mathematically, the water motions (kinematics) and acting forces (dynamics) are in principal prescribed by mass and momentum conservation laws. The wave kinematics and dynamics are non-linear problems. However, by taking some assumptions and simplifications the problem can be linearized yielding simple mathematical expressions for water waves. The derivation of the linearized wave equations can be found in a number of textbooks (Phillips, 1977; Dean and Dalrymple, 1991; Svendsen, 2006; Holthuijsen, 2007, among others) and is therefore not repeated here. In the following section 2.1.2, the *linear wave theory* is introduced and the assumptions taken about the physical properties of linear water waves are listed. The limits of application are described briefly and alternative non-linear wave theories are listed.

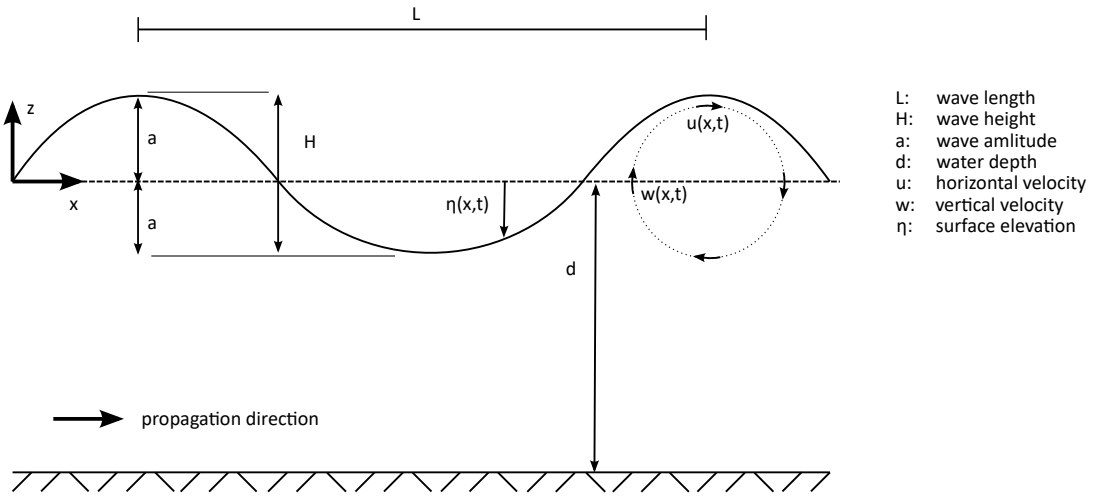

Figure 2.1: Definitions and notations for the description of an infinitesimally long-crested (2DV) sinusoidal harmonic wave in water of finite depth.

2.1.2 Linear Wave Theory

The linear wave theory is also called *Airy wave theory* (Airy, 1845) and describes the dynamics and kinematics of a single harmonic wave as a three-dimensional (horizontal and vertical space + time) problem. The water mass is assumed to be an ideal fluid that is *incompressible* with a *constant density* and *no viscosity*. This assumption can be taken because viscous effects are negligible and the forces acting on the water body are too small to compress the water. Another assumption is that the fluid is *continuous*, meaning that there are no air bubbles are included in the water body and also no water can get disconnected from the water body by leaving the surface. The mentioned assumptions do also imply that the linear wave theory neglects the effect of friction both at the bottom and at the water surface. The only external force considered is the *gravitational acceleration* of the earth's gravity field. The *Coriolis force* induced by the rotation of the earth, as well as *surface tension* effects are neglected. This is reasonable for the scales of waves that are considered within most practical problems because the spatial wave scales are small enough not to be noticeably affected by Coriolis and still large enough not to be altered by the surface tension. This is also the case for the present study. The last necessary assumption is that the flow is *irrotational*. With these assumptions the (linear) mass and momentum balance equations, i.e. the Laplace and Bernoulli equations, can be solved and the following simple analytical expressions follow for the wave kinematics and dynamics (the reader is referred to

Svendsen (2006) or Holthuijsen (2007) for a complete derivation of the equations).

A long-crested, periodical wave in any given constant water depth d is then defined by the amplitude $a = H/2$, the (intrinsic) radial frequency $\omega = 2\pi/T$ and the wave number $k = 2\pi/L$, where H, T and L are wave height, wave period and wave length, respectively. The *surface elevation* is given by

$$\eta(x,t) = a\ \sin(\omega t - kx), \tag{2.1}$$

the *wave orbital velocities* are given by

$$u = \omega a\ \frac{\cosh[k(d+z)]}{\sinh(kd)}\ \sin(\omega t - kx) \tag{2.2}$$

and

$$w = \omega a\ \frac{\sinh[k(d+z)]}{\sinh(kd)}\ \cos(\omega t - kx). \tag{2.3}$$

The *pressure fluctuation* is given by

$$p = -\rho g z + \rho g a \frac{\cosh[k(d+z)]}{\cosh(kd)}\ \sin(\omega t - kx), \tag{2.4}$$

where the summands on the right side reflect the hydrostatic pressure and wave induced dynamic pressure, respectively. ρ is the density of the fluid ($\rho \approx 1025\ kg/m^3$ for sea water) and $g \approx 9.81\ m/s^2$ is the gravitational acceleration.

Another important relationship that follows from the linear wave theory is the *linear dispersion relationship*

$$\omega^2 = gk\ \tanh(kd), \tag{2.5}$$

that relates the frequency of the wave to its wave number (or length). Therefore, eq. 2.5 can be used to estimate the propagation speed

$$c = \frac{\omega}{k} = \sqrt{\frac{g}{k}\tanh(kd)} \tag{2.6}$$

of the wave for a given water depth.

A linear water wave stores a certain amount of potential and kinetic energy. From an integration of the momentum (kinetic energy) and pressure (potential energy) over the wave period and over depth (e.g. Svendsen, 2006), the total amount of energy stored

in one wave per unit horizontal area follows as

$$E_w = E_{kin} + E_{pot} = \frac{1}{2}\rho g a^2 = \frac{1}{8}\rho g H^2. \tag{2.7}$$

The wave energy is transported in the propagation direction of the waves at a certain speed, called the group velocity

$$c_g = \frac{\partial \omega}{\partial k} = n\, c, \;\; \text{with} \;\; n = \frac{1}{2}\left(\frac{2kd}{\sinh(2kd)}\right), \tag{2.8}$$

so that the wave averaged flux of energy per unit crest length is given by

$$F_w = E_w\, c_g. \tag{2.9}$$

The wave energy flux is a quantity that is conserved if there are no sources or sinks of wave energy, i.e. wave growth or dissipation. It is therefore the basis for many (phase-averaged) numerical wave models (see sec. 2.4.2).

Limits of application and non-linear wave theories

The main requirement for the linear wave theory to adequately represent the wave induced motions is the *small-amplitude approximation*. This means that the amplitudes of the waves are small compared to the water depth and the wave length ($a \ll d$ and $ak \ll 2\pi$). In other words, steep waves in deep water or waves in shallow water, where the wave height comes close to the water depth, are not anymore covered within the range of application of the linear wave theory. For such a situation, an application of a non-linear wave theory would become necessary. Widely used non-linear wave theories are e.g. higher order *Stokes theory* (Stokes, 1847), Dean's *stream function theory* (Dean, 1965) or the *cnoidal wave theory* (Korteweg and de Vries, 1895) for waves in shallow water. The reader is referred to the sections about non-linear wave theories in Fenton (1990), or again the textbooks by Svendsen (2006) or Holthuijsen (2007) for a detailed explanation.

2.1.3 Sea State

Any sea surface elevation time series can be expressed as a Fourier series, i.e. a linear superposition of N harmonic waves. In the spectral domain the time series is repre-

sented by the surface elevation spectrum

$$S_\eta(\omega) = \sum_{n=1}^{N} A_n \, e^{i\phi_n} \, , \tag{2.10}$$

where A_n is the complex amplitude and $\phi_n = \omega t$ is the phase of the n-th Fourier component. Similarly, the power spectrum of the sea surface elevation is defined as $S_{\eta\eta} = |S_\eta|^2$.

The capability of equation 2.10 to reproduce an observed surface elevation time series depends only on the selected number N of Fourier components. This fact motivated scientists and engineers to consider the *sea state*, i.e. the evolution of the water surface elevation in a certain area, as a sum of independent individual harmonic wave components. Each wave component is considered to be prescribed by the linear wave theory introduced in the previous section 2.1.2. It is important to notice that there is no complete physical justification for such a treatment, but it provides a convenient solution for a large number of practical problems. Furthermore, the individual wave components can propagate in different directions. Therefore, the wave spectrum is usually represented by a two dimensional spectrum, which can be written as a wave number spectrum $S_{\eta\eta}(\mathbf{k})$ in terms of the wave number vector $\mathbf{k} = (k_x, k_y)$, or likewise as a directional spectrum $S_{\eta\eta}(\omega, \theta_w)$ in terms of the propagation direction θ_w of the individual wave component.

The Rayleigh distribution of wave heights

The complex surface elevation spectrum (eq. 2.10) contains information on both the amplitude and the phase of the individual wave Fourier components. However, the phases of the individual wave components are mostly not known for practical applications. Therefore, the sea state is commonly considered as a Gaussian process, i.e. the phases of each wave component are randomly distributed. The envelope of the time series of a Gaussian process is Rayleigh distributed. Thus, the probability distribution of wave heights for a random sea state is described by the Rayleigh distribution

$$P_r(H) = \frac{2H}{H_{rms}^2} \exp\left(-\left(\frac{H}{H_{rms}} \right)^2 \right) \, , \tag{2.11}$$

where H_{rms} is the root-mean-square value of the wave height ($H_{rms} = 2a_{rms}$ in terms of amplitude). The significant wave height H_s is defined as the mean wave height of the highest one third of the waves. The relationship

$$H_s = \sqrt{2} H_{rms} \tag{2.12}$$

follows from the Rayleigh distribution (e.g. Dean and Dalrymple, 1991).

2.1.4 Wave Breaking

The wavy water surface occasionally collapses and droplets or foam are generated at and bubbles below the water surface. This is generally called *wave breaking*. While also the ordinary person watching the waves from the beach is aware of this process there is still a large knowledge gap in the general understanding of the process and its description. Perlin et al. (2013) presented a detailed review of research that has been conducted in the field of breaking in deep and intermediate waters. Breaking in shallow water was reviewed by Peregrine (1983). This section provides a condensed introduction to the aspects of wave breaking relevant for this thesis.

What is a breaking wave? - Definitions

There is no unique definition available that unambiguously divides surface waves into breaking and non-breaking waves. Within most studies waves are considered as breaking as soon as a detached volume of water, air and small water droplets (or spray) is formed near the crest of the wave (e.g. Melville and Matusov, 2002). This area appears white in visible light optical imagery hence it is called *whitecap*. However, the term whitecap is usually used for relatively young and short breaking waves. For longer and more mature waves, the turbulent region at the front wave of a breaking wave is often called the *surface roller*.

Within this thesis, an alternative breaking definition is used. A wave is considered as breaking if wave energy is removed (dissipated) from the wave and transferred into turbulent motions, bubbles, sediment suspension, currents or heat. Any exchange of energy between waves such as the spectral down shifting of energy due to non-linear wave-wave interactions (Hasselmann, 1962) is not considered as breaking.

Wave breaking in deep and shallow water

Breaking waves do occur in the open ocean as well as in shallow coastal areas. While the mechanisms that initiate wave breaking are different in deep and shallow waters, the physical process is essentially the same in both environments. In shallow water wave breaking is initiated mainly by the steepening of the waves due to shoaling. Instead, deep water waves break due to a steepening by wind shear, the interaction of multiple waves potentially from different directions or by non-linear instability mechanisms such as the Benjamin-Feir instability (Benjamin and Feir, 1967).

Stages of breaking

A breaking wave undergoes a certain evolution during its propagation in space and time. The evolution of the breaking process is illustrated in the sketch shown in fig. 2.2. A non-breaking wave first steepens (*pre-breaking*), then a roller (or a series of capillary waves for very short waves called micro-breakers) is formed at the front face of the wave (*active-breaking*). During this stage, wave energy is dissipated, i.e the wave height decreases. Breaking ceases if the steepness of the wave becomes smaller again. Patches of foam that were generated from active breaking may remain at the surface (*post-breaking*) and the wave crest progresses as a non-breaking wave.

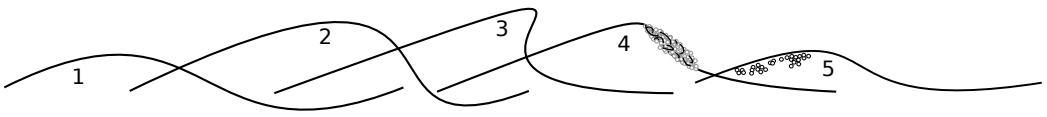

Figure 2.2: Different stages of the breaking process. A non-breaking wave (1) steepens in the pre-breaking stage (2). At the onset of breaking (3) the wave enters the active-breaking stage (4). Right after breaking the cessation of breaking the wave enters the post-breaking stage (5) were foam may be left behind the progressing wave crest.

Wave breaking criteria

The conditions under which an individual wave inevitably breaks have been subject of many studies. A detailed overview is given in the textbook of Babanin (2011). Defining deterministic thresholds for the onset of breaking is required for a number of practical tasks, e.g. for some phase-resolving numerical wave models (see sec.

2.4.1). Breaking criteria can be classified into three categories (eg. Wu and Nepf, 2002), *kinematic*, *geometric* and *dynamic* criteria, respectively.

The *kinematic criterion* is probably the most fundamental approach to the problem. It states that a wave breaks if the horizontal velocity of the water particles in the wave crest exceed the propagation speed of the wave crest. It is the only universal criterion that does not depend on prior assumptions about the form of the wave and is applicable to any water depth (Barthelemy et al., 2018; Saket et al., 2018). However, a measurement of the wave kinematics inside a progressing wave crest in the field is difficult and yet unfeasible. Therefore more practical criteria can be derived from the kinematic criterion applying wave theory.

A *geometrical limit* was found by Stokes (1880) from his theory of irrotational waves. He found that for the maximum wave travelling with constant form, the angle included by the front and rear face is 120°. This leads to the so called Stokes' limit (Michell, 1893) for the critical wave steepness

$$\left(\frac{H}{L}\right)_{crit} = 0.142 \,, \tag{2.13}$$

where H and L are wave height and length, respectively. For sinusoidal waves the critical steepness can also be expressed as

$$(ka)_{crit} = 0.443 \,, \tag{2.14}$$

where k is wave number and a is the amplitude.

On the contrary, *dynamic* breaking criteria consider the critical dynamical properties of waves at breaking. Longuet-Higgins (1963, 1970) showed that the maximum downward acceleration of the water particles at the wave crest is

$$a_{down,crit} = \frac{1}{2}\, g \,, \tag{2.15}$$

where g is the gravitational acceleration. Dynamical breaking criteria are convenient for practical implementations because the calculation of the downward acceleration of the surface is trivial if a sea surface record is available.

For practical applications at arbitrary depth, Miche (1944) proposed the unified

breaker criterion

$$\frac{k\,H_b}{0.88\,\tanh(kd)} = 1, \tag{2.16}$$

that can be used easily to calculate the wave height at breaking H_b. Miche's criterion reduces to the Stokes limit in deep water, where $\tanh(kd) = 1$. In shallow water, where $\tanh(kd) = kd$, it yields $H_b = 0.88\,d$, which is slightly larger than the theoretical result $H_b = 0.78\,d$ derived by McCowan (1894) from solitary wave theory. In order to allow some adjustment and empirically account for other influencing factors such as the beach slope, it has later become common (Battjes, 1972; Battjes and Janssen, 1978; Thornton and Guza, 1983; Whitford, 1988; Baldock et al., 1998; Van Der Westhuysen, 2010, among others) to add an empirical adjustment factor, the so called breaker parameter γ, to Miche's criterion:

$$H_b \simeq \frac{0.88}{k}\,\tanh\left(\frac{\gamma k d}{0.88}\right)\,, \tag{2.17}$$

which in shallow water reduces to $H_b = \gamma d$. Thus the breaker parameter γ relates the wave height at breaking to the water depth in shallow water.

Breaker types

Wave breaking may be classified into *spilling*, *plunging* and *collapsing* or *surging* breakers (Galvin, 1968). The different breaker types are graphically illustrated by the

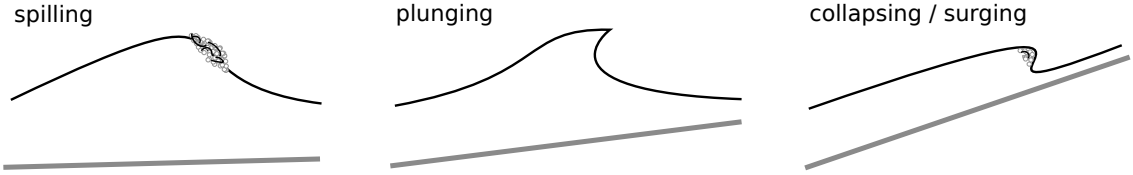

Figure 2.3: Types of breaking waves depending on the wave and beach steepness.

sketch shown in figure 2.3. In shallow water, the type of breaking depends on the offshore wave steepness as well as the beach slope. The predominant breaker type can be predicted from the so called Iribarren number or surf similarity parameter (Iribarren and Nogales, 1949; Battjes, 1974)

$$\xi_0 = \frac{\tan(\alpha_s)}{\sqrt{H_0/L_0}}, \tag{2.18}$$

where α_s is the beach slope angle, H_0 and L_0 are the offshore wave height and wave length in deep water. Values of $\xi_0 < 0.5$ indicate spilling breakers, for $0.5 < \xi_0 < 3.3$ breaking waves are plungers and for $\xi_0 > 3.3$ the predominant breaker type is collapsing or surging.

In deep water, most breaking waves are spilling breakers, whereas plungers are rare (Perlin et al., 2013). Collapsing breakers cannot occur in deep water.

Energy dissipation of a breaking wave - bore or roller?

Two general ways exist to approximate the amount of energy that is dissipated by breaking, the *bore anology* and the *roller concept*, respectively. The sketch in figure 2.4 illustrates a breaking wave in shallow water and the definitions for both concepts.

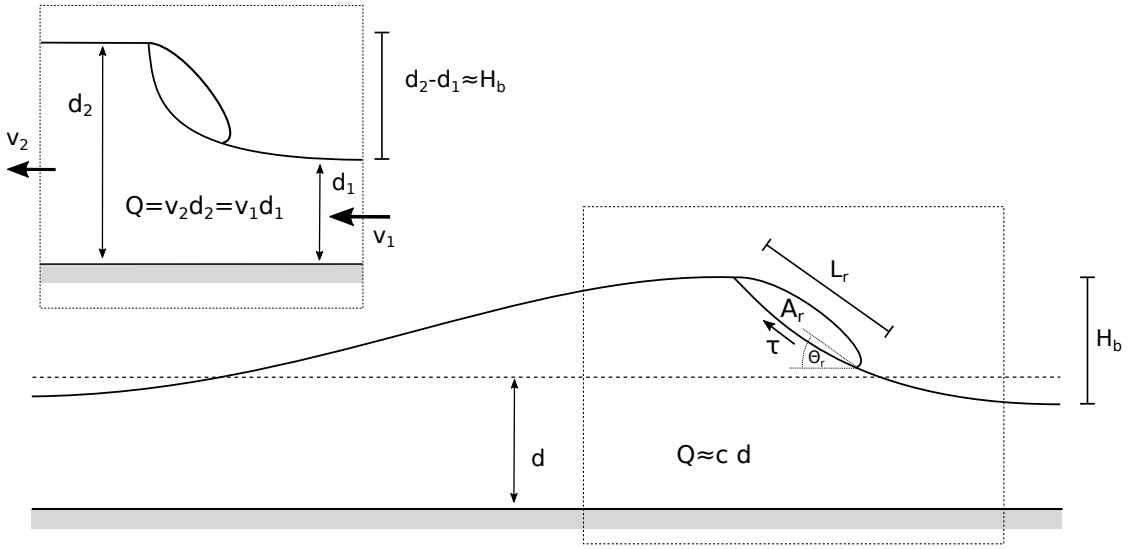

Figure 2.4: Definitions for a quasi-steady breaking wave carrying a surface roller. In a wave following frame of reference, the flow kinematics may be considered as similar to those of an hydraulic jump of the same height as the wave.

The *bore analogy* assumes that a breaking wave in shallow water (where depth uniform flow can be assumed) is similar to a propagating bore (Stoker, 1948). The amount of dissipated energy is then similar to a hydraulic jump that is traveling at the phase speed of the wave. From basic hydromechanic principles of open channel flow (Lamb, 1932), the energy dissipated within a steady hydraulic jump per unit span (perpindicu-

lar to the flow direction) is

$$D_{hj,total} = \frac{1}{4}\rho g \frac{(d_2 - d_1)^3}{d_2 d_1} Q \,, \tag{2.19}$$

where ρ is the water density, g gravitational acceleration and d_1, d_2, v_1 and v_2 are the water depth and (depth averaged) flow velocity upstream and downstream of the hydraulic jump (see upper left panel in fig. 2.4). Q is the total discharge that must be equal up- and downstream due to mass conservation. The following approximations are usually made to apply the same concept to breaking waves (Le Méhauté, 1962). The bore height can be approximated as equal to the breaking wave height, i.e. $d_2 - d_1 = H_b$, and the discharge as $Q = c\ d$, where c is the wave propagation speed. The water depth d is considered as the mean water depth and $d_2 d_1 \approx d^2$. Per unit area, the dissipation rate for a bore-like breaking wave thus becomes

$$D_{hj} = \frac{B}{4}\ \rho g\ \frac{H_b^3}{d^2}\frac{c\ d}{L} = \frac{B}{4}\ \rho g\ f\ \frac{H_b^3}{d}\ , \tag{2.20}$$

where c is the phase speed of the wave, L and f are the wave length and frequency. B is a dimensionless constant to compensate errors in the assumptions made above (Battjes and Janssen, 1978) hence it equals one if the bore analogy is valid.

The *roller concept* was developed for breaking waves in deep water, but does not lose its validity in shallow water. It was first introduced by Duncan (1981) who found from hydraulic experiments that the tangential component of the weight of the detached aerated water mater mass at the surface, i.e the surface roller, gets balanced by the Reynolds stress acting at the interface between the roller and the underlying undisturbed water body:

$$\overline{\rho'} g A_r \sin(\theta_r) = \overline{\tau} L_r \,, \tag{2.21}$$

where $\overline{\rho'}$ is the mean density of the air-water mixture inside the roller. A_r, L_r and θ_r are the roller area, length and angle of inclination as shown in figure 2.4. $\overline{\tau}$ is the mean Reynolds stress generated by the shear that is produced when the roller surfs down the front face of the wave. Duncan's measurements also showed that the dissipation rate scales with the fifth power of the phase speed of the breaking wave. This inspired several authors later (Duncan, 1983; Phillips, 1985; Melville, 1994; Gemmrich et al.,

2008, among others) to express the breaking roller dissipation as

$$D_\tau = b\,\frac{\rho}{g}c^5\ , \tag{2.22}$$

where ρ is water density, g gravitational acceleration and c the phase speed of the breaking wave. The so called breaking strength parameter b is a dimensionless constant that must be determined empirically. The original data of Duncan's (1981) experiments yields $b = 0.044 \pm 0.008$ (Melville, 1994), but several later studies have shown that b varies a lot for different experiments and field observations (Melville, 1994; Drazen et al., 2008, among others).

The bore model is traditionally applied within shallow water studies, whereas the roller model is the standard model for breaking in deep water. However, a modified bore model can also be used in deep water (Chawla and Kirby, 2002) and the roller model is also suited for shallow water applications (Martins et al., 2018). Note that neither the bore analogy nor the roller concept provides an analytical framework to describe the dissipation rate of a breaking wave. Thus, both approaches to the problem must be seen as empirical scalings that still require substantial calibration in order to reproduce available laboratory or field measurements. Therefore, a further understanding and a better parameterization of the calibration parameters within the two approaches is desired.

2.2 Measurement of Surface Waves in the Nearshore

The wave climate in the nearshore is mainly characterized by its high variability in both time and space. The seafloor topography in shallow sandy areas can exhibit rapid changes, which in return are interacting with the local wave field. The placement and maintenance of equipment for measurements of waves in the nearshore is very difficult. Instruments can get covered by sand, misplaced or damaged by the high forces that are acting on the equipment. When placed in a recreational beach area they could even become dangerous for swimmers or surfers or other beach users. An extensive overview about general means of surface wave measurements is given in the textbook of Tucker (1991), who focuses mainly on open ocean wave measurements. Besides brief sections on surfzone wave measurements by Inch (2014) and Davidson-

Arnott (2018), a dedicated compilation of wave measurement techniques applicable in the nearshore is not available. Thus, this section contains an overview about sensors that can be used for nearshore wave measurements and pros and cons are discussed.

The section is subdivided into four main parts. Section 2.2.1 reflects on in-situ instruments. Remote sensing instruments are subject of 2.2.2. In section 2.2.3, the state of the art of observation methods dedicated for breaking waves is reviewed. Special emphasize is herein on the observation of the occurrence frequency of breaking waves and the dissipation of wave energy in the nearshore. Finally, available field experiments to study nearshore wave breaking are listed within section 2.2.4. They are evaluated particularly with respect to observations of the breaking probability.

2.2.1 In-Situ Instrumentation and Point Sensors

This section lists available sensors that provide wave information at one certain location in the nearshore. The term in-situ is used in the context of this thesis for sensors which must be placed at the same (horizontal) position where the wave information is needed. By choosing this definition, sensors that measure the waves from above or below the surface are also referred to as in-situ instruments.

In most cases the quantity of interest is the local sea surface elevation. The first category of instruments listed here are therefore *surface tracking* instruments. Those are *wave rider buoys*, *photo poles* or *wire wave gauges*, *lidar or radar wave gauges* and *upward looking sonar*. Instruments of the second category do not measure the surface elevation, but other wave related quantities. The surface elevation is than derived from the observations by applying an appropriate wave theory. This includes *pressure transducers* and *current meters*. The different types of available in situ instruments for wave measurements are briefly listed in the following and pros and cons for their application are discussed.

Surface following buoys

Floating buoys, often called *wave riders*, follow the surface and track the orbital motions of the waves by monitoring the three dimensional accelerations of the instrument. These are integrated first to vertical and horizontal velocities then to displacements which can be used to extract directional wave information. For most applications, wave buoys need to be moored in order to stay at the desired location. In deep water,

buoy moorings can be designed in a way that the buoy has enough freedom of motion to follow the wave orbital paths. In shallow environments, current speeds are usually higher in some locations and the limited water depth requires short mooring lines. This increases the risk that the mooring lines cause accelerations which are not related to the wave motion, which might cause measurement errors. A general limit for the minimum depth is not easy to define because this strongly depends on the local wave and flow conditions. However, wave buoys are typically not used in shallow waters with depths < 5 m (Meindl, 1996). Depending on the size of the buoy hull and the size and shape of the waves that are to measure, wave buoys show the tendency to cut through the waves, i.e. underestimate the wave height.

Photo-poles and wire wave gauges

Another intuitive way of measuring the water elevation in shallow water is by placing poles at the position of interest. Equipped with rulers or markers, the actual surface elevation can be extracted visually e.g. from video recordings (Suhayda and Pettigrew, 1977; Hotta and Mizuguchi, 1980; Ebersole and Hughes, 1987) hence the name *photo-poles*. A more convenient way to record and store the water elevation at a pole might be to equip the pole with resistance or capacity wires (Thornton and Kraphol, 1974; Guza and Thornton, 1980; Thornton and Guza, 1983). Wire wave gauges have some difficulties at high wind speeds because the interface between water and air can be unclear due to spray and bubbles. Another disadvantage lies in the fact that the mounts for the sensors itself and the wiring of the systems are difficult to deploy and maintain in a breaking wave environment.

Laser, radar and acoustic gauges

If infrastructure such as a pier, a pile or even a platform is available at the study site it is also possible to install downward looking sensors that measure the distance to the surface. Laser (Irish et al., 2006), radar (Van Der Vlugt and Van Der Vlugt, 2014) and ultra-sonic (GE, 2019) wave gauges are available. They spot a specific area at the water surface directly below the sensor. Laser beams are highly focused but (depending on the laser wavelength) they are sensitive to sea spray or other types of aerosols which lead to echoes that do not correspond to the sea surface. Both, ultra-sonic and radar wave gauges are a little bit less sensitive to sea spray, but typically have a rather large

beam opening angle ($\approx 10^{\circ}$ or wider). This results in a larger footprint at the water surface (depending on the installation height) and therefore shorter waves or the sharp crests of non-linear waves are not resolved anymore. Similar to the tendency of wave rider to cut the waves, this leads to an underestimation of the individual wave heights. On the contrary, the presence of sea spray can lead to false echoes in the air which results in an overestimation of the wave heights

Upward looking sonar

With upward looking sonar surface is tracked by emitting and recording sound from a submerged ultrasonic transducer that acts as a reverse echo sounder (Fahrentholz, 1973; Pedersen et al., 2002). However, depending on the sonar frequency, the surface tracking is prone to misreadings due to any sound reflecting elements in the water column, e.g. fish or bubbles. In particular the effect of bubbles makes it almost impossible to use upward looking sonar for surface tracking in the breaking surf.

Pressure gauges

Pressure probes are probably the most widely used wave gauges for nearshore and surf zone applications (Guza and Thornton, 1980; Birkemeier et al., 1996; Sénéchal et al., 2001; Senechal et al., 2011, among others). They can be either buried or mounted slightly above the bottom. and are mostly lightweight and easy to deploy from small vessels or even by hand in very shallow water. However, pressure wave gauges do not measure the surface elevation directly and wave theory must be applied in order to obtain wave amplitudes (Bishop and Donelan, 1987; Nielsen, 1989). When linear wave theory is applied, the error of the surface elevation variance is < 20 % (Guza and Thornton, 1980). Larger errors were found close to the breakpoint. Bonneton et al. (2018) present a weakly dispersive, nonlinear method to recover the wave profile. Their method improves the representation of the non-linear wave shapes in shallow water particularly in the wave crest region. In terms of variance, however, the accuracy is not much improved by this method. Pressure transducers are able to record very low frequency (infragravity) wave motions ($f < 0.0033$ Hz after Munk, 1950). This frequency band cannot be captured by many other sensors due to low frequency sensor noise.

Current meters

Current meters measure wave induced currents that can be transformed to surface elevation using wave theory. There are *acoustic*, *electromagnetic* and *tilt based* current meters. Acoustic Doppler Velocimeters (ADV) measure three-dimensional water motions with a high sampling frequency in a small control volume a few centimeters in front of the sensor. Therefore they can also be used to measure local turbulent motions of the water (Voulgaris and Trowbridge, 1998; Feddersen and Williams, 2007). Electromagnetic current meters (EM) are based on Faraday's principle and can also be utilized for wave measurements (Aubrey and Trowbridge, 1985; Guza et al., 1988). Both techniques, ADV and EM are suitable for wave measurements in the nearshore (Elgar et al., 2001), but ADV seems to be more prone to errors resulting from bubbles and therefore it requires more quality controlling (Elgar et al., 2005). Flow speeds can also be derived from the tilt of the mooring connected to a submerged buoyant body (Figurski et al., 2011; Bendix et al., 2017). This technique possibly facilitates a usage in high energetic, turbulent and bubbly flow conditions under breaking waves in shallow water. However, it requires further testing to evaluate whether it can be used for surface wave measurements (Anarde and Figlus, 2017).

Sensor combinations and arrays

Collocated arrays of multiple synchronized pressure wave gauges can be used to obtain directional wave information (Howell, 1992; Long, 1996). Often, pressure transducers and current meters are combined for directional wave measurements by means of a covariance analysis. This technique, called PUV method (the P stands for pressure, U and V for the horizontal velocity components), is also widely used within nearshore studies (Birkemeier et al., 1989; MacMahan et al., 2005; Senechal et al., 2011, among others). Upward looking Acoustic Doppler Current Profilers (ADCP) with multiple (slanted) beams can also be used for directional wave measurements (Birch et al., 2004; Terray et al., 2008). They combine the acoustic surface tracking technique and beam-wise radial velocity measurements to estimate the directional wave spectrum. However, like all acoustic Doppler methods, ADCP cannot be used within the aereated part of the water column under breaking waves Deane (2016).

2.2.2 Remote Sensing

Observing the waves from a certain (horizontal) distance away from the sensor comes with some important advantages. One point is that the equipment does not have to be placed inside the wave environment. This reduces the chance that the sensor itself or its mount or mooring affects the actual measurement. Also the risk is minimized that the equipment is damaged or displaced under the high loads induced by waves in heavy seas. Furthermore, most remote sensing instruments provide spatial information about the wave field. This is probably the most important virtue with regard to wave observations because it allows for studying the evolution of waves in space and time. Besides these major benefits remote sensing observations typically show larger measurement errors compared to in situ measurements. However, facing the substantial effort that is needed to provide spatial wave measurements using in-situ equipment, a slightly larger uncertainty seems acceptable.

This section gives a brief introduction to available remote sensing instruments for wave observation. For the purpose of the present thesis, i.e. the study of breaking waves in the nearshore, a sensor that is able to provide continuous measurements in space and in time is desired. Space- and airborne instruments only provide snapshots during the overflight of the satellite or airplane and are therefore not listed.

Laser scanners

Laser scanners of a similar type as they are also used for the generation of three-dimensional models of caves or buildings have recently become popular for nearshore wave analysis (Park et al., 2011; Brodie et al., 2015; Martins et al., 2017, 2018). They offer great potential to study the transformation of individual waves in the surf zone. However, experiences of using this technique are limited and the surface identification can be difficult when sea spray is present (L. Lenain, personal communication, Mar 14, 2019). Another limitation of shore based laser scanners is their limited range of operation (which is typically < 200 m).

Stereo cameras

Stereo photogrammetry using synchronized visible light cameras can be used to derive surface elevation maps (Bechle and Wu, 2011; Bergamasco et al., 2017). Most reported studies were conducted from platforms (Mironov et al., 2012) or from ships

(Schwendeman and Thomson, 2017) in deep water. Only a few authors yet have used stereo imaging in the nearshore (de Vries et al., 2011). To ensure a reliability of the measurement, a high camera position is needed which provides a high incidence angle of the camera view. The extent of the area covered by stereo camera systems is therefore typically small ($\approx 100 \times 100$ m). Another drawback of the method is the need for good lighting conditions. Fog, rain, darkness and extreme sun glint can easily make the measurements unfeasible.

Marine radar

Imaging radar, as it is usually used for nautical navigation (typically X- or S-band), can be utilized to derive the directional wave spectrum and the ambient current (Young et al., 1985; Nieto-Borge et al., 1999; Senet et al., 2001), as well as wind speed and direction (Dankert and Horstmann, 2007), and the local water depth (Bell, 1999; Senet et al., 2008; Bell and Osler, 2011). Horstmann et al. (2015) give an overview about the usage of marine radar for hydrographic purposes.

The traditional way to infer the wave spectrum from incoherent marine radar is to identify of the location of the dispersion shell (i.e the three-dimensional representation the Doppler-shifted linear dispersion relation) within the wave number frequency spectrum (Young et al., 1985; Senet et al., 2001). The significant wave height is then retrieved by computing the signal-to-noise ratio of the spectral energy that corresponds to the surface waves (the energy in the vicinity of the dispersion shell) and the noise (all other spectral energy). The signal-to-noise ratio is linearly related to the significant wave height (Alpers and Hasselmann, 1982; Nieto-Borge et al., 1999). However, this classical method for the retrieval of the significant wave height from incoherent radar needs to be calibrated separately for every new radar installation and every individual analysis window using an external wave height measurement. Coherent marine radar systems measure in addition to the backscatter intensity the propagation speed of the scattering elements at the water surface. This can be used to overcome the need for calibration in deep water (Hwang et al., 2010; Carrasco et al., 2017a,b). Spatially varying wave fields, however, were not observed yet by coherent marine radar with the exception of the present work.

Although the mentioned methods to obtain wave information from marine radar are also applicable to neashore environments, they require a three-dimensional spectral analysis of the radar images. Therefore, a certain area (analysis window) must be

selected where homogeneity must be assumed ($\approx 500 \times 500$ m for radars with a 7.5 m range resolution). However, the nearshore water depth as well as the wave and current field often varies on much shorter spatial scales.

2.2.3 Observation of Breaking Waves

The previous sections 2.2.1 and 2.2.2 discussed instrumentation for nearshore wave measurements in general. This section intents to review the state of the art of observation techniques for wave breaking. It is subdivided into three parts. The first part focuses on available methods for the identification or detection of breaking waves. The second part reviews techniques to quantify the amount of dissipation, or breaking severity corresponding to a breaking wave event.

Identification of breaking wave events

Different observation techniques are reported in literature that have been used to detect wave breaking. Those include *human observers*, *visible light* and *infrared cameras*, *passive hydrophones*, *laser scanners* and *radar*.

The most obvious way to observe the occurrence of a breaking wave is from *visual observations*. A certain spot at the sea surface is observed by eye and the beginning and duration of a single wave breaking event is marked down (Thornton and Guza, 1983; Holthuijsen and Herbers, 1986; Kuriyama and Ozaki, 1996). Visual observations may also be achieved by a post-processing of *visible light video* recordings either manually or fully automated (Melville and Matusov, 2002; Callaghan and White, 2009; Kleiss and Melville, 2010; Catalán et al., 2011) . Similar techniques could also be applied to *infrared video* (Jessup et al., 1997; Sutherland and Melville, 2013; Carini et al., 2015). Manasseh et al. (2006) used *passive hydrophones* to detect breaking events from underwater sound. However, a clear allocation of the breaker sound to a specific individual breaking wave within a surface elevation record is difficult. As already mentioned in sec. 2.2.2, *laser scanners* have been used recently to study surf zone waves and identify roller properties in the surf zone (Martins et al., 2017, 2018). The study is restricted to a few waves only and thus it is difficult to judge if this technique can provide reliable breaking statistics. Wave breaking is known to induce bright spots in radar images from the ocean surface, which are called sea spikes (see sec. 2.3). *Incoherent radar* can therefore be used to identify and study wave breaking (Phillips, 1985;

Phillips et al., 2001). However, detecting breakers from incoherent backscatter might be difficult, because steep non-breaking waves also induce high backscatter intensities similar to whitecaps. For dual polarized radars, breaking waves can be identified from the polarization ratio (Kalmykov and Pustovoytenko, 1976; Trizna and Carlson, 1996; Hwang et al., 2008b). Catalán et al. (2011) present a method that utilizes marine radar in combination with collocated visible light images to separate active breakers from steep waves and remaining foam at the surface. The utilization of *coherent radar* for wave breaking detection and for studying the evolution of the breaking process was suggested by many authors to be one of the most promising remote sensing techniques and was used for this purpose in many studies (Jessup, 1990; Jessup et al., 1991a,b; Frasier et al., 1998). However, most of the preceding studies are confined to point measurements recorded from microwave scatterometers that were mounted on platforms in a rather deep water environment. Thus they are not able to observe the spatial variation of the wave breaking characteristics. A few spatio-temporal measurements in deep water environments have been reported (Frasier et al., 1998; Hwang et al., 2008b) and a handful of studies consider nearshore waves (Farquharson et al., 2005; Flampouris et al., 2009; Lin et al., 2013; Catalán et al., 2014; Seemann et al., 2014).

Dissipation estimation

Field measurements of the total amount of energy that is dissipated by an individual breaking wave (or a wave packet) are extremely difficult to carry out. One intuitive way to quantify the dissipated energy would be to follow the path of a breaking wave (or wave group) and balance the flux of wave energy before and after breaking. However, this would require continuous measurement of wave energy in space and time. As it was elaborated in the previous section 2.2.2, laser scanners or stereo cameras basically are able to provide such observations. The limited range of such systems, however, significantly limits the practical feasibility. Wave groups or large waves are often bigger that the covered area which impedes the quantification of pre- and post-breaking wave energy.

Another possibility is thus to directly measure the dissipation of turbulent kinetic energy inside the water column under breaking waves. At one single point the turbulent dissipation rate can be measured using hotfilm anemometers (George et al., 1994) or acoustic Doppler velocimeters (Feddersen and Williams, 2007; Ruessink, 2010; Thomson, 2012; Aagaard et al., 2018, e.g.). However, the full vertical distribution

of turbulent dissipation rate is needed to quantify the total amount of energy dissipated by wave breaking. The use of acoustic Doppler profilers may provide measurements over the full water column, but the acoustic backscatter can get strongly disturbed by bubbles induced by the breakers (Deane, 2016). The study of Sutherland and Melville (2015a) combines infrared stereo-camera measurements to obtain the dissipation rate at the surface (Sutherland and Melville, 2015b) with ADV's and ADCP's which were mounted on vertically profiling platforms to measure subsurface turbulence.

Stokes et al. (2004) proposed a promising technique by relating the bio-luminescent flashes of dinoflagellates to local shear intensities. However, this technique is only feasible under controlled laboratory conditions and is therefore not suited for field applications. Underwater Particle Imaging Velocimetry (PIV) is another possible way to derive vertical maps of turbulent dissipation (Liao et al., 2009), but field installations require a significant amount of infrastructure in place.

2.2.4 Nearshore Field Experiments Reported in Literature

The aim of this section is to provide an overview of reported field experiments that focus on nearshore wave processes and corresponding beach sediment dynamics. The best known field observatories dedicated to study nearshore processes are the *Hazaki Oceanographical Research Station (HORS)* in Japan, the *US Army Corps of Engineers Field Research Facility (FRF)* in Duck, North Carolina and the *Zandmotor* near Ter Heijde in the Netherlands (de Schipper et al., 2016). Some important and well documented nearshore field experiments took place at the FRF in Duck, such as Duck'85 (Ebersole and Hughes, 1987), SUPERDUCK (Crowson et al., 1988), Delilah, Duck'94 and SANDYDUCK (Birkemeier et al., 1996). Substantial progress was also made from the results of temporary field experiments at Torrey Pines Beach, San Diego, California (Guza and Thornton, 1980), the EU-COAST3D project in Egmond an Zee in the Netherlands (Soulsby, 1998), RIPEX in Sand City, Monterey Bay, California (MacMahan et al., 2005) and the ECORS field study at Truc Vert beach, France (Senechal et al., 2011). Needless to say, several smaller field campaigns also brought insight in the understanding of nearshore processes. However, providing a complete overview about all available field studies is far beyond the scope of this thesis.

Field observations of the breaking wave height distribution

Most of the field experiments listed above were conducted to study the cross- and alongshore variation of the wave field, wave induced currents and sediment transport rates. Wave energy and wave induced currents are typically measured by an array of PUV sensors (cf. sec. 2.2.1). However, observations of the occurrence frequency of breaking waves are very rare. This is somewhat surprising, because the fraction of breaking waves is part of most wave breaking parameterizations that are used within phase-averaged wave models for nearshore wave height predictions (see sec. 2.4.3). Moreover, calibration of the models to match observations is usually done through an adjustment of the breaking probability. It should therefore be of high interest to increase the number of observations available for model validation.

Nowadays, ARGUS-like camera systems (Holman and Stanley, 2007) are installed at most nearshore observatories to augment the in-situ observations with spatial information about wave breaking. Bright areas within time-exposure images (time averaged pixel intensities) correspond to breaker zones (shoals), whereas darker regions typically indicate the location of rip channels (with less waves breaking). The average video intensity is a good indicator about the location and the spatial extent of the breaker zone. However, time-exposure images due not provide a true measurement of the occurrence of individual breaking wave events.

To the best of my knowledge, only four nearshore field data sets exist, where the wave breaking probability in terms of the breaking wave height distribution (BWHD) has been explicitly measured. Those are listed table 2.1 together with a few other studies where the integrated breaking probability in terms of the fraction of breaking waves has been measured.

The observation techniques and environmental conditions of the experiments are described in the following.

HORS, Japan 1980 (Hotta et al., 1982) Six sleds equipped with 8 m high target poles were pulled offshore. Those were photographed using synchronized movie cameras from the HORS pier. The breaking state of a wave that passed the poles was visually monitored. The incoming significant wave height during the measurements was $1-1.2$ m with periods of $6-9$ s.

Study	Location	Instruments	BWHD
Hazaki Oceanographical Research Station (HORS)			
Hotta et al. (1982)	Kamisu, Japan, Pacific coast	Photo-poles	yes
Kuriyama and Ozaki (1996)		Photo-poles, ultra-sonic gauges	yes
US Army Corps of Engineers Field Research Facility (FRF)			
Ebersole and Hughes (1987)	Duck, NC, USA, Atlantic coast	Photo-poles	yes
Carini et al. (2015)		Infrared video, ADCP, pressure gauge	no
Other sites			
Thornton and Guza (1983)	Soldiers Beach, Monterey, Calif., USA, Pacific coast	Human observers, pressure gauges, current meters	yes
Díaz Méndez et al. (2015)	New River Inlet, NC USA, Atlantic coast	Incoherent radar, pressure gauges, current meters	no

Table 2.1: Overview of available nearshore field observations of the breaking wave height distribution (BWHD) or the fraction of breaking waves.

Soldiers Beach, California 1981 (Thornton and Guza, 1983) A similar sled system (described in Sallenger et al., 1983) was used by Thornton and Guza (1983) to record breaking wave height distributions in Monterey, California. A winch was connected to the sled allowing for a adaptable positioning of the the sled along the cross-shore transect. The wave heights were recorded using pressure gauges and current meters mounted on the sled. Modes of wave breaking of the individual waves were also observed visually. The wave climate during the measurements was not explicitly mentioned by Thornton and Guza (1983) but it is assumed to be similar to the field campaign at Torrey pines beach, where significant wave heights of $0.5 - 1$ m with period of 14 s were reported.

Duck'85, North Carolina (Ebersole and Hughes, 1987) During the Duck'85 photopole experiment, 14 poles (between 3.2 and 5.5 m long) were jetted into the sand at the FRF, with a spacing of 5.9 m. The poles were filmed using the same movie camera system that was used at HORS 1980. Dally (1992) later reanalyzed the original data set and added information on the breaking state that was identified manually from the video data (from the presence of a whitecap). Wave conditions experienced during the experiment consisted primarily of long-crested swell waves with significant wave heights of $0.4 - 0.7$ m and periods of $9 - 12$ s.

HORS, Japan 1994 (Kuriyama and Ozaki, 1996) Downward looking, ultra-sonic wave gauges were deployed at the HORS pier to monitor wave heights. The mode of breaking was identified by human observers who triggered a signal when active breaking occurred below the wave gauges. The significant wave heights during the observations ranged from $1 - 2.5$ m with wave periods from $6 - 13$ s.

The listed field studies are all restricted to a few point measurements and wave breaking is identified visually by human observation. More recently, the fraction of breaking waves has been estimated in the field from remote sensing using incoherent radar at the dynamic New River Inlet in North Carolina (Díaz Méndez et al., 2015) or infrared video at the FRF in Duck (Carini et al., 2015). At the same site, Catalán et al. (2011) combined collocated optical and radar to detect breaking. Although they did not compute the fraction of breaking waves explicitly, their data should also be usable to infer the breaking probability.

2.3 Microwave Scattering from the Ocean Surface

For traditional applications of marine radar (the identification and tracking of ships and other obstacles) the return signal from the ocean surface, the *sea clutter*, is an unwanted side-effect. However, an analysis of sea clutter within marine radar images offers great potential for geophysical applications. Within the present study, coherent marine radar is used for the analysis of surface waves. Some basic knowledge on radar technology and the theory of microwave scattering from the ocean surface is needed to understand how surface waves are imaged by marine radar.

This section gives an overview on the relevant background of marine radar for oceanographic applications. The technical principles of marine radars (typically operating at X- or S-band) are introduced in 2.3.1. The backscatter theory and modulations due to *surface tilt*, *hydrodynamic modulations*, the effect of *shadowing* and *sea spikes* are described in section 2.3.2. The last section 2.3.3 elaborates on the geophysical interpretation of the Doppler velocity which can be obtained from coherent radar backscatter. For a more detailed overview on the topic, the reader is referred to the paper collection on radio probing of the ocean surface edited by Phillips and Hasselmann (1986). Bole et al. (2014) give a good introduction to the technology of marine radar and Skolnik (2008) extensively describes the principles and technical aspects of radar in general.

2.3.1 Principles of Marine Radar

Within this section the principles of marine radar are explained briefly and common terminology and definitions are introduced. They are graphically composed in figure 2.5. The specifications of the radar used for this work are listed in table 2.2.

The term radar was originally an acronym for RAdio Detecting And Ranging, which represents the technical principle of using actively transmitted electromagnetic radiation to locate a reflecting target. However, the word radar has found its way to current language and the term is today more often used to describe the measurement device made for this purpose rather than the methodology behind. Thus, the word radar is used within this work in this sense as well. The term marine radar refers to radar that is used for (civilian) navigational purposes mostly on vessels.

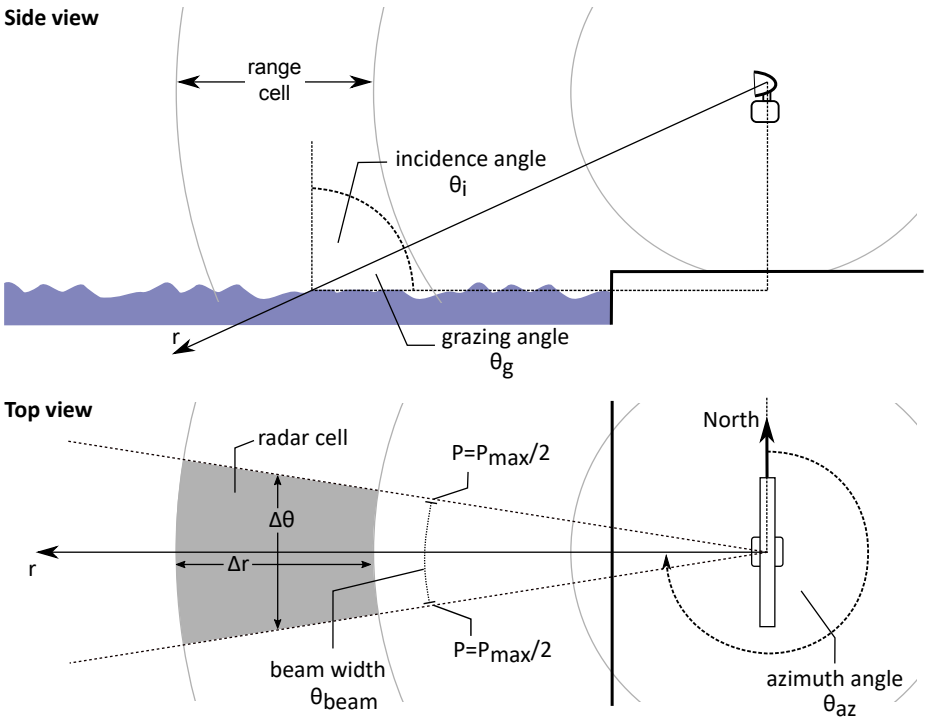

Figure 2.5: Terms and definitions regarding marine radar (modified from Lange, 2019)

Hardware specification	**Value**	**Related property**	**Value**
Signal generation			
Electromagnetic frequency f_{el}	9.48 GHz		
Electromagnetic wave length λ_{el}	0.03 m		
Magnetron power	12 kW		
Pulse duration	$50-70$ ns	Range resolution	7.5 - 10.5 m
Pulse-repetition-frequency (PRF)	2000 Hz	Time step	500 μs
Antenna			
Antenna polarization	VV		
Antenna length	2.3 m	Beam width θ_{beam}	$\approx 1^\circ$
Antenna installation height h_{ant}	28 m	Grazing angle θ_g	$\tan^{-1}\left(\frac{h}{r}\right)$
Signal digitization			
Sampling frequency	20 MHz	Range cell size Δr	7.5 m
Sampled range cells	435	Maximum range	3262.5 m
Distance to first cell	0 m		

Table 2.2: Specifications of the used X-band marine radar.

Electromagnetic frequency

The electromagnetic frequency f_{el} and the wave length λ_{el} of the electromagnetic waves has the largest influence on the propagation dynamics of the radar radiation. Longer waves are less affected by atmospheric attenuation and can therefore reach farther distances with lower signal power. There are two types of (civilian) marine radars (e.g. Bole et al., 2014), X-band radars operating at frequencies between 9.2 and 9.5 GHz ($\approx$ 3 cm long waves) and S-band radars between 2.9 and 3.1 GHz ($\approx$ 10 cm), respectively. This section focuses on X-band which is the radar used within the present study.

Antenna pattern

Most X-band marine radar antennas are designed as slotted wave guides, with either horizontal or vertical alignment of the slots. This defines the polarization of the antenna which is the same for the transmitted and received signal if only one antenna is used (usual setup for navigational radar). Marine radars for navigational purposes are usually horizontally polarized (HH). However, the return signal from surface waves at low winds seems to be stronger for vertically polarized (VV) antennas. The antenna also prescribes the antenna pattern, i.e the spatial distribution of the transmitted electromagnetic radiation. Figure 2.6 shows a typical antenna pattern of a marine radar antenna. A strong focusing of the transmitted energy along the pointing direction of the antenna is usually desired. The length of the antenna beam influences the horizontal beam opening angle θ_{beam}. Thus, it defines the azimuthal resolution of the radar. Longer antennas provide a better focusing of the radar beam in azimuth. The vertical opening angle of marine radar antennas is usually much larger ($> 23^{\circ}$) to make sure

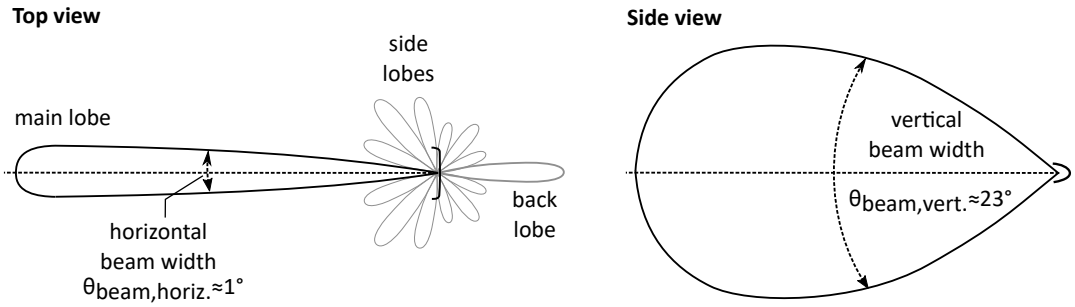

Figure 2.6: Typical antenna pattern of a marine radar.

that targets at the surface are always seen also when the ship is rolling. The transmitted signal is not only radiated in the *main lobe* along the view direction of the radar, but partially also radiates along so called *side lobes*. Depending on the antenna hardware, side lobe effects are more or less pronounced, but generally they are significantly (> 15 dB) weaker than the main lobe.

Radar pulse

Most marine radars are pulsed radars. The radar pulse is generated by the magnetron, which generates a high-power electromagnetic field with. Typical power levels of marine radars are 4 kW for river and $12-25$ kW for ocean usage. A 12 kW magnetron was used within the present study. The radiation is released in pulses which can have variable duration and are released at a specific pulse-repetition-frequency (PRF). The pulse duration is hereby much shorter than the time between two pulses which specifies the PRF. The terms pulse duration, pulse width and pulse length are often used interchangeably. They are usually specified in nanoseconds. Typical pulse widths of marine radar range from 50 ns (short pulse) to 1200 ns (extra long pulse). A longer pulse contains more energy. It can thus reach farther distances and is the standard setting for navigational use. However, because the radiation travels at the speed of light, the duration of a pulse is always directly related to the propagation distance of the radar radiation during this time period. Therefore, the range resolution of a radar is determined by the pulse duration. For hydrographic purposes, a good range resolution is desired and therefore the short pulse setting is used. A pulse duration of 50 ns corresponds to a 7.5 m long range cell that gets illuminated by the radar.

Oversampling and true ground resolution

As described above, the physical resolution (in range and azimuth) of the radar is governed by the dimensions of the antenna and the pulse width hence it is hardware specific. However, the true physical resolution is independent from the sampling resolution. The range cell size of the received signal depends on the frequency of the analog-to-digital (AD) converter. A 50 ns long pulse corresponds to 20 MHz and at this AD conversion frequency, the length of a sampled range cell corresponds to 7.5 m. Sampling at higher resolution results in oversampling and as a consequence a single target is mapped to multiple radar cells without providing further information. It is

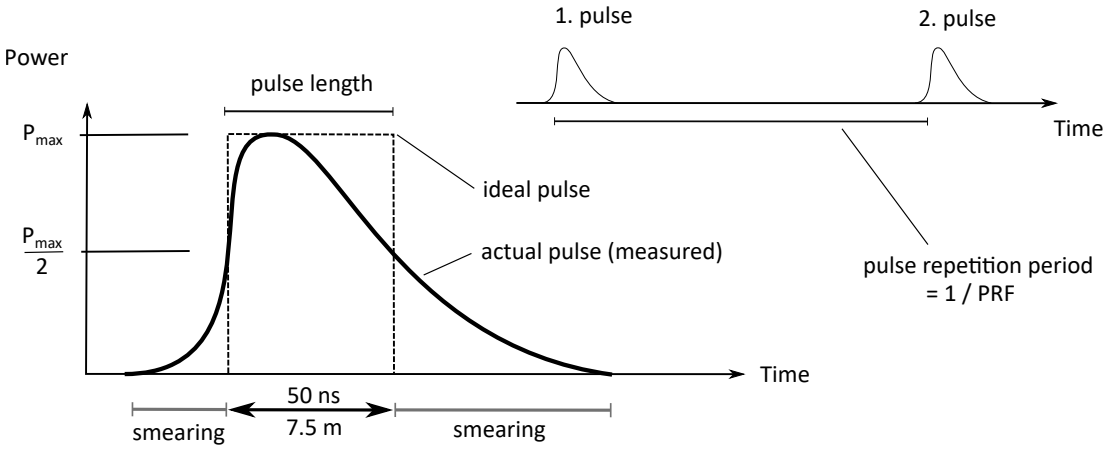

Figure 2.7: Shape of the transmitted radar pulse.

physically not possible to generate a rectangular pulse shape, where the energy increases instantaneously from zero to the maximum power level and drops again after the pulse duration. Pulses created by the magnetrons of marine radar typically show a rapid power increase and followed by a slower decreasing tail. The shape of the pulse of the radar used for the present work is shown schematically in figure 2.7. An actually measured pulse from the used radar is depicted in the appindix, figure A.1. The pulse width is usually defined as the time where the transmitted power exceeds more than half of the maximum level of the transmitted power during one pulse. In other words, the pulse ends when the transmitted power reaches -3 dB of of the maximum transmitted power. Similarly, the half power level also defines the edges of the main antenna lobe to determine the horizontal beam width (see fig. 2.5).

However, because there is also power below the half power limit a small portion of the signal from a target also appears in the neighboring radar cells, even if the spatial dimension of the target does not exceed the range cell size. This causes a "smearing" effect in the radar images which is further denoted as the *sensor impulse response* of the radar. Both the shape of the radar pulse and side lobe effects become important when objects causing a high backscatter are observed. The echo of a ship is usually smeared over one or two range cells due to the sensor oulse shape and sometimes multiple 'ghost echoes' of the same ship appear in a radar image due to side lobe effects.

Radar equation

The power of the received radar signal is given by the the radar equation

$$P_{rec} = \frac{P_{trans} G_{trans}}{4\pi r^2} \times \frac{\sigma}{4\pi r^2} \times A_e \ , \tag{2.23}$$

which is presented in this notation by Skolnik (2008) to emphasize the physical processes that take place. The radar transmits a power P_{trans} through the antenna with a device specific antenna gain G_{trans}. The first factor on the right hand side represents the power density at a certain range (i.e. distance) r from the radar. The power density diverges in three dimensions on its way from the antenna to the target. This yields a power decay proportional to $4\pi r^2$, which follows from the inverse-square law. The second factor represents the return signal from the target to the antenna. It experiences the same power decay on the way back to the antenna. The factor σ is called the radar cross-section (RCS) and represents the amount of returned radar energy from a specific target. The RCS has the unit of an area (i.e. m^2) and can only be determined for objects with very simple geometry, e.g. a sphere which reflects all incident radiation (and no energy is absorbed by the target). The third factor, A_e, is called effective area of the antenna and represents the portion of the returned power P_{rec} that is collected by the antenna.

For hydrographic purposes, the return signal from the ocean surface, the *sea clutter* gets analyzed. The illuminated area of a radar cell at the sea surface is proportional to r (as can be seen in fig. 2.5). This results in the fact that the power received by the radar is proportional to r^3 instead of r^4 as it would be predicted by the radar equation 2.23 (e.g Bole et al., 2014, sec. 2.7.4.1). The transmitted power P_{trans}, the antenna gain G_{trans} and the effective area of the antenna A_e are quantities that can change for individual radar setups, but are constant for a single radar installation. Thus they could be combined into one, hardware dependent constant K. The radar equation can than be written in a different form for sea clutter and the received power is defined as:

$$P_{rec} = \frac{K \sigma_S}{r^3}. \tag{2.24}$$

The RCS of an area of the sea surface σ_S depends on the properties of the sea surface within the area that is illuminated by the radar. The modulation mechanism that govern the backscatter from the ocean surface are introduced in the following section 2.3.2.

2.3.2 Modulation Mechanisms

This section lists the mechanisms that govern the modulation of the received radar backscatter from the ocean surface. The antenna only receives the part of the reflected signal that is re-directed towards the antenna. The slope of the sea surface is usually too small to cause specular reflection, which requires the reflecting surface area to be large compared to the radar wave length and oriented normal to the antenna line-of-sight. Therefore the scattering from the sea surface must have different reasons which will be listed in the following.

Bragg scattering and Composite Surface Model

At moderate incidence ($\theta_i = 10 - 70°$) it is generally accepted, that radar backscatter from the ocean surface is adequately described by the Bragg[1] scattering mechanism. Electromagnetic waves of length λ_{el} coherently interfere with short ocean surface waves of a certain Bragg-resonant wave length with the Bragg wave number

$$k_B = 2\, k_{el}\, \sin\theta_i \,, \tag{2.25}$$

where $k_{el} = 2\pi/\lambda_{el}$ is the wave number of the electromagnetic waves. The received power (per unit surface area) can be computed according to Bragg theory (Valenzuela, 1978, and references therein) as

$$\sigma_0(\theta_i)_{ij} = 4\pi\, k_{el}^4\, \cos^4 |g_{ij}(\theta_i)|^2\, W(k_B, 0) \tag{2.26}$$

where $W(k_B, 0)$ represents the wave number spectral density of the Bragg resonant waves in the antenna view direction, thus it depends on the amplitude of the Bragg waves. The indices ij denote the polarization of the radiated and back-scattered electromagnetic waves and $g_{ij}(\theta_i)$ are scattering coefficients, that are

$$g_{HH}(\theta_i) = \frac{(\varepsilon_r - 1)}{\left[\cos\theta_i + \sqrt{\varepsilon_r - \sin^2\theta}\right]^2} \,, \tag{2.27}$$

[1] named after Lawrence Bragg and his father Sir Henry Wilhelm Bragg who discovered this resonance condition for X-ray radiation incident on a crystalline solid

for HH polarization and

$$g_{VV}(\theta_i) = \frac{(\varepsilon_r - 1)\left[\varepsilon_r(1+\sin^2\theta_i) - \sin^2\theta_i\right]}{\left[\varepsilon_r\cos\theta_i + \sqrt{\varepsilon_r - \sin^2\theta_i}\right]^2}\,, \tag{2.28}$$

for VV polarization, where ε_r is the relative dielectric constant of the ocean. For marine radar this Bragg-resonant wave length is in the range of centimeters (≈ 1.5 cm for X-band). Marine radar therefore 'sees' waves that would be recognized by the human eye as surface roughness (cm scale waves). This small scale roughness is almost always present, as long as the wind speeds exceeds a value of $\approx 3m/s$.

The Bragg model assumes a flat and equally rough surface where radar radiation is incident under a clearly defined angle. This assumption is not true for the ocean surface. For this reason, the surface can be treated as a surface composed of an infinite number of facets, each of them being locally plane and tilted, thus changing the local incidence angle. This is called the *composite surface theory* and was proposed by Bass et al. (1968) and in the same year by Wright (1968) . The local incidence angle of the facets depends on the surface slope on the scale of the dominant wind waves that are much longer compared to the Bragg waves ($k << k_B$). Therefore, this modulation mechanism is called *tilt modulation*. Orbital motions of the longer waves additionally influence the amplitudes of the Bragg waves (Alpers et al., 1981) causing a *hydrodynamic modulation* of the radar signal. A similar effect can be observed at convergent or divergent surface flow fields as they occur for example when tidal currents pass the crests of underwater sand dunes (Hennings and Herbers, 2006). Romeiser et al. (1994) propose a *three scale composite surface model*. In their model, the modulation of the radar signal is decomposed into three scales. The smallest is the scale of the Bragg resonant waves. The Bragg waves are modulated by waves significantly longer than the Bragg waves but still shorter than the length of a radar resolution cell. The third wave scale is longer than the radar range cells and modulates both, the subgrid wave scale and the Bragg waves.

While the composite surface model matches observations for moderate incidence angles, it is known that at grazing incidence ($\theta_i > 85°$) other scattering mechanisms become significant (Valenzuela, 1978). Catalán (2008) provides an extensive review of low grazing angle (LGA) scattering mechanisms other than Bragg scattering. However, there is no generally accepted scattering model available yet that is able to repro-

duce radar backscatter from the ocean surface measurements at LGA.

Sea spikes

Steep and breaking waves are known to cause very high radar backscatter intensities, known as *sea spikes*. Many authors studied the influence of breaking waves of different scales on microwave backscatter (Phillips, 1988; Lee, 1995; Haller and Lyzenga, 2003; Hwang et al., 2008a,c, among others). Sea spikes have a more pronounced effect for HH polarization compared to VV and polarization ratios σ_{HH}/σ_{HH} are close to unity for actively breaking waves, which indicates that the same scattering mechanisms are active. Some approaches to explain the origin of sea spikes within radar backscatter including *multi-path effects* (Sletten and Wu, 1996), *volumetric scattering* (Wetzel, 1986), or increased roughness due to *bound waves* at the front face of a breaker (Plant, 1997). However, an accurate modeling of the backscatter resulting from breaking waves is not needed for many purposes and it is enough to consider the bulk effect of breaking on the backscatter, i.e. a significantly higher backscatter intensity. This will be shown and discussed within chapter 4 of the present thesis.

Shadowing by waves

Radar radiation, especially for VV polarization, can also illuminate parts of the wave profile that are geometrically shadowed (visible light would not reach those parts). Therefore, the term "shadowing" might be misleading as it implies a geometrical shadowing assumption. However, for HH polarized microwave backscatter at grazing incidence the geometrical shadowing assumption was proposed in literature to be a reasonable assumption (Nieto Borge et al., 2004). Plant and Farquharson (2012) investigate the effect of shadowing and conclude that it does not play a significant role for LGA backscatter. All in all, there is no commonly accepted shadowing model available by now. This is mainly due to the fact that the problem itself depends on two non-linear phenomena, the sea state and the electromagnetic wave propagation, respectively. Solving Maxwell's equations, the fundamental equations for electromagnetic waves, is computationally expensive because a discretized representation of the simulation domain on a computational grid fine enough to resolve the electromagnetic wave (grid spacing several times smaller than the electromagnetic wave length) is necessary. At the same time, the sea surface used within the simulation must be discretized

with a similar resolution. This is also not straight forward because short, wind driven (young) waves are known to be highly asymmetric, hence non-linear. Moreover, the shadowing characteristics are also expected to depend of the characteristics of the utilized radar system. A highly sensitive system with a high transmit power might be able to image a larger fraction of the wave profile compared to a less powerful system (Plant and Farquharson, 2012).

Speckle

Speckle noise is a phenomenon that results from random interference of coherent radiation incident on a rough surface (Goodman, 1976). This effect is probably known to most people from the appearance of a spot of laser light obliquely incident on a piece of white paper. The illuminated area consists of several extremely bright spots that stand out from the average brightness. The same effect is apparent for coherent radar backscatter. This is due to the fact, that many scatterers contribute to the backscatter within one radar illumination cell for a rough surface. The part of the signal for each of the scatterers has a different, randomly distributed, amplitude and phase. Some may cause a coherent interference that causes noise within the radar record.

2.3.3 Doppler Velocity

If the received radar signal is coherent, it is possible to determine the Doppler frequency caused by a movement of the target relative to the antenna. This Doppler shift frequency

$$f_d = \frac{2\, v_d}{\lambda_{el}} \cos(\alpha) \tag{2.29}$$

depends on the Doppler speed v_d of the target and the angle α between the direction of the target movement and the line-of-sight of the radar antenna. The Doppler frequency shift can be determined from the recorded radar data either from consecutive pulse-pairs or by means of a spectral analysis. Both approaches are explained in more detail within sec. 3.5. There is an ambiguity of the observed frequency shift due to Nyquist's theorem and the maximum and minimum unambiguous Doppler frequency is the positive and negative Nyquist frequency $\pm f_{Ny} = \pm\,\mathrm{PRF}/2$.

For hydrographic applications of coherent marine radar, the Doppler frequency shift results from the movement of the scattering roughness elements at the ocean sur-

face. However, the geophysical interpretation of this shift frequency it not trivial. The Doppler velocity may be seen as a superposition of several contributions

$$U_d = U_{Bragg} + U_{curr} + U_{orb} + U_{break} + U_{graz} + U_{rem} \ , \tag{2.30}$$

where U_{Bragg} is the phase speed of the Bragg waves, U_{curr} is the ambient current, U_{orb} are wave orbital motions, U_{break} is the breaking wave contribution and U_{graz} is an additional Doppler shift that is apparent at extremely grazing incidence. U_{rem} contains any other influences on the Doppler velocity. A good understanding and the ability to unscramble the individual contributions is crucial for a proper interpretation of the Doppler velocity for geo-scientific purposes. However, the radar imaging is a complex non-linear problem and far from being completely understood. The results presented in chapter 4 of the present thesis and the Doppler ensemble classification algorithm presented in chapter 5 add to the general understanding of the Doppler signal.

2.4 Numerical Models for Breaking Waves

The flow field within breaking waves is mathematically well described by the fundamental equations of fluid motion based on the conservation of mass and momentum, i.e the Navier-Stokes equations. However, the set of differential equations cannot be solved analytically and numerical approximations require an extremely high model grid resolution in order to resolve the flow field down to the scales at which turbulence is finally dissipated into heat. This is computationally costly and despite the rapidly growing computational resources still not feasible for large scale problems which cover larger areas or long time periods. Certain aspects of the flow are therefore simplified and parameterized in order to improve numerical efficiency. The amount of simplification that is required depends on the available computing resources and the temporal and spatial scale of the problem that is to study.

Available types of numerical models are listed in figure 2.8. They are arranged with respect to the geophysical processes that can be modeled and the amount of simplification that is included within the respective model type. Each model type is listed in the following and evaluated with respect to the assumptions taken in order to account for wave breaking. The listing is sorted regarding the amount of simplification needed, starting with the model that is considered most accurate (bottom to top in fig. 2.8). The

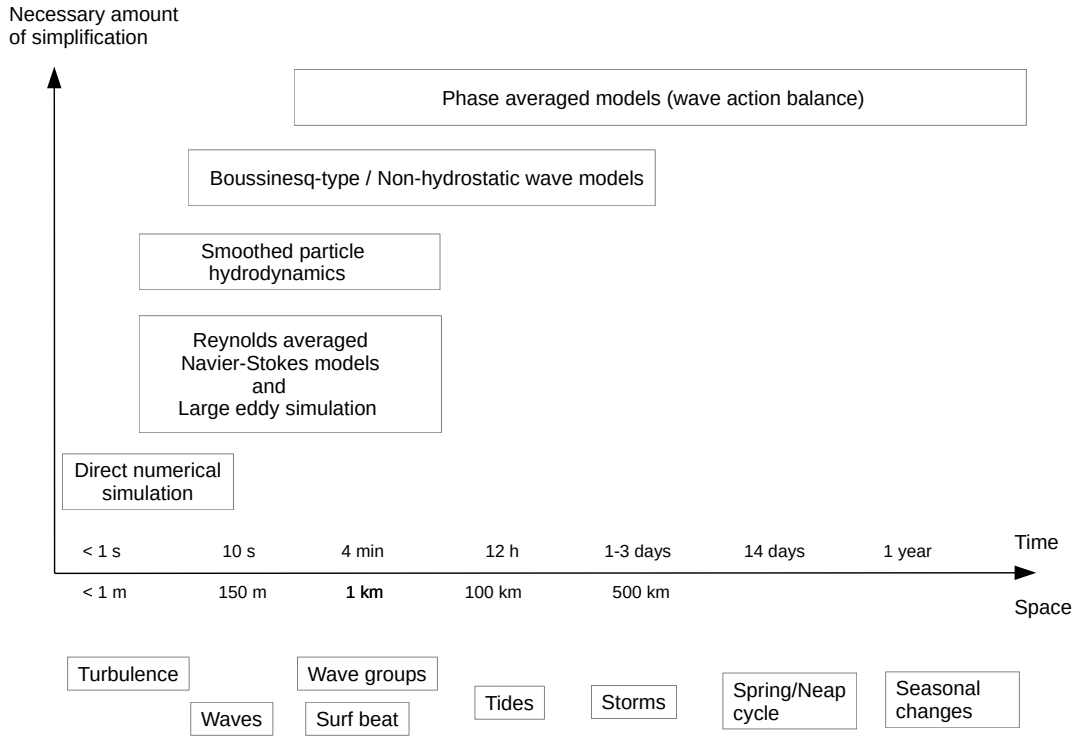

Figure 2.8: Applicability of different wave models regarding their spatial and temporal scale and extent together with the covered wave related geo-physical processes.

models are furthermore categorized into *phase-resolving* models (sec. 2.4.1), which simulate the transient and rapidly varying free surface flow problem in a deterministic manner, and *phase-averaged* models (sec. 2.4.2) where only the statistical properties of the sea state are simulated, i.e the evolution of the wave spectrum. Section 2.4.3 introduces available parameterizations for depth induced breaking of random waves that are used within phase-averaged wave models. Finally, the choice of models that are used for the purpose of the present thesis is explained in sec. 2.5.

2.4.1 Phase-Resolving Models

Hydrodynamics in the nearshore represent an intransient flow problem within two media, i.e. sea water and air. The fundamental equations to describe the kinematics and dynamics in liquids and gases, i.e. the fluid dynamics, are the incompressible Navier-

Stokes equations, which are based on the conservation of mass and momentum (e.g. Svendsen, 2006). As the principle concept of fluid dynamics, they will be introduced here without further explanation. The continuity equation (mass conservation) reads

$$\nabla \cdot \mathbf{v} = 0, \tag{2.31}$$

where bold symbols indicate vector quantities and $\nabla = (\frac{\partial}{\partial x}, \frac{\partial}{\partial y}, \frac{\partial}{\partial z})$ and $\mathbf{v} = (u, v, w)$ are the three components of the flow velocity. The momentum equation is given by

$$\frac{\partial \mathbf{v}}{\partial t} + (\mathbf{v} \cdot \nabla)\,\mathbf{v} = -\frac{1}{\rho}\nabla p + \mathbf{g} + \nu \nabla^2 \mathbf{v}\,, \tag{2.32}$$

where ρ is the fluid density, p is pressure, $\mathbf{g} = (0, 0, g)$ the gravity tensor, and ν the kinamatic viscosity of the fluid. The left-hand side of eq. 2.32 is the Eulerian notation of the temporal and spatial evolution of the fluid velocity, while the right-hand side represents the forces acting on the fluid. The first summand reflects the internal pressure, the second the gravitational acceleration and the third represents the viscous stresses inside the fluid.

Direct numerical simulation

Solving the full Navier-Strokes equations on a grid that is fine enough to resolve the internal viscous stresses inside the fluid is called *direct numerical simulation (DNS)*. The scale that needs to be resolved by the computational grid of the DNS is determined by the Kolmogorov length scale

$$L_k = \left(\frac{\nu^3}{\varepsilon}\right)\,, \tag{2.33}$$

where ν is the kinematic viscosity of the sea water and ε is the turbulence dissipation rate. Turbulence dissipation rates under energetic breaking waves in the surf zone can exceed 10^2 m^2/s^3 (George et al., 1994). Therefore, DNS of energetic breaking waves requires a very fine numerical grid in space (sub-millimeter) and time (milliseconds). While DNS is a valuable and important tool for theoretical and fundamental studies of breaking waves (so called numerical experiments), it's practical applicability is still limited to a small number of individual wave breaking events (e.g. Chen et al., 1999; Song and Sirviente, 2004; Fuster et al., 2009). This may change in future as more and

more computational resources become available.

Viscous dissipation is fully captured by the model equations hence there is no wave breaking parameterization needed when DNS models are used. The air entrainment related to wave breaking is considered to directly generate vorticity (Chen et al., 1999) and is therefore also captured by DNS when both phases (air and water) are modelled.

Large eddy simulation / Reynolds averaged Navier-Stokes models

In order to extend the area and time span of the models, it is possible to increase the grid cell sizes by replacing the kinematic viscosity inside eq. 2.32 by an eddy viscosity ν_t. The eddy viscosity then represents the effect of sub-grid turbulence and must be parameterized. Two different concepts exist which are *Large eddy simulation (LES)* (e.g. Meneveau and Katz, 2000) or *Reynolds averaged Navier-Stokes (RANS)* models (e.g. Kajishima and Taira, 2017). For LES, the Navier-Stokes equations are low-pass filtered in order to decompose the flow problem into an eddy resolving scale and an un-resolved smaller scale where the effect of sub-grid turbulence on the flow is parameterized, e.g. with the Smagorinsky model (Smagorinski, 1963). Instead, RANS models parameterize all scales of turbulence hence the flow is decomposed into (ensemble averaged) mean flow component and turbulent fluctuations (Reynolds decomposition). The production and transport of turbulence must be computed by applying a so called turbulence closure scheme, such as the $k-\varepsilon$-model (Launder and Spalding, 1974), the $k-\omega$-model (Kolmogorov, 1942; Saffman, 1970) or the Prandtl mixing length model (Prandtl, 1925). The practical applicability of LES and RANS models spans an area covering a few wave lengths and time spans of a few wave periods, thus numerical studies that use this model type do focus on a small number of exemplary waves (Torres-Freyermuth et al., 2007; Christensen and Deigaard, 2001; Christensen, 2006; Lubin et al., 2006).

The fully non-linear wave evolution and propagation up to the break point, and also the post-breaking wave evolution is covered by the LES and RANS models. Only the parameterization of the sub-grid turbulence affects the model skill in simulating wave transformation during breaking.

Smoothed-particle hydrodynamics

Smoothed-particle hydrodynamics (SPH) was originally developed in the field of astrophysics (Gingold and Monaghan, 1977; Lucy, 1977) and later also used to model breaking surface waves (Monaghan et al., 1994; Dalrymple and Rogers, 2006; Shao, 2006; Shao and Ji, 2006). In order to simulate breaking waves, SPH is basically similar to RANS or LES models in the sense that the same equations are solved numerically. The difference between both model types is the way the computational domain is discretized. In contrast to the structured grids that are usually used to discretize the domain for LES or RANS models, SPH is a Lagrangian and mesh-free approach. The water body is in SPH simulations approximated by virtual particles that represent the bulk mass, momentum and viscous stresses of a group of water molecules, that can be considered as homogeneous. During the simulation, the free particles interact and exchange mass, momentum and turbulence quantities. The accuracy of SPH models can be improved by including more particles into the simulation. The computational costs are similar to LES or RANS models.

A turbulence parameterization is also needed for SPH, in order to represent the effect of sub-grid turbulence (i.e. here the turbulence within the volume represented by a discrete smoothed particle). Therefore, regarding the representation of wave breaking the same restrictions as for LES or RANS models also apply for SPH.

Boussinesq-type models / non-hydrostatic wave models

Further computational efficiency can be reached by vertical integration of the Navier-Stokes equations, yielding the non-linear shallow water equations (NLSWE), which for the special case of one-dimensional flow are called Saint-Venant equations (de Saint-Venant, 1871). The NLSWE neglect the effect of non-hydrostatic pressure which is acceptable for long waves and hence they are often used to simulate tsunami propagation. However, non-hydrostatic (dynamic) pressure effects are not negligible to simulate short wave propagation. Two different model types were therefore developed both aiming to account for dynamic pressure effects within the NLSWE, *Boussinesq-type* models and *non-hydrostatic* wave models, respectively.

Boussinesq-type wave models add higher order terms that resemble the vertical pressure effects to the NSLWE and are widely used to simulate nearshore wave propagation (Peregrine, 1967; Schäffer et al., 1993; Nwogu, 1996; Lynett, 2006; Johnson and

Pattiaratchi, 2006; Roeber et al., 2010). A detailed overview on Boussinesq-type models was given by Hamm et al. (1993) and more recently by Brocchini (2013). *Non-hydrostatic wave models* include the effect of vertical pressure on the flow by solving the equation for the vertical distribution of the pressure (i.e. Poisson's equation) with only a small number grid points in the vertical (at least two) using the so called Keller-box scheme (Zijlema and Stelling, 2005; Ma et al., 2012). The accuracy of the model in terms of the short wave propagation dynamics, i.e. frequency dispersion, can be improved by increasing the number of vertical layers. For a large number of vertical layers, the non-hydrostatic wave models are eventually equal to a RANS model.

Both, Boussinesq-type models and non-hydrostatic wave models with a small number of vertical layers can well reproduce nonlinear propagation and shapes (skewness and asymmetry) of individual waves and the modes inherently account for non-linear wave-wave interactions. However, the correct estimation of dissipation by wave breaking needs a particular treatment which is realized differently in literature. Schäffer et al. (1993) parameterize breaking by including effects of surface rollers that artificially remove momentum when breaking is present. Kennedy et al. (2000) represent breaking with an adopted eddy viscosity formulation. A different approach was used by Tissier et al. (2011) and later by Smit et al. (2013), who switch of the non-hydrostatic pressure contirbution for the parts of the domain affected by breaking. The flow field within the breaker is then similar to a hydraulic jump which is a common assumption to represent energy dissipation of a breaking wave (see sec. 2.1.4). Note that within all of these approaches to incorporate breaking dissipation, a dedicated criterion that defines the onset and cessation of wave breaking is needed.

2.4.2 Phase-Averaged Models

In the previous section 2.4.1, phase-resolving wave models were introduced. Starting from direct numerical solutions of the Navier-Stokes equations, different simplifications to reduce computational cost were listed. The most efficient phase-resolving wave models available are Boussinesq-type models and non-hydrostatic wave models, respectively. However, models with significantly lower numerical costs are needed if the problems of interest span over large coastal areas (> 100 km^2) or last over longer periods (i.e. over years or decades).

Wave action balance

Phase-averaged wave models reach the required efficiency by discarding the deterministic information about the surface elevation and velocity and instead consider the random sea surface elevation, i.e. the sea-state, as a superposition of independent harmonic waves with random phases (as described in sec. 2.1.2). The evolution of the wave spectrum $S(\mathbf{k},\mathbf{x},t)$ in Cartesian space is given by the wave action balance equation (sometimes called the radiative transfer equation) that was initially proposed by Hasselmann (1960). Today this equation is the basis of almost all modern wave forecast models like WAM (Hasselmann et al., 1988), SWAN (Booij et al., 1997), WAVEWATCH III® (WW3DG, 2019), WWM-II (Roland et al., 2012). It describes the evolution of the wave action density $S(\mathbf{k},\mathbf{x},t)/\sigma(\mathbf{k},\mathbf{x},t)$ as a function of wave number (which includes the wave direction), location and time (Komen et al., 1994)

$$\left\{\frac{\partial}{\partial t}+(\mathbf{c_g}+\mathbf{U})\,\frac{\partial}{\partial \mathbf{x}}\,-(\nabla_x\Omega)\frac{\partial}{\partial \mathbf{k}}\right\}\left(\frac{S}{\sigma}\right)=S_{in}+S_{nl}+S_{ds}\;, \tag{2.34}$$

where $\mathbf{k}=(k_x,k_y)$ is the wave number vector, $\mathbf{x}=(x,y)$ the location, $\mathbf{c_g}=\partial\omega/\partial\mathbf{k}$ the group velocity (eq. 2.8) and $\mathbf{U}=(U_x,U_y)$ the ambient current. $\Omega=\sigma+\mathbf{k}\,\mathbf{U}$ is the Doppler shifted radial frequency and σ is the intrinsic frequency. ∇_x denotes spatial differentiation. For a complete derivation of the wave action balance equation the reader is referred to ch. I.2 in Komen et al. (1994). The summands on the left-hand side of eq. 2.34 represent the evolution in time, advective transport and wave-current interactions, respectively. On the the right-hand side are the sources and sinks of wave action, which are separated into a source term for energy input S_{in}, non-linear wave-wave interactions S_{nl} and dissipation S_{ds}. The model source terms must be parameterized as for most of them there are no analytical solutions available (e.g. Holthuijsen, 2007). The dissipation source term is often further separated into dissipation by bottom friction, vegetation and wave breaking, while breaking in deep water (whitecapping) is traditionally treated separately from depth induced wave breaking. The latter will be further discussed in sec. 2.4.3.

Nearshore wave energy balance

For some nearshore applications the complexity of the wave action balance equation can be significantly reduced. For the special case of a stationary, alongshore uniform

situation, where the wave spectrum is narrow banded and waves are traveling normal to shoreline, the spatial distribution of the wave energy is conserved along a cross-shore transect in the absence of currents. Energy input by wind and frictional losses at the bottom can be neglected if the area of interest is small. Under this circumstances the spatial distribution of wave energy E_w can be estimated from the energy flux balance

$$\frac{\partial F_w}{\partial x} = -D_w \ , \tag{2.35}$$

where $F_w = E_w c_g = \frac{1}{8}\rho g H_{rms} c_g$ is the flux of local wave energy (see also eq. 2.9) and D_w is the dissipation of wave energy due to breaking. In the nearshore, in particular within the surf zone, dissipation by depth induced wave breaking usually dominates and dissipation by whitecapping and bottom friction is negligible (e.g. Thornton and Guza, 1983). D_w must be approximated from a parameterization for depth induced wave breaking which will be introduced in sec 2.4.3.

Roller energy balance

Svendsen (1984) showed that the surface roller, i.e. the detached aerated water mater mass at the front face of a breaking wave (see also sec. 2.1.4), transports a certain amount of mass and momentum and therefore it must be considered within the nearshore momentum balance. This can incorporated into nearshore energy balance by solving a second coupled balance equation for the flux of roller energy

$$\frac{\partial F_r}{\partial x} = D_w - D_\tau \ . \tag{2.36}$$

The roller energy flux $F_r = E_r \ c$ represents the transport of energy stored within the roller E_r by the breaking wave with the characteristic velocity c, which is the phase speed of the wave. The roller is fed from the energy removed from the waves by breaking hence D_w in eq. 2.35 is a source of roller energy. Following Duncan (1981), the dissipation of roller energy $D_\tau = \overline{\tau} c$ can be computed from the work done by the mean Reynolds stress $\overline{\tau}$ at the boundary between the roller and the underlying water body (eq. (2.21) in sec. 2.1.4) and depends on the the geometric properties of the roller and the propagation speed of the wave. In order to close the roller flux balance, the roller's geometrical quantities can be related to the roller energy (Deigaard and

Fredsøe, 1989; Nairn et al., 1990) which yields for the roller dissipation

$$D_\tau = \frac{2E_r g \beta_s}{c}, \tag{2.37}$$

where β_s is a calibration coefficient related to the slope of the breaking wave front.

An inclusion of roller effects into the nearshore momentum balance brings significant improvements in modeling the wave driven circulation in the nearshore (Lippmann et al., 1996). However, the amount of energy D_w that is shifted from the organized wave motions to the surface roller must still be estimated from an appropriate parameterization for the dissipation of energy by depth induced breaking. The following section provides an overview about available parameterizations for depth induced wave breaking.

2.4.3 Parameterizations for Depth Induced Wave Breaking

This section depicts an overview of parameterizations that are commonly used to describe the depth induced wave breaking source term and will be used within the later parts of this thesis. The listing is limited to formulations that are applicable to random sea states, i.e parameterizations that can be used to compute the source term that is needed within phase-averaged wave models which were introduced in sec. 2.4.2. The different formulations are listed in table 2.3 and will be explained in the following.

Basic concept of the depth induced wave breaking source term

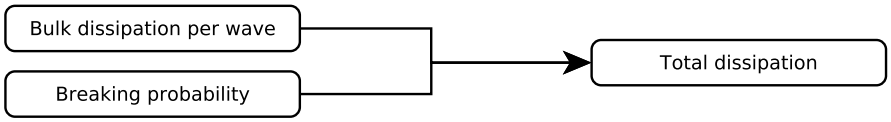

Figure 2.9: Basic concept for the parameterization of depth induced breaking

In a random sea state, the amount of energy dissipated by breaking depends on two factors, the number of breaking waves and the intensity of each breaker, i.e. the amount of dissipated energy per wave (see fig. 2.9). Two components must therefore be known to compute overall dissipation D_w. These are the bulk dissipation of an individual wave

Parameterization	**Breaking probability**	**Free parameters**
BJ78 (Battjes and Janssen, 1978)	clipped Rayleigh	2 (γ, B)
TG83 (Thornton and Guza, 1983)	weighted Rayleigh	3 (γ, n, B)
W88 (Whitford, 1988)	weighted Rayleigh	2 (γ, B)
B98 (Baldock et al., 1998)	step weighted Rayleigh	1 (B)
JB07 (Janssen and Battjes, 2007)	step weighted Rayleigh	1 (B)
CK02 (Chawla and Kirby, 2002)	weighted Rayleigh	2 (γ, B)
FA12 (Filipot and Ardhuin, 2012)	weighted Rayleigh	2 ($\tilde{\beta}$, B_{dw})

Table 2.3: Common parameterizations for depth induced wave breaking with the corresponding type of the empirical formulation of the breaking probability as well as the number of calibration parameters. All formulations rely on the bore analogy and the assumption that the wave heights are Rayleigh distributed.

$\langle D \rangle$ and the breaking wave height probability distribution $P_b(H)$, where $P_b(H) \leq P(H)$ because $P_b(H)$ is a subset of the probability distribution of wave heights $P(H)$. The overall breaking probability is called the fraction of breaking waves $Q_b = \int_0^\infty P_b(H) dH$.

The first basic assumption behind all formulations listed here is that the energy dissipation of a breaking wave can be approximated using eq. 2.20 from the similarity of breaking bores and hydraulic jumps as it was already elucidated within 2.1.4. The second assumption is that wave heights are Rayleigh distributed hence the distribution of wave heights is given by eq. 2.11. The validity of the Rayleigh distribution of wave heights in shallow water is questionable because the distribution of the surface elevation for non-linear waves is not anymore Gaussian. A discussion of the deviations from the Rayleigh distribution is given by Goda (2010). However, given the parametric nature of the wave breaking source terms the Rayleigh distribution is commonly considered as a reasonable approximation for the wave height distribution also inside the surf zone (Thornton and Guza, 1983).

Those two assumptions, the bore analogy and the Rayleigh distribution of wave heights are part of almost all available parameterizations for depth induced wave breaking. Therfore, the main difference between the different formulations is in how the breaking probability is approximated from the wave height distribution. The parameterizations used within the present study (liseted in tab. 2.3) are introduced in the following.

BJ78 Battjes and Janssen (1978) (referred further as BJ78) assume that the maximum wave height of a breaking wave H_b is defined by the modified Miche-type breaker criterion (eq. 2.17) and that every breaking wave always has this critical height. With these assumptions the probability distribution of breaking waves is described by the transcendental relationship

$$\frac{1-Q_b}{\ln Q_b} = -\frac{H_{rms}^2}{H_b^2} \ , \tag{2.38}$$

which can be solved iteratively to compute the fraction of breaking waves Q_b. Because the wave height of all breaking waves is considered to be specified by H_b, the bulk dissipation $\langle D \rangle$ of every individual breaking wave is constant and given by eq. 2.20, hence the total dissipation can be computed from the product of the bulk dissipation and the breaking probability as

$$D_{BJ} = \langle D \rangle \ Q_b = \frac{B}{4} f_{rep} \rho g H_b^2 \ Q_b \ , \tag{2.39}$$

where f_{rep} is a frequency that represents the avarage characteristics of the wave field. Note that BJ78 argue that the water depth is approximately similar to the wave height for depth induced breaking and therefore the dissipation rate after BJ78 scales with H_b^2, instead of H_b^3/d as it would follow from the bore dissipation (eq. 2.20).

TG83 Thornton and Guza (1983) (hereafter TG83) found from field measurements of surf zone waves, that the individual wave heights of breaking waves vary randomly and are not always prescribed by the critical height H_b as it was assumed in BJ78. Their measurements showed, that troughout the entire surf zone the distribution of wave heights (breaking and non-breaking) is reasonably well described by the Rayleigh distribution and that the breaking wave height probability distribution can be described by

$$P_b(H) = P_r(H) \times W(H), \tag{2.40}$$

where $W(H)$ is an empirically found weighting function to describe the subset of breaking waves. They propose two formulations for $W(H)$ one being as simple as possible and another one that better matches the observed breaking probabilities. The former (eq. 20 in the original paper and here denoted further as TG83eq20) reads

$$W(H) = \left(\frac{H_{rms}}{\gamma d} \right)^n \leq 1, \tag{2.41}$$

where the exponent $n = 4$ was found to fit best, and the latter (eq. 21 in TG83 denoted here as TG83eq21)

$$W(H) = \left(\frac{H_{rms}}{\gamma d}\right)^n \left[1 - \exp\left(-\left(\frac{H}{\gamma d}\right)^2\right)\right] \leq 1 \,, \tag{2.42}$$

with $n = 2$. Again following the bore analogy, the average rate of energy dissipation is then given by

$$D = \frac{B^3}{4}\rho g \frac{f_{rep}}{d}\int_0^\infty H^3 P_b(H) dH \,. \tag{2.43}$$

Inserting eq. 2.41 in eq. 2.40 and in 2.43 yields

$$D_{TGeq20} = \frac{3\sqrt{\pi}}{16}\rho g \frac{B^3\, f_{rep}}{\gamma^4\, d^5} H_{rms}^7 \,, \tag{2.44}$$

and similarly

$$D_{TGeq21} = \frac{3\sqrt{\pi}}{16}\rho g B^3 f_{rep}\frac{H_{rms}^5}{\gamma^2 d^5}\left[1 - \frac{1}{\left(1 + \left(\frac{H_{rms}}{\gamma d}\right)^2\right)^{2.5}}\right] \,, \tag{2.45}$$

when eq. 2.42 is considered.

Note that the scaling factor γ influences the shape of the weighting function $W(H)$. This is not directly similar to the function of the breaker parameter which is used within the breaker criterion (eq. 2.17) to estimate maximum height of a breaking wave. However, a change of γ within TG83 or in BJ78 results in the same effect, i.e. a change in the estimated probability of breaking.

W88 An alternative weighting function

$$W(H) = \left[1 + \tanh\left(8\left(\frac{H_{rms}}{\gamma d} - 0.99\right)\right)\right]\left[1 - \exp\left(-\left(\frac{H}{\gamma d}\right)^2\right)\right] \tag{2.46}$$

to be used within the TG83 model was proposed by Whitford (1988) and will be referred hereafter as W88. This equation is again of purely empirical nature and has no specific physical motivation, but the fact that its better suitable to match additional field data from the SUPERDUCK experiment on a barred beach (see sec. 2.2.3).

B98 / JB07 Baldock et al. (1998) (referred here as B98) proposed a more simplistic approximation for the wave breaking probability which was also adopted within the model of Janssen and Battjes (2007) (referred further as JB07). The JB07 parametrization is congruent with the model of B98, except for the fact that the H^3/d dependency is retained, instead of substituting it by H^2 as it was done by B98 who followed the assumption of BJ78, that the wave height of a breaking is approximately equal to the water depth. The same modification was coincidently also reported by Alsina and Baldock (2007) in the same year.

The JB07 parametrization assumes (similar to TG83) that the wave height distribution in both, breaking and non-breaking conditions always follows a Rayleigh distribution (eq. 2.11). However, they propose a more simplistic way for describing $P_b(H)$, assuming that all waves exceeding a critical wave height H_b are breaking, but different to BJ78 the breaking waves are not considered to be of the same height H_b, but can be also smaller. The fraction of breaking waves is then given by

$$Q_b = \int_0^\infty P_b(H)dH = \int_{H_b}^\infty P_r(H)dH \tag{2.47}$$

which can be solved analytically yielding

$$Q_b = \exp\left(-\left(\frac{H_b}{H_{rms}}\right)^2\right) . \tag{2.48}$$

This is much more practical compared to the transcendental relationship for Q_b within the BJ78 parameterization (eq. 2.38). However, there is again no physical justification for this way of describing the breaking probability. An integration of the bore-like dissipation rate for a single wave over all breaking wave heights yields the average dissipation rate per unit surface area

$$D_{JB} = \frac{3\sqrt{\pi}}{16} B\, f_{rep}\, \rho g\, \frac{H_{rms}^3}{d}\left[1 + \frac{4}{3\sqrt{\pi}}\left(R^3 + \frac{3}{2}R\right)\exp\left[R^2\right] - \mathrm{erf}(R)\right] , \tag{2.49}$$

where $R = H_b/H_{rms}$ and $H_b = \gamma d$. Similar to B98, also JB07 use an empirical relationship for the breaker parameter

$$\gamma = \frac{H_b}{d} = 0.39 + 0.56\, \tanh(33\, S_0) , \tag{2.50}$$

which depends on the offshore wave steepness $S_0 = (H_{rms}/L)_{\text{offshore}}$. Equation 2.50 is a slight modification of the expression proposed by Battjes and Stive (1985).

CK02 Chawla and Kirby (2002) (herafter CK02) studied current induced wave breaking at blocking points and show that the bore analogy can also applies to breaking waves in deep water if the vertical length scale (that in shallow water is governed by the water depth) is exchanged by an alternative scaling. Thus, they propose

$$D_{ck} = \frac{B}{8\pi}\,\rho g\,k\,H^3\sqrt{\frac{gk}{\tanh(kd)}} \tag{2.51}$$

to substitute the dissipation rate per wave (eq. 2.20). They also propose a slightly different weighting function

$$W(H) = \left[\frac{kH_{rms}}{\gamma\,\tanh(kd)}\right]^2 \left\{1 - \exp\left[-\left(\frac{kH}{\gamma\,\tanh(kd)}\right)^2\right]\right\}\,, \tag{2.52}$$

to be used in eq. 2.40 to compute the probability distribution of breaking waves. Equation 2.52 better matched the current induced breaking probability in deep water that was observed by Chawla and Kirby (2002) in the laboratory. However, in the free model parameters after calibrating there model using the observations were $B = 0.1$ and $\gamma = 0.6$, which is significantly different from the values used in shallow water studies.

FA12 Motivated by the findings of CK02, Filipot and Ardhuin (2012) (hereafter called FA12) propose a formulation for the dissipation rate of a breaking wave that is supposed to be applicable to both, deep and shallow water breaking waves. They add a hyperbolic tangent term to the CK02 formulation, that makes wave breaking more severe in shallow water (by increasing the scaling factor B). The dissipation rate after FA12 (per unit area) is defined as

$$D_{FA} = \frac{1}{8\pi}\rho g\,k\,\left(\frac{B_{dw}H}{\tanh(kd)^{1.5}}\right)^3\sqrt{\frac{gk}{\tanh(kd)}}\,. \tag{2.53}$$

The subscript of the calibration parameter B_{dw} indicates that the deep water value should be used here (which was 0.1 in CK02). In the study of FA12, $B_{dw} = 0.185$

provided the best fit to field observations. This description for the dissipation rate of a single wave is used by FA12 together with the wave breaking probability formulation of Filipot et al. (2010a) to develop a unified spectral parameterization for wave breaking, that is valid from deep to shallow water and matches a variety of available field observations. Note that the FA12 formulation is explicitly meant to be used within spectral wave models. Therefore the original formulation is formulated for different wave scales that could be used to asses the spectral distribution of the dissipation of wave energy. The reader is referred to the original paper for a description. Within the present thesis, a slightly modified version of the FA12 model is used in oder to apply the model to bulk formulation of the sea state (in terms of H_{rms} and a representative frequency f_{rep}).

The weighting function for the FA12 model to be used within eq. 2.40 in order to derive the breaking wave height probability distribution is defined as

$$W(H) = 1.5 \left[\frac{\beta_r}{\tilde{\beta}}\right]^2 \left\{1 - \exp\left[-\left(\frac{\beta}{\tilde{\beta}}\right)^4\right]\right\} , \tag{2.54}$$

where $\beta_r = k_{rep} H_{rms} / \tanh(k_{rep} d)$ and $\beta = k_{rep} H / \tanh(k_{rep} d)$. The representative wave number k_{rep} to describe the bulk sea state characteristics is found from the representative frequency f_{rep} applying linear wave theory. $\tilde{\beta}$ is a calibration parameter to scale the breaking probability. A value of $\tilde{\beta} = 0.42$ yielded good results.

Alternative scalings for depth induced wave breaking

A variety of studies are available where a better performance of the wave models for finite depth conditions is achieved by scaling the amount of total dissipation through an adjustment of the breaker parameter γ and hence the probability of breaking. The scaling approaches depend on different characteristic wave parameters, e.g. the offshore wave steepness (Battjes and Stive, 1985; Nairn et al., 1990), the relative water depth (Ruessink et al., 2003) or the bi-phase of the wave field as a measure of wave non-linearity (Van Der Westhuysen, 2010). A comprehensive overview of available scalings is given by Salmon et al. (2015), who also present a scaling approach that considers a combination of the local bottom slope and the relative water depth. However, these alternative scalings are not investigated further within this study because they all modify the breaking probability and not the dissipation rate. It will be shown

and discussed within chapter 7 of the present work that this is not expedient for the conditions analyzed here.

2.5 Conclusion and Model Choice

It was shown in section 2.4 that a variety of methods and models are available for the numerical simulation of breaking waves. The right model choice to study the problem at hand is mainly a trade-off between numerical efficiency and the required capability of the model to reproduce the effect of breaking on the flow.

The requirements for the models used for present work are twofold. First, an accurate representation of the internal kinematics of shoaling and breaking waves over a sub-tidal and an inter-tidal sandbar is needed. Second, the amount of energy dissipated by breaking must be estimated over a multi-day storm event. It is not feasible to use DNS for this study because the length and time scale is too large. A sub-grid turbulence parameterization is therefore required. Therefore, either RANS or SPH models are expected to be suited to fulfill the first requirement. However, simulating the entire storm event does not fall into the applicable range of these model types. A more efficient phase-resolving model type must be chosen, e.g. a Boussinesq-type model or a non-hydrostatic wave model. The Simulating WAves till SHore (SWASH) model (Zijlema et al., 2011) was selected for the purpose of the present study. SWASH can be run as a non-hydrostatic phase-resolving wave model, either depth-averaged or with a small number of vertical layers ($2-5$). In this setting its efficiency and accuracy is similar to Boussinesq-type models. However, if SWASH is used with a larger number of vertical layers (>10), the model is similar to a one-phase RANS model and (besides the turbulence closure formulation) there is no additional parameterization needed to account for the effect of wave breaking.

It was also mentioned in section 2.4.2, that phase-resolving wave models cannot be used anymore if the time and length scales of the studied problems further increase. For regional studies of the a series of storm events or even long-term studies of coastal waves hydro- and morphodynamics, further simplification is required and phase-averaged simulations are inevitable. Analytical source terms for the dissipation of wave energy by depth induced wave breaking are yet not existing. Available parameterizations used within phase-averaged wave models are exclusively based on empirical findings (as it was shown in sec. 2.4.3). Empirical models rely on obser-

vations to validate them and to reduce the amount of calibration parameters included, hence the uncertainty. However, most validation data sets stem from laboratory experiments because of the complexity and difficulties of carrying out nearshore wave measurements (see sec. 2.2) and in particular of observing wave breaking (sec. 2.2.3) in the field. The new remote sensing techniques to observe the wave breaking probability and energy dissipation that were developed within the present work can therefore significantly augment the observational basis needed to validate the models. In order to compare the new observations with available source term parameterizations, a simplistic phase-averaged wave model (see sec. 2.4.2) was additionally implemented. The model solves the coupled wave energy and roller energy balance (eq. 2.35 and 2.36) along a cross-shore transect. The breaking probability and wave energy dissipation is computed using the different source term parameterizations which were explained in section 2.4.3. A detailed description of the model setup and the forcing of the different model runs used within the present thesis is given in section 3.6.

Chapter 3

The WaveDiss Experiment - Materials and Methods

The "WaveDiss2016" field experiment was designed and planned as part of the present work. The campaign took place on the island of Sylt, Northern Germany, in September 2016. The experiment is dedicated to improving the general understanding of nearshore wave transformation over complex seafloor topographies as an important determinant for coastal morphodynamics. A major goal of the experiment is the development of reliable and efficient remote sensing techniques that will enable a long-term monitoring of the nearshore bathymetry as well as the (spatially variable) wave and current field at high resolution. Subject of the thesis is the wave breaking probability and energy dissipation which is one important aspects of this. The campaign provided the ground truth data for the radar remote sensing methods developed here.

In the first section 3.1, this chapter provides information about the study area where the experiment site is located. A second section 3.2 describes the design and planning of the field campaign, followed by a brief description of the environmental conditions during the campaign in section 3.3. Subsequently, section 3.4 lists and describes the instrumentation that was used. Within section 3.5, the data processing chain that was implemented to extract Doppler information from the coherent radar raw data is introduced. The numerical simulations that were conducted are presented in 3.6 and, finally, a brief discussion of the expected uncertainties is given in section 3.7.

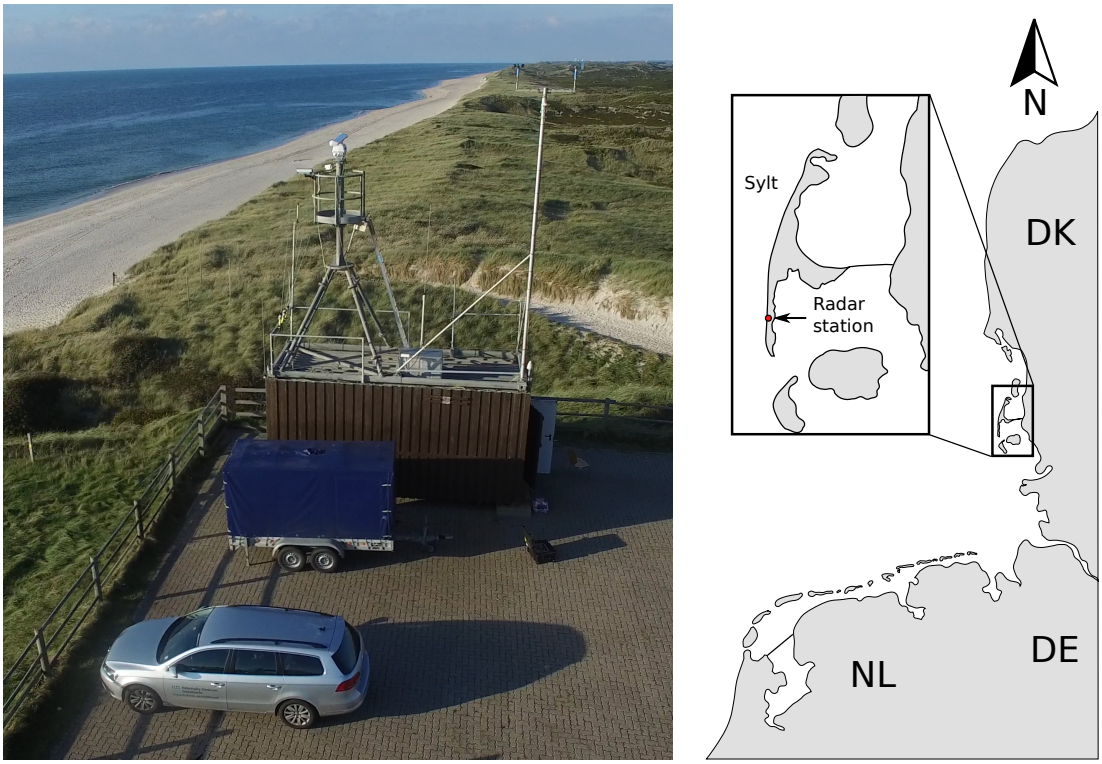

Figure 3.1: Location of the study site on the island Sylt in the German bight. Base map attribution: ©OpenStreetMap contributors.

3.1 Study Area

The experiment site is located on the island of Sylt in Germany. Sylt is a narrow barrier island in the German Bight separating the North Sea from the North Frisian Wadden Sea, an enclosed area consisting of several lagoons with large inter-tidal areas. The study area is located 4 km to the north of the southern tip of the island as illustrated in the map shown in figure 3.1. The whole span of the island from its northern to the southern tip is ≈ 40 km.

Hydrodynamic setting and beach morphology

The western coastline of the Island is a sandy, mixed energy coast (equally influenced by tidal currents and wave action) with a median grain size $D_{50} = 0.55$ mm (LKN.SH, 2015). Wind and waves are predominantly approaching the island from west-northwest. This was also the case during the study period. Tides in the area are semi-diurnal with a tidal range of 1 and 2 m for neap and spring tides, respectively.

Sylt stands out from the other Wadden Sea barrier islands in terms of the residual alongshore transport rates. For most of the islands, there is one clear orientation of the residual transport of sand (eastward for the southern islands and northward in the northern part). This is different for Sylt because the island has an inflection point in the middle of its span. The combined action of tidal currents and waves therefore leads to a net transport of sediments that is directed northward for the upper, and southward for the lower part of the island, respectively. The study site thus experiences a net southward transport of beach sediments. A total volume of ≈ 1.2 mio. m^3 of sand is artificially added yearly to the west coast of the island by regular beach nourishments in order to counteract the natural erosion of the beach face of $1-4$ m/yr (LKN.SH, 2019). Both, sub-tidal and inter-tidal sand bars are present within the study area as it can be seen from the surveyed bathymetry shown in figure 3.4. The sub-tidal bar gets active during high energetic wave conditions, but wave breaking terminates once the waves have passed the outer bar hence two breaker zones and a swash zone are present in stormy conditions. The crest location of the outer sand bar (≈ 500 m away from the shore) is quite stable and does not seem to undergo much seasonal variation. On the contrary, the breaker bar that is located within the inner surf zone (bar crest at 160 m from the shoreline), is highly dynamic and bathymetric changes can take place on time scales of hours or days. Low energetic swells ($H_s < 0.5$ m) from NW dominate during calm weather periods in summer and the oblique angle of wave attack forms a transverse bar and rip system (the reader is referred to Wright and Short (1984) for a definition of the beach states). In winter season, more energetic waves that are generated from high wind conditions, predominatly from west, flatten the beach profile and a ridge-runnel system is formed.

3.2 Experiment Design

The Helmholtz-Zentrum Geesthacht (HZG) operates a shore based, long-term radar and meteorology station (shwon in fig. 3.1) at the west coast of the island as well as a directional wave rider buoy located at 54.790° N 8.267° E, in a water depth of 10 m about 1 km off the coast. Both are part of the the Coastal Observing System for Northern and Arctic Seas (COSYNA, see Baschek et al., 2017). "WaveDiss2016" is part of a series of field experiments that were designed to augment the long-term measurements from the COSYNA station with high quality in-situ data.

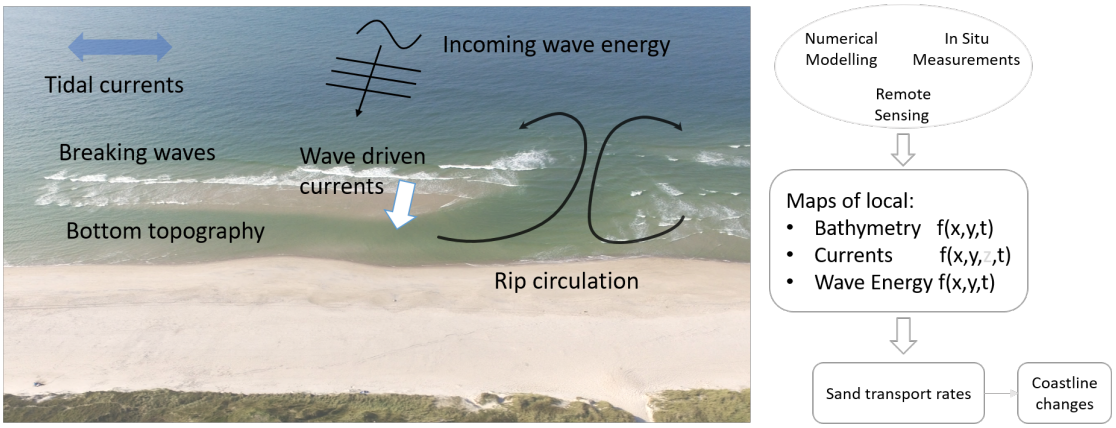

Figure 3.2: An artist's impression of hydro- and morphodynamic interactions in the nearshore (left) and available means to obtain geophysical quantities that govern sediment transport and mophological evolution (right). The image was taken in October 2015.

Long term research goals

The overarching goal of the research within the WaveDiss project is to study nearshore hydro- and morphodynamics. A key requirement to achieve this goal is the development of novel remote sensing techniques to enable a consistent and long-term monitoring of the wave dominated coastal hydro- and morphodynamics at time scales of hours to days and spatial scales of meters. This will create the required data basis for the development and testing of numerical models and parameterizations which is still not available because conventional (affordable) monitoring strategies cannot provide continuous information. The monitoring strategies developed within WaveDiss are therefore supposed to significantly push forward the general understanding of the physical processes that govern coastal dynamics, such as wave driven sediment transport and coastline changes that are strongly linked to wave breaking. Figure 3.2 gives an impression about the processes that drive nearshore hydrodynamics at the study site.

The WaveDiss project aims to combine in-situ measurements, remote-sensing techniques and numerical models seamlessly to create a comprehensive dataset. Primarily, the following parameters and their interactions are to be monitored (in space and time):

1. surface winds,

2. wave heights (i.e. wave energy) and wave periods,

3. wave breaking statistics,

4. currents,

5. water depth and

6. bed level.

A number of secondary parameters, such as turbulence intensities or sediment concentrations and transport rates are directly related to these primary quantities.

Research goals of WaveDiss2016

The particular goal of "WaveDiss2016" was to quantify and understand the amount of wave energy that gets dissipated due to wave breaking at the outer sandbar. The highest priority during the experiment was to obtain an actual bathymetry within the study area and to provide wave information at different locations along the cross-shore transect in front of the radar station. The planned instrumentation for the experiment included (aside from the long-term measurements from the COSYNA station), small wave rider buoys, bottom mounted pressure transducers and a bottom mounted Acoustic-Doppler-Current-Profiler (ADCP) that could also used for acoustic surface tracking. Figure 3.4 gives an overview of the instrument locations during the experiment as well es the bathymetry at the study site. A study of energy losses at the inner sandbar was initially not considered. However, a fortunate coincidence shifted the focus also to this area. The research vessel "Ludwig Prandtl" was only available from September 22 - 26, 2016, which was the initially planned study period. Because a storm event happened at the end of this period, most of the instrumentation in deeper water had to be recovered prior to the arrival of the storm. It was then decided to deploy two pressure wave gauges within the nearshore breaker zone by hand. Even if not planned initially, this additional data will be used within ch. 6 of this thesis to validate the radar measurements and therefore significantly augmented the work. A shore-based visible light camera was also installed together with an infrared camera aiming on an identification of individual breaking wave events, but was not used within the present study.

3.3 Sea State and Weather Conditions

This section describes the environmental conditions during "WaveDiss2016" as observed at the COSYNA wave rider buoy and weather station. In addition to the field observations, the water level, tidal currents and 10-m wind speed are availbable from the operational model BSHcmod (Dick, 2001) by the Federal Hydrographic and Maritime Traffic Agency (BSH).

The entire measurement period spans from September 21 until October 2, 2016 and covers a medium severe, four days lasting storm event at the end of the period. The temporal evolution of the wind and sea state are shown in figure 3.3. Also marked in this figure is the time span of data availability from the different instruments. The sea state is mostly locally generated and grows rapidly from 0.5 m to $\approx$ 2 m significant wave height on the second half of September 27. Simultaneously, the peak wave period

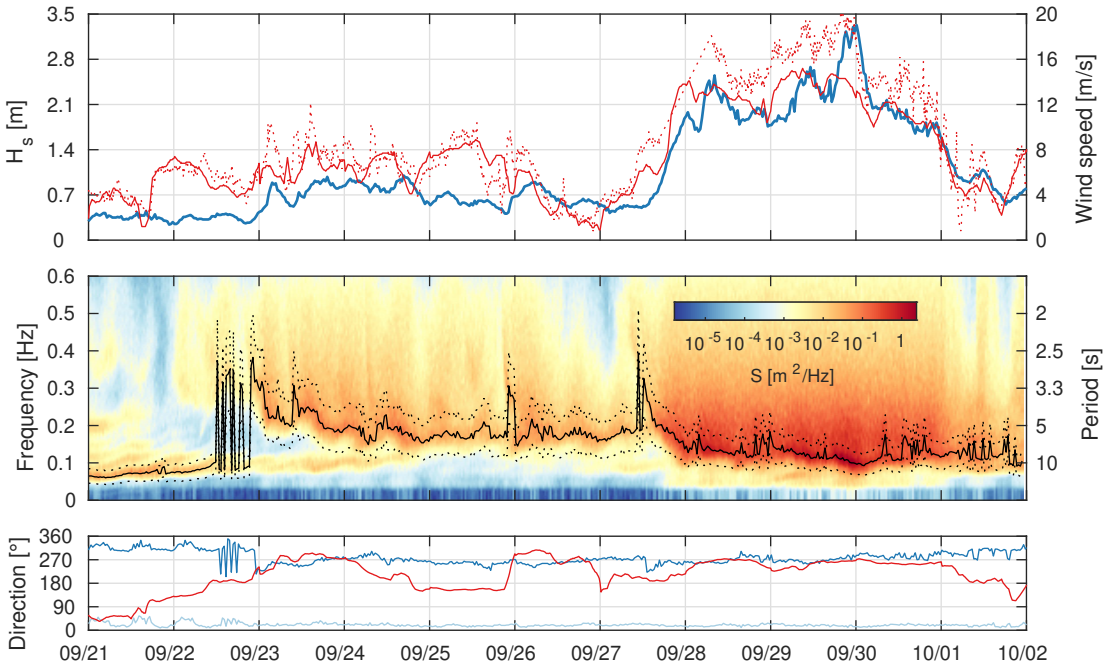

Figure 3.3: Wind speed from BSHcmod (red line) and COSYNA Wind sensor (dashed red line) and signifcant wave height from COSYNA wave rider (blue line). The spectrogram in the middle panel represents the time evolution of the wave spectrum (with a logarithmic color scale). The black line indicates the peak frequency f_p, dashed lines mark the dominant frequency band (0.7 f_p and 1.3 f_p). The bottom panel shows the peak wave direction (blue line) and the wind direction from BSHcmod (red line).

increases from 4 s to around 8 s. While wave periods remain constant around 8 s on the 28th of September, they increase further on the 29th reaching a maximum of 10.5 s on September 30th 1:00 am. The maximum significant wave height of 3.3 m is reached a little earlier, at 22:00 PM and remained constant on this level for 3 hours. Afterwards the significant wave height decreases rapidly to 2 m on September 30th, 3:00 AM and during the following 24 hours it drops further to a level of about 1 m on October 1st, 3:00 AM. The wind shows a similar evolution throughout the storm as the wave height. This also indicates a young, locally generated sea state. Both, waves and winds during the storm were directed onshore (approaching from west, i.e 270°). Several showers occurred during the storm. There is no record of rain intensity available.

3.4 Field Instrumentation and Observations

The field instrumentation that was used during the first part of the campaign (from Sept. 22, 12:00 UTC to Sept. 26, 12:00 UTC) comprised small GPS-based wave rider buoys, bottom mounted pressure transducers and a bottom mounted ADCP. The present study focuses on the storm event after this period and therefore the calm weather data was not used in here. After their recovery on September 26, 16:00 UTC two pressure gauges (PG1 and PG3) were re-deployed at the inter-tidal sandbar seaward of the bar crest (PG1) and at the bar trough (PG3). PG1 recorded data until October 1, 23:00 UTC and PG3 only until September 30, 6:00 UTC. Data from the wave rider (WR), the coherent marine radar, and the wind sensor are available during the whole campaign. Figure 3.4 gives an overview of the instrument locations during the experiment as well es the bathymetry at the study site. The local coordinate reference system has the origin at the location of the radar station (54.7903° N, 8.2833° E) and the x- and y-axis are pointing towards east and north, respectively. The observations are further described in the following.

Depth soundings and beach topography

The sea floor topography was recorded between September 22 - 26, 2016. The "Zwergseeschwalbe", a small (7 m long) vessel was equipped with a RTK-GPS system to monitor highly accurate horizontal (±1 cm) and vertical (±2.5 cm) position and ship motions (heading, ptich and roll). The depth was measured using a 210 kHz single

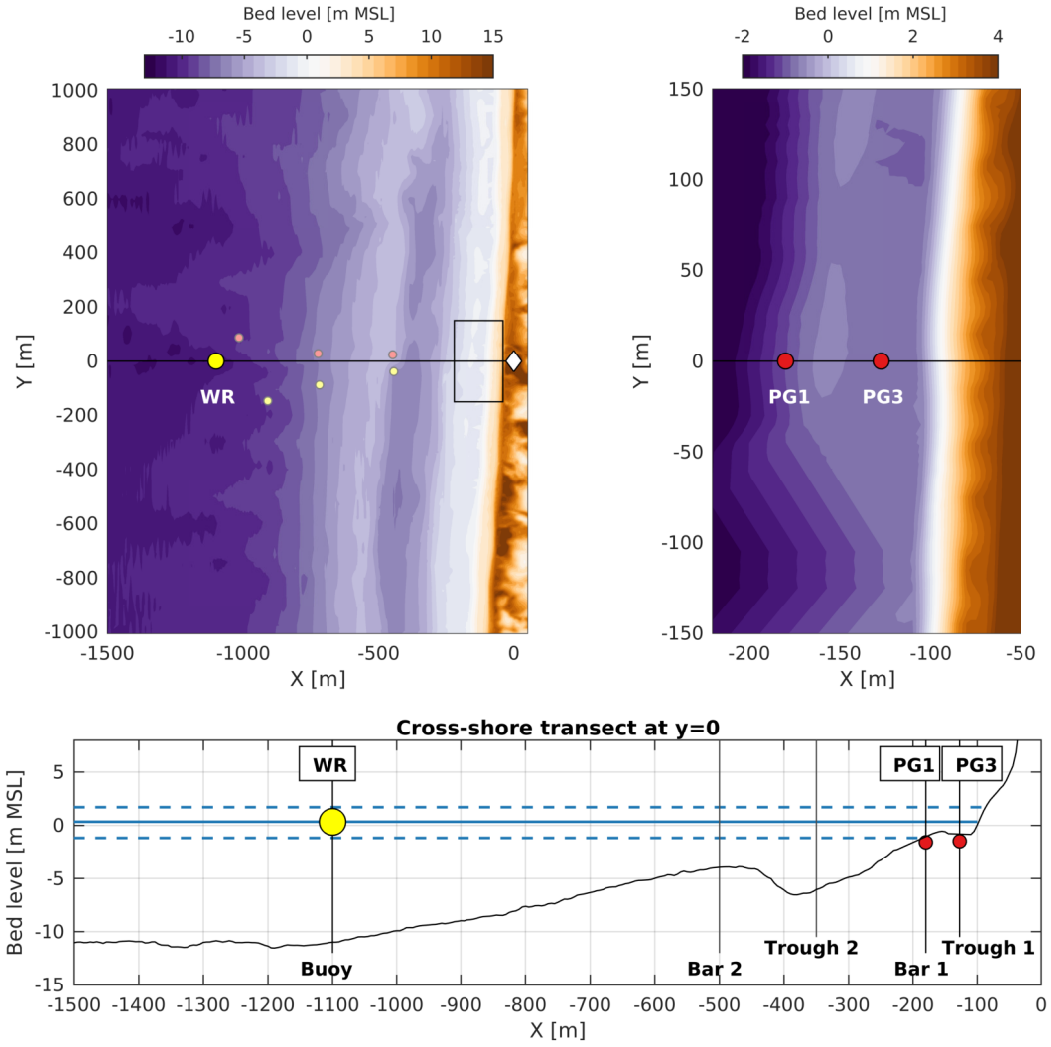

Figure 3.4: Bathymetry with locations of the instruments used during WaveDiss2016. Shown is the location of the radar station (white diamond), the COSYNA wave rider buoy (large yellow dot) and the bottom mounted pressure gauges that were deployed during the storm (large red dots). The smaller dots indicate the locations of the bottom mounted pressure gauges (pink) and the small wave rider buoys (yellow) that needed to be recovered prior to the storm event. The lower plot shows the cross-shore transect at y=0 with the locations of four characteristic stations. The blue lines indicate the mean (solid), and minimum/maximum (dashed) water level during the campaign.

beam echo sounder. The tide corrected and quality checked dataset of the seafloor bathymetry is available from the PANGEA data portal (Cysewski et al., 2018). The intertidal area and dry beach as well as the dune face is covered by an additional topographic data set aqcuired using airborne LiDAR on September 26, 2016. This data set is provided by the state of Schleswig-Holstein's Government-Owned Company for Coastal Protection, National Parks and Ocean Protection (LKN.SH).

The bathymetric data was then mapped to a 5x5 m grid by averaging all data points within one grid cell. Grid cells without data points were filled using linear interpolation. Because the density of measurements in the cross-shore direction is much larger, the linear interpolation was undertaken only in the alongshore direction.

Wave buoys

The offshore directional wave spectrum is available from the continuously operated, COSYNA wave rider buoy (WR) which is a Datawell Directional Waverider MkIII (0.9 m diameter spherical hull). It is located 1.1 km from the beach in a water depth of 10 m. Three smaller GPS based Datawell Directional Waveriders DWR-G (0.4 m diameter spherical hull) were deployed on September 22, 10:15 UTC and provided measurements during the first part of the experiment until they needed to be recovered on September 26, 12:00 UTC before the storm event at the end of the study period. The COSYNA wave rider measured continuously also throughout the storm.

All wave buoys provide time series of the buoy displacements (heave, north and east) at a frequency 1.28 Hz, as well as processed directional wave spectra and integrated wave parameters (such as significant wave height, peak period, peak wave direction, among others). The manufacturer specifies an accuracy of ± 0.5 % for the vertical displacement that is measured with a resolution of 0.01 m.

Bottom mounted ADCP

A Nortek Signature1000 AD2CP that operates at 1000 kHz was deployed on September 22, 10:45 UTC until September 26, 12:00 UTC. The instrument was placed in a trawl resistant bottom mount ≈ 0.7 m above the bottom. The instrument continuously recorded data with all five beams at a sampling frequency of 8 Hz, and a vertical cell size of 0.3 m.

A time series of surface elevation was then extracted from the data using acoustic

surface tracking and the mean current profile (10-min average) was calculated. However, the storm event is not covered by the data set, because the instruments had to be recovered prior to the storm. It was therefore not possible to utilize the wave measurements from the ADCP to infer the amount of dissipated energy due to breaking over the outer sand bar.

Pressure transducers

Bottom mounted pressure transducers were deployed together with the small wave riders and the ADCP. After recovery of the small wave rider buoys and pressure gauges on September 26, two pressure sensors were deployed manually from the beach on the intertidal bar crest to provide measurements throughout the storm. Their position (see fig. 3.4) was estimated after deployment and is considered to be accurate within 10 m. The pressure gauges consist of an industrial temperature compensated absolute piezoresistive silicon pressure sensor (86BSD-050PA). The specified accuracy of the pressure transducer is ± 0.009 bar with a resolution of 0.0003 bar. The digital output was logged to a custom made, low-energy consuming logger board, that was designed at the Technical University of Hamburg (TUHH) by Jens Winkelbauer. Pressure sensors and logger boards were enclosed by a waterproof custom-made polyvinyl chloride (PVC) housing.

The pressure signal logged at 10 Hz was then transformed to surface elevation using the weakly non-linear method proposed by (Bonneton et al., 2018). This method to recover the wave profile can improve the reconstruction of the non-linear wave shapes from pressure recordings (Bonneton et al., 2018).

On recovery, the nearshore pressures gauges (PG1 and PG3 in fig. 3.4) were immersed into the sand by ≈ 30 cm. Considering a damping of the the pressure variation due to the burial that increases exponentially with burial depth (Raubenheimer et al., 1998), the expected error to to burial is less than 3 %.

Coherent marine radar

Two devices of HZG's coherent-on-receive marine radar were operated during the entire experiment. One at the land station and the other one on a mobile trailer equipped with an extendable rod (shown in fig. 3.1). Both radar systems were located close together (distance < 5 m) at 54.790° N and 8.283° E. The height of both radar antennas

for this installation was at 28 m above mean sea level. The radar system consists of an off-the-shelf X-band (9.48 GHz) marine radar (GEM Leonardo series) with a 7.5 feet (2.286 m) wide antenna with either horizontal (HH) or vertical (VV) polarization in transmit and receive. The radar contains a dedicated motherboard developed together with the Technical University of St. Petersburg, Russia, for the digitization and coherentization of the electromagnetic signal (see Braun et al. (2008) or Seemann et al. (2017) for a description). A major difference to commonly used navigational radars is that the received signal runs through an ultra low noise linear amplifier (usually logarithmic amplifiers are used) before being digitized by a 4 channel 13 bit analog-to-digital converter. The radar is equipped with a stepmotor that allows to steer the antenna in a fixed direction.

The radar was operated at a pulse repetition frequency (PRF) of 2 kHz. The duration of the transmitted pulse is ≈ 70 ns. Analog-to-digital conversion is realized at 20 MHz which corresponds to a footprint size of 7.5 m for one radar range cell. Thus, the signal is slightly oversampled in range (see sec. 2.3.1). A total number of 435 range cells were sampled. This results in a maximum range of 3.2 km. At the beginning of each hour, the radar was operated for 10 minutes in (standard) rotational mode with an antenna rotation frequency of ≈ 0.5 Hz. This is followed by a 10 min record with the antenna pointing fix along the cross-shore transect towards the wave rider buoy ($\theta_{az} = 271^{\circ}$). The output of the radar is the digital complex (I and Q channel) coherent electromagnetic signal of each pulse at every range cell. The raw signal must be further processed to estimate the Doppler velocity. The applied Doppler processing chain is explained in following section 3.5.

3.5 Doppler Processing

This section contains a description of the processing algorithms, that were applied to extract Doppler information from the coherent marine radar raw data. The radar data are stored as an array of complex numbers

$$C_{el}(r,t,\theta_{az}) = A_{el}\, e^{i\phi_{el}}, \tag{3.1}$$

where A_{el} and ϕ_{el} are amplitude and phase of the radar signal, respectively. The amplitude of the radar signal has not been calibrated and is thus given in analog-digital-units

(ADU) with a possible maximum of 5792.6 ADU that is specified by the the digitizer. The measured ADU are linearly related to the electric field amplitude of the radar radiation. The range r has a equidistant spacing equal to the radar range cell size $\Delta r = 7.5$ m. The time step of the raw data follows from the pulse repetition period and is $\Delta t_{raw} = PRF^{-1} = 0.0005$ s. The azimuth angle θ_{az} is kept constant for the fix pointing antenna data which is analyzed within the present work.

The Doppler shift frequency must be computed from the coherent radar signal. For this purpose, a certain number of consecutive radar pulses is aggregated to form Doppler ensemble. An ensemble size $n_{ens} = 1024$ was chosen which corresponds to sampling time spacing between the processed Doppler ensembles of $\Delta t = 0.512$ s (the PRF was 2000 Hz). There are generally two common ways to estimate the Doppler shift frequency from coherent backscatter. The first one is from the first moment of the Doppler spectrum inferred by means of a *short term Fourier transformation* and the second one is from the change of the instantaneous phase estimated from *pulse-pairs*. Both methods were were used within the present work and therefore the processing steps are explained in the following.

First moment and pulse-pair Doppler velocity

Each Doppler ensemble is transformed to the spectral domain using the fast-Fourier-transform (FFT) to get the Doppler spectrum $S_d(f)$. The first moment of the Doppler spectrum defines the first moment Doppler shift frequency

$$f_d = \frac{\int f\, S_d(f)}{\int S_d(f)} \,, \tag{3.2}$$

which can be directly transformed to a Doppler velocity using eq. 2.29.

Alternatively, the Doppler shift frequency can also be computed from two consecutive pulse-pairs the time domain (Benham et al., 1972). This pulse pair-estimate of the Doppler shift is very similar to the first moment of the Doppler spectrum for sea clutter (Hwang et al., 2010). The pulse-pair estimate Doppler frequency shift is related to the temporal change of instantaneous phase of the coherent radar signal and can be estimated from a pair of consecutive radar pulses as

$$f_d = \frac{1}{2\pi}\frac{\partial \phi_{el}}{\partial t} \approx \frac{1}{2\pi} d\phi_{el}\ \mathrm{PRF} \,, \tag{3.3}$$

where ϕ_{el} is the instantaneous phase of the radar signal, $d\phi_{el} = \phi_{el,i+1} - \phi_{el,i}$ is the phase difference between two consecutive pulses. The pulse-pair method generally provides a measure for the Doppler frequency shift at the same frequency as the signal is sampled (the PRF). However, an ensemble averaged Doppler frequency shift is computed using the same ensemble size as it was also used to compute the Doppler spectrum ($n_{ens} = 1024$) to reduce noise. Following Carrasco et al. (2017a), the alignment of the vectors pointing to the phase difference in the complex domain is used as confidence measure:

$$Conf = \frac{|\sum C_{el,j}|}{\sum |C_{el,j}|},\ C_{el,j} = A_{el,j+1}\ e^{i(\phi_{el,j+1} - \phi_{el,j})}\ j = 1,2,\ \ldots\ n_{ens} - 1\ , \tag{3.4}$$

where C is the complex radar signal specified in 3.1. The confidence tends to one if all vectors are aligned in the same direction hence the Doppler shift estimate is stable. A low confidence means a random distribution of of Doppler shifts within one ensemble which means that the Doppler velocity is ambiguous. The confidence can therefore be used as a quality indicator and to discard unreliable ensembles.

Doppler peak identification

The pulse-pair method is a straight forward and efficient way of computing the Doppler shift frequency. However, the Doppler spectra can provide additional information about the velocity distribution within the ensemble. A Doppler spectrum represents a power weighted distribution of the scatterers causing the backscatter of the Doppler ensemble within one radar range cell. Eventually it happens that multiple sources for the backscatter are present within the spatial or temporal integration area or period. Each group of scatterers then produces a peak within the Doppler spectrum. The location of the each peak indicates the Doppler frequency shift of the respective subpopulation of scatterers within the ensemble. Different scatterer populations appear for instance when wave breaking is present hence it is relevant for the present study. The non-breaking surface moves at a different (slower) speed than the breaker. This results in a multi-modal Doppler spectrum with one (faster) peak induced by the breaker and a (slower) peak that corresponds to motion of the undisturbed surface. Other sources of multi-modal Doppler spectra might be the presence of birds or marine mammals.

In order to identify and separate individual peaks in the Doppler spectra the following processing steps were therefore applied. The result for two exemplary spectra is

shown in figure 3.5.

1. *Remove noise floor.*
   The power level of the noise floor of a Doppler spectrum was estimated from the median value of the Doppler spectrum as

   $$P_{noise} = 2 \times \text{median}(S_d(f)) \ . \tag{3.5}$$

   All energy below this level is removed from the spectrum prior to the peak identification.

2. *Smooth spectrum.*
   The spectrum was then smoothed using a pyramid moving average scheme (3 times). The window span for the moving average was 30 discrete frequency bins (which corresponds to 58.6 Hz).

3. *Peak identification.*
   Doppler peaks were then identified using the function 'findpeaks' within the signal processing toolbox of MATLAB®. Not more than three peaks were allowed to be identified by the peak finder. The width of a peak is defined as the span of the peak at half of its height. Peaks that were smaller than three times the noise level identified in step 1 were discarded. For each identified peak, the location (i.e frequency) and height was stored.

The location of each individual peak defines its Doppler shift frequency.

Final quantities: Intensity and Doppler velocity

The Doppler shift frequency determined using eq. 3.2, 3.3 or the peak finding algorithm described above can be easily transformed to Doppler velocity using eq. 2.29. For each ensemble, the Doppler velocities $U_{d,pp}$ using the pulse-pair method and $U_{d,1}$, $U_{d,2}$, $U_{d,3}$ from the first, second and third (from slow to fast) peak inside the Doppler spectrum were stored. The ensemble backscatter intensity I is defined as the averaged magnitude of the complex raw data (eq. 3.1), which equals the mean amplitude of the Doppler spectrum.

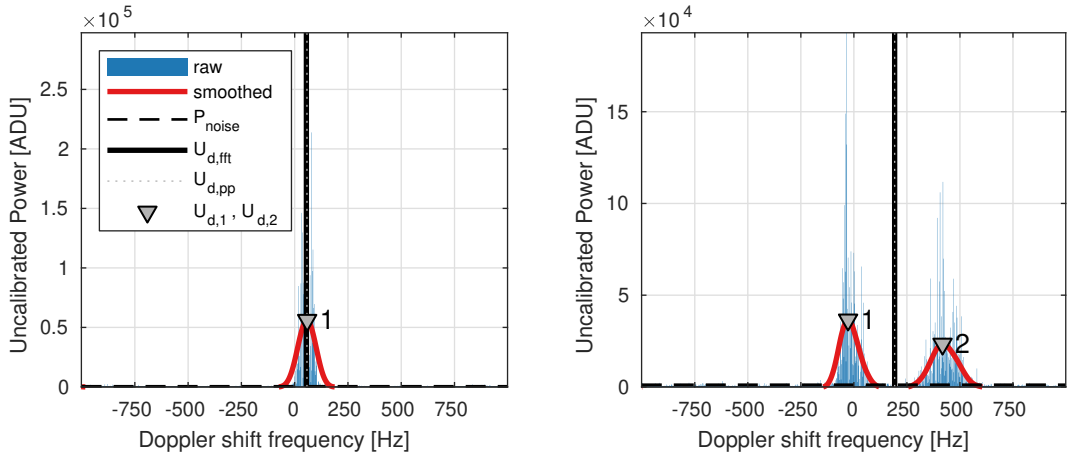

Figure 3.5: Examples of a single-peaked (left) and a double-peaked (right) Doppler spectrum. Shown is the raw (blue bars) and the smoothed (red) spectrum, the noise level (horizontal black dashed line) and the Doppler shift frequency from the first moment (vertical black line), the pulse pair method (vertical dotted gray line) and the first and the location of the first and second peak identified by the peak finding algorithm (gray triangles).

The height of the identified peaks was taken as a measure for the power of each peak, P_1, P_2 and P_3 hence the peak intensity is $I_1 = \sqrt{P_1}$, $I_2 = \sqrt{P_2}$,and $I_3 = \sqrt{P_3}$, respectively.

3.6 Numerical Simulations

The deployed in-situ instrumentation described in the previous section 3.4 is restricted to a few locations along the cross-shore transect. Numerical simulations were therefore conducted in order to provide additional spatial information. Both, phase-resolving and a phase-averaged simulations were used for two different purposes. The first purpose is an accurate representation of the near surface velocity and the surface elevation for shoaling breaking waves which is needed within chapter 4 for a comparison to the observed radar backscatter intensity and Doppler velocity. The second purpose is a comparison of available paramaterizations for depth induced wave breaking to the radar observations of the spatial variation of the breaking probability and energy dissipation based on the methods developed within chapter 5 and 6. A detailed listing of models that are generally available for this purpose was given in section 2.4 and the particular choice of models to be used within this thesis was discussed in section

2.5. This section describes the specific model setup, i.e computational grid, boundary conditions and utilized parameterizations of the utilized models which are the *SWASH* model for the phase-resolving (sec. 3.6.1) and *SimpleWaves1D*, a self-implemented wave and roller energy flux balance model, for the phase-resolved simulations (sec. 3.6.2).

3.6.1 Phase-Resolving Simulations using SWASH

Phase-resolved wave simulations were done using the non-hydrostatic wave model SWASH (Zijlema et al., 2011). The model is capable of simulating rapidly varying flow fields as they occur in a nearshore wave environment, including non-linear wave-wave interactions, wave-current interactions and energy dissipation by wave breaking or bottom friction. As explained in sec. 2.5, SWASH can be run as a one-phase RANS model, if the water column is resolved by a sufficient number of vertical layers, or as a non-hydrostatic wave model. The RANS simulation provides a realistic estimate of the near surface velocity and wave breaking is captured by the model without the need to specify additional calibration parameters. On the contrary, the non-hydrostatic simulation is much faster. Therefore, both ways of operating the model were used in a setup with 20 vertical layers (referred further as NH20) and a more efficient setup with 2 vertical layers (NH2). Both model setups will be described in the following.

Computational grid and boundary conditions

The horizontal grid and the specified boundary conditions are the same for both setups. Because the wave direction was about $270 \pm 10^{\circ}$ throughout the storm event, the model domain was simplified as a cross-shore transect with an open boundary on the western side, the beach on the eastern side, and closed boundaries north and south of the model domain. Like the locations of the in-situ instruments the model coordinate system has its origin at the position of the radar with the positive x- and y-axis pointing east and north, respectively. The model domain spans from $x = -1100$ m to $x = -80$ m. The horizontal grid spacing was equidistantly set to $dx_s = 0.4$ m which was found to be small enough to reasonably represent the spatial gradients, while still providing a reasonable numerical efficiency. The number of grid points is therefore $nx \times ny \times nz = 2400 \times 1 \times 20 = 4.8 \times 10^4$ for the NH20 and $nx \times ny \times nz = 2400 \times 1 \times 2 = 4.8 \times 10^3$ for the NH2 simulation.

The model was forced at the westward open boundary by applying a weakly reflective spectral boundary condition (Blayo and Debreu, 2005) that is implemented in SWASH. The required one-dimensional spectrum that is needed to synthesize the surface elevation and velocity time series at the boundary was generated from the observed wave rider buoy spectrum assuming a random phase distribution. Swash and shoreline motions and associated wave reflection were not considered in the present study. Instead, a numerical beach represented by a sponge layer was implemented at the eastern domain boundary.

20 layer simulation (NH20)

Twenty terrain and water surface following (sigma-)layers were used for the NH20 simulations. Each layer represents a constant portion of the local water depth (i.e. mean water depth + instantaneous water surface elevation). The uppermost vertical grid cell represents the upper 5 percent of the water column. The largest expected local water depth occurs at the offshore boundary of the model domain and does not exceed 15 m, which leads to a maximum vertical near surface cell size of ≈ 0.75 m. This should be seen as the upper limit, whereas in most parts of the model domain the expected water levels are smaller than 5 meters (cell sizes < 0.25 m). Vertical turbulence production an transport was estimated by using the $k-\varepsilon$ formulation (Launder and Spalding, 1974). In this configuration, the SWASH model is similar to a one-phase RANS model (c.f. sec. 2.4).

A total time of 30 minutes was simulated, while the first 10 minutes were discarded to ensure enough spin-up time for the model to reach a quasi-steady state throughout the full model domain. The last 20 minutes of the simulation were then used to generate a statistically representative sea state. The spectrum specified at the boundary was observed by the wave rider buoy on Sep. 29, 2016, 22:17 UTC and is shown in the appendix in figure. B.1.

2 layer simulation (NH2)

Additional simulations with 2 vertical layers (NH2) where run covering the entire storm event. In this setup, SWASH is a non-hydrostatic wave model (as explained in sec. 2.4.1). The pressure term within the momentum equation (eq. 2.32) was approximated using a Keller-box scheme (see or Zijlema and Stelling (2005) for a de-

scription). To reasonably well represent wave breaking, the so called hydrostatic front approximation (HFA) was applied (Smit et al., 2013). The HFA switches of the non-hydrostatic pressure correction when a steepness threshold, specified by the parameters α for the onset, and β for the termination of breaking is exceed. This ensures a rapid development of a bore-like wave when those thresholds are exceeded. The energy dissipation of this hydraulic jump-like flow is then correctly determined by the model equation through the applied numerical scheme which strictly conserves momentum (eplained in datail by Smit et al., 2013). Default parameters are $\alpha_b = 0.6$ and $\beta_b = 0.3$. Here, a lower value $\alpha_b = 0.4$ was found to produce better results. Nicolae Lerma et al. (2017) also reported that lower values for α_b were needed for 1D simulations with a low number of vertical layers.

One model run per hour (starting Sep. 27, 2016, 00:00 UTC until Oct. 01, 2016, 23:00 UTC) was simulated using the corresponding spectrum measured by the wave rider buoy and the mean water level extracted from BSHcmod. The significant wave heights along the cross-shore transect were calculated from the model output as $H_s = 4\,\sigma_\eta$, where σ_η is the standard deviation of the surface excursion η.

3.6.2 Phase-Averaged Simulations using SimpleWaves1D

It was explained within sec. 2.4.2, that for some nearshore applications it is possible to simulate the phase-averaged transformation of wave energy using a simple energy flux balance instead of the spectral wave action balance. Following this strategy, a simplistic cross-shore wave transformation model called *SimpleWaves1D*[1] was implemented. The main purpose of the phase-averaged simulations is to compare commonly used parameterizations for depth induced wave breaking and analyze and validate them in terms of the breaking probability. SimpleWaves1D solves the wave energy flux balance (eq. 2.35) coupled to a roller flux balance (eq. 2.36). To specify the dissipation by depth induced wave breaking D_w, all parameterizations that were introduced in sec. 2.4.3 and listed in table 2.3 were implemented in SimpleWaves1D. Source terms for both bottom friction and input by wind are neglected. They are considered to be small compared to dissipation by depth induced wave breaking in the surf zone. Shore-normal circulation is also considered to be negligible for the present case.

[1] the source code is available at `https://github.com/mstresser/SimpleWaves1D`

Computational grid and boundary conditions

The wave and roller energy balance are solved on the same computational grid. The model domain spans from $x = -1500$ m to $x = 0$ m, where the origin is again the location of the radar. The horizontal grid spacing was set to $dx = 7.5$ m, which is similar to the range resolution of the radar. SimpleWaves1D simulates the wave energy integrated over all frequencies. Therefore, a wave frequency that reasonably represents the wave conditions must be specified instead. The frequency at the spectral peak f_p deduced from the buoy spectrum was considered here as the the representative frequency of the wave field f_{rep}. The wave height $H_{rms,0}$ at the offshore boundary ($x = -1500$ m) was set according to the wave height measured by the wave rider buoy. The dissipation of roller energy D_τ was estimated using eq. 2.37 with the slope coefficient $\beta_s = 0.1$, which is a commonly used value (e.g. Nairn et al., 1990). The dissipation of organized wave energy D_w was estimated using one of the different wave breaking source term formulations introduced in sec. 2.4.3. The free parameters within each parameterization were specified with the default value that was reported within the respective publication. The reason for this choice is explained in the following section 3.6.3.

Numerical scheme

The balance equations are solved using a simple first order upwind scheme: $F_w(x_{i+1}) = F_w(x_i) - dx\ D_w(x_i)$. Thornton and Guza (1983) analyzed the performance of different higher order numerical schemes and found that the accuracy of a simple upwind scheme is enough to solve the one dimensional wave energy balance.

3.6.3 Simulation Results

In this section, the results from phase-resolving non-hydrostatic wave simulation (NH2) and the phase-avaraged simulations (SW) are presented. It is expected that the phase-resolving simulations is capable of predicting the the nearshore wave height without the need for calibration. This was mentioned already in section 2.4, where the different available types of wave models were introduced. However, it was also mentioned there that such phase-resolving simulations are computationally expensive and phase-averaged simulations are often the only option for studies that cover larger ar-

Model setup	Breaking parameterization	Specified parameters
SW-BJ78	Battjes and Janssen (1978)	$\gamma = 0.78$, $B = 1$
SW-TG83	Thornton and Guza (1983) eq. 21	$\gamma = 0.42$, $B = 1$
SW-JB07	Janssen and Battjes (2007)	$\gamma = 0.39 + 0.56 \tanh(33\, S_0)$, $B = 1, S_0 = (H_{rms}/L)_{\text{offshore}}$
SW-FA12	Filipot and Ardhuin (2012)	$\tilde{\beta} = 0.42$, $B_{dw} = 0.185$
NH2	Smit et al. (2013)	$\alpha_b = 0.4$, $\beta_b = 0.3$
NH20	-	-

Table 3.1: Values chosen for the parameters affecting the breaking parameterizations. Refer to sec. 2.4.3 for a detailed description of the parameterizations.

eas or longer study periods. Therefore the results from the phase-averaged model using the different breaking parameterizations BJ78 (eq. 2.39), TG83 (eq. 2.45), JB07 (eq. 2.49) and FA12 (eq. 2.53) are also analyzed here with the goal to demonstrate the discrepancies of the different breaking parameterizations to each other, and also to the phase-resolving model run. During the short period of the WaveDiss2016 experiment nearshore in-situ measurements are available from the pressure gauges. These could generally be used for calibration of the coefficients within the breaking parameterizations. In most cases, however, the nearshore wave height is not available from measurements and the parameters within the wave models need to be specified by the user. The present investigation does therefore not attempt to force the models to the right result by intensive calibration, but rather to analyze the variability of the results from different breaking parameterizations run with the default parameters that are proposed in the respective paper. The default parameters that were used to generate the results are listed in tab. 3.1.

The results are evaluated in terms of the cross-shore evolution of the significant wave height and the fraction of breaking waves (shown in figure 3.6) at the peak of the storm (Sept. 29, 22:20 UTC), and time evolution of the simulated nearshore wave heights over the course of the storm event. The latter is evaluated at the stations "Trough 1" and "Bar 1" (cf. fig. 3.4), where in-situ observations from the pressure gauges PG1 and PG3 are available during the storm.

It can be seen from the cross-shore evolution of the significant wave height H_s at the peak of the storm shown in the upper panel of figure 3.6, that the NH2 model matches the observation at the pressure gauge PG1 and shows a slight overestimation of about 20 cm at PG3. This confirms the expected good skill of the NH2 simulation. The

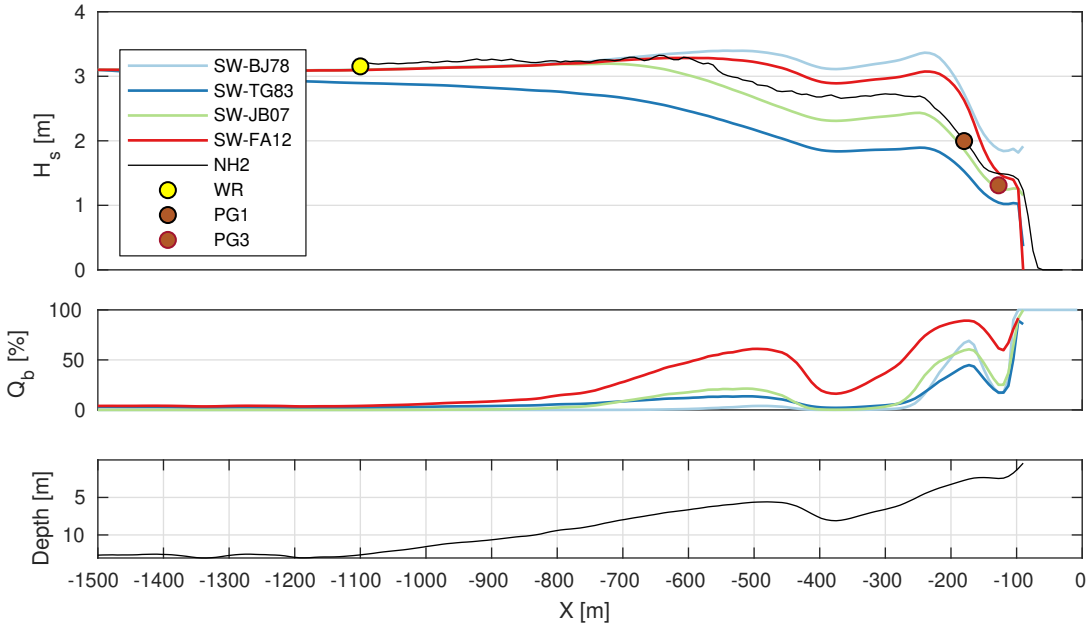

Figure 3.6: Cross-shore transect of the simulated significant wave heights at the peak of the storm.

cross-shore evolution also reveals that the estimates of H_s from the different models significantly vary at the outer bar trough (around $X = -350$ m). At this location the model estimates of H_s range from 1.8 m (estimated by the TG83 model) to 3 m (estimated by JB78 model). The underestimation of the energy loss is typical for the JB78 parameterization if default values are used (Battjes and Stive, 1985). It be smaller when a different scaling for the breaker parameter is used instead of the default value of $\gamma = 0.78$. As there are no in-situ measurements of H_s available at this location during the storm, it cannot be evaluated which model gives the best result here. However, because of the good match of the NH2 simulation at PG1 and PG3, the NH2 result is considered as the most trustful estimate of H_s in this area.

For the cross-shore evolution of the fraction of breaking waves Q_b (middle panel in fig. 3.6), almost all models predict very low (< 25 %) fractions of breaking waves at the outer bar. The lowest values for Q_b were estimated by the SW-BJ78 model run which predicts $Q_b < 5$ % at the outer bar. However, the SW-FA12 model run is the only one that predicts $Q_b > 50$ % at the outer bar, and also at the inner bar the SW-FA12 model run estimates higher values for Q_b compared to all other models. This evolution of Q_b will be studied in more detail in chapter 5.2.

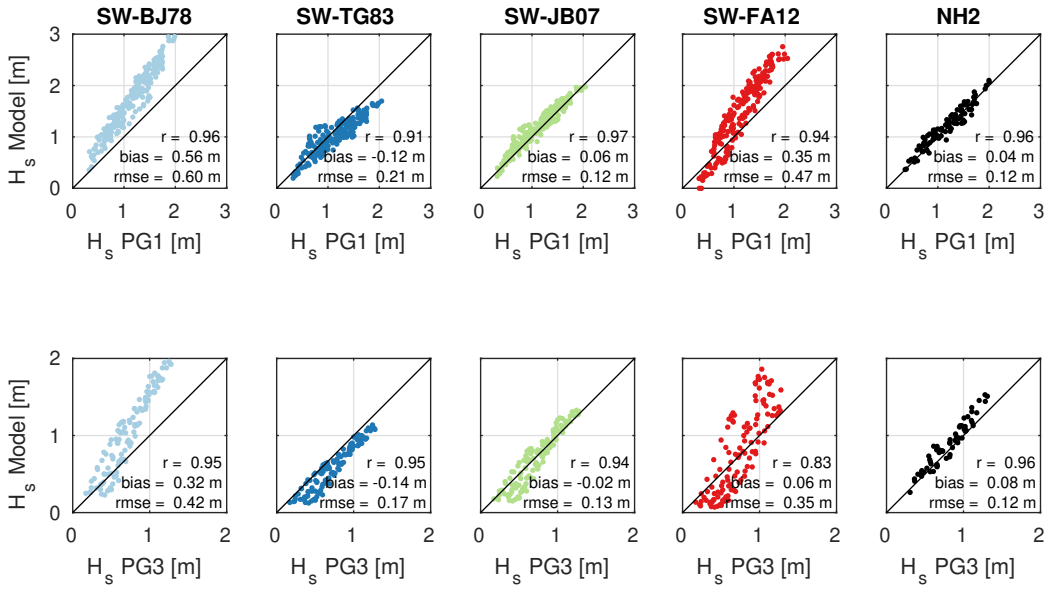

Figure 3.7: Comparison of the simulated significant wave heights to in-situ measurements from the pressure gauges PG1 at $x = -180$ m and PG3 at $x = -127.5$ m.

On the inner sandbar, at station "Bar 1" and "Trough 1", in-situ observations of H_s are available from pressure gauge PG1 and PG3. Therefore, the error of the different models in predicting H_s at these two locations could be quantified and the results are shown in the respective scatter diagrams in figure 3.7. From the scatter diagrams it becomes clear, that the NH2 model is able to estimate the observed wave height at the location of the pressure gauges with an root-mean-square-error (rmse) of 0.12 m. This is a good match considering the statistical nature of the parameter H_s. The NH2 model yields the best results of all models throughout the whole storm event, which was also expected and gets confirmed by the results. The underestimation of the wave height that was found for the SW-JB78 model run in figure 3.6, is also clearly apparent in the scatter diagram. This results in the fact that the SW-BJ78 shows the largest rmse of all simulations (rmse = 60 cm at PG1 and rmse = 42 cm at PG3). Both the SW-TG83 and the SW-JB07 model run show good results at both pressure gauges with rmse's < 21 cm, while the result is slightly better for the SW-JB07 model run. This is surprising, because the two models predicted different estimates of H_s at the outer bar trough in figure 3.6. The SW-FA12 model run deviates more from the measured wave height (rmse$=$ 47 cm at PG3 and rmse$=$ 35 cm). However, this might be due to the fact that the FA12 parameterization was used here in a modified bulk version which deviates

from the originally proposed spectral form (see sec. 2.4.3).

In summary, the model results revealed that most parameterizations for depth induced wave breaking are able to predict the observed nearshore significant wave height with reasonable accuracy, even if they are used with the default parameters without further calibration. However, significant differences between the different model runs are found for the predicted decrease of the wave height due to breaking at the outer sandbar, and the fraction of breaking waves. The breaking probability will be further investigated in chapter 5.2 of the present work, by a comparison to the radar observations.

3.7 Discussion of Uncertainty

Within this section, a brief discussion of the sources of uncertainty for the observations and models used within the present work is provided. The focus is hereby on the primary quantities that are used within the study. Those are the local *water depth*, *wave height* and *wave frequency* (as integral parameters of the sea state).

As mentioned in section 3.4, the quantities measured in situ are the surface excursion, the pressure at the bottom and the echo sounder depth, respectively. Those directly observed quantities are expected to be relatively accurate with an expected uncertainty < 1 % of the observed value (see sec. 3.4). However, a much higher source of uncertainty is due to the approximations and assumptions that need to be taken to obtain the required local sea state information from the direct measurements. Three main sources of uncertainty must be considered hereby. The first one is due to *positioning, timing* and *interpolation* errors. The second one is the *propagated uncertainty* from external input, and the third one results from the *application of wave theory*. The associated degree of uncertainty largely depends on site specific conditions. In slowly varying (homogeneous and quasi steady-state) conditions, the first error source (positioning, timing and interpolation) is expected to be small. Instead, in highly dynamic and rapidly varying conditions it is most likely increased. The smallest error due to imprecise timing and positioning is therefore expected at the wave rider buoy, where the water depth is roughly constant ($\approx 10 - 12$ m). Larger errors are expected at the pressure gauges within the inner surf zone where wave heights vary on much smaller distances. This region is also expected to be morphodynamically more active and therefore rapid bed level changes can occur (within hours in storm conditions).

The only external input used within this work is the mean water level from the operational model BSHcmod which includes astronomical tides and surge (cf. sec. 3.3). Because the considered local water depth consists of the re-interpolated depth soundings and the mean tidal elevation extracted from the model the uncertainty of the input directly affects the accuracy of the water depth estimate. This in turn affects the estimate of the local wave phase speed as well as the results from the numerical simulations. The third source of uncertainty, the application of wave theory, does mainly affect the surf zone wave measurements from the pressure gauges. As described in sec. 2.2.1, wave theory must be applied to retrieve wave height from pressure measurements. The pressure gauges are located in very shallow water and therefore strongly non-linear wave shapes are expected in this region.

A sound quantification of the uncertainty that results from the different sources is therefore only possible in an empirical manner and would require additional control measurements at each location of interest. This was not feasible for the present study. Instead, a rough and conservative estimate of the expected uncertainty for the environmental conditions at hand is made in the following. Considering the discussed sources of uncertainty (interpolation, propagated uncertainty a and wave theory) it can be concluded, that the smallest error is expected for the measurements at the wave rider buoy and is estimated here roughly to be < 5 %. The accuracy of the significant wave height measured by the pressure wave gauges is ≈ 10 % (similar to the findings of Guza and Thornton, 1980) and the results from the numerical simulations are accurate approximately within 20 % for phase-averaged simulations (Apotsos et al., 2007) and around $10 - 15$ % for the phase-resolving, non-hydrostatic wave model (see sec. 3.6.3).

Chapter 3: Key content

- The WaveDiss2016 field experiment on the North Sea island Sylt was planned and conducted to study the transformation of shoaling and breaking waves in the nearshore.
- The data set covers a 2 weeks calm period and a 4 day storm event with $H_s > 3$ m recorded using both, in-situ instruments and remote sensing.
- Phase-resolving and phase-averaged numerical simulations of the cross-shore transformation of significant wave heights were conducted and compared to the field measurements.
- The models results differ significantly regarding the estimated wave height decrease at the outer bar and the simulated fraction of breaking waves.

Chapter 4

Coherent Marine Radar Backscatter from Nearshore Breaking Waves

Coherent marine radar remotely senses the sea surface in space and time. This provides great potential to study the spatio-temporal evolution and transformation of ocean waves, especially for studying the complex process of wave breaking. However, only few studies are so far available, where coherent radar backscatter from shoaling and breaking waves in the surf zone is analyzed (Plant et al., 1978; Farquharson et al., 2005; Keller et al., 1986; Catalán et al., 2014; Seemann et al., 2014). Shallow water wave dynamics differ significantly from the open ocean because wave non-linearity increases with decreasing water depth. Also, wave breaking characteristics change completely from deep to shallow water. Therefore, findings from deep water studies regarding radar backscatter characteristics do not necessarily apply to shoaling and breaking surf zone waves. Thus, the present work aims on a better understanding of the coherent radar backscatter characteristics from a spatially varying wave field with a strong focus on wave breaking in the nearshore. This knowledge is paramount for a future application of coherent marine radar to invert coastal wave hydrodynamics in space and in time from the backscatter.

The radar backscatter is strongly influenced by the local inclination of the water surface due to the wave motion and by the appearance of breaking waves (cf. sec. 2.3.2). It is therefore a reasonable assumption that wave information can be retrieved from the backscatter. However, due to the highly non-linear radar imaging effects and the loss of information due to the limited range resolution of the radar (cf. sec. 2.3.1), it is not possible to obtain the local wave shape and its evolution directly from the radar

measurements. To address this, a forward model is presented within this chapter that can be used to approximate the backscatter intensity and Doppler velocity from waves with known characteristics.

In order to identify the main influences on the backscatter, a detailed analysis of the observed time-range evolution of the intensity and Doppler velocity from nearshore breaking waves is presented within section 4.1. Based on this, a simplistic forward model is suggested in section 4.2 that accounts for the main contributions to the scattering, namely surface tilt, wave breaking, shadowing and the range smearing due to the sensor impulse response. The scattering model is applied to the output of the phase resolving simulation of the non-linear wave hydrodynamics. Finally, within section 4.3 the results are compared to the radar observations and possible reasons for the observed discrepancies are discussed. The highest wave non-linearity and breaking intensity is expected at the most energetic wave conditions. An exemplary 10 minute radar record at the peak of the storm (starting 29-Sep-2016 22:11 UTC) was therefore selected for the analysis.

4.1 Intensity and Doppler Velocity: Measurements

Within this section, the time range evolution of the observed backscatter intensity and Doppler velocity is analyzed. The goal is hereby to identify and study the influence of the changing water depth (i.e. wave shoaling and increased wave skeweness and asymmetry), shadowing and in particular the influence of breaking waves on the received radar signal. For this purpose, time-range diagrams were generated from the radar measurements with fixed antenna pointing offshore ($\theta_{az} = 271^{\circ}$). The raw data was processed using the procedure explained in section 3.5. Ensembles of 1024 individual radar pulses were used to compute the intensity and Doppler velocity from the Doppler spectra. This corresponds to 0.512 s at the given sampling frequency of 2000 Hz. If the Doppler spectrum was multi-modal, the velocities $U_{d,1}$ and $U_{d,2}$ that correspond to the first two peaks inside the Doppler spectrum (from slow to fast) were extracted. Additionally, the Doppler velocity computed via the pulse-pair-method $U_{d,pp}$ was extracted as it is a very common and effective way to estimate the first moment Doppler velocity and is used widely within other studies (e.g. Miller and Rochwarger, 1972; Farquharson et al., 2005; Hwang et al., 2008c; Carrasco et al., 2017a,b). For both the pulse-pair method as well as for the calculation of the Doppler spectra, the same amount of radar

pulses (1024) were used to compose a radar ensemble. This results in a stable measure for $U_{d,pp}$ and a convenient way to assess the quality of the measurement from the confidence parameter (eq. 3.4).

4.1.1 Time-Range Diagrams

Figure 4.1 shows the time-range diagrams of the backscatter intensity and the Doppler velocity for the given radar record. The backscatter intensity is shown in logarithmic scale (1 dB = 10 $\log_{10}\left(\frac{I}{1\ ADU}\right)$). The peak wave direction was $Dir_p = 280°$ during the time of the radar record, i.e. waves were approaching the coast almost normal to the shoreline.

The stripe-like pattern in both of the sub-figures can be interpreted as wave crests traveling towards the shoreline. For the given tidal elevation at the time of the measurement ($\zeta = 1.61$ m), the shoreline is located approximately at $r = 55$ m. The backscatter intensity and Doppler velocity is increased significantly when wave breaking is

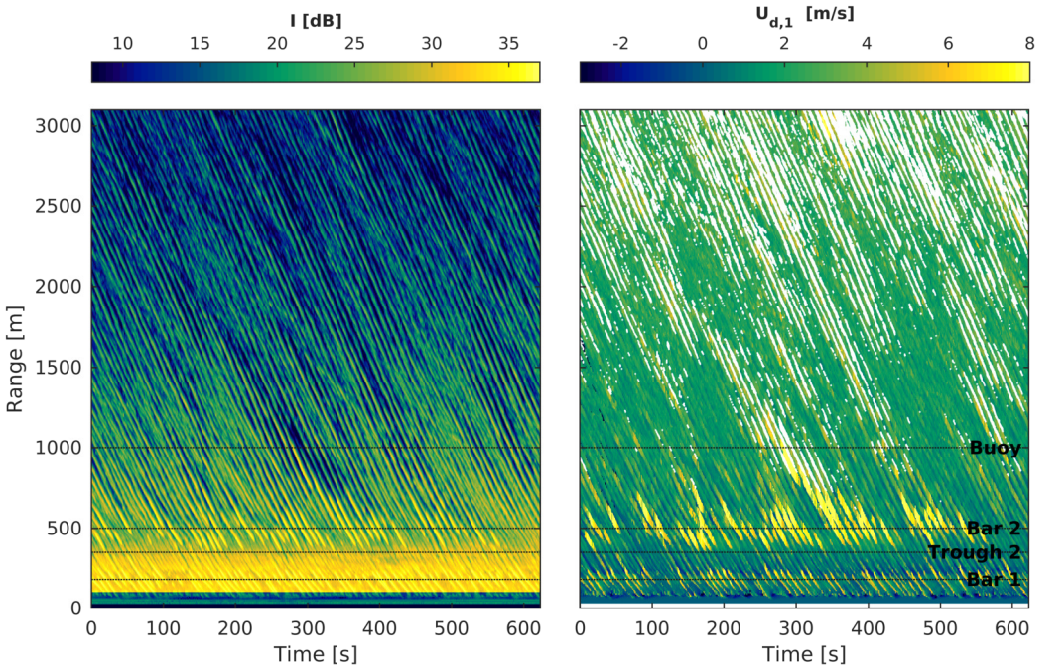

Figure 4.1: Time-range diagram of the measured backscatter intensity I and the first peak Doppler velocity $U_{d,1}$ for the 10 min fix pointing antenna record, starting 29-Sep-2016 22:11 UTC. Dashed horizontal lines indicate the locations or the stations "Bar 1" ($r = 180$ m), "Trough 2" ($r = 350$ m), "Bar 2" ($r = 500$ m) and "Buoy" ($r = 1000$ m).

present. Therefore, breaker zones can be easily identified from the time-range plots. The first one (seen from the shore line) spans from $r = 70$ m to $r = 230$ m and the second one from $r = 380$ m to $r = 750$ m. The radar equation (eq. 2.24) prescribes that the power received by the radar exhibits a cubic decay with increasing range. This range decay is clearly visible within the backscatter intensity record. Areas with very low backscatter intensities (dark blue colors within the left time-range diagram in fig. 4.1) where no Doppler velocity could be determined (white colors within the right time-range diagram in fig. 4.1) become apparent from a range of ≈ 800 m and further offshore and they occur more frequently with increasing range. This can be clearly assigned to sheltering effects from the preceding waves. This effect becomes more and more apparent for lower grazing angles (increasing range). Within those areas the signal is is close to (or below) the noise floor of the radar. It is therefore not possible to derive reliable Doppler velocities for these regions. A region with relatively low backscatter intensities is apparent in the near range ($r > 90$ m). The radar signal within the first 10 radar cells was not amplified before digitization. No influence was found on the estimated Doppler velocities within this non-amplified region, i.e. the data can also be analyzed.

4.1.2 Distributions of Intensity and Doppler Velocity

Four stations along the cross-shore transect have been selected at different distances from the radar to further elucidate range (or grazing angle) dependent characteristics of the backscatter. The four stations "Bouy", "Bar 2", "Trough 2" and "Bar 1" where chosen as lowest number of stations to cover all important specific regions along the transect. A second selection criterion for the station location was the availability of in-situ observations. Figure 3.4 shows the location of the stations along the cross-shore depth profile. The station "Bouy" is located at ($r = 1100$ m) at the toe of the outer bar, where the COSYNA wave rider bouy is located. The wave conditions at this station hence represent the incoming wave forcing that is not yet influenced by the nearshore sandbars. Station "Bar 2" ($r = 500$ m) and "Trough 2" ($r = 350$ m) are located at the outer (sub-tidal) sand bar crest and trough, respectively. The location of "Bar 2" was selected to be located within the breaker zone at the outer bar. At "Through 2" most breaking has already terminated, i.e the wave field is expected to be altered due to the influence of breaking but not anymore affected by the the presence of actively breaking waves. In-situ observations at the outer bar are not available at the time of

the radar record, because the instruments placed there had to be recovered prior to the storm event (see sec. 3.4). However, this does not affect the results of the analysis in the present chapter. The station "Bar 1" is located at $r = 180$ m, which is the position of the pressure gauge "PG1" during the storm (as shown in fig. 3.4). This station is located within the inner surf zone where most of the waves are breaking.

Time series of the measured radar quantities were extracted from the data set at each station, corresponding to the horizontal gray lines in the time-range diagrams shown in fig. 4.1. The time series of five adjacent range cells were compiled in order to extract a statistically representative set of observations for each station. Then, histograms were calculated from the extracted time series in order to analyze the statistical distribution of the measured quantities. The histograms are shown in 4.2 where rows represent different quantities. The columns of the figure stand for the different stations. Sub-figures 4.2 (a)-(d) show the extracted histograms of the measured backscatter intensities. The histograms of Doppler velocity $U_{d,pp}$ calculated using pulse-pairs are shown in the sub-figures 4.2 (e)-(h). Sub-figures (i)-(l) and (m)-(p) represent first and second peak Doppler velocities $U_{d,1}$ and $U_{d,2}$ derived from the Doppler spectra. The processing steps to infer $U_{d,pp}$, $U_{d,1}$ and $U_{d,2}$ are described within sec. 3.5. The historgam bin size to compute the histograms was 20 ADU for the intensity and 0.1 m/s for the velocity.

Backscatter intensity

The distributions of ensemble intensities shown in figure 4.2 (a) - (d) are analyzed first. The backscatter intensity decays rapidly with increasing range, which is expected due to the cubic power decay prescribed by the radar equation (eq. 2.24). This rapid power decay results in the fact, that at the locations "Bar 2" and "Buoy" most of the intensity values are already smaller than 1000 ADU (the intensity is not calibrated and therefore given in analog-to-digital units with $I_{max,ADC} = 5792.6$ ADU as explained in sec. 3.4). At the station "Buoy", located at $r = 1$ km, the first histogram bin (from 0 to 20 ADU) has already 800 counts. This means that 13% of the data at this position has already very low intensity levels that are close to the radar noise floor. This can be attributed to the shadowing effect behind large wave crest.

In contrast, such low intensity ensembles do not appear at the stations "Bar 1" and "Trough 2" which are closer to the radar. At Station "Bar 1", two clear peaks are observable in the histogram, which indicates the presence of two distinct sources for the

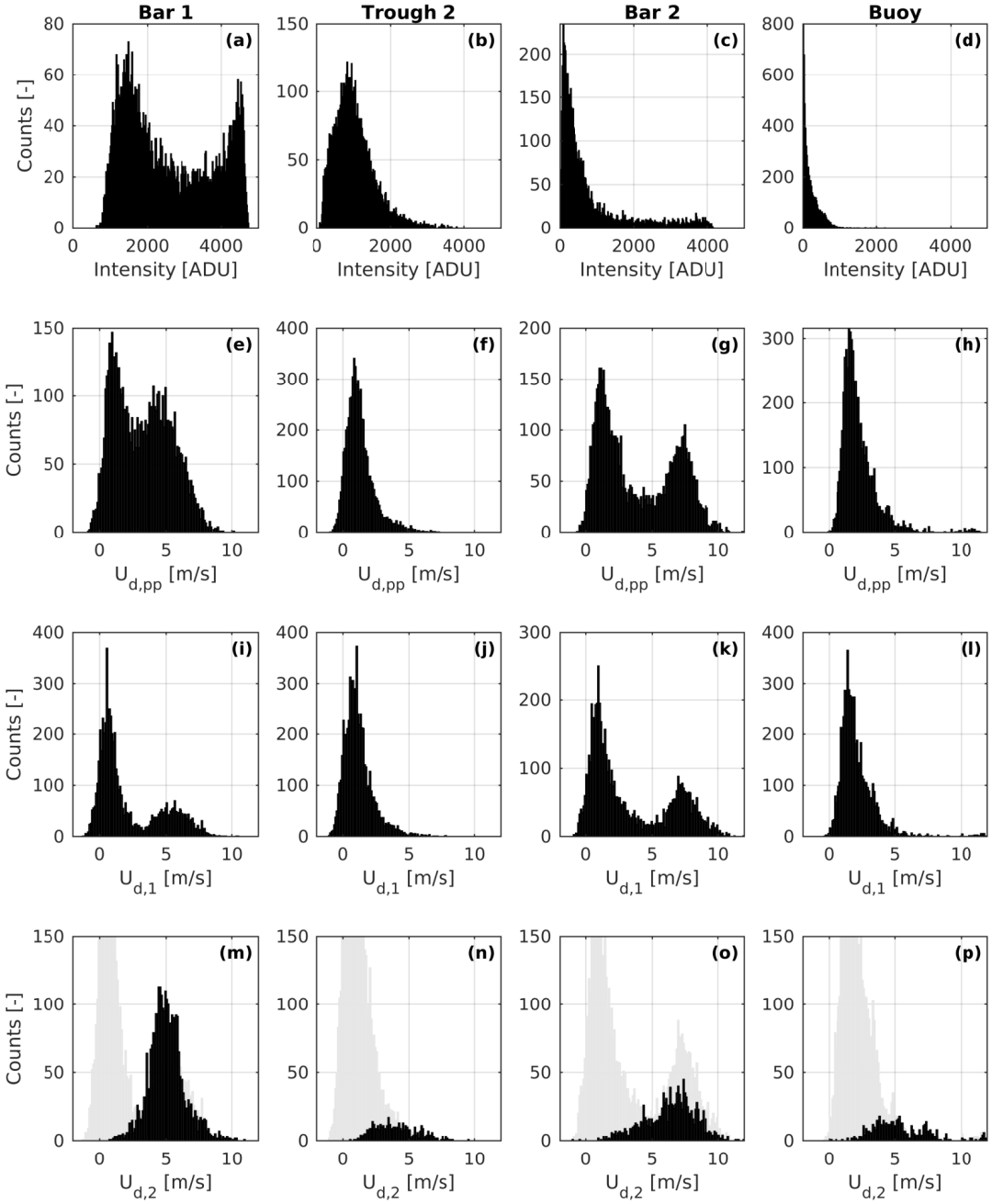

Figure 4.2: Histograms of the measured backscatter intensities (a - e), the Doppler velocity U_{pp} calculated using pulse-pairs (f - i), first peak Doppler velocities derived from the Doppler spectra $U_{d,1}$ (i - l) and second peak Doppler velocities $U_{d,2}$ (m - p) at different locations. Columns correspond to the different locations "Bar 1" ($r = 180$ m), "Trough 2" ($r = 350$ m), "Bar 2" ($r = 500$ m) and "Buoy" ($r = 1000$ m). The light grey bars in the panels (m - o) represent the histograms of $U_{d,1}$ (i-l) and are shown for reference.

scattering. This is expected because the station "Bar 1" is located inside the nearshore breaker zone and the backscatter from actively breaking waves is known to be significantly higher as the backscatter coming from non-breaking waves. The second peak (with higher intensities) seems to have a sharp drop at the right end. This possibly indicates sensor saturation because as there are no higher intensity values found at this location. However, the highest values observed (around 4700) are still below the technical saturation level of the analog-to-digital converter (ADC) $I_{max,ADC} = 5792.6$ ADU. A possible reason for such a behavior is that only one channel of the ADC is saturated and therefore the theoretical maximum is not reached. However saturation effects were not further analyzed here. "Trough 2" is located in between the two breaker zones. The time-range diagram (fig. 4.1) reveals that not many strong breaking events occur at this location. The distribution of intensities in fig. 4.2 (b) is clearly skewed towards higher values, though. The reason for this skewed distribution could not be yet be identified.

At station "Bar 2" one would expect a strong influence of large waves that are breaking at the outer bar. Wave breaking is evidently present at the outer bar because the yellow stripes in the time-range diagram in fig. 4.1 indicate extremely high backscatter intensities and at the same time fast Doppler velocities. This is a strong indication for the presence of actively breaking waves as it was discussed in section 2.3.2 and can be used to identify breaking (see also sec. 2.2.3). Nonetheless, the histogram at this station does not show a clear bi-modality, but a long tail at the right side of the distribution is present. This is most likely due to "smearing" effect induced by the transmitted pulse and will be further studied in sec. 4.2.

Doppler velocity from pulse pairs

The panels (e) - (h) in 4.2 show the histograms of the Doppler velocity $U_{d,pp}$ which was calculated using the pulse-pair method. At the inner "Bar 1" the slow population peaks at approx. 0.5 m/s. Another peak is apparent in the histogram at 5 m/s which is slightly lower than the linear theory estimate of the peak phase speed ($c_p = 4.8$ m/s) at this location. This faster population is slightly broader distributed than the slower population. Like it was the case for the intensity, the bi-modality of the histogram of Doppler speeds is also an indication for the presence of breaking waves at this location. At "Through 2" which is located between the two breaker bars the distribution is unimodal. The intensity distribution at this position was clearly skewed towards higher

values. For the distribution of $U_{d,pp}$ there is also a slight skewness apparent, but much weaker compared to the intensity. A very pronounced bi-modality visible within the histogram of $U_{d,pp}$ at "Bar 2". The peak of the second (faster) population is located at $\approx$ 7.5 m/s. The peak of the slower population (at $\approx$ 1.1 m/s) is higher, but also narrower. All in all, the amount of ensembles that belong to the breaking and non-breaking population are almost equal at this location. The Doppler speed distribution at station "Buoy" shows only one clear peak located at 1.7 m/s. Very few samples with velocities near c_p ($\approx$ 10 m/s) are still present. Again, the main peak is skewed towards higher velocities.

Slow- and fast peak Doppler velocity

The two last rows of fig. 4.2 (i) - (p) correspond to $U_{d,1}$ and $U_{d,2}$, i.e Doppler velocities of the first and second peak, respectively. The Doppler peak identification algorithm was explained in detail within 3.5. While there is always a valid measurement for $U_{d,1}$ as long as there is an identifiable peak in the Doppler spectrum, $U_{d,2}$ is only available for bi-modal Doppler spectra. The most obvious difference when comparing $U_{d,1}$ to $U_{d,pp}$ is found at the two breaker zones The bi-modality within the histograms of $U_{d,1}$ is much clearer and two populations clearly separate from each other. Moreover, the amount of ensembles with Doppler velocities around the peak wave phase speed (the breaker population) is significantly lower for $U_{d,1}$ than for $U_{d,pp}$. At the same time it can be seen that second peak Doppler velocities are present at all four stations, but they are significantly more frequent at "Bar 1" compared to the rest of the stations. At "Bar 1" the population of fast moving scatterers distributes around c_p (which is 5 m/s at this location) and its distribution appears to be Gaussian shaped and relatively broad. A similar behavior can be found at "Bar 2" with one significant difference. The majority of the Doppler ensembles that correspond to breaking waves (because the speed is close to or even higher than c_p) belongs to the $U_{d,1}$ distribution. From the intensity distributions we know already, that wave breaking is connected to significantly stronger backscatter. As a consequence the signal from the non-breaking surface eventually is not strong enough to induce an identifiable peak in the Doppler spectra and the breaker peak is the only peak present. It therefore appears as $U_{d,1}$ at "Bar 2" while at "Bar 1" the signal of both peaks was still strong enough to identify both of them. This also means that at "Bar 1" the likelihood is increased, that the estimate for $U_{d,pp}$ contains errors because the power weighted average would be somewhere in between the two

peaks. It also means that the farther away the area of interest is located from the radar the more the Doppler signal is influenced by breaking events, also when the proposed peak finding procedure is applied. One last point to mention regarding the appearance of second peaks becomes visible within the distributions of $U_{d,2}$ at "Trough 2" and "Buoy". Those stations are clearly located outside the main breaker zones. However, bi-modal Doppler spectra are also present also at these locations. The Doppler velocities of the faster peak $U_{d,2}$ range from $\approx$ 1 to 6 m/s. This indicates the presence of smaller (or slower) breakers, usually called whitecaps, at those locations. The spatial extent of such whitecaps is usually smaller than the radar footprint. Nevertheless, because the signal from breaking waves is much higher than from non-breaking parts of the surface, these small breaking events will certainly have an influence on the Doppler when they are not properly identified. With increasing range and thus decreasing power of the received radar signal, it becomes more and more likely that these sub-grid breaking events dominate the Doppler ensemble, i.e. they appear as the only valid Doppler peak hence they belong to $U_{d,1}$. This induces a bias of the Doppler velocity towards higher velocities due to small breakers which becomes stronger with increasing range.

4.1.3 General Remarks on the Measurements

From the presented characteristics of the radar backscatter from shoaling and breaking waves observed within the range-time diagram of intensity and Doppler velocity (sec. 4.1.1) and the histograms at different locations (sec. 4.1.2), the following general issues could be stated.

Consistent with previously reported findings (Farquharson et al., 2005; Catalán et al., 2014; Seemann et al., 2014) depth induced wave breaking induces a distinct signature within coherent radar backscatter. The histograms of both the backscatter intensity and the Doppler velocity are significantly influenced by the presence of breakers. The measured Doppler velocities for the breaking parts of the waves are close to the shallow water phase velocity of the waves. Moreover, wave breaking is also a source for bi-modal Doppler spectra, which can lead to first moment and also pulse-pair Doppler velocities that neither represent the non-breaking surface nor the speed of the breaker but something in between those two values. However, even if a peak separation is conducted within the Doppler processing, with increasing distance the chance is increased

that only the breaker peak has enough power to be identified within a Doppler spectrum. As a result the Doppler measurements are biased towards higher velocities. This effect is expected to affect predominantly the right (faster) side of the velocity distribution because the probability of occurrence for small breakers (whitecaps) is increased at the front face of the wave. As opposed to this, shadowing is expected to occur at the lee side of the wave crest and in the wave trough, where horizontal orbital velocities are directed against the propagation direction of the wave. Shadowing is therefore responsible for lowering the occurrence of the left edge of the velocity distribution (slow velocities).

All the effects listed here induce a skewness to the distribution function of intensity and Doppler velocity. This skewness effect is apparent for all distributions shown in fig. 4.2. In addition to this skewness induced by the radar imaging, also the wave field itself is non-linear in shallow waters which also causes a non-Gaussian distribution. When utilizing coherent marine radar backscatter for studying the nearshore wave or current field, it is therefore crucial to properly identify the contribution of those individual constituents to the overall backscatter recorded by the radar. This will be addressed in the following section.

4.2 Intensity and Doppler Velocity: Forward Model

The theoretical background on microwave scattering from the sea surface was introduced in chapter 2.3. Based upon this, a simplified forward model is presented here to compute the wave induced modulation of the two main radar quantities, the backscatter intensity and the Doppler velocity, respectively. The major goal of this simplified scattering model is to adequately reproduce the observed radar scattering from the ocean waves while, at the same time, staying simple enough to be efficient and robust. The number of calibration parameters included within the model was kept at a minimum. Free parameters within the scattering model are intensity level for the actively breaking part of the wave, as well as the critical slope for both the onset and the cessation of wave breaking. There is reason to believe that the findings presented here are not sensitive to small changes of those free parameters because the chosen values are motivated by physics and observations. However, an extensive sensitivity study would be

needed to confirm this hypothesis which is beyond the scope of the present thesis. The following steps were applied to simulate the intensity and Doppler velocity:

1. Generate a phase-resolving representation of of the water surface elevation and near surface velocity along a cross-shore transect over 20 minutes using the SWASH model.

2. Estimate local tilt induced modulation of the radar backscatter.

3. Account for wave breaking based on the slope at the front face of the waves.

4. (optional) Account for geometrical shadowing.

5. Apply convolution to simulate the sensor impulse response.

6. Estimate the Doppler velocity as a power weighted sum of the simulated surface velocity.

The individual steps of the forward model are now explained in more detail. A hat on the respective symbols denotes simulated quantities (e.g. $\hat{U}_d$ is the simulated Doppler velocity). Appendix C contains all the time-range maps that are computed within the individual steps. An illustration of the representation of a breaking wave and the definitions of the angles needed to describe the scattering is shown in fig. 4.3.

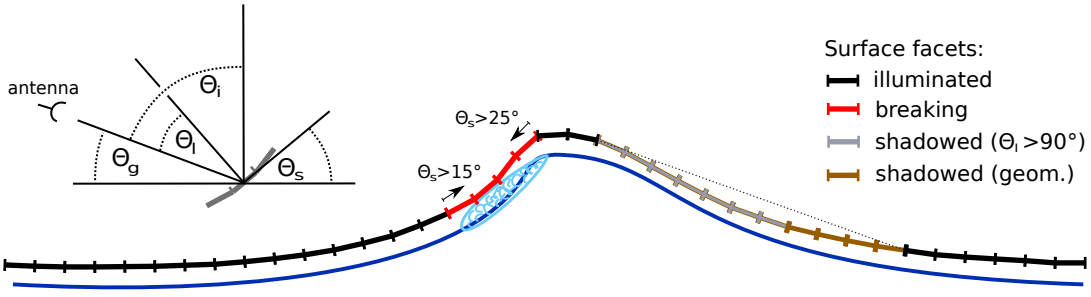

Figure 4.3: Illustration of a breaking wave represented by the proposed scattering model and angle definitions. The radar antenna is located on the left side. The patches correspond to the simulated facets of the ocean surface with a length of 0.4 m. Red facets belong to the actively breaking part of the wave, grey facets are shadowed after the tilt modulation model, brown facets are geometrically shadowed.

Wave hydrodynamics

For the relatively short analysis time, homogeneous and steady wind speed current conditions can be assumed. In this conditions, the radar signal is mainly modulated by the local perturbations of the water surface, i.e. the surface waves. The first step is hence to create a realistic, phase-resolving representation of the random sea state. For this purpose, the simulated surface elevation and near-surface velocity time series were extracted from the NH20 simulations that were described in section 3.6.1. For simplicity, only the fix pointing antenna radar data (cf. ch. 3) were considered. For this case the radar acquires a projection of the measured quantities in the line-of-sight of the radar antenna, which was pointing offshore and normal to the shoreline. The angle between the peak wave direction and the antenna line-of-sight was below 10° and thus the projection effect is negligible ($\cos(10^\circ) = 0.985$) and the simulated shore-normal horizontal flow velocity can be considered as the line-of-sight component. The sea-surface excursion $\hat{\eta}$ and the horizontal near-surface velocity $\hat{U}$ were extracted with the same resolution as the computational grid ($dx_s = 0.4$ m). Considering the number of vertical grid layers (20), the extracted velocity $\hat{U}$ corresponds to the upper 5 % of the water column. However, the Doppler signal measured by the radar is related to the velocity in the uppermost millimeters of the water column. To account for this, a wind drift contribution of 3% of the local wind speed U_{10} (Wright and Keller, 1971; Shemdin, 1972) is added to the simulated near-surface velocity. The phase speed of the Bragg waves $c_{Bragg} = 0.153$ m/s contributes to the Doppler signal and must be added too. The simulated surface velocity is thus given by

$$\hat{U}_s(r,t) = \hat{U} + 0.03\, U_{10} + c_{Bragg}\ . \tag{4.1}$$

Tilt modulation

The variation of the local surface tilt is a major determinant for the overall modulation of the radar backscatter from the ocean surface. Bragg scattering theory is well understood, but only valid for moderate incidence (grazing angles $\theta_g > 20^\circ$, e.g Valenzuela, 1978). At grazing incidence ($\theta_g < 5^\circ$) there is still no commonly accepted formulation for the tilt induced modulation of the backscatter available (see sec. 2.3.2). Following the works of Nieto Borge et al. (2004) and Støle-Hentschel et al. (2018), the most simple approximation is to assume that the signal depends mainly on the local incidence

angle and the backscatter power is maximum at nadir, which would mean specular reflection conditions. To first order this could be modelled by considering the backscatter intensity as proportional to the cosine of the local incidence angle θ_l:

$$I = \sqrt{P} \propto \sqrt{\sigma_0} \propto \cos(\theta_l) \ , \tag{4.2}$$

where P is the received power, σ_0 the normalized radar cross-section and the local incidence angle$\theta_l = \theta_i - \theta_s$ which depends on the mean incidence angle with respect to the still water level

$$\theta_i = \tan^{-1}\left(\frac{|x|}{h_{ant}}\right) \ , \tag{4.3}$$

where h_{ant} is the radar antenna height above mean sea level, and the local surface slope angle

$$\theta_s = \tan^{-1}\left(\frac{\partial \eta}{\partial x}\right) \ . \tag{4.4}$$

Following the above definitions and the simple tilt modulation model, the received power can therefore be modeled as

$$\hat{P}(r,t) = \overline{P_{rec}}(r)\ cos^2(\theta_l(r,t)) \ , \tag{4.5}$$

or in terms of intensity

$$\hat{I}(r,t) = \sqrt{\overline{P_{rec}}(r)}\ cos(\theta_l(r,t)) \ , \tag{4.6}$$

where $\overline{P_{rec}}$ represents the mean value of the received power which is range dependent and according to the radar equation (eq. 2.24) it shows a cubic falloff with increasing distance. However, the expected mean power $\overline{P_{rec}}$ is assumed to be constant throughout one radar record (10 min) because it varies on longer time scales, mainly depending on the wind speed and direction. Subsequently, for the purpose of the present study only the modulation of the intensity is considered, which is described by

$$\hat{I}_m(r,t) = \begin{cases} cos(\theta_l(r,t)) & \text{, if } \ \theta_l \leq 90^\circ \\ 0 & \text{, if } \ \theta_l > 90^\circ \end{cases} \ , \tag{4.7}$$

Negative intensity values are physically not possible and are therefore set to zero. It should be noted here that this treatment entails a certain shadowing assumption for

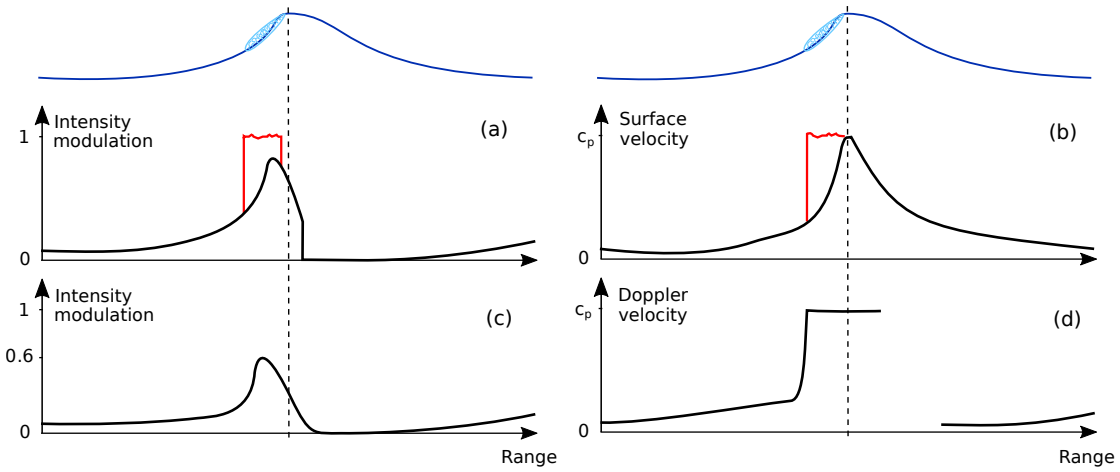

Figure 4.4: Illustration of the simulated intensity modulation $\hat{I}_m$ (panel (a), black line) and surface velocity $\hat{U}_s$ (panel (b), black line) as well as the breaking affected intensity $\hat{I}_{brk}$ (panel (a), red line) and velocity $\hat{U}_{s,brk}$ (panel (b), red line). The intensity $\hat{I}_{brk,conv}$ and Doppler velocity $\hat{U}_{d,brk,conv}$ affected by the sensor impulse response are shown in panel (c) and (d).

all surface facets that are pointing away from the radar. This type of shadowing is further referred to as the local incidence shadowing model. Assuming local incidence shadowing may not be correct as the radar radiation potentially also refracts into areas with negative local incidence angles.

The simulation grid spacing of 0.4 m is significantly larger than the electromagnetic wave length $\lambda_{em} = 3.16$ cm. The surface slope angle θ_s (eq. 4.4) calculated from the model output is therefore an appropriate measure to compute the expected modulation of the radar backscatter intensity on the scale of computational grid of the wave model. However, the radar range cell size is 7.5 m (cf. sec. 2.3.1) which is much larger and therefore the computed surface slopes between two wave model grid points correspond to the modulation on a sub-grid scale in terms of the radar range footprint. The consequence of this will also be discussed at a later part within this chapter. Figure 4.4 (a) illustrates the qualitative spatial evolution of $\hat{I}_m$ for a typical shape of a breaking wave in shallow water.

Wave breaking

As it was elucidated in section 2.3.2, wave breaking is known to cause a sudden increase of both the radar backscatter intensity and the Doppler velocity (e.g. Jessup, 1990; Keller et al., 1986; Hwang et al., 2008b). This effect can be addressed to the

scattering mechanisms of electromagnetic waves at breaking waves, which are different from the scattering at the non-breaking surface. Additionally, the droplets within the surface roller (defined in sec. 2.1.4 as the aerated region at the breaking front face) are moving at speeds close to the propagation speed of the breaking wave that carries the roller (Svendsen, 1984). Investigations of coherent radar backscatter from surf zone waves including the present study revealed, that the measured Doppler velocities from actively breaking waves are close to the shallow water phase speed of depth induced breaking waves (Farquharson et al., 2005; Catalán et al., 2014; Seemann et al., 2014).

To incorporate the influence of wave breaking within the forward model, a breaking criterion is needed to identify regions affected by breaking within the simulation results. This was done here by defining a slope based wave breaking criterion. The choice of the critical values is motivated from the findings of Schäffer et al. (1993), who used 20° and 10° for the breaking onset and termination, respectively. However, they argue that the Boussinesq model that they were using tends to underestimate they surface slopes which motivated the choice of $\theta_{crit} = 20°$, which is lower than the slope of the breaking limit of a cnoidal wave ($\theta_{crit} = 27°$) and also the Stokes limit ($\theta_{crit} = 24°$) . For the vertically resolved wave model used in present work this underestimation is not expected. Therefore, a facet of the sea surface is considered as breaking when a critical slope angle of

$$\theta_{crit} = 24° \tag{4.8}$$

is exceeded. For a sinusoidal wave, this corresponds to Stokes' breaking criterion (cf. sec. 2.1.4). The actively breaking region spans from the first model grid cell where the local slope exceeds θ_{crit} and lasts until the slope is again smaller than a second slope threshold

$$\theta_{crit,toe} = 10° \tag{4.9}$$

that defines the slope at the toe (the lower front end) of the breaking region. The physical motivation behind this second threshold is that the surface roller which forms at the front face continuously slides down the wave face. The slope of the underlying water surface at the toe of the roller expected to be smaller than the critical slope (Deigaard and Fredsøe, 1989). The actively breaking surface facets are marked in red for the exemplary breaker shown in figure 4.3. The simulated intensity including the

effect of breaking is then given by

$$\hat{I}_{brk}(r,t) = \begin{cases} 1 & \text{, for breaking facets} \\ \hat{I}_m & \text{, for non-breaking facets} \end{cases} . \tag{4.10}$$

As it is not known, how pronounced the effect of breaking will be, it is considered here as a first assumption that during wave breaking the maximum intensity modulation occurs, i.e. $\hat{I}_{m,brk} = \cos(0) = 1$.

The surface velocity for all breaking facets that are affected by wave breaking is prescribed by the phase speed of dominant (peak) wave c_p which is depth dependent and was computed for every grid cell using the peak frequency measured by the buoy and the actual water depth within eq. 2.6. The simulated surface velocity affected by breaking is thus given by

$$\hat{U}_{s,brk}(r,t) = \begin{cases} c_p & \text{, for breaking parts} \\ \hat{U}_s & \text{, for non-breaking parts} \end{cases} . \tag{4.11}$$

Both, the sizes and the speeds of the droplets inside the roller are not homogeneously distributed. To address this, a small amount of Gaussian noise was added to the prescribed values of $\hat{I}_{brk}$ and $\hat{U}_{s,brk}$ at the breaking surface facets. The standard deviation of the added noise was 2% and 5% of the prescribed value for $\hat{I}_{brk}$ and $\hat{U}_{s,brk}$, respectively. The red curves in fig. 4.4 (a) and (b) sketch the influence of wave breaking on the simulated backscatter intensity modulation and the surface velocity.

Shadowing

The complex nature of the shadowing effect behind wave crest in microwave backscatter was discussed in detail within sec. 2.3.2. As mentioned, there is no general shadowing model available for low grazing angle microwave backscatter from the sea surface. However, shadowed areas are evidently present in the time-range plots (see fig. 4.1) in far range. Therefore, this effect should be somehow accounted for when modeling the backscatter. To some extent this is already the case for the model because the applied tilt modulation model (4.7) results in zero backscatter at surface facets that are tilted away from the radar, i.e. $\theta_l > 90°$. However, the surface slopes are simulated with a higher resolution than the radar range resolution ($dx_S = 0.4$ m and $\Delta r = 7.5$ m). This

implies that a facet of the simulated surface will contribute to the backscatter intensity, as long as one facet within a radar grid cell (sub-grid scale) is tilted towards the radar line of sight. This can also happen at the lee side of the waves, where the mean slope on the scale of large waves might be tilted away from the antenna, but steep smaller waves still tilt some of the facets towards the radar.

Another possible shadowing model would be a geometrical shadowing consideration. This would result in a significantly larger area that cannot be seen by the radar at grazing incidence. Geometrical shadowing was also implemented for analysis purposes and was realized by means of a ray tracing calculation. For every instantaneous surface representation a facet on the water surface is considered as shadowed if it is not visible from the radar antenna (large wave crests obscure the surface behind). This yields the following, shadowing affected, simulated quantities (with and without accounting for wave breaking):

$$\hat{I}_{sh}(r,t) = \begin{cases} \hat{I}_m & \text{, if illuminated} \\ 0 & \text{, if shadowed} \end{cases}, \tag{4.12}$$

$$\hat{I}_{sh,brk}(r,t) = \begin{cases} \hat{I}_{brk} & \text{, if illuminated} \\ \hat{I}_{sh} & \text{, if shadowed} \end{cases}. \tag{4.13}$$

Sensor impulse response

The shape of the electromagnetic pulse that is generated and transmitted by the radar system affects the range resolution of the radar. This leads to a specific impulse response of the utilized marine radar system, which effectively leads to smearing effect in range of the received signal over more than one range cell (see sec. 2.3.1 for a more detailed expainaion). This smearing effect is considered within the forward model by applying a convolution operation in range (not time) on the intensity signal:

$$\hat{I}_{m,conv}(r,t) = (\hat{I}_m * F)(r,t). \tag{4.14}$$

The kernel of the convolution function $F(r)$ was chosen in a way that is represents the shape of the transmitted pulse. The pulse is represented by a cubic spline approximation of the pulse shape measured in the lab (see appendix, fig. A.1). The area below the convolution function F(r) was chosen such that the integral $\int_r F(r)\,dr$ equals unity.

Therefore, an application the convolution operation given in eq. 4.14 simply results in redistribution of the intensity while keeping the same total energy. This induces as a "smearing" in range with the effect that sharp gradients are flattened. In particular at the strong gradients, as they appear at the fronts of breaking waves, this leads to a significant decrease in the maximum intensity value that appears. The plots on the left side of 4.4 illustrate the consequence of this "smearing" effect. The maximum value of $\hat{I}_{brk,conv}$ is around 0.6 which is significantly lower than the maximum of $\hat{I}_{brk}$ (that was set to 1 for the active breaking parts at the waves front face) before applying the convolution operation.

Doppler velocity

Because the scale of a simulated surface facet is much larger than the electromagnetic wavelength ($dx_s \gg \lambda_{el}$) one simulated facet contains a large number of individual scattering elements. The contribution of each individual scattering element to the overall Doppler velocity of a Doppler ensemble depends on the amount of energy that is backscattered to the radar antenna from an individual scatterer (see sec. 2.3.3). With this assumption, the Doppler velocity can be interpreted as a power weighted average of the speed of the scatters at the surface. Similarly, on the scale of the radar range resolution the Doppler velocity can thus be interpreted as the power weighted average of the simulated line-of-sight surface velocity. Including the same convolution function as in 4.14 to model the sensor impulse response the forward estimate of the mean Doppler velocity is defined as

$$\hat{U}_d(r,t) = \frac{(\hat{U}_s\, \hat{I}_m^2) * F}{\hat{I}_m^2 * F}\ . \tag{4.15}$$

Similarly, $\hat{U}_{d,brk}$, $\hat{U}_{d,sh}$ and $\hat{U}_{d,sh,brk}$ are defined through a replacement of $\hat{I}_m$ in equation 4.15 by $\hat{I}_{brk}$,$\hat{I}_{sh}$ or $\hat{I}_{sh,brk}$. The result of this Doppler velocity model is qualitatively shown for an exemplary breaking wave in fig. 4.4 (d). It can be seen that the power weighting, together with the influence of wave breaking leads to a formation of a "plateau" with Doppler velocities close to the phase velocity of the wave.

Disregarded Doppler contributions

Speckle, hydrodynamic modulation and multi-path scattering effects are intentionally disregarded within the proposed scattering model. Speckle noise does not significantly alter the distribution of the backscatter modulation. It is therefore not included here because results are not expected to be affected by this. Hydrodynamic modulation is considered to be negligible at low-grazing angles compared to the modulation induced by the local surface tilt (Nieto Borge et al., 2004). Multi-path effects that may occur at steep or breaking waves are not explicitly part of the forward model, but are considered to be heuristically covered by the proposed simplistic way of including the effect of wave breaking on the backscatter intensity.

4.3 Direct Comparison

After the forward model was introduced in the previous section, the field measurements are compared to the simulated results generated from the phase-resolving simulations using the forward model. A time series was generated to force the simulation at the offshore boundary that matches the observed buoy spectrum (cf. sec. 3.6.1). Because the phases were specified randomly, the comparisons were conducted in a statistical sense only. Two statistical comparisons will be discussed in the following. The probability distributions of measured and simulated Doppler velocities are discussed first. After that, the joint probability distributions of intensity and velocity observed by the radar are compared to the simulation results.

4.3.1 Doppler Velocity Distributions

Figure 4.5 shows the measured and simulated distributions of the Doppler velocity at four selected stations across the shore normal transect. Again the first panel (fig. 4.5 (a) corresponds to station "Bar 1". Station "Through 2" is shown in 4.5 (b). Panel (c) and (d) correspond the stations "Bar 2" and "Buoy", respectively. The shown probability distributions reflect histograms of the measured/simulated parameters with a width of 0.25 m/s for each bin. The counts are then transformed to probabilities by dividing by the total amount of samples.

Station "Bar 1" (fig. 4.5 a) is located at $r = 180$ m. At this distance the simulation yields the same velocity distribution with and without applying the geometrical

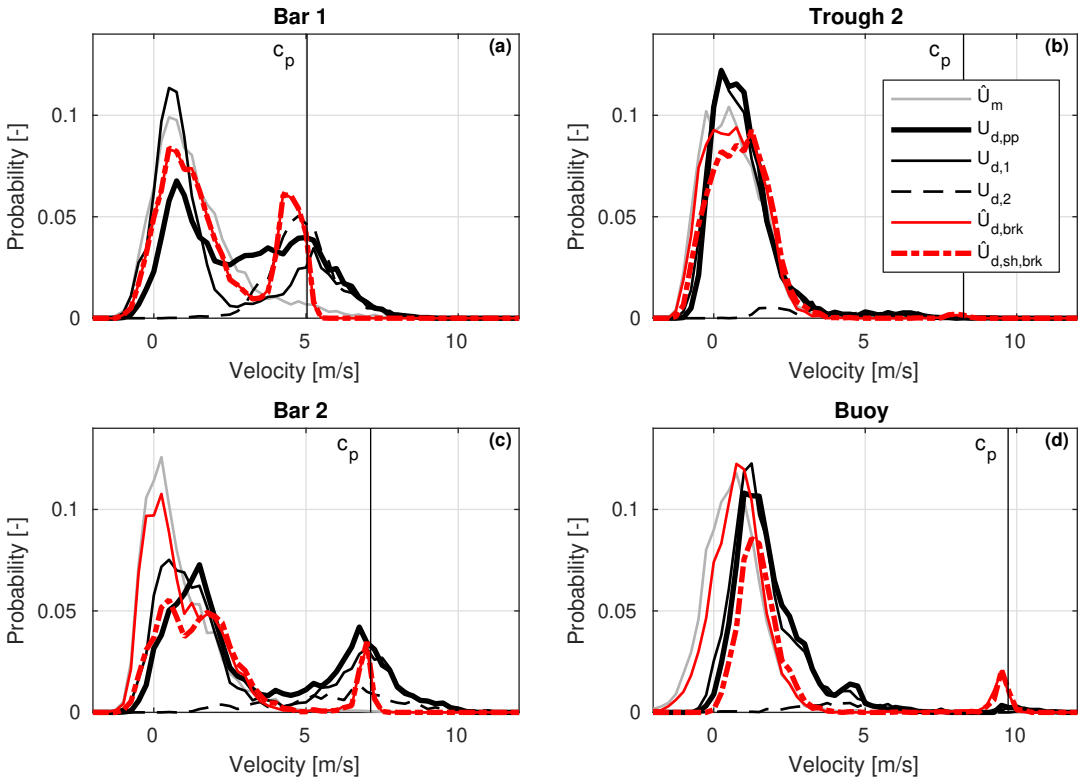

Figure 4.5: Distributions of the measured (black) and simulated (red) Doppler velocity at the stations "Bar 1" (a), "Trough 2" (b), "Bar 2" (c) and "Buoy" (d). Shown are the pulse-pair method $U_{d,pp}$ (thick black line) as well as the first- and second peak Doppler $U_{d,1}$ (thin black line) and $U_{d,2}$ (dashed black line). Simulation results correspond to the Doppler velocity with (dashed-dotted red curve) and without (thin red curve) geometrical shadowing ($\hat{U}_{d,sh,brk}$ and $\hat{U}_{d,brk}$). Also shown is the simulated surface velocity $\hat{U}_s$ (grey line) without applying the forward model. The black vertical line indicates the dominant phase velocity according to linear theory.

shadowing approach. This is expected as the grazing angle at this distance is still relatively large ($\theta_g = 8.5°$) and thus the influence of shadowing is small. If both, the proposed scattering model and the non-hydrostatic simulation results are correct, the red line should match the thick black line. The general features of the measured Doppler distribution are covered by the forward model. The distribution is bi-modal with the main peak around 1 m/s. A second peak is apparent for the measured distribution at 5 m/s. This coincides with the linear estimate of the peak phase speed c_p at this position. The second peak of the distribution of the measured Doppler $U_{d,pp}$ is at slightly slower speeds (4.5 m/s). It is worth to notice that within the forward model, the speed of the breaking facets is forced to match c_p. The fact that the distributions of

$\hat{U}_{d,brk}$ and $\hat{U}_{d,sh,brk}$ show a breaker induced peak at slightly lower speeds indicates that this is a result of the convolution operation to account for the sensor impulse response. As the measured Doppler signal is supposed to be affected by the same "smearing" effect, it is possible that the actual speed of the surface scattering elements is slightly larger than c_p. Panel (b) in fig. 4.5 corresponds to the station "Trough 2" at $r = 350$ m. The still water grazing angle here is 4.5°. It can be seen from the comparison of $\hat{U}_{d,brk}$ and $\hat{U}_{d,sh,brk}$ that the effect of shadowing starts to become evident. The probability to observe slow Doppler velocities below 2 m/s (which correspond to the wave through level) is reduced. At the same time, higher Doppler velocities between 2 and 5 m/s (at the wave crests) become more frequent. This implies that the distribution becomes skewed towards higher velocities. Depth induced wave breaking is not frequent at this position because the local water depth is relatively large (≈ 8 m). Therefore, the observed Doppler speed distribution is uni-modal at this location.

At station "Bar 2" ($r = 500$ m) the distribution is clearly bi-modal. This is expected as it this position is located inside the second breaker zone. Unlike what was found at station "Bar 1" the faster peaks of the distributions for both, the model and the simulations, are located closely around c_p (≈ 7 m/s). When comparing the observations to simulation results for this velocity range (from 5 to 10 m/s) it should be noticed that the breaker peak in the the simulated distribution is narrower than the observed one. This is similar to what was found at "Bar 1" and can be explained by the fact that not all waves are exactly propagating at c_p, but rather have slightly different individual phase speeds. The wave phase speed of an individual wave is also changed due to amplitude and frequency dispersion effects, that depend on the height and length of each individual wave as well as on the local water depth. For the velocity range attributed to non breaking waves (first peak in the distribution) a distinct difference between the geometrical shadowing assumption (dashed red line) and the local incidence shadowing model (thin red line) is apparent. The distribution of $\hat{U}_{d,sh,brk}$ comes much closer to the observed distribution for both the location and the height of the peak. The local incidence shadowing assumption does not reproduce the observed shift of the peak towards higher velocities.

At the station "Buoy", which is located at $r = 1000$ m, the still water grazing angle is already below 3°. The distribution curves are almost uni-modal at this location except for a small peak close to $c_p \approx 9.5$ m/s, that is induced by breaking waves. A small breaker peak is visible within the observation and the simulation results, while

the observed breaker velocities are slightly faster ($\approx$ 10 m/s). For the non breaking waves, only the geometrical shadowing assumption exhibits a similar shift to higher speeds as it is the case for the observations. This is similar to what was found at "Bar 2". However, the probability at the peak becomes underestimated by assuming geometrical shadowing. In fact the observed probability at the peak lies in the middle between local incidence shadowing and geometrical shadowing. Moreover, the right part (speeds from 1.5 to 6 m/s) of the observed distribution shows generally higher probabilities when compared to $\hat{U}_{d,sh,brk}$, while the left side is close the observations. This is also the range of velocities where smaller breakers (whitecaps) appear, which are indicated by the presence of second peak Doppler velocities (black dashed line). The effect of sub-grid breaking on the backscatter will be further discussed in sec. 4.4.

4.3.2 Joint Intensity-Velocity Probability Distributions

Wave breaking goes along with a simultaneous high level of intensity and Doppler velocity for the radar range cell that covers the actively breaking part of a wave. This increase gets weakened by the effect of the radar imaging. Within the present section the consequences of the radar imaging are demonstrated with regard to the joint behavior of intensity and Doppler velocity.

Figure 4.6 plots the joint probability distribution (JPD) of intensity and velocity at the four stations "Bar 1", "Trough 2", "Bar 2" and "Buoy". The upper row (panel a - d) displays the simulated intensity from tilt modulation and wave breaking $\hat{I}_{brk}$ and its corresponding surface velocity with the full resolution of the phase-resolving simulations. Within the second row (panel e -h) the simulation results after applying the convolution operation to account for the sensor impulse response are shown ($\hat{I}_{sh,brk}$ and $\hat{U}_{d,sh,brk}$). The last row depicts the JPD measured by the radar. The measured intensity values are normalized by the largest possible non saturated intensity value that is given by the ADC of the radar ($I_{max,ADC} = 5792.6$ ADU).

Before the convolution is applied, the two contributions from wave breaking are clearly separated. This is expected because the intensity level for the breaking facets was set to a significantly higher level to simulate the change in scattering mechanisms at the breaking fronts. After applying the convolution on the data, the point cloud belonging to breaking experiences a significant shift towards lower intensity levels whereas the simulated Doppler velocity remains the same. As a result, the impulse

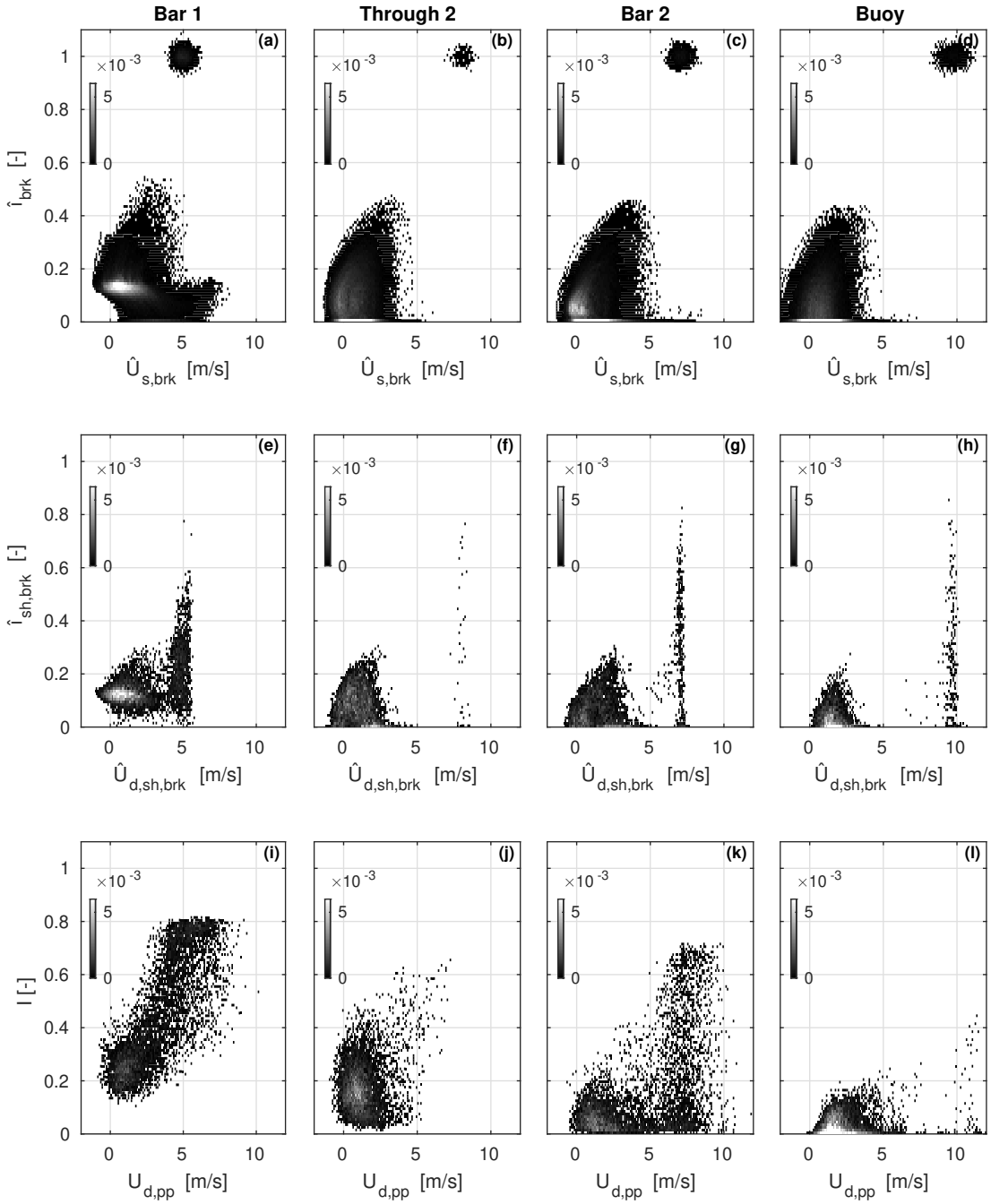

Figure 4.6: Joint probability distributions of the simulated intensity modulation and the simulated surface velocity without accounting for the sensor impulse response ($\hat{I}_{m,brk}$ and $\hat{U}_{m,brk}$, panel (a)-(d)) and with accounting for the impulse response and geometrical shadowing ($\hat{I}_{sh,brk}$ and $\hat{U}_{d,sh,brk}$, panel (e)-(h)). Shown in panel (i)-(l) are the observed joint distributions of intensity I and Doppler velocity $U_{d,pp}$. The observed intensity values are normalized by the largest possible non saturated intensity value that is given by the ADC of the radar ($I_{max,ADC} = 5792.6$ ADU).

response of the sensor artificially creates ensembles that show high Doppler velocities but low intensity levels. Those Doppler ensembles are solely caused by the "smearing" effect caused by the shape of the transmitted radar pulse. In reality, the surface particles at those locations are not moving at the observed speed because the signal still originates from the previous radar cell. This effect has to be considered when interpreting the observed radar signal and is particularly important for the wave breaking detection algorithm presented in sec. 5.1. Simulated JPDs in panel (e)-(f) generally agree well with the observations which are shown in panel (i)-(l) at all four stations. However, one clear difference is the level of the highest intensity values for the breaking parts when compared to the level of the non-breaking surface. The measurements show significantly higher intensities for the breaking contribution. This indicates that the chosen intensity level for a surface facet affected by breaking within the forward model might be still too low. However, an identification of the correct breaking intensity level would require dedicated additional measurements. This is beyond the scope of the present work. Moreover, it is expected that the simulated Doppler velocity will be less affected by a false breaking intensity level as long as this level is significantly larger than the average non-breaking intensity level.

4.4 Discussion and Concluding Remarks

The results presented in section 4.1 showed a strong influence of wave breaking for both the backscatter intensity and the Doppeler velocity. This confirms the findings from earlier studies of breaking waves affecting coherent radar backscatter. The reason for this behavior is mainly the fact that the scattering mechanisms for breaking and non-breaking parts of the surface are significantly different from each other. For the actively breaking part of the wave, where a turbulent roller is present at the breaking front face of the wave, the intensity is significantly increased. At the same time, the observed Doppler velocity is close to the propagation speed of the breaking wave. At the two breaker bars, the two different sources for the scattering are clearly visible as separate peaks in the distribution of intensity and Doppler velocity. The forward model presented in sec. 4.2 was able to reproduce this bi-modality. This supports the validity of the applied simplifications within the forward model.

A second distinctive feature is the shift of Doppler velocities towards higher values, which increases with range. This is clearly a combined result of the effect of

shadowing and wave breaking on the backscatter. Both are expected to cause higher mean Doppler speeds. Shadowing does so because it lowers the influence of the wave troughs (with low or negative velocities) on the Doppler speed. Wave breaking also increases the Doppler velocity because the surface particles move faster when a roller is present. It was also found that bi-modal Doppler spectra (see sec. 3.5) are present at all stations, regardless of the range. For bi-modal spectra, the first moment (hence also the pulse-pair) estimate of the Doppler speed would both compute a value in between the breaker and the non-breaker peak. Thus, the computed Doppler corresponds neither to the velocity of the breaker nor to the non-breaking surface velocity, but somewhere in between these two velocities. Performing a peak separation when processing the Doppler velocity can reduce this error, but with increasing range it becomes more likely that only the breaker contribution is strong enough to induce a detectable peak inside the Doppler spectrum.

Additionally, it was shown from the simulation results in sec. 4.2, that the influence of the sensor impulse response significantly decreases the intensity values. If the intensity level of the non-breaking surface is low the Doppler speed is more affected, or even dominated, by the faster scatterer speeds of breaking waves. Because breaking causes much stronger backscatter a small breaker inside one radar cell can easily dominate the backscatter, even if the non-breaking surface covers a much larger area. Due to the spread of the transmitted pulse energy over more than one range cell the breaking contribution from the previous range cell may still be present inside the Doppler spectrum of the following range cell and potentially it is still strong enough to dominate the backscatter.

All the listed influences on the Doppler signal of the sea surface acquired by coherent marine radar occur simultaneously and it is difficult to identify and separate the individual contributions. When applying the forward model, false assumptions for one certain contribution is possibly canceled out by opposing errors of a another one. Thus, the results can match the observations, even if the physical assumptions were wrong. This must be considered if coherent marine radar is used to deduce information about geophysical quantities from the backscatter, e.g. surface velocities or wave heights.

Chapter 4: Key findings

- Wave breaking induces Doppler velocities close to c_p that could be identified in observations and were reproduced by the proposed forward model.
- A peak separation during Doppler processing leads to a better separability of breaking and non-breaking Doppler ensembles.
- Small breakers sometimes dominate the backscatter and bias the Doppler velocity towards higher values.
- The shape of the transmitted pulse and the associated sensor response causes a "smearing" in range. Therefore, strong signals from breaking waves might affect more than one range cell.

Chapter 5

Wave Breaking Probability

Modern wave prediction models typically estimate the (scale dependent) wave breaking probability (or fraction of breaking waves) and additionally assume a bulk number for the energy dissipation by a single breaking wave (see sec. 2.4.3). The product of probability and bulk dissipation yields the total amount of dissipated energy. Such a treatment implies that opposing errors for the probability and the dissipation would systematically cancel out and therefore the total amount of dissipated wave energy is potentially still correct, even if the assumptions made regarding the wave physics and the breaking process itself were wrong. Additional difficulties arise when other wave related effects such as dissipation by bottom friction or vegetation, non-linear wave-wave interaction or energy input by wind cannot be neglected for the given problem to study. Wave prediction models generally perform well for (typically uniform) open ocean conditions (e.g. Cavaleri et al., 2007). However, wave models show some weaknesses during severe storms, as well as when complex topography or current situations are present (Van Der Westhuysen, 2010; Salmon and Holthuijsen, 2015; Cavaleri et al., 2018). This is particularly the case at tidal inlets or locations where shallow features such as reefs or tidal flats are present, e.g. within estuaries or the Wadden sea (Salmon et al., 2015). New observation based parameterizations are required, that better incorporate the physics behind the processes involved. Establishing a large collection of field observations covering as many circumstances as possible is crucial to accomplish this goal. Having said this, field observations of breaking waves and related quantities are difficult to realize and therefore only a few field data sets are available by now (see sec. 2.2.3). In particular, the automated identification of individual breaking events and an unambiguous assessment of the properties of the wave (height and length/period)

is often not possible. The development of a robust and automated detection method for individual wave breaking events within coherent marine radar backscatter will enable scientists to build the data basis needed to develop more physical wave breaking parameterizations. It is therefore the main subject of the present chapter.

The microwave backscatter from shoaling and breaking waves observed with coherent marine radar has been analyzed extensively within the previous chapter 4. Based on these findings, a new algorithm to automatically identify wave breaking from the Doppler spectra is introduced within the present chapter (sec. 5.1). Hereby, the evolution of neighboring Doppler spectra in space and time is used to classify different types of ensembles affected by breaking, i.e. dominant breaking, small breakers and radar imaging artifacts. Within section 5.2, the new wave breaking detection algorithm is then used to calculate wave breaking probabilities for different wave and tide conditions over the course of a 4-day long storm event . The observations are compared to different parameterizations for the wave breaking probability that are part of the depth induced wave breaking source term parameterizations that were introduced in sec. 2.4.3. Finally, it is shown briefly within section 5.3 that the suggested detection algorithm can also be used to quantify the occurrence frequency of oceanic whitecaps.

5.1 Automated Breaker Detection

Within this section, a new algorithm is introduced to identify wave breaking from characteristic features of breaking waves in the Doppler spectra. The main physical feature utilized for the detection is the jump of the surface velocity from the orbital speed of the wave to its phase speed during wave breaking and the simultaneous significant increase of the radar backscatter intensity. The proposed algorithm should generally also be applicable to other radar setups, but is described and applied here only to a situation when waves where traveling approximately perpendicular to the shoreline with the radar antenna fixed and pointing into the incoming waves. This avoids some challenges resulting from projection effects when waves are moving obliquely to the radar view direction.

The main goal of the detection algorithm is to classify an individual Doppler ensemble represented by its Doppler spectrum (computed from the raw data behind one pixel in the range-time diagram using the processing chain described in 3.5) as "breaking" or "not breaking". If the Doppler spectrum is multi-modal , the decision has to be made

whether the individual peaks are valid measurements or caused by imaging effects the like smearing effect of the sensor impulse response. The latter should be seen as a radar imaging artifact and thus it should be excluded from a statistical analysis of the occurrence of wave breaking. However, for double peaked spectra it is possible under some circumstances that both of the peaks within the spectrum are valid measurements. Therefore the ensemble contains information on the speed of both the breaking and non-breaking parts of the ocean surface covered by the radar cell. This happens in two cases. The first case appears at the leading edge of the surface roller at the front face of a breaking wave. The propagation speed of a dominant breaker can reach up to more than 10 m/s. Taking this into account it is likely that the wave propagates into the next radar cell over the 0.512 s integration time. This way it could happen that, for example, for the first half of the integration time the illuminated part of the water surface is not yet breaking while for the second half the breaker is present. If the breaking event is long enough (in space and in time), the following Doppler spectrum is expected to be fully dominated by wave breaking meaning that only one peak is present which must be classified as "breaking". Slightly more effort must be undertaken in order to identify detection failures resulting from the radar imaging artifacts.

The developed classification algorithm is briefly outlined in the following. The classification is undertaken based on the properties of the identified peaks within the Doppler spectra, the Doppler velocity and the power of the peak, respectively. Currently, only the first two (from slow to fast) peaks are considered. The result of the classification algorithm are binary masks that indicate the location of the ensembles of the classes *dominant breaking* B_{dom}, *dominant artifacts* $B_{cp,out}$, *small breakers* B_{small}, and *possible artifacts* B_{trail} within the time-range diagram. Table 5.1 lists the resulting ensemble classes that will be explained in more detail in the following. The result of the classification is graphically illustrated in figures 5.1 and 5.2. The following three steps are applied in order to categorize each identified peak:

Step 1: Identify dominant breakers by the Doppler to phase velocity ratio

The first step of the algorithm aims on an identification of all Doppler ensembles that correspond to the dominant breakers of the wave field. Following Banner et al. (2000), a dominant breaker is defined as a breaking wave with an intrinsic frequency in the vicinity ($\pm 30\%$) of the spectral peak frequency ($0.7 f_p < f < 1.3 f_p$). With the assumption that for a breaking wave the value of the measured Doppler velocity reaches

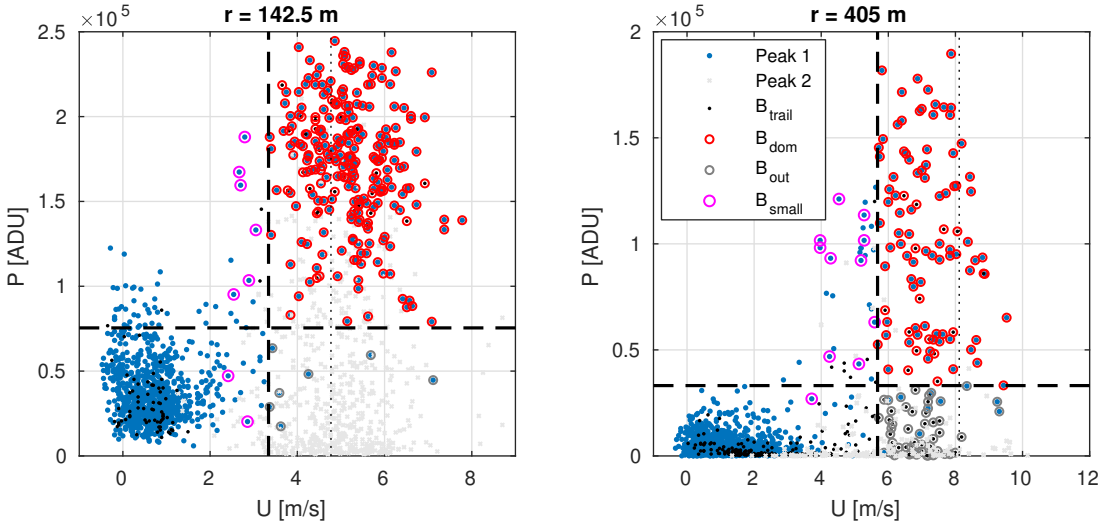

Figure 5.1: Classification results shown in a scatter plot of peak power against the Doppler velocity for the range cell at 142.5 m (a) and 405 m (b). Blue points correspond to first (slower), light grey points to second (faster) Doppler peaks. Points were classified into the classes "dominant breaking B_{dom}" (red) "dominant artifacts" $B_{cp,out}$" (grey), "small breakers B_{small}" (magenta) and "possible artifacts" B_{trail} (black).

or slightly exceeds the phase velocity of the breaking wave, the following condition is used to identify ensembles resulting from dominant wave breaking:

$$U_{d,1} > 0.7\, c_p\ , \tag{5.1}$$

where $U_{d,1}$ is the Doppler velocity from the first peak in the Doppler spectrum (see sec. 3.5) and c_p is the (range dependent) peak phase velocity of the wave field. The binary mask that indicates the locations of the Doppler ensembles where condition 5.1 is met will be further denoted as B_{cp} (with the dimension $nr \times nt$). For the particular case when multiple peaks are present, the ensemble is only added to B_{cp} when the condition is already satisfied for the slowest of the present peaks. This is ensured here by the fact that the first (slower) peak velocity $U_{d,1}$ is considered when the spectrum was multi-modal.

The computation of the peak phase velocity c_p has a direct effect on the results. For the present study, the expected local phase velocity is calculated from the linear gravity wave dispersion relationship (eq. 2.6). Taking into account the instantaneous tidal elevation from the operational model BSHcmod that includes tide and surge effects, the

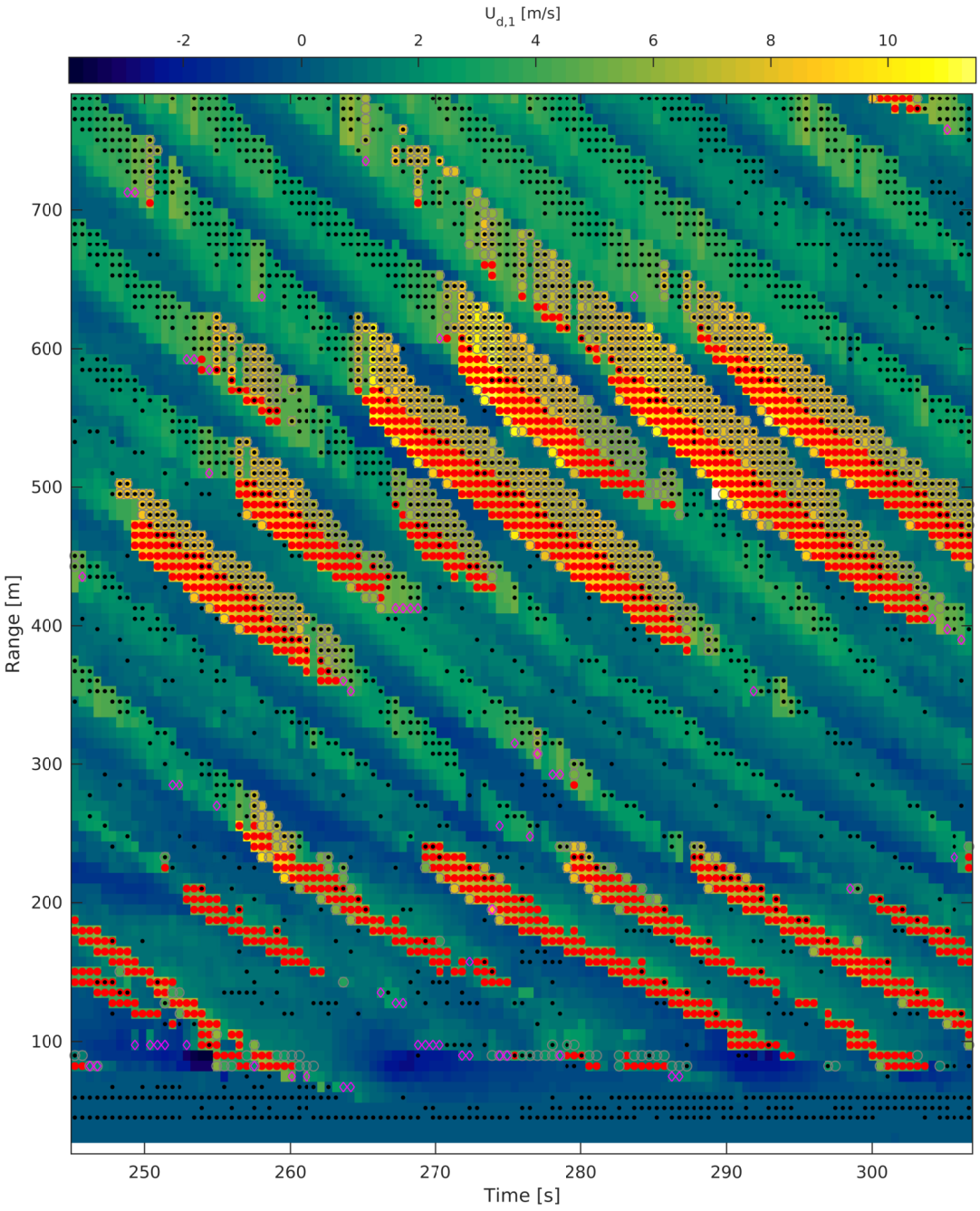

Figure 5.2: Time-range diagram of first peak Doppler velocity $U_{d,1}$. Dots indicate ensembles classified as "dominant breaking" B_{dom} (red) "dominant artifacts" $B_{cp,out}$" (grey), "small breakers" B_{small} (magenta) and "possible artifacts" B_{trail} (black).

local water depth was extracted from the depth soundings taken during WaveDiss2016 (see sec. 3.4). The peak frequency of the sea state was extracted from the spectra measured by the COSYNA wave rider buoy.

If actual information about the bathymetry, sea state and actual tidal elevation is not available, these parameters could also be derived directly from the radar data. Water depths can be derived from marine radar images by applying a depth inversion algorithm (Bell, 1999; Senet et al., 2008; Honegger et al., 2019). The phase speed c_p can be estimated directly from the time-range diagrams using the structure tensor method (Jähne, 2004). The method is applicable to the time-range diagrams of intensity (Streßer, 2014), but further research is required to confirm the robustness and range of application in terms of the environmental conditions.

Step 2: Remove artifacts due to the "smearing" effect of the radar pulse

The second step of the algorithm deals with the effect of the sensor impulse response of the radar (cf. sec. 2.3.1). At the rear face of a breaking wave crest the surface roughness often disappears completely because vertical turbulence and vorticity generated by the breaking causes slicks at the water surface. Together with fact that the surface at the lee side of the crest is titled away from the radar antenna this leads to very low intensity values in this area. As it was already mentioned in chapter 4, such circumstances increase the likelihood that the high intensity values from the actively breaking part of the waves still dominate the Doppler spectra of the subsequent range cell because the transmitted pulse is over-sampled in range. Additionally, this effect is expected to become stronger in far range (lower grazing angles) because the area of the wave profile that is not illuminated increases. It was also discussed within chapter 4 that the impulse response of the radar causes Doppler velocities close to c_p but a low corresponding intensity. To identify the Doppler ensembles with high velocity but low intensity values, a range dependent power level threshold

$$P_{thresh}(r_i) = med(U_{d,1}(r_i,t) \notin B_{cp}) + 2\ std(U_{d,1}(r_i,t) \notin B_{cp}),\ \ i = 1,2,...,nr\ , \quad (5.2)$$

is computed from the remaining (non-breaking) velocities indentified by negating the binary mask found in step 1, hence $B_{nobrk} = \neg\, B_{cp}$. The horizontal dashed lines in fig. 5.1 indicate the level of P_{thresh}. The mask $B_{cp,out} \in B_{cp}$ indicates the Doppler ensembles that are supposed to be discarded when only active breaking pixels are to

Binary Mask	Description	Condition
B_{cp}	Doppler velocity from dominant breakers	$U_{d,1} > 0.7\ c_p$
B_{nobrk}	not affected by dominant breaking	$B_{nobrk} = \neg\, B_{cp}$
$B_{cp,out}$	pulse smearing artifact	$(P \in B_{cp}) < P_{thresh}$
B_{trail}	(possible) pulse smearing artifact	see text of step 3
B_{dom}	valid dominant breakers	$B_{dom} = B_{cp} \notin B_{cp,out}$
B_{small}	valid smaller (slow) breakers	see text of step 3

Table 5.1: Binary masks containing the resulting classes for the Doppler ensemble classification algorithm to detect wave breaking.

be identified because $(P \in B_{cp}) < P_{thresh}$. The pixels that are classified as a valid dominant breaker ensemble can be found by taking the remaining breaker ensembles $B_{dom} = B_{cp} \notin B_{cp,out}$.

Step 3: Identify slow breakers from neighboring Doppler peak evolution

The purpose of the first two steps of the classification procedure was to identify the dominant breaker pixels in the time-range diagram. However, also shorter and therefore slower waves ($U_{d,1} < 0.7\ c_p$) possibly break. As mentioned already in sec. 2.3 and 3.5, the presence of multiple peaks inside a Doppler spectrum indicates different sources for the scattering at this particular range cell that could be caused by breaking waves which may be not resolved by the radar. The following assumptions are made to detect such slower breaking events. Considering the radar range cell spacing of 7.5 m it is unlikely to find the same or a very similar Doppler velocity at two adjacent range cells for the same time step. A single-peaked Doppler ensemble will be marked as "slow breaker" when the Doppler spectrum of the previous range cell (at the same time) consists of two distinct peaks, provided that the second (faster) peak of the preceding spectrum shows a similar (± 0.05 m/s) Doppler speed compared to the peak inside the Doppler spectrum of the present cell. Additionally, it must apply that the peak power of the actual peak is larger than the power the previous second peak. If the power of the peak with a similar Doppler speed is smaller compared to the previous cell, the peak is flagged as a trailing "possible artifact" peak. The set B_{small} consists of all the Doppler velocities that belong to a valid, small breaker according to the characteristics mentioned above.

5.2 Dominant Wave Breaking Probability

Within this section, the classification algorithm developed within the previous section 5.1 is used to infer the probability for dominant wave breaking and results are compared to different commonly used breaking parameterizations for depth induced wave breaking (see sec. 2.4.3). Namely these are the parameterizations BJ78 (Battjes and Janssen, 1978), TG83 (Thornton and Guza, 1983), CK02 (Chawla and Kirby, 2002), W88 (Whitford, 1988), JB07 (Janssen and Battjes, 2007) which is similar to B98 (Baldock et al., 1998) in terms of the breaking probability and, finally, the unified formulation of Filipot et al. (2010b) as it is implemented within the breaking parameterization FA12 (Filipot and Ardhuin, 2012).

First it is explained how the breaking probability is derived from the radar data. The evolution of the observations in space and time are analyzed in sec. 5.2.2 and comparison to the different models is presented in 5.2.3.

5.2.1 Computation of the Breaking Probability

The wave breaking probability is usually defined as a function of wave height $P_b(H)$. Because individual wave heights are not known in the present case, the fraction of breaking waves $Q_b = \int_H P_b(H)$ is considered which is a measure for the overall breaking probability. In a deterministic manner, Q_b is defined as the number of breaking waves N_b divided by the total number waves N_w that pass a certain point during a certain time. It therefore represents the probability to observe a breaking wave of arbitrary height and period (or length) at a given location. Technically, there are two different ways to determine the total number of waves from a recorded time series, a level crossing approach or a statistical approach, respectively.

If a record of the surface elevation is available, individual waves are commonly determined using a zero-up or zero-down crossing analysis (e.g. Banner et al., 2002). The characteristic properties of the wave, such as height and period, but also higher order quantities like skewness and asymmetry can then easily be computed between the two crossing points. If wave breaking occurs between the two crossing points, the wave is marked as a breaking event. This approach, however, gets problematic if waves of different scales are present. In this case, a detected event might originate from a smaller breaking wave, rather than from the dominant wave that is identified by the crossing analysis. A distinctive attribution to a certain wave scale is therefore not

always possible.

If only one (dominant) wave scale is considered, the total number of waves could be also computed statistically from the total duration of a record D_{rec} and a representative period for the wave field T_r. The total number of waves is then defined as

$$N_w = \frac{D_{rec}}{T_{rep}} \, . \tag{5.3}$$

T_{rep} in this equation is a period that is representative for the sea state, e.g the period at the spectral peak of the wave spectrum T_p.

The radar derived fraction of breaking waves

Considering the different general ways of computing the Q_b described above, the radar derived breaking probability was calculated for the present study by applying the mentioned statistical method (eq. 5.3). The number of breaking waves N_b is determined for each range cell by counting the number of ensembles where wave breaking starts. For this purpose, the binary mask $B_{dom,start}$ was derived from B_{dom} which contains all pixels that indicate a starting point of wave breaking (i.e. the transition from a pixel that was marked as not breaking to a pixel marked as breaking). The radar derived breaking probability was then determined from $B_{dom,start}$ following eq. 5.3 as

$$Q_{b,radar} = \frac{N_b}{N_w} = \sum_{t=0}^{D_{rec}} B_{dom,start} \, \frac{T_{rep}}{D_{rec}} \, . \tag{5.4}$$

The peak period measured by the buoy was used as a representative period ($T_{rep} = T_p$) and the total duration D_{rec} represents the total length of the radar record ($D_{rec} = t_{max} - t_{min}$).

5.2.2 Time-Range Evolution of the Fraction of Breaking Waves

The presence of breaking waves at a particular location in shallow water qualitatively reveals information about the hydrodynamic conditions in place. Wave breaking produces an onshore directed shear current at the water surface which generates offshore directed undertow currents. Generally, this leads to a net transport of sand that is directed offshore. On the contrast, the strongly skewed and asymmetric wave shape that appears for shoaling but not yet breaking waves induces an onshore sand move-

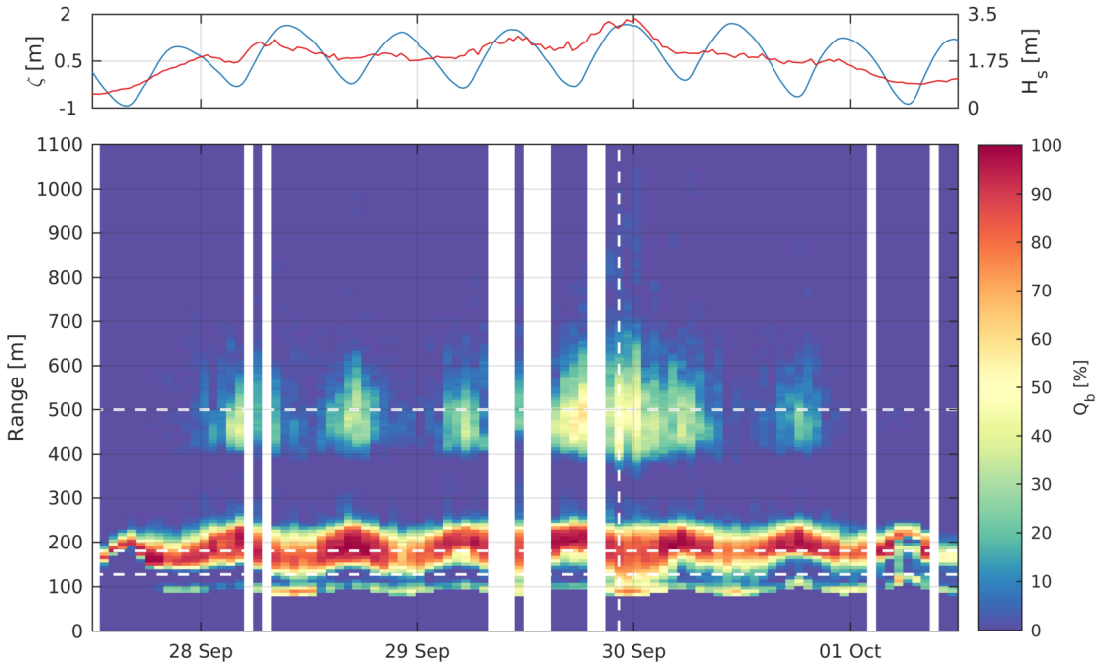

Figure 5.3: Time-range diagram of the fraction of breaking waves Q_b during the storm event (Sep. 27, 12:00 AM to Oct. 1, 12:00 AM). Dashed white lines indicate the measurement time (vertical) of the transect shown in fig. 5.4 and the location (horizontal) of the time series shown in fig. 5.5, 5.6 and 5.7. Upper panel shows the tidal elevation ζ from BSHcmod (blue) and the signifcant wave height H_s (red) observed at the wave rider.

ment. The net sand transport integrated over the cross-shore beach profile is therefore directed offshore in storm conditions and onshore during calm periods.

The observation of the spatial variation of the occurrence breaking waves from field data over a large distance is a difficult task (cf. sec. 2.2.3). However, by applying the classification algorithm introduced in sec. 5.1, it is now easily possible to extract the fraction of breaking waves Q_b from the fixed antenna radar data. This yields a 10-min average for Q_b every 7.5 m along the whole cross-shore transect once per hour. Figure 5.3 shows the time-range evolution of Q_b for the study period over the course of the storm event. The highest breaking rates ($Q_b > 80\%$) appear at the breaker zone on the inner sandbar (110 m $<$ r $<$ 300 m). The location and extent of this inner surf zone is strongly modulated by the semi-diurnal tides. At low tide, the beginning (from an offshore point of view traveling with the waves) of the inner breaker zone moves further offshore. Additionally, it can be seen that Q_b reaches 100% at this inner breaker zone during low tide. Less waves are breaking ($Q_b \approx 80\%$) on the inner bar at high tide

and a narrow (only 2 or 3 range cells wide) swash zone seems to become apparent at $r = 100$ m. The width of the breaker zone at the inner bar doesn't seem to be affected much by the tide, but rather it seems to be correlated with the offshore wave height measured by the wave rider buoy.

At the outer bar (300 m $< r <$ 800 m) the highest breaking rates also occur during low tide, but the largest values ($Q_b \approx 50$ - 60%) are significantly lower compared to the inner bar. Only at the peak of the storm, when significant wave heights reach up to 3 m and more, wave breaking continuously occurs at this location. Before and after the storm peak, when H_s was around 2 m, the outer bar was only active during low water. The width of the breaker zone at the outer bar seems to be related to both, the wave height and the water level.

For a more detailed analysis of the cross-shore behavior of Q_b, the radar derived cross-shore variation of the breaking probability at the peak of the storm (Sep. 29, 22:10 AM) is displayed in figure 5.4. Also shown is the sea floor elevation along this transect and the actual mean water level elevation taken from BSHopmod at the time of the measurement. The wave height observed at the buoy was $H_{rms} = 2.33$ m and the peak period was $T_p = 10$ s. Coming from offshore, wave breaking starts to occur at ≈ 700 m and the observed Q_b is gradually increasing until the crest of the outer bar (at $r = 450$ m) is reached. About 50% of the waves that pass the outer bar crest break

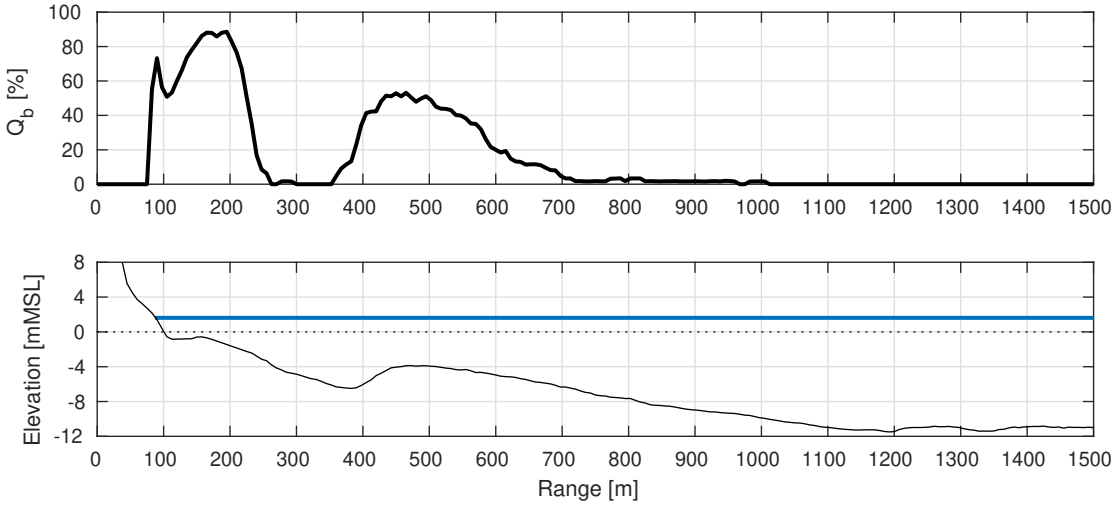

Figure 5.4: Cross-shore transect of the radar derived fraction of breaking waves Q_b (upper panel) at the peak of the storm (Sep. 29, 22:10 PM) together with the mean sea surface elevation and the bed level (lower panel) at the time of the measurement.

at this outer bar. From this point the wave breaking rapidly becomes less frequent due to the fact that the water depth increases again. However, it requires some distance until all waves have stopped to break. This indicates that some waves, and probably the larger ones, travel a longer distance before they actually stop breaking.

The inner bar breaker zone starts around $r = 250$ m. A decrease in Q_b is apparent after the bar crest, but still more than 50% of the waves are breaking at the bar through region. This might be because the water for such an energetic wave situation is still not deep enough and the bigger waves continue to travel towards the beach as quasi-steady bores. Once they reach the beach, Q_b increases again to $\approx 80\%$ before it drops rapidly when the dry beach is reached, which is trivial.

5.2.3 Comparison to Probability Parameterizations

In this section, the observed breaking probabilities are compared to six different shallow water wave breaking parameterizations that are explained in sec. 2.4.3 and listed in table 2.3. Most of the different formulations were developed originally to prescribe the source term for the energy dissipation due to depth induced breaking within a wave model. The estimation of the wave breaking probability therefore is not the main purpose of the formulations but rather a by-catch product that is necessary to estimate the total amount of dissipation. However, because the bore analogy (cf. sec. 2.4.3) is the basic assumption behind all of the formulations, the fraction of breaking waves directly influences the total amount of dissipated energy.

It is explicitly not the goal here to analyze the performance of the breaking source term formulations in terms of the total dissipation. This is already subject of several other studies (e.g. Battjes and Stive (1985); Ruessink et al. (2003); Rattanapitikon (2007); Van Der Westhuysen (2010); Salmon et al. (2015), among others). However, validations of the different parameterizations in terms of Q_b are extremely rare. This is mainly because only very few field data sets are available by now, where Q_b was explitcitly measured in the field (cf. sec. 2.2.3). The goal of the present work is to compare the results from the different breaking parameterizations to the radar observations of Q_b. Radar observations are available along the whole cross-shore transect, whereas the in-situ wave measurements during the storm event are restricted to the location of the wave rider buoy ($r = 1100$ m) and the two pressure wave gauges PG1 at station "Bar 1" ($r = 180$ m) at the nearshore sandbar and PG3 at station "Trough 1"

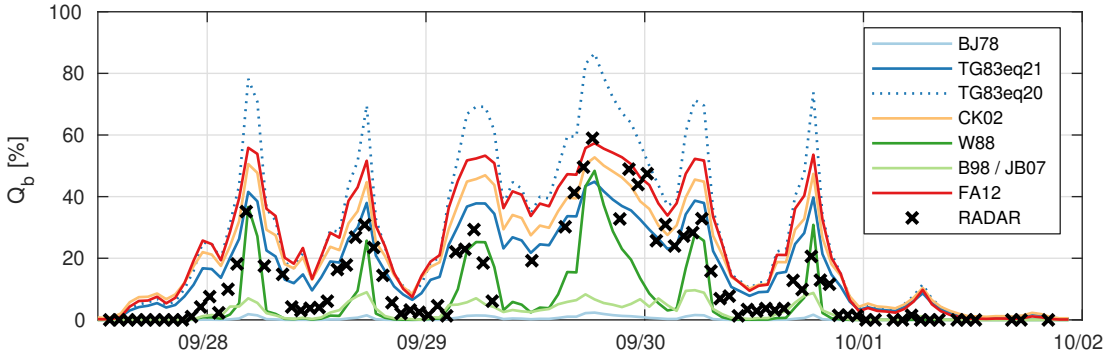

Figure 5.5: Time series of the fraction of breaking waves Q_b at the outer bar crest (at station "Bar 2", $r = 500$ m). Q_b was estimated from the parameterizations BJ78 (light blue), TG83 (blue), CK02 (yellow), W88 (green), B98 which is similar to JB07 (light green) and FA12 (red) (see sec. 2.4.3 for a description). H_{rms} was taken from the NH2 simulation and f_{rep} from the wave rider buy measurement. The radar observations are marked by the black crosses.

($r = 127$ m) at the through of the inner bar (see fig. 3.4). It can be seen from fig. 5.3 that no (or only very few) dominant breaking waves appear at the wave rider position. However, a considerable amount of waves are apparently breaking on the outer sandbar depending on the incident wave height and tide conditions.

Figure 5.5 shows a time series of the observed Q_b at station "Bar 2" ($r = 500$ m). The sea floor elevation with respect to MSL is -4 m at this location. The figure also plots the results from the different breaking probability parameterizations BJ78, TG83, CK02, W88, B98 (which is equal to JB07 in terms of the breaking probability) and FA12 (see tab. 2.3 for a listing of the parameterizations). There is no measured wave height information available at this position. Therefore, H_{rms} was extracted from the two-layer non-hydrsotatic wave model simulation (NH2). The NH2 simulation was chosen because the phase-resolved model was shown to give the best result when compared to the in-situ measurements (cf. sec 3.6.3). It can be seen that both BJ78 and B98 predict extremely low values for Q_b that do not exceed 15%. This is significantly (≈ 5 times) less than what is observed by the radar at this location. The TG83eq20 formulation shows a slight overprediction of about $10-20\%$ throughout the entire study period. However, Thornton and Guza (1983) note already within the original paper, that their motivation of presenting eq. 20 was to provide a simple analytical expression for the cross-shore wave height evolution, whereas their eq. 21 matched the observed breaking wave height distribution much better. This is also the case for the obser-

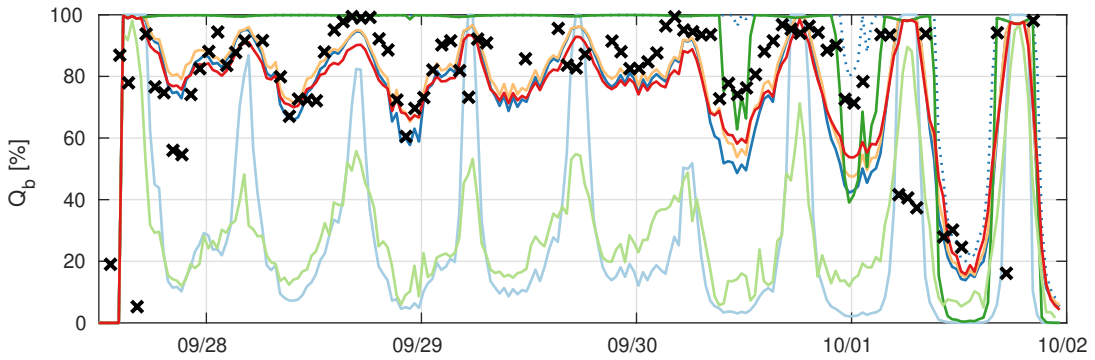

Figure 5.6: Time series of the fraction of breaking waves Q_b within the inner bar breaking zone at station "Bar 1" (where PG1 is located, $r = 180$ m). Refer to fig. 5.5 for the color coding. Wave parameters were directly measured by the pressure gauge. The radar observations are marked by the black crosses.

vations presented here as it can be seen that the evolution of TG83eq21 matches the observations remarkably well. Also CK02 parameterization and the parameterization of FA12 are able to reproduce the observed Q_b, even if the both predict slightly higher values at the present location at the outer bar crest. This is not surprising because FA12 followed the idea of CK02 to provide an expression that reduces to the TG83 formulation in shallow water.

The Q_b time series at the station "Bar 1" where the pressure gauge PG1 was located is shown in fig. 5.6. At this location, H_{rms} could be inferred directly from the pressure measurement. From the time-range evolution of Q_b shown in fig. 5.3 it turned out, that the relative position of this station with respect to the extent and position of the inner bar breaker zone varies throughout the study period. As already mentioned earlier, fig. 5.3 also reveals that the main influence for the inner breaker zone location is the tidal elevation while its spatial extent is related to the offshore wave height. For most of the study period, "Bar 1" is thus located within the inner breaker zone, but with some distance to the offshore starting point of the breaker zone. This means that the majority of the waves within the radar record started breaking already further offshore so that enough time (or distance) has passed already to allow them to transform to quasi-steady bore-like waves. These conditions are therefore similar to those at the time and location of the field data set used to derive the TG83 formulation. Consequently, TG83eq21 produces very similar results to what was observed by the radar at this location. Moreover, it is visible that the difference of the TG83eq21 prediction to

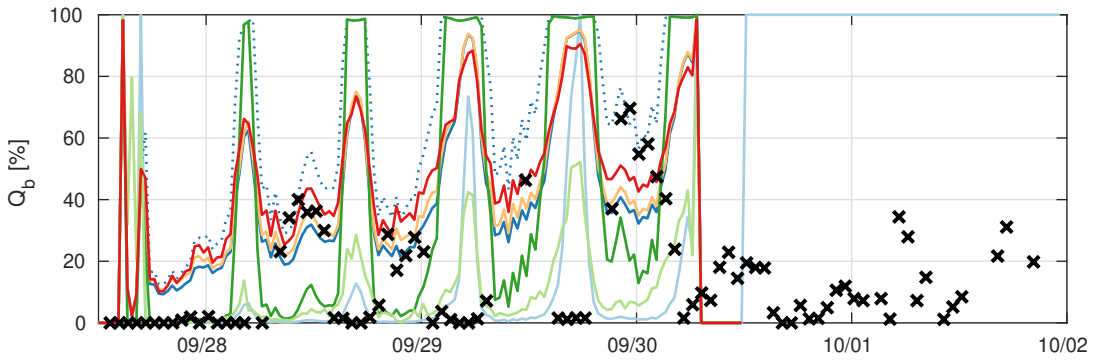

Figure 5.7: Time series of the fraction of breaking waves Q_b at the inner bar trough (at station "Trough 1" where PG3 was placed, $r = 127.5$ m). Refer to fig. 5.5 for the color coding. Wave parameters were directly measured by the pressure gauge. The radar observations are marked by the black crosses.

CK02 and FA12 becomes smaller than the difference at "Bar 2". This is because the water depth at "Bar 1" is much shallower, hence the shallow water limit is reached and all three expressions converge to the same solution. A slightly larger discrepancy appears after the climax of the storm was reached and wave heights decrease (after Sep. 29, 23:00 PM). This might indicate different breaking characteristics for decaying sea states, but more research is needed to verify this. The BJ78 as well as the B98 show again significantly smaller values but this time the differences between the two expressions is even more pronounced. Especially at low water, the BJ78 formulation shows significantly larger Q_b values (compared to B98) that reach 100% and therefore comes close to the observations when the water depth becomes extremely shallow. However, the fraction of breaking waves at "Bar 1" on average is significantly underestimated (about 70 percentage points) by the BJ78 or the B98 parameterization.

The last time series to consider is located at the bar through between the inner bar and the swash zone at station "Trough 1" were the pressure transducer PG3 was placed ($r = 127.5$ m). Figure 5.7 shows the result at this location. Again, the wave height H_{rms} has been extracted directly from the pressure record. It seems that none of the expressions is able to reproduce the evolution of Q_b at this location. All formulations show a similar trend with low fractions of breaking waves during high tide and high peaks of Q_b $(80-100\%)$ at low tide. The observations, however, show a similar periodicity but the peaks in Q_b seem to be phase shifted with respect to the tidal wave. This means that high Q_b values are observed during high tide and not during low tide as the

parameterizations predict. The reason for this can be found by considering again at the full time-range evolution shown in fig. 5.3. From this figure it comes clear, that if dominant wave breaking occurs at station "Trough 1" this is due to fact that the onshore end of the inner bar breaker zone spans farther than this location. This means that the breaking process of the waves that are still breaking at "Trough 1" was initiated already further offshore, on the bar crest or before. It is likely that during low tide, when the inner bar breaker zone moves offshore, the breaking process already terminated completely because the water depth at the inter-tidal bar crest is either extremely shallow (a few decimeters), or the crest of the bar even falls dry so that the waves cannot pass it. At situations when waves are able to pass the bar, the persistence of breakers at the bar trough might be captured when the effects roller formation and decay (see sec. 2.1) is correctly accounted for. However, the transformation process that waves undergo when the travel over submerged bars is a heavily non-linear process and the results here show that common parameterizations are not able to cope with this.

5.3 Whitecap Statistics

Within the previous section the focus was on the quantification of the probability of dominant wave breaking, hence waves with frequencies close to the spectral peak were considered. The breaking process for the dominant breakers was mainly induced by the shoaling process as they were entering shallower water. However, it was shown in sec. 5.1 that the proposed detection algorithm is also able to identify Doppler ensembles that resulting from smaller breakers (the magenta circles in fig. 5.1 and 5.2) from the coherent marine radar backscatter. Such small breakers can be detected from the presence of a second peak within the Doppler spectrum at the moment when they enter a radar resolution cell. The measured Doppler speeds for these small breaking events are slower than the threshold velocity for dominant breaking ($U_{d,1} > 0.7\ c_p$). Small breakers in the ocean are usually called whitecaps and they influence many exchange processes at the air-sea interface. Although whitecaps are not the main subject of the present thesis, a brief demonstration of the capacities of the proposed detection algorithm for studying oceanic whitecaps is given in the following. For this, the homogeneous region area seaward of the outer breaker bar was considered. The water depth there is constant $\approx 11 \pm 1$ m, depending on the tidal elevation. Figure 5.8 shows time-range positions of Doppler ensembles that were classified as "small breakers" (or

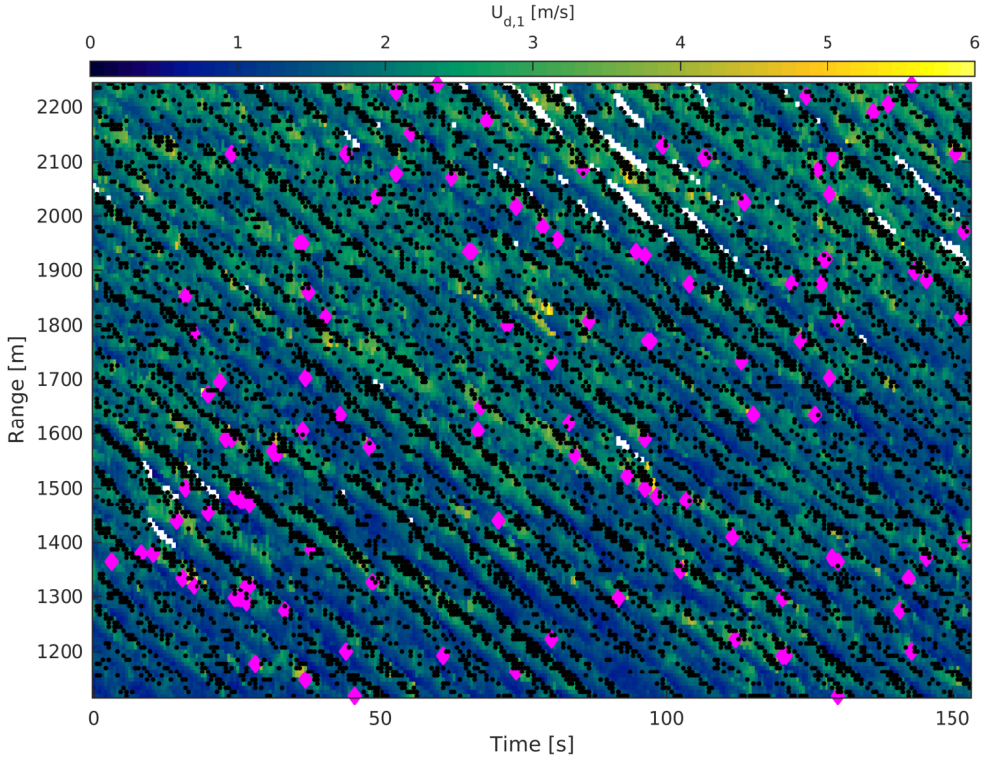

Figure 5.8: Time-range diagram of the first peak Doppler velocity $U_{d,1}$ seaward of the outer bar on 28-Sep-2016 10:16:38 AM. Detected "small breaker" ensembles are marked by magenta diamonds. Black dots indicate ensembles categorized as "possible artifacts" which are not considered as a valid Doppler measurement.

whitecaps) for the fix-antenna radar record on 28-Sep-2016 10:16:38 AM.

For open ocean whitecap studies it became standard to make use of the so called Λ-framework introduced by Phillips (1985), who defined $\Lambda(c)$ such that $\int \Lambda(c)\, dc$ equals the length (perpendicular to the waves propagation direction) of breaking wave fronts per unit area of ocean surface. The Λ-function depends on the phase speed c of the breaking wave and because it is meant to be applied in deep water, c is directly related to a specific frequency (or wave length). With this definition, the Λ-function provides some important information about the whitecap characteristics at the ocean surface for waves of all scales. The frequency of occurrence, or passage rate of whitecaps of all scales can be computed from the Λ-function as

$$R_b = \int c\, \Lambda(c)\, dc\ . \tag{5.5}$$

The scale-dependent amount of dissipated wave energy per unit area can be estimated as

$$\varepsilon(c)dc = b\frac{\rho_w}{g}c^5\Lambda(c)\,dc\,, \tag{5.6}$$

where g is the gravitational acceleration, ρ_w is the density of the sea water and b is a dimensionless breaking strength parameter. Thus, the total amount of dissipated energy by white capping can be estimated as

$$D_{wc} = \frac{\rho_w}{g}\int b\,c^5\Lambda(c)\,dc\,. \tag{5.7}$$

In order to obtain the Λ-function from the coherent marine radar backscatter, the (speed dependent) number of whitecaps was computed first. Similar to the previous section, it is assumed that surface particle speeds during wave breaking reach or exceed the propagation velocity of the wave. Therefore, the Doppler velocity $U_{d,1}$ of an ensemble that belongs to a breaking wave can be taken as a measure for the phase speed c of the wave. Again, the Doppler ensembles were composed of 1024 radar pulses and the classification algorithm introduced in section 5.1 was used to categorize the ensembles. All "small breaker" ensembles with speeds between c and $c+dc$ were counted to define the speed dependent number of whitecaps $N_{wc}(c)$. When multiple Doppler ensembles were affected by one breaking event, only the first ensemble was considered for the calculation to make sure the breaking event is counted only once. In order to get a representative estimate of $N_{wc}(c)$ for the 10-min long radar records, the computation was conducted at every range cell range cell between cell number 150 and 300 (1125 m $< r <$ 2250 m) and the result was averaged. By considering the relationship given in eq. 5.5, the Λ-function was derived from the measured number of whitecaps as

$$\Lambda(c) = \frac{N_{wc}}{D_{rec}\,c\,dc}\,, \tag{5.8}$$

where D_{rec} is the total duration of the radar record. The discrete binning size was chosen as $dc = 0.25$ m/s. Figure 5.9 shows the radar derived Λ-function for the radar record shown in fig. 5.8 on 28-Sep-2016 10:16:38 AM. The individual phase speed measures shown on the abscissa of the figure were normalized by the peak phase speed $c_p = 9.58$ m/s that was obtained from the wave rider peak frequency by applying linear wave theory. Please note, that this study does not intent to completely verify the presented coherent marine radar measurement of the Λ-function. This would require

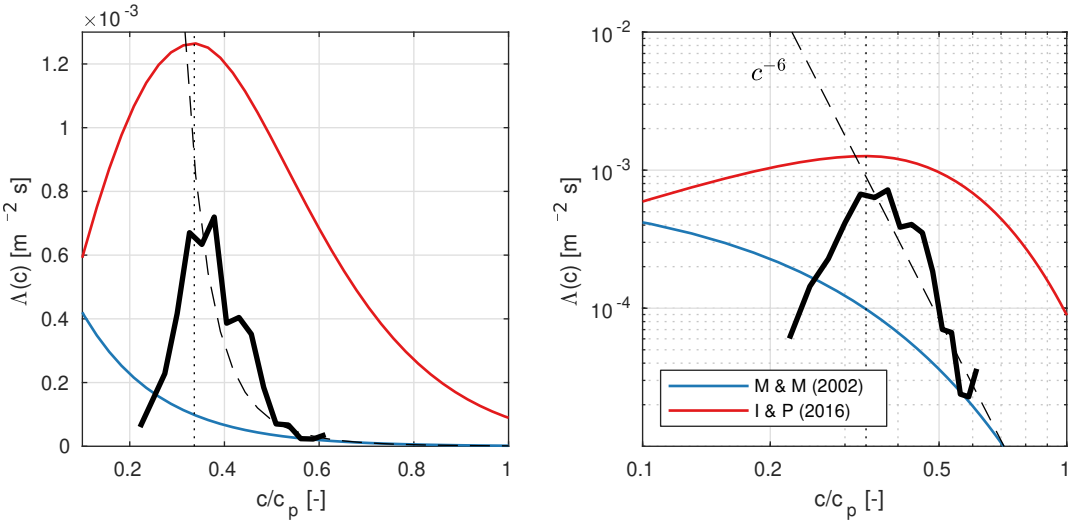

Figure 5.9: Radar derived Λ-function in linear (a) and double-logarithmic (b) scale between $r = 1125$ m and $r = 2250$ m observed on 28-Sep-2016 10:16:38 AM. The recorded buoy wave height $H_{rms} = 1.52$ m and the peak phase speed was $c_p = 9.58$ m/s. Wind speed from BSHopmod was $U_{10} = 13.3$ m/s. Also shown are the parameterizations of Melville and Matusov (2002) (eq. 5.9) and Irisov and Plant (2016) (eq. 5.12) indicated by blue and red lines, respectively. Dotted black vertical line marks the location of the peak of the Λ-function calculated from eq. 5.10. The dashed black line plots c^{-6} for reference.

a thorough comparison to field observations applying different techniques to obtain $\Lambda(c)$. However, a plausibility test of the measurements is done here by comparing the result to parameterizations reported in literature. Melville and Matusov (2002) found an empirical expression

$$\Lambda(c) = 3.3 \times 10^{-4} \left(\frac{U_{10}}{10}\right)^3 \mathrm{e}^{-0.64\,c} \tag{5.9}$$

that matched their observations. Irisov and Plant (2016) performed Monte Carlo simulations of free surface representations and found the following expression that was consistent with their simulation results and also with the observations by Kleiss and Melville (2011). They proposed a best-fit function that peaks at

$$c_0 = 0.22 + 0.39\,c_p - 0.008\,c_p^2\,, \tag{5.10}$$

and the height of the peak is defined by

$$\Lambda_{peak} = 0.00024 \left(\frac{ak - 0.02}{0.02} \right) \left(\frac{U_{10}}{10} \right)^3 , \tag{5.11}$$

where ak is the rms wave slope, computed from the rms amplitude $a = H_{rms}/2$ and the peak wave number k_p. With $\xi = c/c_0$, the Λ-function proposed by Irisov and Plant (2016) is

$$\Lambda(c) = \Lambda_{peak} \times \begin{cases} \xi \exp\left(\frac{1-\xi^2}{2}\right), & \text{if } 0 < \xi < 1 \\ \xi^3 \exp\left(3(1-\xi)\right), & \text{if } \xi \geq 1 \end{cases} . \tag{5.12}$$

Both, the empirical equation proposed by Melville and Matusov (2002) (eq. 5.9) and the formula introduced by (Irisov and Plant, 2016) (eq. 5.12) are shown in fig. 5.9. The location of the peak of the Λ-function as estimated from eq. 5.10 matches the location of the radar derived Λ-distribution well. The observed peak shows slightly faster speeds ($c/c_p = 0.37$) than the expected peak location computed from eq. 5.10 ($c/c_p = 0.34$). The I & P 2016 parameterization gives higher values over the whole range of speeds compared to the observations. However, the general shape of the distribution is consistent with the observations. Some differences are visible on both sides of the distribution, where the observed Λ-distribution decays faster. Equation 5.9 predicts lower values for Λ. Thus, the radar based observations are within the same range as previously reported observations of the Λ-function. This strongly indicates a general applicability of coherent marine radar for further studies on the dependencies of Λ under different weather conditions and at different locations.

5.4 Discussion and Concluding Remarks

An in-depth validation of the developed classifications algorithm would require a deterministic comparison of the results to other wave breaking detection methods such as infrared or visible light video. This is beyond the scope of the present thesis. Nevertheless, the results have shown that the algorithm is capable of producing reasonable results for both the fraction of dominant depth induced breaking waves and the occurrence of whitecaps. In the following, a brief discussion of the sensitivity of the algorithm with respect to the choice of the free parameters is given.

The general concept behind the breaking detection algorithm is a bi-variate thresh-

olding. Only Doppler ensembles that show a high backscatter intensity and at the same time a high Doppler velocity are considered as a valid breaker ensemble The threshold levels were chosen relative to the peak phase speed of the wave field and the median non-breaking intensity level at a given range. For the present sea state and water levels, the two populations (breaking and non-breaking ensembles) clearly separate from each other as it can be seen in figure 5.1. For shorter waves or shallow water depths, the peak phase speed and the orbital speeds are closer together. In such conditions, the ensemble populations might have more overlap and the threshold based detection gets ambiguous. Additionally, what wave scale is considered a dominant breaker is always a matter of definition and cannot be seen as a distinct separation. However, due to the clear separation that was found for the analyzed data, a slightly different choice of the relative velocity threshold ($\approx 0.7 \pm 0.2\ c_p$) is not considered to alter the results, in particular not regarding the computed fraction of breaking waves. Even if the classification algorithm can not be considered as methodology that is free of assumptions, it is considered as robust and powerful tool which is well suited for an automated analysis of large amounts of data.

Also interesting points for discussion are the implications of the findings of section 5.2.3, where the observed breaking probablity was compared to different parameterizations for depth induced breaking. Most parameterizations underestimate the observed breaking probability along the entire cross-shore transect. However, the results of the numerical simulations (sec. 3.6.3) showed that most wave models give reasonable results for the nearshore wave height, even if the breaking probability is underestimated. This demonstrates nicely the problem that errors for the breaking probability can get canceled out by opposing errors for dissipation rate. The data here confirm this hypothesis which was already mentioned by Filipot et al. (2010b) and was also a motivation for the universal observation based breaking parameterization by Filipot and Ardhuin (2012). This parameterization is the only one that is able to reproduce the observed cross-shore evolution of the fraction of breaking waves. The data here therefore support the idea of Filipot and Ardhuin (2012) to scale the bulk dissipation instead of the commonly applied scaling of the breaking probability. However, the results from the simulations using the parameterization of Filipot and Ardhuin (2012) yielded larger errors in terms of the significant wave height. The available parameterizations therefore can either predict the wave height or the breaking probability with good accuracy and further improvements are required if correct predictions of both quantities are needed.

Chapter 5: Key findings

- A novel algorithm is presented to detect wave breaking within microwave backscatter from the ocean surface recorded by coherent marine radar.
- Observed fractions of breaking waves Q_b are consistent with the parameterizations by Thornton and Guza (1983), Filipot and Ardhuin (2012) and Chawla and Kirby (2002) for depth induced wave breaking.
- Parameterizations of Battjes and Janssen (1978), Baldock et al. (1998) and Janssen and Battjes (2007) predict up to $5\times$ lower values for Q_b as observed at the outer bar and up to $3\times$ at the inner bar.
- Whitecap statistics in terms of Philipps' Λ-function were within the same order of magnitude in comparison with the empirical equations by Melville and Matusov (2002) and Irisov and Plant (2016).

Chapter 6

Wave Energy Dissipation

The dissipation of surface wave energy affects many nearshore processes such as the generation of turbulence, wave induced currents and sediment transport. The aim of the present chapter is thus to quantify and investigate the cross-shore distribution of wave energy dissipation in the nearshore. For this purpose, a new methodology is presented that can be used to estimate wave energy dissipation from the Doppler velocity observed by coherent marine radar.

In a homogeneous, deep water area the significant wave height (hence the wave energy) can be estimated from the variation of the Doppler velocity (Carrasco et al., 2017a,b). Within section 6.1, the empirical approach by Carrasco et al. (2017b) is modified for an application in conditions where the wave kinematics are influenced by the water depth. Doppler ensembles affected by wave breaking are identified using the detetection algorithm described in section 5.1. They are omitted from the analysis because the Doppler velocity of breaking waves does not correspond to the wave orbital speed, but to its phase speed (see findings in chap. 4). Within section 6.2, a novel methodology is presented to quantify the energy stored in the surface roller at the front face of a breaking wave from the measured Doppler velocity. The method relates the increase of the Doppler velocity at the transition from non-breaking to breaking parts of the ocean surface to the roller energy which can be used to estimate the dissipation of organized wave energy as well as the roller induced shear force that acts at the water surface. This surface shear is directly linked to turbulence production and mainly drives surf zone circulation. The results from the different methods are evaluated in section 6.3.

6.1 Significant Wave Height from Doppler Variation

The goal is to estimate the wave energy dissipation rate along a cross-shore transect. A direct quantification of the amount of energy dissipation from in-situ instruments is difficult to realize, in particular if a high spatial resolution is required (see sec. 2.2.3). Alternatively, if the wave heights are known at two positions along the propagation direction of the wave (quasi 1D) and all other dissipation mechanisms are negligible, the dissipation of organized wave energy can be computed directly from the wave energy flux balance

$$D_w = \frac{F_2 - F_1}{|x_2 - x_1|} \,, \tag{6.1}$$

where $F = Ec_g$ is the flux of wave energy at two adjacent locations (x_1 and x_2). The wave energy that is contained in a stationary wave field can be determined from the significant wave height of the sea state as $E = \frac{1}{16}\rho g H_s^2$.

The Doppler velocity is modulated by the wave orbital motions. Thus, it is reasonable to investigate whether the Doppler signal can be used to infer H_s from the Doppler velocity records along the radar range. The energy dissipation then follows from equation 6.1.

6.1.1 Horizontal Orbital Velocity to Heave Conversion

According to linear theory (see sec. 2.1.2), the horizontal component of the wave orbital velocity u (eq. 2.2) at a given location is related to the surface elevation η by

$$\eta(t) = \frac{u(t)\ \sinh(kd)}{\omega\ \cosh(kd)}. \tag{6.2}$$

Thus, the power spectrum of surface elevation $S_{\eta\eta}(\omega)$ is related to the spectrum of the horizontal orbital velocity at the surface $S_{uu}(\omega)$ by

$$S_{\eta\eta}(\omega) = \frac{S_{uu}(\omega)\ \sinh^2(kd)}{\omega^2\ \cosh^2(kd)} \,. \tag{6.3}$$

The (energy based) significant wave height can be computed from from the first moment (or the variance) of the spectrum as

$$H_s = 4\ \sqrt{m_0} \,. \tag{6.4}$$

McGregor et al. (1998) used equation 6.3 to convert the Doppler velocities measured by coherent S-band radar to surface elevation. They were motivated by the findings of Plant et al. (1983) who used the same transfer function in deep water for X- and L-band radar measurements from the German research platform NORDSEE in the North Sea. However, the grazing angle of their measurements was quite large (about 30°). At low-grazing incidence, the signal is strongly influenced by other radar imaging effects and the observed Doppler velocities deviate from wave induced velocities (Farquharson et al., 2005). The applicability of the linear wave theory to invert the Doppler velocity to surface elevation is therefore questionable. Nevertheless, it was also computed here as a reference. Note that the orbital motions observed by the radar are always projected to the antenna line-of-sight. Projection effects due to the incidence angle are negligible at grazing incidence ($\cos(\theta_g) < 2.5\%$ for $\theta_g < 10°$). Azimuthal projection effects, however, must generally be considered, but where small for the dataset analyzed within the present study because the radar antenna was pointing towards the main wave direction ($\theta_{az} - \theta_w < 10°$).

6.1.2 Empirical Approach

The radar is not able to measure the surface velocity directly (see sec. 2.3). The observed Doppler velocity U_d results from a complex interplay between different influencing factors. However, many of the listed contributions to the measured Doppler velocity are expected to be constant in time. Periodic oscillations of the Doppler velocity are expected to to be mainly caused by wave orbital motion, but complex and not yet fully understood radar imaging effects additionally influence U_d at grazing incidence. To address this, Hwang et al. (2010) and later Carrasco et al. (2017b) developed empirical transfer functions. However, both studies were undertaken in a deep water environment where the wave field was homogeneous, i.e. the wave height was constant in space. Therefore, the empirical methods for deep water are revised in the following in order to test them on the shallow water dataset of the present study.

Deep water

Hwang et al. (2010) proposed the empirical relationship

$$H_s = 4\,X\,\frac{u_{DRMS}}{\omega_p}\,, \tag{6.5}$$

where u_{DRMS} is the root-mean-square Doppler velocity (which is equivalent to the standard deviation, if the mean value of the Doppler is 0), ω_p is the radial frequency at the peak of the wave spetrum and X is a dimensionless correction factor, that was found to be 1 for HH and 1.3 for VV backscatter.

Later, Carrasco et al. (2017b) analyzed an extensive coherent marine radar data set recorded from an offshore platform over several months. For this homogeneous environment, where the wave field is not significantly influenced by the local water depth, their results show that the significant wave height can be estimated from coherent marine radar backscatter using the simple empirical relation:

$$H_s = 4\sigma_D \ , \tag{6.6}$$

where σ_D is the standard deviation of the measured line-of-sight Doppler velocity U_d. Since this relationship is purely empirical, the units on the right-hand side need to be adjusted to match the unit of H_s (meters), or in other words the proportionality constant must be dimensional (with the unit seconds). Comparisons to a wave rider buoy and ADCP wave measurements yielded a root-mean-square-error of 20 cm. In addition to the homogeneous environment, the study in Carrasco et al. (2017b) only considered data at grazing angles where influence of shadowing is still small. Moreover, a large distance spanning over ≈ 700 m was considered to compute one spatially integrated value for the significant wave height. In depth limited areas the wave field is mostly non-homogeneous and it can change on much smaller distances, because wave characteristics are strongly altered by the local water depth. A spatial integration as it was done by Carrasco et al. (2017b) is therefore not an option.

Arbitrary water depth

With increasingly shallow water, the orbital motions of the waves are altered and the variation of the horizontal motions is larger compared to the vertical motions. Equation 6.2 accounts for the influence of the relative water depth on the orbital motions and is therefore applicable to waves at arbitrary water depths. However, the empirical relation given in eq. 6.6 suggests a better performance in deep water without dividing by ω. A slightly different formulation is therefore proposed here in order to apply a similar

empirical method in waters of arbitrary depth:

$$H_s = 4 \, \frac{\sigma_D \, \sinh(kd)}{\omega_p^{\beta_{emp}} \, \cosh(kd)} \, . \tag{6.7}$$

By choosing $\beta_{emp} = 0$, eq. 6.7 reduces to the empirical formulation of Carrasco et al. (2017b) in deep water and for $\beta_{emp} = 1$ it corresponds to the equation proposed by Hwang et al. (2010).

Breaking waves cause high Doppler speeds that are not anymore related to wave orbitals, but rather to the phase speed of the breaker (cf. sec. 4). Therefore, Doppler ensembles affected by breaking were identified using the detection algorithm introduced in sec. 5.1. The identified breaking ensembles were omitted for the computation of σ_D in eq. 6.7. The need for the removal of breaking waves prior to the analysis makes a direct comparison to the deep water formulations impossible. An additional difference to the mentioned previous studies lies in the fact, that the Doppler velocity $U_{d,1}$ was calculated from the slowest peak of the Doppler spectrum within the present study. Hwang et al. (2010) as well as Carrasco et al. (2017b) considered the pulse-pair estimate of the first moment of the Doppler spectrum $U_{d,pp}$.

6.2 Energy Dissipation of the Surface Roller

When a wave is actively breaking, water particles tumble down the front face of the breaker and form a highly turbulent area that consists of a mix water droplets and air. This area, called the surface roller, contains a certain kinetic and potential energy. The storage of momentum within the roller leads to a flux of energy (in addition the wave energy flux), which needs to be considered within the surf zone momentum balance in order to accurately predict the wave setup (Svendsen, 1984) and wave induced currents (Ruessink et al., 2001). Therefore it has become common to model nearshore hydrodynamics with a coupled set of transport equations for the transformation of wave and roller energy (eq. 2.35 and 2.36 introduced in sec. 2.4.2).

The radar is highly sensitive to breaking waves, hence it is an excellent instrument to detect individual breaking wave events (as done within chap. 5). Additionally, coherent radar is able to measure the Doppler speed of the scatters at the surface. For actively breaking waves, the observed Doppler speed is in the range of the phase speed of the wave (see ch. 4). Based on these findings, a novel approach to derive roller

properties from the Doppler signal is presented within the following section 6.2.1. The dissipation of roller energy causes strong surface shear stresses that drive currents and are the main source for the production of turbulence. Whithin section 6.2.2 the measured roller energy and roller dissipation is used to compute the cross-shore evolution of wave energy from the coupled wave and roller energy balance equations.

6.2.1 Roller Properties Inferred from the Doppler Velocity

The surface roller is defined as the turbulent region at the front face of a breaking wave which consists of water droplets and air and is separated from the underlying water mass. For infinitesimally long crested waves in the direction of wave propagation, its (bulk) kinetic energy per unit span is given by

$$E_{r,total} = \frac{1}{2}\rho' A_r \left(\overline{u_r^2} + \overline{w_r^2}\right) , \tag{6.8}$$

where A_r is the roller area, u_r and w_r are the bulk horizontal and vertical motions of the roller and ρ' is the bulk density of the roller (including water and air), that can be expressed as

$$\rho' = \beta_\rho \, \rho_w , \tag{6.9}$$

with the calibration factor β_ρ representing the proportion of water with respect to air inside the roller. Phase-averaging the total roller energy yields the roller energy per unit area

$$E_r = \frac{E_{r,total}}{L} . \tag{6.10}$$

With the assumption that the vertical component of the roller motion is small ($w_r \ll u_r$), the roller moves approximately with the same speed as the breaking wave, and thus

$$\left(\overline{u_r^2} + \overline{w_r^2}\right) \approx c^2 . \tag{6.11}$$

Svendsen (1984) re-analyzed the data of Duncan (1981) who studied quasi-steady breakers produced in the laboratory by a towed hydrofoil in deep water conditions. He found that the geometric properties of the rollers are self-similar and

$$\frac{A_r}{H^2} \approx 0.9 = const. \tag{6.12}$$

Later, Okayasu et al. (1986) studied the wave induced nearshore circulation including roller effects and proposed the relationship

$$\frac{A_r}{HL} \approx 0.06 \text{ to } 0.7 = const \ , \tag{6.13}$$

which resulted a in better match to their experiments. Eq. 6.13 is used within the present work and thus thus the roller area is given by

$$A_r = \kappa \, HL \ , \tag{6.14}$$

where κ is a proportionality constant that varies between 0.06 and 0.07 (Okayasu et al., 1986; Svendsen, 2006). A value of $\kappa = 0.07$ was used within here. Substituting eq. 6.11 and 6.14 into eq. 6.8 and 6.10 finally yields the expression

$$E_r = \frac{1}{2} \, \rho' \, \kappa \, H \, c^2 \ , \tag{6.15}$$

for the roller energy that depends on the roller density ρ', the local wave height H and the wave phase speed c.

Substitution of the wave height

Equation 6.15 requires the knowledge of the local wave height H. If the spatial distribution of the wave height - hence the wave energy - would be known beforehand, the amount of local wave energy dissipation would also be known, because it could be readily computed from equation 6.1. Therefore, a substitute for H needs to be found.

Shallow water waves are not anymore affected by frequency dispersion and the propagation speed depends mainly on the local water depth. However, the effect of amplitude dispersion increases in shallow water as the wave shape gets more and more non-linear. The non-linear shallow water phase speed can be estimated by the empirical predictor (Booij, 1981)

$$c = \sqrt{g(d + \alpha_{ad} H)} \ . \tag{6.16}$$

The calibration coefficient α_{ad} determines to what extent the amplitude dispersion is considered. By choosing $\alpha_{ad} = 0$, eq. 6.16 corresponds to the shallow water phase velocity according to linear wave theory, whereas for $\alpha_{ad} = 0.5$ it corresponds to solitary wave theory. Using the most common formulation for the breaker parameter $\gamma = 0.78$,

the water depth at the breakpoint can be roughly estimated as

$$d = \frac{H}{\gamma} \,. \tag{6.17}$$

Combining eq. 6.16 and 6.17 yields the approximate expression

$$H = \frac{c^2}{g\left(\frac{1}{\gamma} + \alpha_{ad}\right)} \,, \tag{6.18}$$

which relates the wave height of a breaking wave in shallow water to its phase speed. While this scaling for the breaking wave height may be a reasonable assumption for breaking in shallow water, it must not necessarily apply to deep water breakers. However, the laboratory experiments of Duncan (1981) show that the height of the studied deep water breaking waves scales with the phase speed squared and find

$$H = 0.6\,\frac{c^2}{g} \,. \tag{6.19}$$

Using the above mentioned typical values for γ and α_{ad} within eq. 6.18 yields

$$H = \frac{c^2}{g\left(\frac{1}{0.78} + 0.5\right)} = 0.5612\,\frac{c^2}{g} \approx 0.6\,\frac{c^2}{g} \,. \tag{6.20}$$

Thus, the proposed scaling also matches the results of Duncan (1981) and is supposedly also valid for deep water breaking waves. Combining equations 6.15, 6.22 and 6.18 finally yields an equation for the roller energy as a function of the phase speed c of the breaker

$$E_r = \frac{\beta_\rho\ \kappa\ \rho_w}{2g\left(\frac{1}{\gamma} + \alpha_{ad}\right)}\,c^4 \,. \tag{6.21}$$

Main hypothesis to infer the phase speed c from the Doppler velocity

In order to obtain the roller energy from 6.21 using quantities measured by the radar, the following hypotheses are made:

1. The Doppler velocity U_d resulting from the scatterers within the actively breaking part of the wave is equal, or slightly larger than the wave propagation speed c.

2. The Doppler speed within the radar cell before the active breaking region (in space) is small.

The former assumption is backed by the findings in chap. 4. The latter is motivated by the fact that horizontal orbital velocities are typically small at the toe of the roller (that slides into the wave trough). With these assumptions the phase speed of the breaking wave can be obtained from the spatial increase in Doppler velocity $dU_d = U_{d,r_{i+1}} - U_{d,r_i}$ at a given range cell number r_i as

$$c = \beta_d \; dU_d \; . \tag{6.22}$$

The calibration parameter β_d was introduced to correct for small misconceptions within the hypothesis and should equal 1 if the assumptions made are correct.

The explained approximation of c is only valid for the change from slow to fast moving scatterers at the toe of the roller. Therefore, only positive velocity shifts are considered for the computation of c in eq. 6.22. This also ensures that every breaking wave appears only once in the computation of the time averaged roller measures described below.

Radar derived roller properties

In order to provide a more convenient formulation for the radar derived roller energy, all calibration parameters within equation 6.21 are combined and the factor $B_r = \beta_\rho \; \kappa \; \rho_w \left(2g\left(\gamma^{-1} + \alpha_{ad}\right)\right)^{-1}$ is introduced to scale the radar derived roller energy. The radar derived roller energy therefore simply reads

$$E_r = B_r \; \frac{\rho_w}{g} \; \overline{\left(\beta_d \; dU_d\right)^4} \; , \tag{6.23}$$

where the over-bar indicates time averaging over the full radar record (10 min for the present study). Thus, the flux of roller energy is given by

$$F_r = E_r \; c = B_r \; \frac{\rho_w}{g} \; \overline{\left(\beta_d \; dU_d\right)^5} \; . \tag{6.24}$$

The radar derived dissipation of roller energy follows from eq. 2.37 and reads

$$D_\tau = 2 \; B_r \; \rho_w \; \overline{\left(\beta_d \; dU_d\right)^3} \; \beta_s \; . \tag{6.25}$$

Parameter	Symbol	Default value	Expected range
Relative roller density	β_ρ	0.9	$[0.3, 0.9]$
Roller area scaling factor	κ	0.07	$[0.06, 0.07]$
Breaker parameter	γ	0.78	$[0.4, 0.88]$
Amplitude dispersion factor	α_{ad}	0.5	$[0.0, 0.5]$
Breaker slope parameter	β_s	0.1	$[0.05, 0.15]$
dU_d to c conversion factor	β_d	1	$[0.7, 1.3]$

Table 6.1: Calibration parameters for the scaling of the radar derived energy of the surface roller.

The radar provides the spatial variation of the roller energy and thus the spatial roller energy flux gradient which is needed in eq. 2.36 can be determined directly from the data. All calibration parameters that affect B_r are listed in tab. 6.1. The assumed default values and the expected minimum and maximum values are also listed for each parameter. The default value for the radar roller dissipation scaling factor is $B_r = 0.0177$. Given the expected ranges of each calibration factor (shown in tab. 6.1) that contributes to B_r, this factor is expected to range within 0.003 an 0.027.

6.2.2 Backward Difference of the Wave Energy Flux

The roller energy (eq. 6.23), the flux of roller energy (eq. 6.24) and the dissipation of roller energy (eq. 6.25) can be directly estimated from the spatial difference of the Doppler velocity measured by the radar. Therefore, all quantities to solve the coupled wave energy and roller energy balance equations (eq. 2.35 and 2.36) are known. At the dry beach, both wave and roller energy cannot exist and are therefore set to zero for any dry radar cells. With this boundary condition, the differential equations can be solved numerically by applying a simple first order backward finite difference scheme which is briefly outlined in the following. The source term for the roller energy, the dissipation of organized wave energy D_w, is given at the previous radar cell at the range cell number r_{i+1} as

$$D_{w,r_{i+1}} = \frac{F_{r,r_i} - F_{r,r_{i+1}}}{\Delta r} + D_{\tau,r_i} \; . \tag{6.26}$$

The flux of organized wave energy (eq. 2.9) was derived using the representative group velocity that was computed from linear wave theory (eq. 2.8) considering the local water depth and the peak wave number measured by the wave rider buoy (converted from the peak frequency using eq. 2.5). The wave energy flux at r_{i+1} was

computed as

$$F_{w,r_{i+1}} = F_{w,r_i} + D_{w,r_i}\,\Delta r\ . \tag{6.27}$$

The wave energy and root-mean-square wave height along the full radar transect are

$$E_{rms,r_i} = \frac{F_{w,r_i}}{c_{g,r_i}} \tag{6.28}$$

and

$$H_{rms,r_i} = \sqrt{\frac{8\,E_{w,r_i}}{\rho_w\,g}}\ , \tag{6.29}$$

respectively.

Any measurement and therefore also the radar estimates along the cross-shore transect are affected by noise. To avoid unrealistic estimations of the gradients needed to compute the transformation of wave energy, the roller energy (eq. 6.23), the flux of roller energy (eq. 6.24) and the dissipation of roller energy (eq. 6.25) were smoothed with a 5 point moving average filter. This suppresses extremely fast changes, which are not expected for the given beach profile. However, this could be problematic in different environments where quick depth changes occur, e.g. reefs. Another option to address this problem would be the implementation of a higher order scheme for the computation of the gradients. This was, however, not investigated within the present work.

6.3 Results

The aim of the present section is to evaluate the performance of the three methods to infer the significant wave height from the radar, i.e. the linear wave theory (sec. 6.1.1), the empirical approach (sec. 6.1.2) and the roller concept (sec. 6.2), respectively. Therefore, the results are compared to the available in-situ observations during the storm event at the wave rider buoy (WR) as well as the two pressure gauges (PG1 and PG3) within the inner surf zone (see sec. 3.4). The cross-shore evolution of H_s derived from the three methods is only qualitatively analyzed because no other spatial observations are available for reference. Finally, the time-range evolution of the dissipation rate observed by the radar is studied. For both the linear wave theory and the empirical method, Doppler velocities affected by wave breaking were identified

using the detection method developed within chap. 5. Those Doppler velocities were omitted for the computation of the Doppler variance because they do not represent wave orbitals, but the wave phase speed. For the present study, the exponent β_{emp} within the empirical method has been set to zero which makes the method in deep water similar the formulation proposed by Carrasco et al. (2017b).

6.3.1 Significant Wave Height

Whitin this section, the performance of the three radar based methods, the linear wave theory (sec. 6.1.1), the empirical approach (sec. 6.1.2) and the roller concept (sec. 6.2) is analyzed in terms of the significant wave height H_s. Similarly, the study could also be undertaken in terms of wave energy, which is related to the wave height squared (see sec. 2.1.2). However, H_s is commonly used to asses the error of instrumentation for wave measurements and was therefore selected here.

Time Series

First, the time evolution of the results from the three proposed methods to infer the local significant wave height from the Doppler velocity are compared to the in-situ observations by the wave rider buoy and the bottom mounted pressure transducers that were placed inside the inner surf zone. The time series at the three stations are shown in figure 6.1. The statistical measures that correspond to the scatter plots are listed in table 6.2.

The top panel shows the time series and the corresponding scatter diagram at the wave rider buoy. The wave height estimated using linear wave theory (light blue) matches the observations well at the first half of the storm event. At the peak of the storm, when the measured wave heights reach 3 m and more, the linear wave theory estimate of H_s yields significantly larger values compared to the buoy observations. After the storm peak, when the wave heights were decreasing, the overestimation is not apparent anymore except for a few occasional peaks that are most likely caused by the influence of rain on the measurement. The resulting root-mean square error (rmse) is 0.64 m at this location with a bias of 0.19 m and a correlation coefficient R is 0.83. At the position of the pressure gauge PG1, which is located inside the inner breaker zone, the linear wave theory method permanently overestimates measured wave heights. The corresponding statistical measures are 0.89, 0.61 m and 0.61 m for correlation, bias and

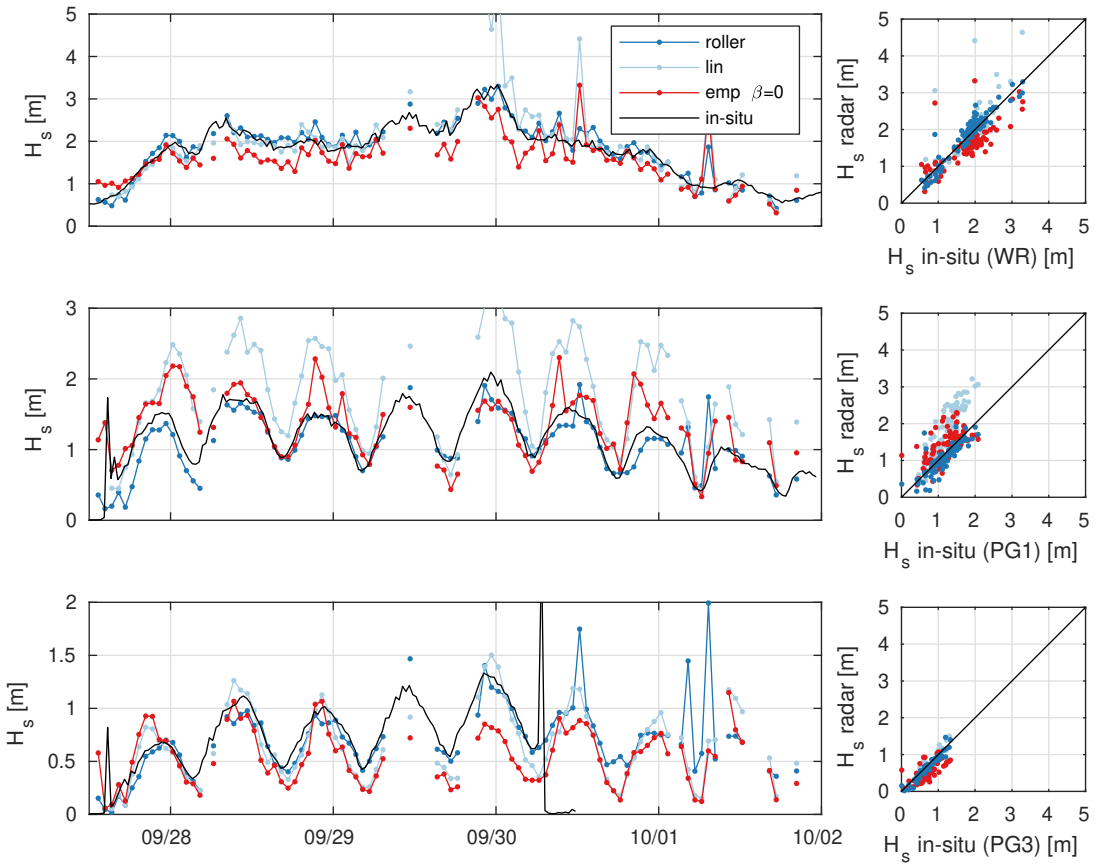

Figure 6.1: Time series and scatter diagrams of the significant wave height estimated from the radar using the linear wave theory (light blue), the empirical method (red) and the roller concept (blue). Black lines show the in-situ observations from the wave rider buoy (top panel), the pressure gauge PG1 within the inner breaker zone (middle panel) and PG3 at the trough of the inner bar (bottom panel).

rsme, respectively. However, the results at this location must be interpreted with care because most of the waves passing this location are breaking. This can influence both, the radar estimates but also the in-situ measurements. At the pressure gauge at trough of the inner bar (PG3) the linear method matches well with the observations for the entire period when in-situ data were available ($R = 0.92$, bias$= -0.08$ m, rmse$= 0.16$ m).

Next, the performance of the empirical method (red color) is investigated. A slight underestimation of H_s is apparent at the wave rider position which results in a negative bias of -0.20 m, a rmse of 0.43 m and correlation of 0.78. The buoy is located at $r = 1100$ m. Carrasco et al. (2017b) validated the empirical method on data from closer

			Linear theory	Empirical method	Roller concept
	R	-	0.92	0.69	0.96
PG3	bias	[m]	-0.08	-0.18	-0.06
	rmse	[m]	0.16	0.29	0.11
	R	-	0.89	0.67	0.85
PG1	bias	[m]	0.61	0.19	-0.08
	rmse	[m]	0.73	0.40	0.24
	R	-	0.83	0.78	0.95
WR	bias	[m]	0.19	-0.20	0.06
	rmse	[m]	0.64	0.43	0.21
	R	-	0.84	0.81	0.96
All	bias	[m]	0.28	-0.05	-0.02
	rmse	[m]	0.60	-0.39	0.20

Table 6.2: Error statistics of the significant wave height derived from the radar and the in-situ measurements at the pressure gauge PG3 at the inner bar trough, PG1 inside the inner breaker zone, the wave rider buoy (WR) and all three together. Statistics are shown in terms of the correlation coefficient (R), the bias and the root-mean-square-error (rmse).

distances while the antenna in their study was located at a even higher position (40 m instead of the 28 m antenna height of the present study). Therefore, the underestimation is possibly caused by the influence of shadowing, which results in less Doppler variation because the wave troughs are not entirely imaged anymore. On the contrary, H_s is overestimated by the empirical method at the position of pressure gauge PG1, which is indicated by a positive bias of 0.19 m. At the pressure gauge PG3, which is closest to the shore, the empirical method matches the observations well in the first half of the data set, but clearly underestimates H_s at the peak of the storm. The correlation, bias and rmse are 0.69, -0.18 m and 0.29 m, respectively. Hence the linear theory is performing better at this location.

The third of the proposed methods estimates the energy and dissipation of the surface roller. The wave height distribution is then estimated indirectly from the dissipation. This is a major difference to the two other methods because the wave height measurement at an individual location is not independent from the measurements before. For this method, only the change in wave height is known at every location along the transect. Thus, all errors along the cross-shore transect accumulate and affect every measurement location further offshore. However, the roller method matches the observed wave heights well at all three stations indicated by good correlation coefficients of 0.96, 0.85 and 0.96, small rmse values of 0.11 m, 0.24 m and 0.21 m, and small

bias values of -0.06 m, -0.08 m and 0.06 m, at the pressure gauge PG3, PG1 and the wave rider buoy, respectively.

Cross-shore transect

Figure 6.2 shows the result of the three methods along a cross-shore transect at the storm peak (September 29, 2016 22:20 UTC). Because in-situ observations are only available at three locations across the transect, the result from the phase-resolving model run NH2 (see sec. 3.6.1) is also shown as a reference. This model was found to fit best to all available in-situ observations (as shown in sec. 3.6.3) and is therefore considered here as the most suitable reference.

If the simulated cross-shore evolution of H_s is compared to the radar measurements it can be clearly seen that the linear theory method gives unrealistically high values for H_s on the outer bar crest. This increase of H_s can not be attributed to wave shoaling, which is well captured by the non-hydrostatic wave simulation (NH2). The result from the simulation would show a similar behavior if shoaling was the reason. This

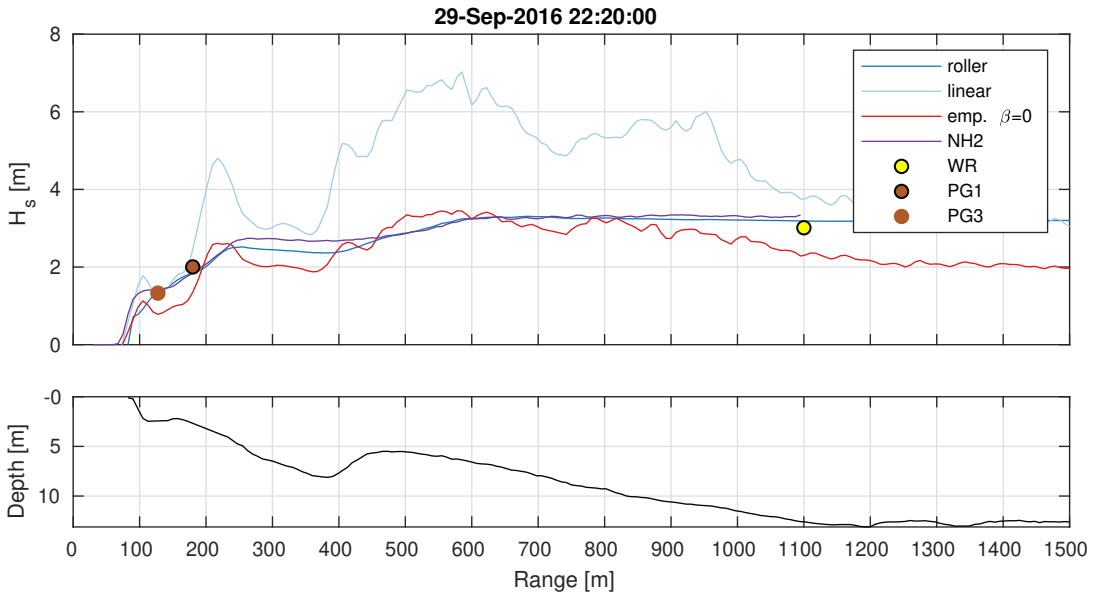

Figure 6.2: Cross-shore evolution of the significant wave height H_s at the peak of the storm (Sep. 29,2016 22:20 UTC) estimated from the radar using the linear wave theory (light blue), the empirical method (red) and the roller concept (blue). The result from the phase resolving wave simulation (NH2) is shown in purple. The in-situ observations from the wave rider buoy and the pressure gauge PG1 and PG3 are indicated by yellow and brown markers.

strong overestimation gets compensated if the empirical method is applied. However, in between the two breaker zones (250 m $< r <$ 350 m) the empirical method shows smaller wave heights compared to the NH2 model. A similar underestimation of H_s is observed at the location of the pressure gauges PG1 and PG3. Also noticeable are the considerable fluctuations that appear in range for the results of both the linear theory and the empirical method. The dissipation is related to the spatial change of the wave energy flux (see eq. 6.1), hence the gradient of the wave energy is needed. The fluctuations would cause erroneous estimates for the wave energy flux gradient (i.e. the dissipation).

On the contrary, the roller method matches both the NH2 simulation and the in-situ observations. A small discrepancy is apparent at the outer bar trough ($r = 350$ m). No in-situ observations are available at this location. It was therefore not possible to further investigate the performance of the results within this region. However, the small errors that were found from the comparisons of time series at the available in-situ sensors suggests that the roller method gives good results along the entire transect.

6.3.2 Time-Range Evolution of Wave Energy Dissipation

The goal of this section is to investigate the spatial distribution of wave energy dissipation due to depth induced breaking along a cross-shore transect of a double-barred beach. Within sec. 6.3.1, it was shown that the linear wave theory and the empirical method are not able to provide a consistent measurement of the significant wave height (or wave energy) along the cross-shore transect due to unrealistic results within the breaker zone and strong fluctuations in range. This inconsistency impedes a correct estimation of the wave energy flux gradient, which is needed to compute the dissipation rate (from eq. 6.1). By contrast, the roller concept (developed in sec. 6.2) estimates the dissipation from the roller energy inferred from the radar instead of the wave energy flux gradients. This is a more direct way to estimate the dissipation rate. Furthermore, the roller concept yielded the best results of all three methods compared to the available in-situ observations. Therefore it will be used in the following to analyze the cross-shore evolution of wave energy dissipation. Figure 6.3 shows the time-range evolution of the 10-min average of the dissipation rate estimates together with the mean water level from BSHcmod (including tide and surge) and offshore wave height measured at the wave rider buoy (see sec. 3.3).

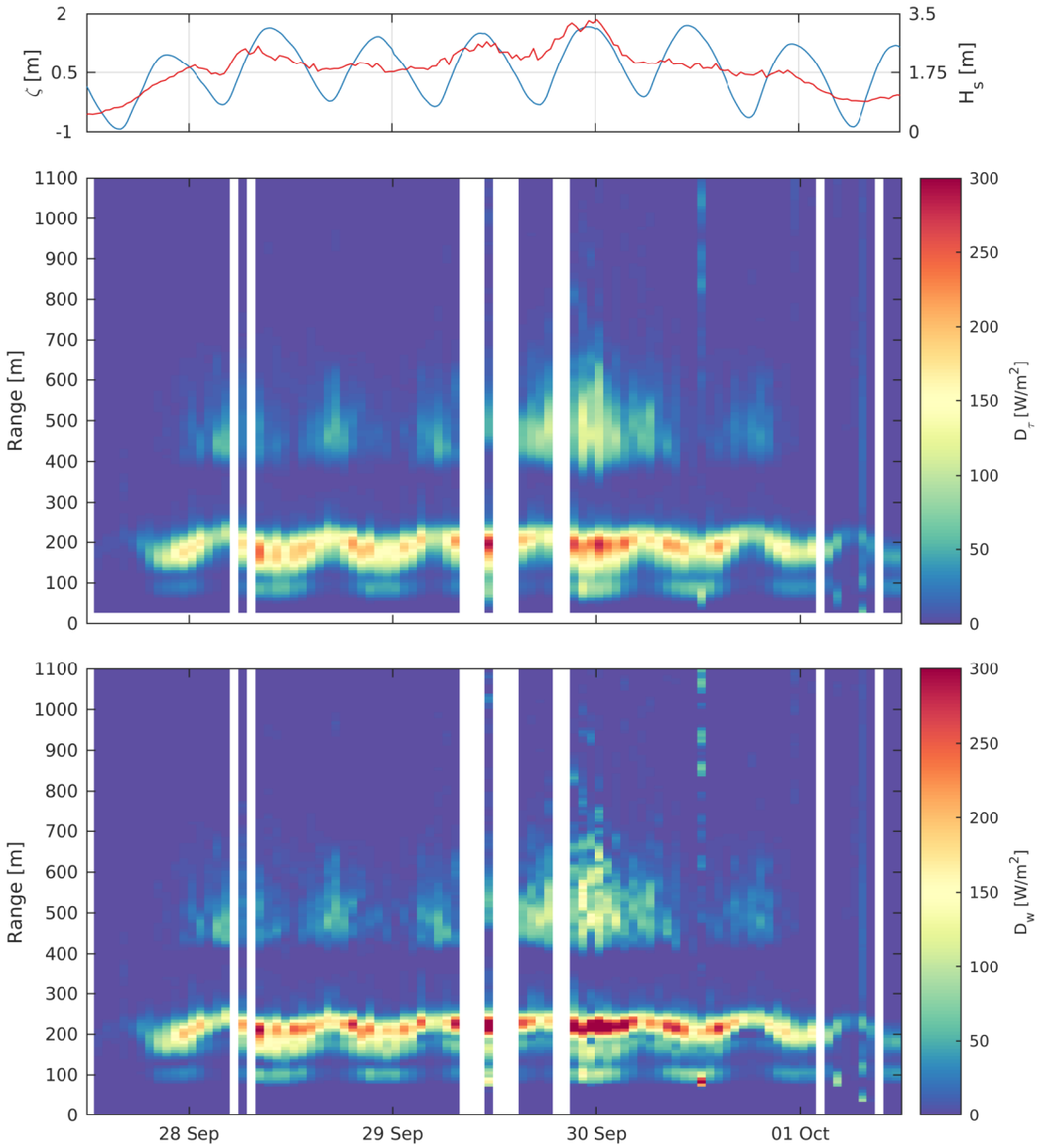

Figure 6.3: Time-range evolution of the radar derived dissipation of roller energy D_τ (eq. 6.25) and dissipation organized wave energy D_w (eq. 6.26) derived from the roller dissipation. The top panel shows the mean water level ζ (blue line) including tide and surge from BSHcmod and the offshore significant wave height H_s (red line) observed by the wave rider buoy at $r = 1100$ m.

The dissipation of roller energy D_τ (shown in the middle panel of figure 6.3) is investigated first. The results from section 5.2.2 already have shown that wave breaking only occurs at the outer bar during energetic wave conditions and that the fraction of breaking waves is strongly modulated by the tides. This circumstance is also visible within the observations of the dissipation rate. The highest roller dissipation rates are observed at the peak of the storm when values at the crest of the outer bar ($r = 500$ m) reach ≈ 120 W/m^2. At the inner breaker zone ($r \approx 200$ m, depending on the tide), the local roller dissipation rates are generally higher and reach values up to 300 W/m^2. It is interesting to note that the area were such a high dissipation rate occurs is relatively narrow (≈ 50 m), which is in the same range as the peak wave length at this location (which is 53 m). The location of the inner breaker zone is strongly modulated by the tide. A third region where roller energy is dissipated becomes apparent at high tide in the swash area right at the beach face (≈ 90 m). At high tide, the crest of the inter-tidal bar is submerged and thus some wave energy can pass it. This is not the case at low tide when the crest of the sandbar falls dry.

From the spatial gradients of the roller dissipation rate, the dissipation of organized wave energy can be dervived using eq. 6.26. The lower panel in figure 6.3 depicts the spatio-temporal evolution of the 10-min average dissipation of organized wave energy D_w inferred from the radar observations. Compared to the dissipation of roller energy D_τ, the pattern of the dissipation of organized wave energy D_w appears to be more noisy. This is expected because the gradient computation is sensitive to noise. As it was mentioned in section 6.2.2, the roller dissipation was therefore smoothed prior to the computation of the roller flux gradients that are needed to derive the dissipation of organized wave energy from the radar observations. The magnitude of dissipation of organized wave energy D_w is similar to dissipation of roller energy D_τ at the outer bar, but the dissipation of organized wave energy stops earlier as the roller dissipation (in the onshore direction). This is the expected effect of the storage of dissipated wave energy within the surface roller (Svendsen, 1984), which causes a delay in the production of wave induced currents (see sec. 2.4.2). The most obvious difference is the region of intense dissipation at the beginning of the inner breaker zone (between $r = 220$ m and $r = 180$ m) depending on the tide where the dissipation rate exceeds 300 W/m^2 . This particular effect will be discussed in more detail within sec. 7.1.

The backward difference scheme described in section 6.2.2 yields a measure of the wave energy flux at every radar range cell along the cross-shore transect. This is used

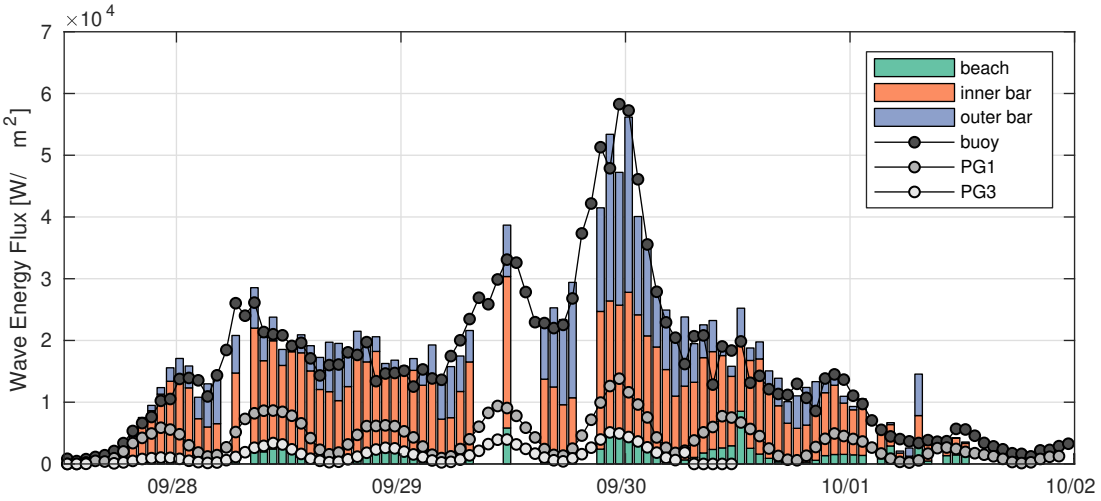

Figure 6.4: Flux of incoming wave energy measured at the wave rider buoy and the pressure gauges (PG1 and PG3) together with the radar derived wave energy flux represented by the bar plot. The color coding indicates the energy flux dissipated at the outer bar (between $r = 1100$ m and $r = 330$ m, purple), the inner bar (between $r = 330$ m and $r = 127.5$ m, orange) and the swash zone at the beach face (between $r = 127.5$ m and $r = 0$ m, green).

now to quantify and attribute the amount dissipated wave energy to the different morphological features, the outer (sub-tidal) bar, the inner (inter-tidal) bar and the swash zone at the beach. The incoming flux of wave energy drives the nearshore circulation, turbulence production, sediment mobilization and thus morphological changes of the beach profile. Figure 6.4 shows the in-situ measurements of the flux of incoming wave energy by the wave rider buoy and the two pressure gauges that were placed within the surf zone. The bar plot represents the radar derived flux of wave energy, which was split into the portion of energy dissipated at the outer bar, the inner bar, and the swash zone at the beach face. As already shown in figure 6.1, the offshore wave forcing derived from radar using the roller concept matches the observations at the buoy. The energy flux at the pressure gauge PG3, which is located at the trough of the inner bar ($r = 127.5$ m) is also well captured by the radar estimate. PG1 is located at $r = 180$ m, which is within the area were energy is dissipated by breaking waves at the inner bar. It can be seen, that more than 50% of the energy flux that passes the outer bar was already dissipated offshore of PG1 through the entire period. Whether the outer bar is active (dissipates energy) or not, depends on the tidal elevation as well as on the total incoming wave energy. The dissipated amount of wave energy at the outer bar is usually small compared to the total incoming energy flux. This is different at the

storm peak when H_s measured at the buoy exceeded 3 m. During such high energetic wave conditions, about 50% of the total wave energy flux that approaches the coast is already dissipated at the outer sandbar.

6.4 Discussion and Concluding Remarks

Different methods to estimate the significant wave height from the measured Doppler velocity were introduced within the sections 6.1 and 6.2. The first method directly relates the Doppler velocity time series to surface elevation applying linear wave theory, similar to the work of McGregor et al. (1998) who used S-band Doppler radar. This assumes that the Doppler velocity is (except for breaking Doppler ensembles which where identified using the detection algorithm developed in sec. 5.1) a measure of the horizontal orbital velocity at the surface. However, as mentioned in section 2.3.3 and further investigated within chapter 4, the contributions to the Doppler velocity are more complex. Therefore, a second method was introduced which is modified version of an existing empirical relationship for deep water applications (Carrasco et al., 2017b). The modified relationship additionally accounts for the deformation of the wave orbitals in shallower water. In addition to these methods, a novel method was developed within the present work. The new concept relates an instantaneous spatial increase of the Doppler velocity to the energy that is stored within the surface roller at the front face of a breaking wave. The dissipation of roller energy and the dissipation of organized wave energy is then deduced from those quantities which was used to compute the transformation of the significant wave height along a cross-shore transect of a double barred beach.

Linear theory and empirical approach

The results presented in section 6.3 showed that linear wave theory cannot be used to transform the Doppler velocity to heave for shoaling and breaking waves. Linear theory strongly overestimates the wave height in particular within the two breaking zones that were present at a sub-tidal and an inter-tidal sand bar. An over estimation of the wave height is typically attributed to the influence of breaking on the Doppler velocity (McGregor et al., 1998). However, even if wave breaking was detected and removed prior to the analysis using the detection algorithm developed in section 5.1 this

overestimation persists. This confirms that the Doppler velocity is not a direct measurement of the surface velocity and other effects must be considered when the signal is analyzed (cf. sec. 2.3). There are two different causes of non-linearities within the Doppler signal. The shape of water waves in shallow water exhibits both, horizontal and vertical asymmetries. The saw-tooth shape of waves in the inner surf zone is the most extreme example of a skewed and asymmetric wave. This leads to non-linearities inside the measured Doppler velocity which are a purely geophysical effect. Therefore, this might be addressed through the application of a non-linear wave theory, such as the cnoidal theory (Korteweg and de Vries, 1895). However, another source of non-linearity within low-grazing angle coherent marine radar backscatter is the effect of the shadowing and the sensor impulse response. Both effects were investigated within chapter 4 and both are included within the forward model proposed in section 4.2. In deep water, the non-linearities resulting from the radar imaging can be removed by filtering the radar signal using a dispersion relation based bandpass filter (Carrasco et al., 2017a). However, such a filter technique requires homogeneity within the analysis window, which needs to be relatively large if Fast-Fourier-transformation (FFT) is being used (≈ 64 radar cells $= 480$ m). This is not the case for the present study as the wave energy as well as the bathymetry varies on much smaller scales. Dispersion filtering is therefore not an option. The empirical methods by Hwang et al. (2010) and Carrasco et al. (2017b) attempt to address the issues that result from the complex imaging effects empirically without dispersion filtering. The approach of Carrasco et al. (2017b) was validated for deep water on an extensive data set. The present study was a first attempt to apply and validate the methods in shallow water. Unfortunately, in-situ observations of H_s are only available at three positions along the transect. This makes a comprehensive investigation of the perfomance of the methods in shallow water difficult. However, two findings were made which are independent from the availability of in-situ observations. High Doppler velocities induced by breaking must be identified and omitted from the computation of H_s. Even if the breaking detection was successful, this treatment removes the crests of the highest waves (which are the ones that are breaking). Therefore, the Doppler variation will be underestimated within the breaker zones if this effect is not empirically addressed. The second finding was that the estimate for H_s showed some fluctuations in range. Those are problematic when the spatial gradient of the wave energy flux is calculated from the measurements, which is needed to compute dissipation.

Roller concept

In order to overcome these restrictions, an alternative concept which is based on the concept of surface rollers was proposed in section 6.2. It was shown that the new method provides a much more realistic cross-shore profile of the significant wave height (shown in fig. 6.2). The roller concept estimates the energy of the surface roller, a quantity that is closely related to the actual dissipation of energy by the Reynolds stress acting at the water surface. For many research questions, the surface stress is the quantity of interest, because it is the physical cause for the generation of wave induced currents and the production of turbulence (e.g. Svendsen, 2006). The linear wave theory method and the empirical approach estimate the significant wave height from the Doppler shift induced by the orbital velocity of the waves. The orbital motion is directly related to the wave height. Instead, the roller concept estimates the significant wave height indirectly from the spatial gradient of the roller energy. The gradient is then used to determine the dissipation of organized wave energy which finally yields the change of the wave energy flux, hence the wave height. However, the comparisons to in-situ observations showed that the roller concept also outperformed the other methods in estimating the significant wave height.

A small disadvantage of the roller concept is that the wave height must be known at least at one location along the transect beforehand. This was not problematic for the present study site because the dry beach (where the wave height must be zero) is always covered. Furthermore, errors made at a specific position are not independent from the neighboring points. A systematic underestimation at either the swash zone or at one of the breaker bars are possibly canceled out by an overestimation at a different location, or vice versa.

Expected uncertainty and sensitivity

There are two general sources of uncertainty for the estimation of the roller energy. The first one results from the fact that the exact value of the physically motivated calibration parameter B_r is not known and very difficult to measure in the field. The second is due to the fact that the spatial increase of the Doppler velocity dU_d does not always exactly represent the wave phase speed c. Both sources of error and their consequences will be discussed here briefly. Some speculative dependencies will be mentioned without being investigated in detail. A profound analysis would require

additional in-situ measurements and is therefore beyond the scope of the present work.

The condensed calibration parameter B_r is composed of multiple components. Each calibration parameter within B_r has a specific physical meaning and its default value was selected preferably from well accepted approximations available from literature. However, most of parameters stem from empirical studies hence they need to be adjusted for every individual situation. Some parameters, e.g. the air fraction within the roller represented by the relative density β_ρ or the roller area scaling factor κ, are very difficult to determine in the field. The combined scaling factor B_r can therefore be interpreted as a general calibration factor for the roller concept that yields very good results for the environmental conditions of the present study. A very likely dependency is the breaker type. The assumptions made for the choice of the parameters within the roller concept are mostly based on reported studies of spilling breakers. This is also the most frequent breaker type for the present study study site, but could be different at other locations. As mentioned in section 6.2, the default value for the radar roller dissipation scaling factor is $B_r = 0.0177$ and the estimated lower and upper bounds of B_r are 0.003 and 0.027, respectively. However, these limits reflect the biggest deviations from the correct value of B_r, which is expected to be much closer to the default value in most circumstances. An in depth investigation of the variability of the radar energy dissipation calibration factor B_r will definitely be an interesting subject for future research.

To compensate the second source of error, i.e. a discrepancy between the measured spatial increase in Doppler velocity dU_d and wave phase speed c, the calibration factor β_d was introduced. Within the present work β_d was set to one, which means that the $dU_d = c$ was assumed. However, the correct choice of β_d may depend on environmental conditions such as the sea state or the wind but probably also on site specific quantities such as the radar installation height. At extremely grazing incidence, an additional Doppler frequency shift appears within coherent radar backscatter (Miret et al., 2014). This effect would reduce the observed Doppler velocity difference dU between the non-breaking and breaking water surface. As a consequence, lower roller energies would be observed, hence lower dissipation rates. Winds were blowing along with the waves in the onshore direction for the analyzed storm event. The wind also contributes to the Doppler velocity of the non-breaking surface (cf. sec. 2.3). Offshore winds can therefore influence dU_d and an adjustment of the values for β_d might be required for such situations. A systematic analysis of the dependency of β_d on those

external factors possibly brings a significant reduction of the uncertainty.

An empirical quantification of the measurement uncertainty is not possible with the data set at hand. However, a rough discussion of the implications of a theoretical uncertainty will be given here. If we assume that β_d ranges from 0.7 to 1.3 this would imply an error of ± 30 % within the main assumption (i.e. $c = dU_d \pm 0.3$). Because we consider the mean roller energy over one 10-min radar record, this error will be significantly reduced by the averaging. Assuming that the measurements of dU_d are independent from each other and there is no bias, the 30% error of the individual measurements would result in an approximate error for the mean roller energy ($\sim dU_d^4$) of

$$4 \cdot \frac{error}{\sqrt{N-1}} = 4 \cdot \frac{0.3}{\sqrt{1170}} = 3.5\% \ , \tag{6.30}$$

where $N = D_{rec}/dt$ are the number of Doppler ensembles within one radar record of the duration $D_{rec} = 10$ min and $dt = 0.512$ s is the ensemble duration. This also shows that a small error in the determination of the Doppler velocity itself has no conceivable influence on the radar derived roller energy.

Another requirement for the roller concept to apply is the fact that the jump from slow to fast Doppler ensembles at the toe of the breaker must be covered. If the peak wave length of the wave field is short, the complete wave through is possibly shadowed and it therefore it is not possible to estimate the Doppler velocity at the toe of the roller. In this case the fundamental assumption of the roller concept is violated and dU_d is not anymore related to the wave phase speed c, and the dissipation rate would be strongly underestimated. This kind of error can not anymore be compensated by adjusting β_d because the underestimation stems from missing information rather than from a systematic bias.

For all the above mentioned reasons, more in-situ observations are needed in order to analyze the roller model in more detail. However, the very good match of the radar observations using the roller concept to the available in-situ observations over an entire storm event is very promising.

Wave damping at the outer bar

Wave breaking at the outer bar dissipates a considerable amount of the wave energy during energetic wave conditions. It was shown in fig. 6.4, that the radar observations indicate a loss of 50% of the total incoming wave energy flux already at the outer bar.

The wave energy that approaches the beach, and thus the expected beach erosion, is therefore reduced.

Results from widely used phase-averaged parameterizations, which were analyzed in section 3.6.3, varied significantly in this region (see fig. 3.6). Phase-resolving simulations (NH2) provided a good match to the available observations, but figure 6.2 shows that the wave height estimated using the roller concept slightly deviates from the NH2 result, in particular at the outer bar trough. The linear wave theory method and the empirical method also indicate different wave heights at this location. The observed disrepancies between the models and the radar observations demonstrate nicely that the complex process of wave breaking over a submerged bar and the reformation of the wave field after breaking is still poorly understood. The model that is expected to capture this complex dynamics most properly is the NH2 model. However, from the dataset at hand it cannot be conclusively stated whether the radar or the NH2 simulations provides a better estimation of the amount of dissipated energy at the outer bar. Nevertheless, the new roller based observation technique is able to provide measurements of the dissipation with a high spatial resolution over large distances. The radar system is easy to deploy and maintain and can be run operationally over long periods. Long-term investigations and comparisons of the simulations and the radar observations can identify potential weaknesses of both the models and the radar methods. Additional in-situ measurements are therefore desired to further investigate both, the performance of the wave models and the remote sensing methods to quantify wave energy dissipation at the outer bar.

Chapter 6: Key findings

- An existting empirical method of Carrasco et al. (2017b) to estimate H_s in deep water was revised to be applicable in shallow water, but the method is not stable enough to compute reliable energy dissipation rates from the spatial variation of H_s.
- A new technique was developed to infer the energy and dissipation of the surface roller from the an instantaneous increase of the Doppler velocity.
- The new concept can be used to estimate the dissipation rate of the surface roller (hence the surface stress) and transformation of wave energy along the entire cross-shore transect (on a distance of more than one kilometer).
- The observations indicate that 50% of the incoming wave energy flux is dissipated at the outer bar during high energetic wave conditions.

Chapter 7

Discussion

Within the present chapter, the findings from the previous chapters are discussed regarding their implications for geophysical processes. In section 7.1, the effect of the energy storage within the surface roller the corresponding onshore shift of the location of the wave induced surface stress is discussed. After that, section 7.2 contains an investigation of the bulk dissipation of an individual wave along the cross-shore transect and the validity of the bore analogy is discussed. Section 7.3 discusses potential effects of the strong onshore winds on the breaking dynamics during the storm event that was studied in this work and gives a speculative assessment of the transferability of the findings to other locations and wind conditions. Finally, section 7.4 deals with possible consequences of the findings for the production of turbulence and sediment transport.

7.1 Effect of the Surface Roller

It was shown in sec. 6.3.2 (lower panel of fig. 6.3), that most of the organized wave energy at the inner bar is dissipated over a short distance right after the beginning of the breaker zone (seen from offshore). This effect is further analyzed here. Figure 7.1 shows the radar derived dissipation of roller energy and organized wave energy along the cross-shore transect at the peak of the storm (Sep. 29, 22:20 UTC). Also shown is the result from the phase-avaraged simulation with the breaker model of Janssen and Battjes (2007) (denoted as SW-JB07, see sec. 3.6.3). The radar derived dissipation of wave energy is largest at the beginning of the breaker zone at the inner bar (at $r \approx 220$

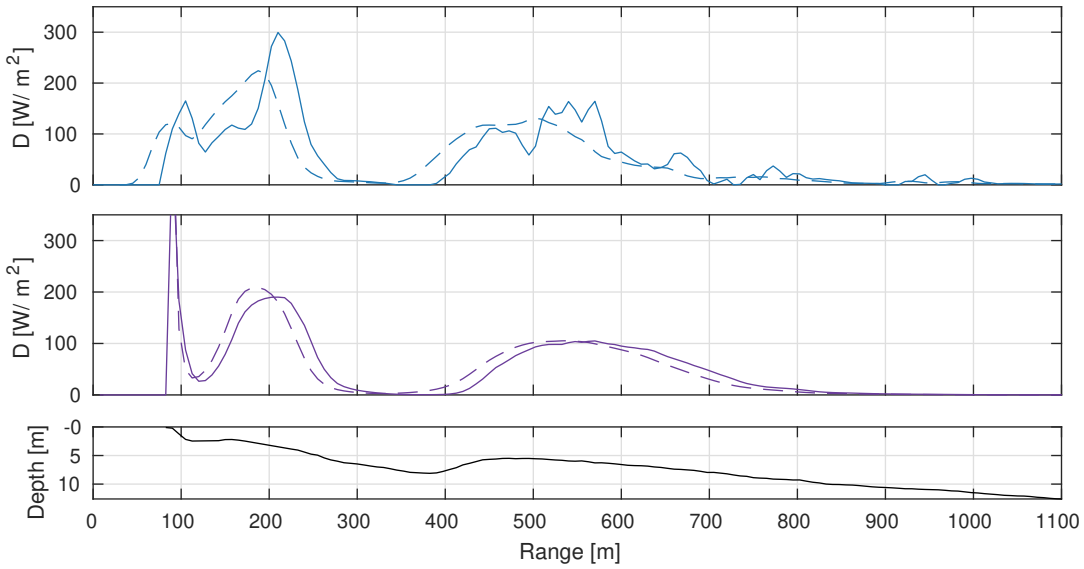

Figure 7.1: Cross-shore transect dissipation rate of roller energy D_τ (dashed lines) and dissipation rate of organized wave energy D_w (solid lines) observed by the radar (top panel) and simulated using the JB07 parameterization (middle panel). The bottom panel shows the depth profile.

m). Dissipation rates reach 300 W/m^2 at this point but drop rapidly to a level of $\approx$ 100 W/m^2 at $r = 180$ m. At the inner bar, the model predicts also highest dissipation rates at $r = 220$ m. However, the value of D_w predicted by the model is much lower (200 W/m^2). Surprisingly, the resulting roller dissipation rates show similar values for both the radar observation and the simulation result. Even if the dissipation of organized wave energy by wave breaking seems to take place over a very short distance of less than one wave length (< 50 m), the storage effect of the surface roller dampens these large dissipation rates. This results in a smooth distribution of the surface stress which finally dissipates the energy. This redistribution from wave energy to roller energy does not affect the overall energy flux budget (that includes wave energy flux and the roller energy flux), which remains similar.

At the outer bar, the radar measures a dissipation of roller energy between $r = 800$ m and $r = 350$ m. Seen from offshore, the dissipation rate gradually increases until it reaches values around 110 W/m^2 at the bar crest ($r \approx 500$ m). When water depths increase again the roller dissipation rate also decreases. The radar estimate of the dissipation of organized wave energy is a bit noisy in this area. It shows a similar trend except for the fact that the roller dissipation lags behind the dissipation of organized

wave energy. This is exactly the expected effect of the storage of energy within the surface roller (Deigaard and Fredsøe, 1989; Nairn et al., 1990; Dally and Brown, 1995) before it gets dissipated and the energy is transferred to turbulence and generated currents. The SW-JB07 simulation predicts a similar behavior at the outer bar with similar values for the maximum dissipation rate at the bar crest. The radar observations reveal that the end of the area where the roller energy is dissipated (at $r = 350$ m) is located about 50 m further onshore compared to the model prediction. A reason for this could be that the roller dissipation is weaker than assumed. The dissipation of roller energy depends on the slope of the breaking front. A constant slope parameter $\beta_s = 0.1$ was assumed for both the radar and the model to compute the roller dissipation from the roller energy. A lower value for β_s would yield a longer storage of roller energy hence a larger lag between D_τ and D_w. The beach slope at the outer bar is $\tan(\alpha_s) = 0.0125$, which gives a maximum Iribarren number (eq. 2.26) at the outer bar of $\xi_0 \approx 0.2$. Therefore, only spilling breakers are expected to occur at the outer bar. The selected value of $\beta_s = 0.1$ is possibly too high because the slope of the breaking front face for spilling breakers is expected to be small. However, this is different at the inner bar where the beach slope is 0.05. The reduced wave height due to breaking at the outer bar and thus the reduced wave steepness results in an approximate Iribarren number of 0.5 at the inner bar, which indicates plunging breakers. The different breaker types at the two sandbars might require a spatially varying breaker slope parameter to accurately model the roller dissipation. However, this not only holds for the radar observations but also for the simulations because the breaker slope parameter also needs to be specified within the wave model.

7.2 Bulk Breaking Probability and Energy Dissipation

The methodology developed within the preceding chapter 6 facilitates an investigation of the bulk amount of energy dissipated by breaking for waves that are approaching the shore. It was explained within section 2.4.3 that most parameterizations for dissipation by depth induced wave breaking estimate the total dissipation as a product of the breaking probability and the bulk amount of dissipation of an individual wave. The former is commonly estimated from empirically found probability distributions of breaking wave heights, and the latter by the bore analogy, which considers a spilling breaker in shallow water as similar to tidal bore (cf. sec 2.1.4). The dissipation rate per unit area

D_{hj} of such a bore-like wave can be computed using eq. 2.20 from the dissipation that takes place in an hydraulic jump of the same height as breaking wave. Calibration of the wave models is commonly realized by adjusting the breaking probability trough an adjustment of the breaker parameter γ (see sec. 2.4.3), even though most parameterizations also contain the free parameter B that accounts for the relative difference of the actual bulk dissipation rate to the hydraulic jump dissipation D_{hj}. However, calibration is generally also possible by an adjustment of B instead of γ. The parameterizations by Filipot and Ardhuin (2012) is the only example where B gets scaled and thus the bulk dissipation instead of the breaking probability. For all other parameterizations the calibration factor B is constant parameter and in the vast majority of studies it is assumed to equal unity.

The radar observations provide a measure for the bulk breaking probability in terms of the fraction of breaking waves Q_b (eq. 5.4) and a measure of the bulk energy that is dissipated by breaking D_w from the roller concept (eq. 6.26). With the assumption that the bulk dissipation rate can be expressed as

$$D_w = B\, D_{hj,rep}\, Q_b = B\, \frac{1}{4}\rho g f_{rep} \frac{H_{rms}^3}{d}\, Q_b\ , \tag{7.1}$$

where the factor B represents the relative difference of the actual bulk dissipation rate to the bulk dissipation rate $D_{hj,rep}$ of a hydraulic jump of height H_{rms}. Similar to the previous chapters, the representative frequency of the wave field f_{rep} was specified by the peak f_p measured by the wave rider buoy and d is the local water depth. Figure 7.2 shows the factor $B = D_w\, Q_b^{-1}\, D_{hj,rep}^{-1}$ determined from the radar observations.

At the outer bar, the blue colors indicate that the bulk dissipation rate is about 70% of the dissipation rate of a hydraulic jump of height H_{rms}. Similar values are observed inside the inner breaker zone (between $r = 200$ m and $r = 150$). There are a little more white parts apparent in this area compared to the outer bar. The bulk dissipation rates in the inner surf zone are slightly smaller, but close to the dissipation of a bore. This confirms the hydraulic jump analogy for waves in very shallow water as soon as the bore-like wave has formed. Dissipation rates at the beginning (offshore end) off the breaker zone at the inner bar are significantly larger ($B > 3$). Within the transition zone between the breaking onset and the point when the wave is propagating as a quasi-steady hydraulic jump the bore analogy does not apply (e.g. Svendsen, 1984). None of the breaking models that are based on the bore analogy account for this effect

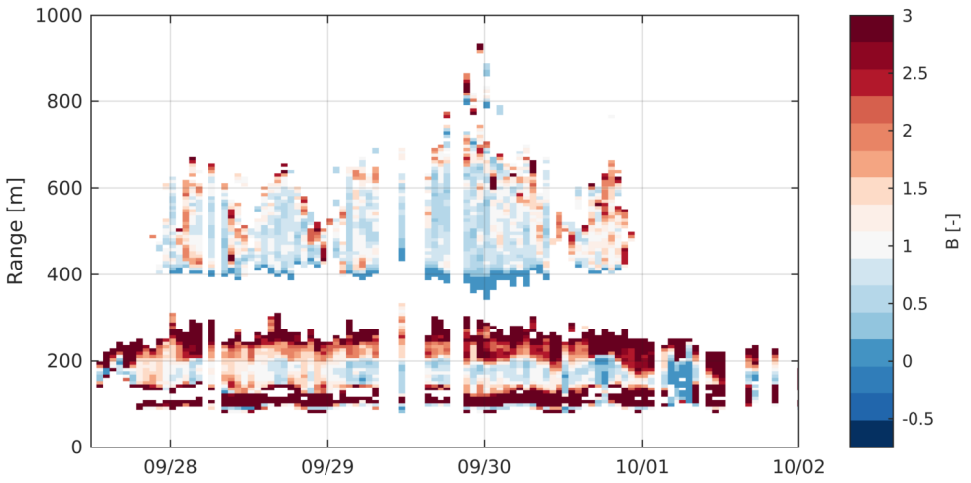

Figure 7.2: Time range evolution of the factor $B = D_w \, Q_b^{-1} \, D_{hj,rep}^{-1}$. The color scale indicates if the observed bulk dissipation rate is higher (warm colors) or lower (cold colors) compared to the dissipation rate $D_{hj,rep}$ of a hydraulic jump of height H_{rms}.

as the transition is considered to occur rapidly within a distance of less than one wave length. The transition zone is less pronounced at the outer bar. Red colors are also visible in this area, but the results for D_w in this area are also noisy. Therefore, no final assessment of the bulk dissipation was possible yet for this area. The values of B at the onshore edge of the outer bar even turn negative ($r = 400$ m). This happens because the water depth increases again in this area after the waves have passed the bar crest. The breaking waves that are detected in this region are not breaking anymore due to the shallow water depth, but because it takes some distance until the breaking process ceases. The bore analogy is thus not expected to be valid in this area which is confirmed by the observations.

7.3 Wind Effects

None of the available parameterizations for the depth induced breaking source term (listed in sec. 2.4.3) account for the effect of wind on the wave breaking characteristics. On the contrary, whitecapping is sometimes parameterized as a function of wind-speed only (e.g. Goddijn-Murphy et al., 2011). Onshore winds alter the shape of shoaling waves (Feddersen and Veron, 2005). Higher order quantities like wave skeweness and asymmetry increase. It is assumed that under onshore wind forcing, wave breaking

starts earlier (in deeper water) but might be more of a spilling type, i.e. wave breaking is less severe. Offshore winds favor plunging breakers because the wave can enter shallower water. For the present storm event, the wind was continuously blowing onshore with speeds between 10 and 15 m/s (see fig. 3.3). Therefore, the observed overestimation of the bulk dissipation by the bore model (indicated by $B < 1$) is most likely attributed to effect of the onshore directed wind. Offshore winds may have an opposite effect, but where not observed during the study period thus this cannot not be investigated with the present data set.

The probability of wave breaking is presumably increased for onshore wind situations and decreased for offshore winds. It was shown within sec. 5.2.2, that common breaking parameterizations (e.g. Battjes and Janssen, 1978; Baldock et al., 1998) strongly underestimate the breaking probability. The parameterization by Thornton and Guza (1983) yields good results for the breaking probability, but the model results shown in sec. 3.6.3 reveal that the model strongly overestimates the dissipation at the outer bar, at least if it is run with the default parameters. Therefore, some of the commonly used depth induced wave breaking parameterizations possibly compensate this wind induced increase of the breaking probability with contradicting erroneous computations of the dissipation rate. Or in other words: for onshore winds wave breaking is more frequent but less severe in reality. It is thus possible that the overall dissipation is still estimated correctly by the model, even if the physics are not correctly captured. Without wind influences the breaking probability and also the amount of dissipated energy would probably by closer to D_{hj}. This would explain the disagreement between the models and the observations in the present study and the fact that the wave models match the observations of Q_b in the laboratory (Baldock et al., 1998), where no wind was present.

7.4 Implications for Sediment Transport

Turbulence production

The production of turbulent kinetic energy in the nearshore is correlated to the spatial decrease of the wave energy flux, i.e. the wave energy dissipation (e.g. Feddersen, 2012a). However, as discussed in sec 7.1 the energy that is lost by breaking is first transferred to roller energy and is then dissipated by the Reynolds stress acting at the

interface between the roller and the underlying water mass. If the entire dissipated energy is only transferred to roller energy, the turbulence intensity at the surface is directly related to the roller dissipation rate. This is a reasonable assumption for spilling type breaking waves. As the source of turbulence, the roller dissipation (and hence the surface stress) observed by the radar is therefore exactly the quantity that is required, when the spatial distribution of turbulence across the surf zone is to be studied. There is no need to estimate the dissipation from a wave model, which always requires a knowledge of the actual bathymetry. The radar observations also allow a much better positioning of the location of increased turbulence generation, which lags behind the wave energy dissipation (Feddersen, 2012b).

Sediment suspension by wave stirring

For plunging breakers, the energy of a breaking wave is not completely transferred to roller energy. The plunging jet also generates coherent vortex motions which can affect the production of turbulence over the entire water column. These breaking wave induced motions are known to stir and suspend sediments in the surf zone (Voulgaris and Collins, 2000; Aagaard and Hughes, 2010; Aagaard and Jensen, 2013). The radar is not able to provide direct information about the turbulence in the surf zone, in particular not about its vertical distribution. However, the unique ability of the radar to observe the spatial distribution of the roller energy brings information about the roller energy creation which previously was not available. A sudden increase of roller energy over short distances indicates more intense breaking. This effect is clearly visible at the beginning of the inner breaker zone (in fig. 6.3, from Sep. 29, 22:00 UTC to Sep. 30, 02:00 UTC, between $r = 250$ m and $r = 190$ m). The total flux of energy always contains both the roller energy flux and the flux of organized wave energy. The radar derived wave energy flux is computed from the gradient of the roller energy and thus the two quantities are not independent from each other. However, if the wave energy is measured at two positions by an independent device, the radar derived roller energy and the independently computed flux of organized wave can be balanced. From this balance, the amount of energy that is directly transferred to turbulence can be determined. The radar observations can therefore also help to further investigate understand sediment suspension in the the surf zone.

Chapter 7: Key findings

- Radar observations indicate large (> 300 W/m^2) wave energy dissipation rates over a short (≈ 50 m) distance at the inner bar. This was not captured by the phase-averaged simulation using the breaking parameterization of Janssen and Battjes (2007).
- The temporary storage of wave energy within the surface roller compensates the rapid wave energy decay. Hence the magnitudes of the simulated and the observed roller dissipation rates are similar.
- At the outer bar, the bulk dissipation rate of an individual breaker is 30 % smaller compared to the dissipation rate of a bore of height H_{rms}. Within the inner surf zone values are closer (10 % smaller). The dissipation rate in the transition zone at the inner bar is more than 200 % larger.
- The observations indicate that strong onshore blowing winds cause an increase in the occurrence frequency of breaking, but individual breakers are less severe.

Chapter 8

Conclusion and Outlook

Wave breaking is a highly non-linear process that occurs rapidly, involves multiple scales and includes a certain amount of randomness. This makes it extremely difficult to investigate the phenomenon and thus wave breaking is one of the least understood processes related to ocean surface waves. However, wave breaking has a considerable influence on coastal and ocean dynamics. A good understanding of the process is therefore crucial for a reliable assessment of the impacts of climate change and human influences on the coastal system.

The present study focuses on wave breaking in the nearshore and addresses an open scientific question: How do the breaking dynamics vary in space and time for waves propagating over multiple breaker bars under certain environmental conditions? Within this chapter, the contents of the present work are conclusively summarized. Significant findings that result from the study are highlighted and recommendations for further research are given.

Summary and Conclusion

The theory, measurement and numerical modelling of surface waves in the nearshore (ch. 2) is outlined first. Numerical simulations that accurately model the hydrodynamics of breaking waves require extremely high computational resources. Therefore, wave breaking is parameterized and highly simplified within phase-averaged wave models, which are still essential for studies of coastal dynamics on large scales. The availability of field observations of breaking waves is crucial to improve the general understanding of the process and thus to improve wave breaking parameterizations.

Reliable wave measurements in the nearshore are nowadays possible from well developed in-situ instruments like pressure transducers, current meters or reverse echo sounders. However, one important feature of the nearshore wave field is its high variability in both space and time. Moreover, the wave dynamics at a given location are not independent from the history of the waves. Studies of nearshore breaking waves therefore require a good spatial coverage, which - using traditional measurement means - can only be achieved by the deployment of many sensors. This is extremely costly and difficult to carry out under breaking wave conditions. This limitation motivated scientists to develop and utilize shore-based remote sensing techniques such as visible light or infrared video, laser scanners or radar.

Marine radars do not require daylight conditions, they are easy to install and maintain and provide spatial and temporal data over a large distance. This offers unique abilities to investigate the dynamics of wave breaking in the nearshore. A shore-based coherent marine radar was therefore used during the WaveDiss2016 field experiment (ch. 3), which was designed and conducted as part of the present work. The study area is located on the island of Sylt in the German Bight at a sandy double-barred beach which is exposed to the North Sea. The recorded dataset covers a period of calm weather as well as a 4-day long storm event with significant wave heights above 3 m. The observations include the offshore wave forcing recorded by a wave rider buoy, nearshore wave heights from pressure transducers, the bathymetry recorded from a small vessel as well as continuous wind measurements from a land-based weather station. The study combines in-situ point measurements with (less accurate but spatial) radar observations and mathematically consistent numerical simulations. Thus, it provides a comprehensive view on the hydrodynamics of nearshore breaking waves.

The marine radar has a very good spatial and temporal coverage (the maximum range is 3.2 km with a ground resolution of $\approx$ 15 m). However, the complex radar backscatter must be carefully interpreted to infer wave parameters. Prior to the present work, marine radar based wave measurements were not possible in shallow water, where the wave field changes rapidly on short distances. With the goal to use the radar to estimate wave quantities, the observed coherent radar backscatter from shoaling and breaking waves (ch. 4) was intensively analyzed. The study shows that besides the influence of the local surface tilt and shadowing effects, also wave breaking and the sensor impulse response need to be considered to reproduce the observed backscatter. The investigation resulted in the development of a simplified forward model for the two

main quantities recorded by the radar, i.e. the backscatter intensity and the Doppler velocity. If the surface slopes and velocities are known, the forward model can be used to compute the backscatter. However, due to the radar imaging effects, a direct inversion of the signal to surface elevation profiles is not possible. To address this problem, two empirical methods (Hwang et al., 2010; Carrasco et al., 2017b) are available to estimate the significant wave height (H_s) in homogeneous deep water conditions. The present study was a first approach to revise and apply these methods in shallow water. However, even if the influence of the water depth on the wave orbital velocity is considered and high velocities that result from breaking are excluded from the analysis, the empirical method was not stable enough to measure the spatial transformation of H_s.

The aforementioned issues do not affect the investigation of breaking waves from the radar backscatter. Regarding wave breaking, two quantities are of scientific interest: The frequency of occurrence of individual breaking waves and the breaking strength, i.e. the amount of wave energy dissipated per breaking event. Both quantities are equally relevant for coastal dynamics because a small number of strong breakers can dissipate the same amount of energy as weaker breakers that are more frequent. Breaking waves induce strong signatures within coherent radar backscatter, which is well known (e.g. Jessup et al., 1991a; Hwang et al., 2008c; Farquharson et al., 2005; Keller et al., 1986). Within the present work the radar signatures of breaking waves were used to investigate the spatio-temporal evolution of the wave breaking probability (ch. 5) and the wave energy dissipation associated to breaking (ch. 6). For this purpose, a new classification algorithm was developed to identify dominant breaking waves, whitecaps and radar imaging artifacts within the radar backscatter. The algorithm is tailored for marine radar, where the sensor impulse response has a considerable influence on the backscatter due to the typical range smearing effect of pulsed marine radars. Another development is a new methodology to infer the energy stored in the surface roller at the front face of a breaking wave from an instantaneous spatial increase of the Doppler velocity. The roller energy is related to the dissipation of roller energy hence the stress acting at the undisturbed surface under a breaking wave. The dissipation of organized wave energy can be estimated from the spatial gradient of roller energy by solving the coupled wave and roller energy balance equations. Therefore, the new roller based concept yields the transformation of wave energy and along the entire cross-shore transect. As mentioned above, this was not possible before us-

ing traditional means of radar based wave height retrievals. Comparisons to in-situ observations of the significant wave height at two nearshore pressure gauges (located at a range of $r = 127.5$ m, $r = 180$ m) and a wave rider buoy ($r = 1100$ m) show a root-mean-square error of 0.11 m, 0.24 m and 0.20 m, which indicates a very good performance of the new method.

Using the developed methodologies, field observations of the spatio-temporal variation of the breaking probability and associated wave energy dissipation were achieved for the first time over a large distance of more than 1 km during high energetic storm conditions using coherent marine radar. This opens new avenues to study the dynamics of the observed waves as they propagate and break over a sub-tidal and an inter-tidal sandbar and eventually reach the shoreline. A rapid wave height decay was observed by the radar at the inner bar, which was not apparent within phase-averaged simulations using the breaking parameterization of Janssen and Battjes (2007). However, the temporary storage of the wave energy within the surface roller prevents the energy from being dissipated quickly. This has a delaying and smoothing effect on the resulting surface shear. As a result, the magnitudes of the observed and the simulated dissipation of roller energy were similar along the transect, even though the observed dissipation of wave energy happens on a much smaller distance. A comparison of the observations of the bulk breaking probability (represented by the fraction of breaking waves) to commonly used parameterizations for depth induced wave breaking reveals that only the parameterizations by Thornton and Guza (1983), Filipot and Ardhuin (2012) and Chawla and Kirby (2002) are able to reproduce the observed fraction of breaking waves. Other formulations by Battjes and Janssen (1978), Baldock et al. (1998) and Janssen and Battjes (2007) predict up to five times lower values compared to the radar measurements. The simultaneous measurement of the bulk dissipation and the fraction of breaking waves also facilitates an examination of the bore analogy, which is the basis of most parameterizations for depth induced wave breaking. The bulk dissipation rate of breaking waves at the outer bar was found to be 70% of the dissipation rate of a bore of same height as the root-mean-square wave height H_{rms}. The reduced dissipation must be considered within nearshore wave models if accurate predictions of the breaking probability are required. A possible explanation for the discrepancy between the modeled and the observed breaking probability is the influence of wind on the breaking dynamics, which is not considered within the breaking parameterizations. The strong on-shore blowing winds during the storm possibly make wave

breaking more frequent but less severe during the studied conditions. Even if the average dissipation is the same, a reduced dissipation rate per wave influences the vertical distribution of generated turbulence, which affects sediment suspension (Voulgaris and Collins, 2000; Aagaard and Jensen, 2013). The new radar observations are therefore also of high relevance for studies of the wave induced sediment transport across the surf zone.

Outlook

The methodologies developed within this work can be used to efficiently measure the spatio-temporal evolution of the nearshore wave field. The availability of spatial wave observations over large distances is an extremely valuable information and will therefore augment nearshore field experiments in future. The innovative methodology to remotely quantify wave and roller energy dissipation rates using HZG's Doppler marine radar has already sparked interest among the international nearshore community. A deployment of the radar is planned during DUNEX[1] at the Field Research Facility in Duck, North Carolina.

Until now, the presented methods were validated on a relatively small amount of in-situ data. However, different sea state conditions from young, wind forced waves over highly energetic storm waves to the decaying sea state when the storm has passed are already covered by the present dataset. The good performance during all phases of the studied storm gives reason to believe that the methodology will also work under different environmental conditions or at other sites, which may show different wave characteristics. Further field testing will verify this.

Within this work, promising first attempts to use the radar to deduce whitecap statistics were conducted. The radar based observations of Phillips' Λ-function were within the same order of magnitude as the results from the parameterizations by Melville and Matusov (2002) and Irisov and Plant (2016), whereas the latter was better suited to reproduce the shape and peak location of the observed Λ-distribution. This strongly indicates that the radar can also be used to study breaking dynamics in deep water. Comparisons to other means of wave breaking detection such as visible light or infrared video will further validate the radar based method in future.

[1] `https://uscoastalresearch.org/dunex`, accessed on January 13, 2020

So far, the study was carried out for radar data with a fixed antenna pointing offshore. This guaranteed enough radar pulses from the same direction to compute a stable estimate for the Doppler velocity from the Doppler spectrum. In general the algorithms can also be applied to radar data acquired with rotating antenna. A two-dimensional analysis of the radar images significantly increases the coverage. This will facilitate an investigation of alongshore variability of the breaking dynamics in addition to the cross-shore evolution that was studied in the present work. Furthermore, rotating-antenna data will provide insight on the propagation direction of the waves which is needed when the waves are not normally incident on the beach. Currently, HZG is developing a new radar with an adjustable antenna rotation speed. Slower rotation speeds will result in more radar pulses per degree in azimuth and therefore a more stable Doppler velocity.

A higher density of in-situ measurements together with a more stable Doppler velocity estimate for rotating-antenna radar data will facilitate further developments of the forward model to compute the radar backscatter. If the forward model can be validated on the scale of individual waves, it can be used in future to solve the inverse problem and infer the evolution of individual waves directly from the radar measurements. Combined with the radar based breaking detection method, this will bring new possibilities of studying the break point, the breaking distance and the amount of dissipated energy at different stages of the breaking process of individual waves in a random sea state. Such measurements will provide the observational data required for an improvement of the existing empirical breaking parameterizations but can also push forward attempts to develop analytical formulations for the dissipation of wave energy by breaking.

References

Aagaard, T., Hughes, M. G., 2010. Breaker turbulence and sediment suspension in the surf zone. Marine Geology 271 (3-4), 250–259.
URL http://dx.doi.org/10.1016/j.margeo.2010.02.019

Aagaard, T., Hughes, M. G., Ruessink, G., 2018. Field Observations of Turbulence, Sand Suspension, and Cross-Shore Transport Under Spilling and Plunging Breakers. Journal of Geophysical Research: Earth Surface 123 (11), 2844–2862.

Aagaard, T., Jensen, S. G., 2013. Sediment concentration and vertical mixing under breaking waves. Marine Geology 336, 146–159.
URL http://dx.doi.org/10.1016/j.margeo.2012.11.015

Airy, G. B., 1845. Tides and waves. Encyclopaedia Metropolitana, 241 – 396.

Alpers, W., Hasselmann, K., 1982. Spectral signal to clutter and thermal noise properties of ocean wave imaging synthetic aperture radars. International Journal of Remote Sensing 3 (4), 423–446.

Alpers, W., Ross, D. B., Rufenach, C. L., 1981. On the Detectability of Ocean Surface Waves by Real and Synthetic Aperture Radar. Journal of Geophysical Research 86 (1), 6481–6498.

Alsina, J. M., Baldock, T. E., 2007. Improved representation of breaking wave energy dissipation in parametric wave transformation models. Coastal Engineering 54 (10), 765–769.

Anarde, K., Figlus, J., 2017. Tilt current meters in the surf zone: benchmarking utility in high-frequency oscillatory flow. In: Coastal Dynamics. No. June.

Apotsos, A., Raubenheimer, B., Elgar, S., Guza, R. T., Smith, J. A., 2007. Effects of wave rollers and bottom stress on wave setup. Journal of Geophysical Research: Oceans 112 (2), 1–10.

Aubrey, D. G., Trowbridge, J. H., 1985. Kinematic and dynamic estimates from electromagnetic current meter data. Journal of Geophysical Research 90 (C5), 9137.

Babanin, A., 2011. Breaking and dissipation of Ocean surface waves.

Baldock, T., Holmes, P., Bunker, S., Van Weert, P., 1998. Cross-shore hydrodynamics within an unsaturated surf zone. Coastal Engineering 34, 173–196.

Banner, M., Gemmrich, J., Farmer, D., 2002. Multiscale Measurements of Ocean Wave Breaking Probability. Journal of Physical Oceanography 32 (12), 3364–3375.

Banner, M. L., Babanin, A. V., Young, I. R., dec 2000. Breaking Probability for Dominant Waves on the Sea Surface. Journal of Physical Oceanography 30 (12), 3145–3160.
URL https://doi.org/10.1175/1520-0485(2000)030{%}3C3145:BPFDWO{%}3E2.0.CO;2

Barthelemy, X., Banner, M. L., Peirson, W. L., Fedele, F., Allis, M., Dias, F., 2018. On a unified breaking onset threshold for gravity waves in deep and intermediate depth water. Journal of Fluid Mechanics 841, 463–488.

Baschek, B., Schroeder, F., Brix, H., Riethmüller, R., Badewien, T. H., Breitbach, G., Brügge, B., Colijn, F., Doerffer, R., Eschenbach, C., Friedrich, J., Fischer, P., Garthe, S., Horstmann, J., Krasemann, H., Metfies, K., Merckelbach, L., Ohle, N., Petersen, W., Pröfrock, D., Röttgers, R., Schlüter, M., Schulz, J., Schulz-Stellenfleth, J., Stanev, E., Staneva, J., Winter, C., Wirtz, K., Wollschläger, J., Zielinski, O., Ziemer, F., 2017. The Coastal Observing System for Northern and Arctic Seas (COSYNA). Ocean Science 13 (3), 379–410.

Bass, F. G., Fuks, I. M., Kalmykov, A. I., Ostrovsky, I. E., Rosenberg, A. D., 1968. Very High Frequency Radiowave Scattering by a Disturbed Sea Surface Part II: Scattering from an actual sea surface. IEEE Transactions on Antennas and Propagation AP-16 (5), 560–568.

Battjes, J., 1972. Set-Up Due To Irregular Waves. Coastal Engineering Proceedings 1 (13), 109.

Battjes, J., 1974. Surf similarity. In: Proceedings 14th International Conference on Coastal Engineering. pp. 466–480.

Battjes, J., Stive, M., 1985. Calibration and verification of a dissipation model for random breaking waves. Journal of Geophysical Research 90 (C5), 9159–9167.

Battjes, J. A., Janssen, J. P. F. M., 1978. Energy loss and set-up due to breaking of random waves. Proceedings of 16th International Conference on Coastal Engineering, Am. Soc. of Civ. Eng., New York (1), 569–587.

Bechle, A. J., Wu, C. H., 2011. Virtual wave gauges based upon stereo imaging for measuring surface wave characteristics. Coastal Engineering 58 (4), 305–316.
URL http://dx.doi.org/10.1016/j.coastaleng.2010.11.003

Bell, P. S., 1999. Shallow water bathymetry derived from an analysis of X-band marine radar images of waves. Coastal Engineering 37 (3-4), 513–527.

Bell, P. S., Osler, J. C., 2011. Mapping bathymetry using X-band marine radar data recorded from a moving vessel. Ocean Dynamics 61 (12), 2141–2156.

Bendix, A., Carstensen, S., Fritzbøger, D., Troels, A., 2017. Performance of a Tilt Current Meter in the Surf Zone. In: Proceedings of Coastal Dynamics 2017. pp. 944–954.

Benham, F. C., Groginsky, H. L., Soltes, A. S., Works, G., 1972. Pulse Pair Estimation of Doppler Spectrum Parameters. Tech. rep., Raytheon Company, Wayland.

Benjamin, T. B., Feir, J. E., 1967. The disintegration of wave trains on deep water Part 1. Theory. Journal of Fluid Mechanics 27 (3), 417–430.

Bergamasco, F., Torsello, A., Sclavo, M., Barbariol, F., Benetazzo, A., 2017. WASS: An open-source pipeline for 3D stereo reconstruction of ocean waves. Computers and Geosciences 107 (June), 28–36.
URL http://dx.doi.org/10.1016/j.cageo.2017.07.001

Birch, R., Fissel, D., Borg, K., Lee, V., English, D., 2004. The capabilities of Doppler current profilers for directional wave measurements in coastal and nearshore waters. In: Oceans '04 MTS/IEEE Techno-Ocean '04 (IEEE Cat. No.04CH37600). Vol. 3. IEEE, pp. 1418–1427.
URL http://ieeexplore.ieee.org/document/1406330/

Birkemeier, W. A., Baron, C. F., Leffler, M. W., Hathaway, K. K., Miller, H. C., Strider, J. B., 1989. Superduck Nearshore Processes Experiment Data Summary CERC Field Reserch Facility. Tech. rep., USACE.

Birkemeier, W. A., Long, C. E., Hathaway, K. K., 1996. DELILAH, DUCK94 & SandyDuck: Three Nearshore Field Experiments. Coastal Engineering, 4052–4065.

Bishop, C. T., Donelan, M. A., 1987. Measuring waves with pressure transducers. Coastal Engineering 11 (4), 309–328.

Blayo, E., Debreu, L., 2005. Revisiting open boundary conditions from the point of view of characteristic variables. Ocean Modelling 9 (3), 231–252.
URL http://www.sciencedirect.com/science/article/pii/S1463500304000447

Bole, A., Wall, A., Norris, A., 2014. The Radar System - Technical Principles. In: Radar and ARPA Manual. Elsevier, pp. 29–137.
URL https://linkinghub.elsevier.com/retrieve/pii/B9780080977522000027

Bonneton, P., Lannes, D., Martins, K., Michallet, H., 2018. A nonlinear weakly dispersive method for recovering the elevation of irrotational surface waves from pressure measurements. Coastal Engineering 138 (June 2017), 1–8.
URL https://doi.org/10.1016/j.coastaleng.2018.04.005

Booij, N., 1981. Gravity waves on water with non-uniform depth and current. Ph.D. thesis, TU Delft.

Booij, N., Holthuijsen, L., Ris, R., aug 1997. The "Swan" Wave Model for Shallow Water. American Society of Civil Engineers, New York, NY, pp. 668–676.
URL http://ascelibrary.org/doi/10.1061/9780784402429.053

Braun, N., Ziemer, F., Bezuglov, A., Cysewski, M., Schymura, G., 2008. Sea-surface current features observed by Doppler radar. IEEE Transactions on Geoscience and Remote Sensing 46 (4), 1125–1133.

Brocchini, M., 2013. A reasoned overview on Boussinesq-type models: the interplay between physics, mathematics and numerics. Proceedings of the Royal Society A: Mathematical, Physical and Engineering Sciences 469 (2160), 1–27.
URL http://rspa.royalsocietypublishing.org/cgi/doi/10.1098/rspa.2013.0496

Brodie, K. L., Raubenheimer, B., Elgar, S., Slocum, R. K., McNinch, J. E., 2015. Lidar and pressure measurements of inner-surfzone waves and setup. Journal of Atmospheric and Oceanic Technology 32 (10), 1945–1959.

Callaghan, A. H., White, M., 2009. Automated processing of sea surface images for the determination of whitecap coverage. Journal of Atmospheric and Oceanic Technology 26 (2), 383–394.

Carini, R. J., Chickadel, C. C., Jessup, A. T., Thompson, J., 2015. Estimating wave energy dissipation in the surf zone using thermal infrared imagery. Journal of Geophysical Research: Oceans 120 (6), 3937–3957.

Carrasco, R., Horstmann, J., Seemann, J., 2017a. Significant Wave Height Measured by Coherent X-Band Radar. IEEE Transactions on Geoscience and Remote Sensing 55 (9), 5355–5365.

Carrasco, R., Streßer, M., Horstmann, J., 2017b. A simple method for retrieving significant wave height from Dopplerized X-band radar. Ocean Science 13 (1), 95–103.

Catalán, P. A., 2008. Microwave scattering from Surf Zone Waves. Ph.D. thesis, Oregon State University.

Catalán, P. A., Haller, M. C., Holman, R. A., Plant, W. J., 2011. Optical and microwave detection of wave breaking in the surf zone. IEEE Transactions on Geoscience and Remote Sensing 49 (6 PART 1), 1879–1893.

Catalán, P. A., Haller, M. C., Plant, W. J., may 2014. Microwave backscattering from surf zone waves. Journal of Geophysical Research: Oceans 119 (5), 3098–3120.
URL http://doi.wiley.com/10.1002/2014JC009880

Cavaleri, L., Abdalla, S., Benetazzo, A., Bertotti, L., Bidlot, J.-R., Breivik, Ø., Carniel, S., Jensen, R., Portilla-Yandun, J., Rogers, W., Roland, A., Sanchez-Arcilla, A., Smith, J., Staneva, J., Toledo, Y., van Vledder, G., van der Westhuysen, A., oct 2018. Wave modelling in coastal and inner seas. Progress in Oceanography 167 (February), 164–233.
URL https://doi.org/10.1016/j.pocean.2018.03.010https://linkinghub.elsevier.com/retrieve/pii/S0079661117302975

Cavaleri, L., Alves, J. H., Ardhuin, F., Babanin, A., Banner, M., Belibassakis, K., Benoit, M., Donelan, M., Groeneweg, J., Herbers, T. H., Hwang, P., Janssen, P. A., Janssen, T., Lavrenov, I. V., Magne, R., Monbaliu, J., Onorato, M., Polnikov, V., Resio, D., Rogers, W. E., Sheremet, A., McKee Smith, J., Tolman, H. L., van Vledder, G., Wolf, J., Young, I., 2007. Wave modelling - The state of the art. Progress in Oceanography 75 (4), 603–674.

Chawla, A., Kirby, J. T., 2002. Monochromatic and random wave breaking at blocking points. Journal of Geophysical Research 107 (C7), 1–19.

Chen, G., Kharif, C., Zaleski, S., Li, J., jan 1999. Two-dimensional NavierâĂŞStokes simulation of breaking waves. Physics of Fluids 11 (1), 121–133.
URL http://aip.scitation.org/doi/10.1063/1.869907

Christensen, E. D., 2006. Large eddy simulation of spilling and plunging breakers. Coastal Engineering 53 (5), 463–485.
URL http://www.sciencedirect.com/science/article/pii/S0378383905001705

Christensen, E. D., Deigaard, R., 2001. Large eddy simulation of breaking waves. Coastal Engineering 42 (1), 53–86.

Crowson, R. A., Birkemeier, W. A., Klein, H. M., Miller, H. C., 1988. SUPERDUCK nearshore processes experiment: summary of studies, CERC field research facility. Tech. rep.

Cysewski, M., Seemann, J., Horstmann, J., 2018. Artifacts or nature? Data processing and interpretation of 3D current fields recorded with vessel mounted acoustic doppler current profiler in different regions and conditions. 2018 OCEANS - MTS/IEEE Kobe Techno-Oceans, OCEANS - Kobe 2018 (October).

Dally, W. R., 1992. Random breaking waves: Field verification of a wave-by-wave algorithm for engineering application. Coastal Engineering 16 (4), 369–397.

Dally, W. R., Brown, C. A., 1995. A modeling investigation of the breaking wave roller with application to cross-shore currents. Journal of Geophysical Research 100 (C12), 24873.
URL http://doi.wiley.com/10.1029/95JC02868

Dalrymple, R. A., Rogers, B. D., 2006. Numerical modeling of water waves with the SPH method. Coastal Engineering 53 (2), 141–147.
URL http://www.sciencedirect.com/science/article/pii/S0378383905001304

Dankert, H., Horstmann, J., sep 2007. A Marine Radar Wind Sensor. Journal of Atmospheric and Oceanic Technology 24 (9), 1629–1642.
URL http://journals.ametsoc.org/doi/abs/10.1175/JTECH2083.1

Davidson-Arnott, R., 2018. Beach and Nearshore Instrumentation BT - Encyclopedia of Coastal Science. Springer International Publishing, Cham, pp. 1–12.
URL https://doi.org/10.1007/978-3-319-48657-4{_}30-2

de Saint-Venant, A. J. C. B., 1871. Théorie du mouvement non permanent des eaux, avec application aux crues des rivières et à l'introduction des marées dans leurs lits. Comptes Rendus des séances de l'Académie des Sciences.

de Schipper, M. A., de Vries, S., Ruessink, G., de Zeeuw, R. C., Rutten, J., van Gelder-Maas, C., Stive, M. J., 2016. Initial spreading of a mega feeder nourishment: Observations of the Sand Engine pilot project. Coastal Engineering 111, 23–38. URL http://dx.doi.org/10.1016/j.coastaleng.2015.10.011

de Vries, S., Hill, D. F., de Schipper, M. A., Stive, M. J., 2011. Remote sensing of surf zone waves using stereo imaging. Coastal Engineering.

Dean, R., Dalrymple, R., 1991. Water wave mechanics for engineers and scientists.

Dean, R. G., 1965. Stream function representation of nonlinear ocean waves. Journal of Geophysical Research 70 (18), 4561–4572.

Deane, G. B., 2016. The Performance of High-Frequency Doppler Sonars in Actively Breaking Wave Crests. IEEE Journal of Oceanic Engineering 41 (4), 1028–1034.

Deigaard, R., Fredsøe, J., 1989. Shear stress distribution in dissipative water waves. Coastal Engineering 13 (4), 357–378.

Díaz Méndez, G. M., Haller, M. C., Raubenheimer, B., Elgar, S., Honegger, D. A., 2015. Radar remote sensing estimates of waves and wave forcing at a Tidal inlet. Journal of Atmospheric and Oceanic Technology 32 (4), 842–854.

Dick, S., 2001. The Operational Circulation Model of BSH(BSHcmod): Model Description and Validation.

Drazen, D. A., Melville, W. K., Lenain, L., 2008. Inertial scaling of dissipation in unsteady breaking waves. Journal of Fluid Mechanics 611, 307–332.

Duncan, J. H., 1981. An experimental investigation of breaking waves produced by a towed hydrofoil. Proc. R. Soc. Lon. A 377, 331–348.

Duncan, J. H., 1983. The breaking and non-breaking wave resistance of a two-dimensional hydrofoil. Journal of Fluid Mechanics 126, 507–520.

Ebersole, B. A., Hughes, S. A., 1987. DUCK85 Photopole Experiment. Tech. rep., Coastal Engineering Research Center.

Elgar, S., Raubenheimer, B., Guza, R. T., 2001. Current meter performance in the surf zone. Journal of Atmospheric and Oceanic Technology 18 (10), 1735–1746.

Elgar, S., Raubenheimer, B., Guza, R. T., 2005. Quality control of acoustic Doppler velocimeter datain the surfzone. Measurement Science and Technology 16, 1889–1893.

Fahrentholz, S. R., 1973. Wellen- und Wasserstandsmessungen in freier See mit Hilfe des akustischen Echolotverfahrens (in german). In: 2nd International Congress Interocean.

Farquharson, G., Frasier, S. J., Raubenheimer, B., Elgar, S., 2005. Microwave radar cross sections and Doppler velocities measured in the surf zone. Journal of Geophysical Research: Oceans 110 (12), 1–12.

Feddersen, F., 2012a. Observations of the Surf-Zone Turbulent Dissipation Rate. Journal of Physical Oceanography 42 (3), 386–399.
URL http://journals.ametsoc.org/doi/abs/10.1175/JPO-D-11-082.1

Feddersen, F., 2012b. Scaling surf zone turbulence. Geophysical Research Letters 39 (17), 1–5.

Feddersen, F., Veron, F., 2005. Wind effects on shoaling wave shape. Journal of Physical Oceanography 35, 1223–1228.

Feddersen, F., Williams, I. J., 2007. Direct estimation of the Reynolds stress vertical structure in the nearshore. Journal of Atmospheric and Oceanic Technology 24 (1), 102–116.

Fenton, J. D., 1990. Nonlinear Wave Theories. In: The Sea: Ocean Engineering Science. Vol. 9. pp. 3–20.

Figurski, J. D., Malone, D., Lacy, J. R., Denny, M., 2011. An inexpensive instrument for measuring wave exposure and water velocity. Limnology and Oceanography: Methods 9 (MAY), 204–214.

Filipot, J. F., Ardhuin, F., 2012. A unified spectral parameterization for wave breaking: From the deep ocean to the surf zone. Journal of Geophysical Research: Oceans 117 (4), 1–19.

Filipot, J. F., Ardhuin, F., Babanin, A. V., 2010a. A unified deep-to-shallow water wave-breaking probability parameterization. Journal of Geophysical Research: Oceans 115 (4), 1–15.

Filipot, J.-F., Ardhuin, F., Magne, R., 2010b. Validation d'un terme source de dissipation par déferlement applicable du large à la côte. XIèmes Journées Nationales Génie Civil - Génie CôtierJournées Nationales Génie Civil - Génie Côtier, 87–94.
URL http://www.paralia.fr/jngcgc/11{_}11{_}filipot.pdf

Flampouris, S., Seemann, J., Ziemer, F., 2009. Observing littoral waves by Doppler radar. In: International Geoscience and Remote Sensing Symposium (IGARSS). Vol. 3. IEEE, pp. III–757–III–760.

Frasier, S. J., Liu, Y., Mcintosh, R. E., 1998. Space-time properties of radar sea spikes and their relation to wind and wave conditions. Journal of Geophysical Research 103 (18), 745–757.

Fuster, D., Agbaglah, G., Josserand, C., Popinet, S., Zaleski, S., 2009. Numerical simulation of droplets, bubbles and waves: State of the art. Fluid Dynamics Research 41 (6).

Galvin, C. J., 1968. Breaker type classification on three laboratory beaches. Journal of Geophysical Research 73 (12), 3651–3659.

GE, 2019. LOG_aLevel LR - Ease of Water Level and Wave Measurement for Offshore Applications. General Acoustics - Application note. Downloaded on 12/20/2019.
URL https://www.generalacoustics.com/wp-content/uploads/2017/05/AN{_}offshore{_}Log{_}aLevel{_}LR{_}en.pdf

Gemmrich, J. R., Banner, M. L., Garrett, C., 2008. Spectrally Resolved Energy Dissipation Rate and Momentum Flux of Breaking Waves. Journal of Physical Oceanography 38 (6), 1296–1312.
URL http://journals.ametsoc.org/doi/abs/10.1175/2007JPO3762.1

George, R., Flick, R. E., Guza, R. T., 1994. Observations of turbulence in the surf zone. Journal of Geophysical Research 99 (C1), 801–810.

Gingold, R. A., Monaghan, J. J., 1977. Smoothed particle hydrodynamics - Theory and application to non-spherical stars. Monthly Notices of the Royal Astronomical Society 181, 375–389.
URL http://adsabs.harvard.edu/abs/1977MNRAS.181..375G

Goda, Y., 2010. Reanalysis of regular and random breaking wave statistics. Coastal Engineering Journal 52 (1), 71–106.

Goddijn-Murphy, L., Woolf, D. K., Callaghan, A. H., 2011. Parameterizations and Algorithms for Oceanic Whitecap Coverage. J. Physical Oceanogr. 41 (4), 742–756.

Goodman, J. W., nov 1976. Some fundamental properties of speckle. J. Opt. Soc. Am. 66 (11), 1145–1150.
URL http://www.osapublishing.org/abstract.cfm?URI=josa-66-11-1145

Guza, R. T., Clifton, M. C., Rezvani, F., 1988. Field intercomparisons of electromagnetic current meters. Journal of Geophysical Research 93 (C8), 9302–9314.

Guza, R. T., Thornton, E. B., 1980. Local and shoaled comparisons of sea surface elevations, pressures, and velocities. Journal of Geophysical Research 85 (C3), 1524–1530.

Haller, M. C., Lyzenga, D. R., 2003. Comparison of radar and video observations of shallow water breaking waves. Ieee Transactions on Geoscience and Remote Sensing 41 (4), 832–844.

Hamm, L., Madsen, P. A., Peregrine, D. H., 1993. Wave transformation in the nearshore zone: A review. Coastal Engineering 21 (1-3), 5–39.

Hasselmann, K., 1960. Grundgleichugen der Seegangsvorhersage. Schifftechnik 7, 191–195.

Hasselmann, K., apr 1962. On the non-linear energy transfer in a gravity-wave spectrum Part 1. General theory. Journal of Fluid Mechanics 12 (04), 481.
URL http://www.journals.cambridge.org/abstract{_}S0022112062000373

Hasselmann, K., Hasselmann, S., Bauer, E., Janssen, P. A., Komen, G. J., Bertotti, L., Lionello, P., Guillaume, A., Cardone, V. C., Greenwood, J. A., Reistad, M., Zambresky, L., Ewing, J. A., 1988. The WAM model - a third generation ocean wave prediction model.

Hennings, I., Herbers, D., 2006. Radar imaging mechanism of marine sand waves at very low grazing angle illumination caused by unique hydrodynamic interactions. Journal of Geophysical Research: Oceans 111 (10), 1–15.

Holman, R. A., Stanley, J., 2007. The history and technical capabilities of Argus. Coastal Engineering 54 (6), 477–491.
URL http://www.sciencedirect.com/science/article/pii/S037838390700018X

Holthuijsen, L. H., 2007. Waves in Oceanic and Coastal Waters. Cambridge University Press, Cambridge.
URL http://ebooks.cambridge.org/ref/id/CBO9780511618536

Holthuijsen, L. H., Herbers, T. H. C., feb 1986. Statistics of Breaking Waves Observed as Whitecaps in the Open Sea. Journal of Physical Oceanography 16 (2), 290–297.
URL https://doi.org/10.1175/1520-0485(1986)016{%}3C0290:SOBWOA{%}3E2.0.CO

Honegger, D. A., Haller, M. C., Holman, R. A., 2019. High-resolution bathymetry estimates via X-band marine radar : 1 . beaches High-resolution bathymetry estimates via X-band marine radar : 1 . beaches. Coastal Engineering 149 (April), 39–48.
URL https://doi.org/10.1016/j.coastaleng.2019.03.003

Horstmann, J., Borge, J. C. N., Seemann, J., Carrasco, R., Lund, B., 2015. Wind, Wave and Current retrieval utilizing X-Band Marine Radars in Coastal Ocean Observing Systems. Elsevier, Ch. 16, pp. 281–304.

Hotta, S., Mizuguchi, M., dec 1980. A Field Study of Waves in the Surf Zone. Coastal Engineering in Japan 23 (1), 59–79.
URL https://doi.org/10.1080/05785634.1980.11924299

Hotta, S., Mizuguchi, M., Isobe, M., 1982. Field Study of Waves in the Nearshore Zone. Proceedings of the Coastal Engineering Conference 1, 38–57.

Howell, G. L., 1992. A New Nearshore Directional Wave Gage. Coastal Engineering, 295–307.

Hwang, P. A., Sletten, M. A., Toporkov, J. V., 2008a. An Empirical Study of Breaking Wave Contribution To Radar Backscatter From the Ocean Surface at Low Grazing Angle. In: Igarss. pp. 113–116.

Hwang, P. A., Sletten, M. A., Toporkov, J. V., 2008b. Analysis of radar sea return for breaking wave investigation. Journal of Geophysical Research: Oceans.

Hwang, P. A., Sletten, M. A., Toporkov, J. V., 2008c. Breaking wave contribution to low grazing angle radar backscatter from the ocean surface. Journal of Geophysical Research: Oceans 113 (9), 1–12.

Hwang, P. A., Sletten, M. A., Toporkov, J. V., 2010. A note on Doppler processing of coherent radar backscatter from the water surface: With application to ocean surface wave measurements. Journal of Geophysical Research: Oceans 115 (3), 1–8.

Inch, K. W., 2014. Surf Zone Hydrodynamics: Measuring Waves and Currents. In: Cook, S., Clarke, L., Nield, J. (Eds.), Geomorphological Techniques, online edi Edition. Vol. 3. British Society for Geomorphology, London, Ch. Chap. 3, S, pp. 1–13.

Iribarren, C., Nogales, C., 1949. Protection des ports. In: Proceedings XVIIth International Navigation Congress, Section II, Comm. 4,. Lisbon, pp. 31–80.

Irish, J. L., Wozencraft, J. M., Cunningham, A. G., Giroud, C., 2006. Nonintrusive measurement of ocean waves: Lidar wave gauge. Journal of Atmospheric and Oceanic Technology 23 (11), 1559–1572.

Irisov, V., Plant, W., 2016. Phillips' Lambda function: Data summary and physical model. Geophysical Research Letters 43 (5), 2053–2058.

Jähne, B., 2004. Practical Handbook on Image Processing for Scientific and Technical Applications, 2nd Edition. CRC Press.

Janssen, T. T., Battjes, J. A., 2007. A note on wave energy dissipation over steep beaches. Coastal Engineering 54 (9), 711–716.

Jessup, A. T., 1990. Detection and Characterization of Deep Water Wave Breaking Using Moderate Incidence Angle Microwave Backscatter from the Sea Surface. Ph.D. thesis.

Jessup, A. T., Melville, W. K., Keller, W. C., 1991a. Breaking waves affecting microwave backscatter: 1. Detection and verification. Journal of Geophysical Research 96 (C11), 20547.
URL http://doi.wiley.com/10.1029/91JC01993

Jessup, A. T., Melville, W. K., Keller, W. C., 1991b. Breaking waves affecting microwave backscatter: 2. Detection and verification. Journal of Geophysical Research 96 (C11), 20,547–20,569.

Jessup, A. T., Zappa, C. J., Loewen, M. R., Hesany, V., 1997. Infrared remote sensing of breaking waves. Nature 385 (6611), 52–55.

Johnson, D., Pattiaratchi, C., apr 2006. Boussinesq modelling of transient rip currents. Coastal Engineering 53 (5-6), 419–439.
URL http://www.sciencedirect.com/science/article/pii/S0378383905001730

Kajishima, T., Taira, K., 2017. Reynolds-Averaged NavierâĂŞStokes Equations. In: Computational Fluid Dynamics. Springer International Publishing, Cham, pp. 237–268.
URL http://link.springer.com/10.1007/978-3-319-45304-0{_}7

Kalmykov, A. I., Pustovoytenko, V. V., 1976. On Polarization Features of Radio Sighals Scattered From the Sea Surface at Small Grazing Angle 81 (12), 1960–1964.

Keller, W. C., Plant, W. J., Valenzuela, G. R., 1986. Observation of Breaking Ocean Waves with Coherent Microwave Radar. In: Wave Dynamics and Radio Probing of the Ocean Surface. Springer US, Boston, MA, pp. 285–293.
URL http://link.springer.com/10.1007/978-1-4684-8980-4{_}20

Kennedy, A. B., Chen, Q., Kirby, J. T., Dalrymple, R. A., jan 2000. Boussinesq Modeling of Wave Transformation, Breaking, and Runup. I: 1D. Journal of Waterway, Port, Coastal, and Ocean Engineering 126 (1), 39–47.
URL http://ascelibrary.org/doi/10.1061/{%}28ASCE{%}290733-950X{%}282000{%}29126{%}3A1{%}2839{%}29

Kleiss, J. M., Melville, W. K., 2010. Observations of Wave Breaking Kinematics in Fetch-Limited Seas. Journal of Physical Oceanography 40 (12), 2575–2604.

Kleiss, J. M., Melville, W. K., 2011. The analysis of sea surface imagery for whitecap kinematics. Journal of Atmospheric and Oceanic Technology 28 (2), 219–243.

Kolmogorov, A. N., 1942. Equations of turbulent motion of an incompressible flow. Physics.

Komen, G. J., Cavaleri, L., Donelan, M., Hasselmann, K., Hasselmann, S., Janssen, P. A. E. M., 1994. Dynamics and Modelling of Ocean Waves.

Korteweg, D. J., de Vries, G., 1895. XLI. On the change of form of long waves advancing in a rectangular canal, and on a new type of long stationary waves . The London, Edinburgh, and Dublin Philosophical Magazine and Journal of Science 39 (240), 422–443.

Kuriyama, Y., Ozaki, Y., 1996. Wave Height and Fraction of Breaking Waves on a Bar-Trough Beach - Field Measurements and Modeling -. Tech. rep., Port and Harbour Research Institute.

Lamb, H., 1932. Hydrodynamics, 6th Edition. Cambridge Univ. Press, Cambridge.

Lange, L., 2019. Foreshore Morphodynamics from Shore-based Marine Radar. Msc. thesis, TU Delft (in collaboration with Helmholtz-Zentrum Geesthacht).

Launder, B. E., Spalding, D. B., 1974. The numerical computation of turbulent flows. Computer Methods in Applied Mechanics and Engineering 3 (2), 269–289.

Le Méhauté, B., 1962. On non-saturated breakers and the wave run-up. Proc. 8th Int. Conf. on Coastal Engineering (Figure 1), 77–92.

Lee, P. H., 1995. X band microwave backscattering from ocean waves. Journal of Geophysical Research 100 (C2), 2591–2611.

Liao, Q., Bootsma, H. A., Xiao, J., Klump, J. V., Hume, A., Long, M. H., Berg, P., 2009. Development of an in situ underwater particle image velocimetry (UWPIV) system. LIMNOLOGY and OCEANOGRAPHY: METHODS (7), 169–184.

Lin, Y. C., Chang, C. C., Lee, M. C., Chan, H. C., Leu, J. M., 2013. Detection of breaking waves using X-band pulse radar in the nearshore region. China Ocean Engineering 27 (4), 549–556.

Lippmann, T. C., Brookins, A. H., Thornton, E. B., 1996. Wave energy transformation on natural profiles. Coastal Engineering 27 (1-2), 1–20.

LKN.SH, 2015. Fachplan Küstenschutz Sylt Historisches zur Entwicklung der Insel Sylt (Einleitung).

LKN.SH, 2019. Entwicklung der Insel Sylt (Web page), accessed on 7-6-2019.
URL https://www.schleswig-holstein.de/DE/Fachinhalte/K/kuestenschutz{_}fachplaene/Sylt/1{_}2{_}einleitung{_}entwicklung.html

Long, C. E., 1996. Index and bulk parameters for frequency-direction spectra measured at CERC Field Research Facility, June 1994 to August 1995. Tech. rep.

Longuet-Higgins, M. S., 1963. The generation of capillary waves by steep gravity waves. Journal of Fluid Mechanics 16 (1), 138–159.

Longuet-Higgins, M. S., 1970. Longshore currents generated by obliquely incident sea waves: 1. Journal of Geophysical Research 75 (33), 6790–6801.
URL http://doi.wiley.com/10.1029/JC075i033p06790

Lubin, P., Vincent, S., Abadie, S., Caltagirone, J.-P., 2006. Three-dimensional Large Eddy Simulation of air entrainment under plunging breaking waves. Coastal Engineering 53 (8), 631–655.
URL http://www.sciencedirect.com/science/article/pii/S0378383906000330

Lucy, L. B., 1977. A numerical approach to the testing of the fission hypothesis. the Astronomical Journal 82.

Lynett, P. J., 2006. Boussinesq-Type Equations (October), 348–357.

Ma, G., Shi, F., Kirby, J. T., 2012. Shock-capturing non-hydrostatic model for fully dispersive surface wave processes. Ocean Modelling 43-44, 22–35.
URL http://dx.doi.org/10.1016/j.ocemod.2011.12.002

MacMahan, J. H., Thornton, E. B., Stanton, T. P., Reniers, A. J. H. M., 2005. RIPEX: Observations of a rip current system. Marine Geology 218 (1-4), 113–134.

Manasseh, R., Babanin, A. V., Forbes, C., Rickards, K., Bobevski, I., Ooi, A., 2006. Passive acoustic determination of wave-breaking events and their severity across the spectrum. Journal of Atmospheric and Oceanic Technology 23 (4), 599–618.

Martins, K., Blenkinsopp, C. E., Deigaard, R., Power, H. E., 2018. Energy Dissipation in the Inner Surf Zone: New Insights From LiDAR-Based Roller Geometry Measurements. Journal of Geophysical Research: Oceans, 3386–3407.

Martins, K., Blenkinsopp, C. E., Power, H. E., Bruder, B., Puleo, J. A., Bergsma, E. W., 2017. High-resolution monitoring of wave transformation in the surf zone using a LiDAR scanner array. Coastal Engineering 128 (July), 37–43.

McCowan, J., 1894. On the highest wave of permanent type. The London, Edinburgh, and Dublin Philosophical Magazine and Journal of Science 38 (233), 351–358.

McGregor, J. A., Poulter, E. M., Smith, M. J., 1998. S band Doppler radar measurements of bathymetry, wave energy fluxes, and dissipation across an offshore bar. Journal of Geophysical Research: Oceans 103 (C9), 779–789.

Meindl, A., 1996. Guide to moored buoys and other ocean data acquisition systems. Tech. rep.

Melville, W. K., 1994. Energy Dissipation by Breaking Waves.
URL http://journals.ametsoc.org/doi/abs/10.1175/1520-0485(1994)024{%}3C2041:EDBBW{%}3E2.0.CO;2

Melville, W. K., Matusov, P., 2002. Distribution of breaking waves at the ocean surface. Nature 417, 58–62.

Meneveau, C., Katz, J., 2000. Scale-Invariance and Turbulence Models for Large-Eddy Simulation. Annual Review of Fluid Mechanics 32 (1), 1–32.

Miche, R., 1944. Mouvements ondulatoires de la mer en profondeur croissante ou décroissante. Forme limite de la houle lors de son déferlement. Application aux digues maritimes. Annales des Ponts et Chaussées 114, 369–406.

Michell, J. H., 1893. XLIV. The highest waves in water . The London, Edinburgh, and Dublin Philosophical Magazine and Journal of Science 36 (222), 430–437.

Miller, K., Rochwarger, M., 1972. A covariance approach to spectral moment estimation. IEEE Transactions on Information Theory 18 (5), 588–596.
URL http://ieeexplore.ieee.org/document/1054886/

Miret, D., Soriano, G., Nouguier, F., Forget, P., Saillard, M., Guerin, C. A., 2014. Sea surface microwave scattering at extreme grazing angle: Numerical investigation of the doppler shift. IEEE Transactions on Geoscience and Remote Sensing 52 (11), 7120–7129.

Mironov, A. S., Yurovskaya, M. V., Dulov, V. A., Hauser, D., Guérin, C. A., 2012. Statistical characterization of short wind waves from stereo images of the sea surface. Journal of Geophysical Research: Oceans 117 (12).

Monaghan, J. J., Bicknell, P. J., Humble, R. J., 1994. Volcanoes, Tsunamis and the demise of the Minoans. Physica D: Nonlinear Phenomena 77 (1-3), 217–228.

Munk, W. H., 1950. Origin and Generation of Waves. Coastal Engineering Proceedings 1 (1), 1–4.

Nairn, R., Roelvink, J. A., Southgate, H., 1990. Transition zone width and implications for modeling surfzone hydrodynamics. Proceedings 22th International Conference on Coastal Engineering, 68–81.

Nicolae Lerma, A., Pedreros, R., Robinet, A., Sénéchal, N., 2017. Simulating wave setup and runup during storm conditions on a complex barred beach. Coastal Engineering 123 (January), 29–41.
URL http://dx.doi.org/10.1016/j.coastaleng.2017.01.011

Nielsen, P., 1989. Measuring waves with pressure transducers, by C.T. Bishop and M.A. Donelan. Coastal Engineering 12 (4), 381–384.

Nieto-Borge, J. C., Reichert, K., Dittmer, J., 1999. Use of marine radar as a wave monitoring instrument. Coastal Engineering 37, 331–342.

Nieto Borge, J. C., Rodríguez Rodríguez, G., Hessner, K., González Izquerdo, P., 2004. Inversion of marine radar images for surface wave analysis. Journal of Atmospheric and Oceanic Technology 21 (8), 1291–1300.

Nwogu, O. G., 1996. Numerical Prediction of Breaking Waves and Currents with a Boussinesq Model. Coastal Engineering (1978), 4807–4820.

Okayasu, A., Shibayama, T., Mimura, N., 1986. Velocity Field under Plunging Waves. Coastal Engineering 1986, 660–674.
URL http://ascelibrary.org/doi/10.1061/9780872626003.050

Park, H., Sim, J., Yoo, J., 2011. Breaking wave measurement using Terrestrial LIDAR: validation with field experiment on the Mallipo Beach. Journal of Coastal Research, ICS (64), 1718–1721.
URL http://www.ics2011.pl/artic/SP64{_}1718-1721{_}H.S.Park.pdf

Pedersen, T., Nylund, S., Dolle, A., 2002. Wave height measurements using acoustic surface tracking. In: Oceans '02 Mts/Ieee. Vol. 3. pp. 1234–1241.

Peregrine, D. H., 1967. Long waves on a beach. Journal of Fluid Mechanics.

Peregrine, D. H., 1983. Breaking waves on beaches. Annual review of fluid mechanics. Volume 15, 149–178.

Perlin, M., Choi, W., Tian, Z., 2013. Breaking Waves in Deep and Intermediate Waters. Annual Review of Fluid Mechanics 45 (1), 115–145.
URL http://www.annualreviews.org/doi/10.1146/annurev-fluid-011212-140721

Phillips, O. M., 1977. The Dynamics of the Upper Ocean, 2nd Edition. Cambridge University Press.

Phillips, O. M., 1985. Spectral and statistical properties of the equilbrium range in wind-generated gravity waves. J. Fluid Mech. 156, 505–531.

Phillips, O. M., 1988. Radar Returns from the Sea Surface - Bragg Scattering and Breaking Waves.
URL http://journals.ametsoc.org/doi/abs/10.1175/1520-0485(1988)018{%}3C1065:RRFTSS{%}3E2.0.CO;2

Phillips, O. M., Hasselmann, K., 1986. Wave Dynamics and Radio Probing of the Ocean Surface. Springer US, Boston, MA.
URL http://link.springer.com/10.1007/978-1-4684-8980-4

Phillips, O. M., Posner, F. L., Hansen, J. P., 2001. High Range Resolution Radar Measurements of the Speed Distribution of Breaking Events in Wind-Generated Ocean Waves: Surface Impulse and Wave Energy Dissipation Rates. Journal of Physical Oceanography 31 (2), 450–460.
URL http://journals.ametsoc.org/doi/abs/10.1175/1520-0485(2001)031{%}3C0450:HRRRMO{%}3E2.0.CO;2

Plant, W. J., 1997. A model for microwave Doppler sea return at high incidence angles: Bragg scattering from bound, Tilted waves. Journal of Geophysical Research: Oceans 102 (C9), 21131–21146.

Plant, W. J., Farquharson, G., 2012. Wave shadowing and modulation of microwave backscatter from the ocean. Journal of Geophysical Research: Oceans 117 (8), 1–14.

Plant, W. J., Keller, W. C., Cross, A., 1983. Parametric dependence of ocean wave-radar modulation transfer functions. Journal of Geophysical Research 88 (C14), 9747–9756.

Plant, W. J., Keller, W. C., Wright, J. W., 1978. Modulation of coherent microwave backscatter by shoaling waves. J. Geophys. Res. 83 (C3), 1347–1352.

Prandtl, L., 1925. 7. Bericht über Untersuchungen zur ausgebildeten Turbulenz. ZAMM - Journal of Applied Mathematics and Mechanics / Zeitschrift für Angewandte Mathematik und Mechanik.

Rattanapitikon, W., 2007. Calibration and modification of energy dissipation models for irregular wave breaking. Ocean Engineering 34 (11-12), 1592–1601.

Raubenheimer, B., Elgar, S., Guza, R. T., 1998. Estimating wave heights from pressure measured in sand bed. Journal of Waterway, Port, Coastal and Ocean Engineering 124 (3), 151–154.

Roeber, V., Cheung, K. F., Kobayashi, M. H., 2010. Shock-capturing Boussinesq-type model for nearshore wave processes. Coastal Engineering 57 (4), 407–423.
URL http://dx.doi.org/10.1016/j.coastaleng.2009.11.007

Roland, A., Zhang, Y. J., Wang, H. V., Meng, Y., Teng, Y. C., Maderich, V., Brovchenko, I., Dutour-Sikiric, M., Zanke, U., 2012. A fully coupled 3D wave-current interaction model on unstructured grids. Journal of Geophysical Research: Oceans 117 (9), 1–18.

Romeiser, R., Schmidt, A., Alpers, W., 1994. A three-scale composite surface model for the ocean wave-radar modulation transfer function. Journal of Geophysical Research 99 (C5), 9785–9801.

Ruessink, B. G., 2010. Observations of Turbulence within a Natural Surf Zone. Journal of Physical Oceanography 40 (12), 2696–2712.

Ruessink, B. G., Miles, J. R., Feddersen, F., Guza, R. T., Elgar, S., 2001. Modeling the alongshore current on barred beaches. Journal of Geophysical Research 106 (C10), 22451.

Ruessink, B. G., Walstra, D. J., Southgate, H. N., 2003. Calibration and verification of a parametric wave model on barred beaches. Coastal Engineering 48 (3), 139–149.

Saffman, P. G., jun 1970. A Model for Inhomogeneous Turbulent Flow. Proceedings of the Royal Society A: Mathematical, Physical and Engineering Sciences 317 (1530), 417–433.
URL http://rspa.royalsocietypublishing.org/cgi/doi/10.1098/rspa.1970.0125

Saket, A., Peirson, W. L., Banner, M. L., Allis, M. J., 2018. On the influence of wave breaking on the height limits of two-dimensional wave groups propagating in uniform intermediate depth water. Coastal Engineering 133, 159–165.
URL http://www.sciencedirect.com/science/article/pii/S0378383917305069

Sallenger, A. H., Howard, P. C., Fletcher, C. H., Howd, P. A., 1983. A system for measuring bottom profile, waves and currents in the high-energy nearshore environment. Marine Geology 51 (1-2), 63–76.

Salmon, J. E., Holthuijsen, L. H., 2015. Modeling depth-induced wave breaking over complex coastal bathymetries. Coastal Engineering 105, 21–35.
URL http://dx.doi.org/10.1016/j.coastaleng.2015.08.002

Salmon, J. E., Holthuijsen, L. H., Zijlema, M., van Vledder, G. P., Pietrzak, J. D., 2015. Scaling depth-induced wave-breaking in two-dimensional spectral wave models. Ocean Modelling 87, 30–47.
URL http://dx.doi.org/10.1016/j.ocemod.2014.12.011

Schäffer, H. A., Madsen, P. A., Deigaard, R., 1993. A Boussinesq model for waves breaking in shallow water. Coastal Engineering 20 (3-4), 185–202.

Schwendeman, M. S., Thomson, J., 2017. Sharp-Crested Breaking Surface Waves Observed from a Ship-Based Stereo Video System. Journal of Physical Oceanography 47 (4), 775–792.
URL http://journals.ametsoc.org/doi/10.1175/JPO-D-16-0187.1

Seemann, J., Carrasco, R., Stresser, M., Horstmann, J., Støle-Hentschel, S., Trulsen, K., Borge, J. C., 2017. An operational wave monitoring system based on a Dopplerized marine radar. OCEANS 2017 - Aberdeen 2017-Octob, 1–4.

Seemann, J., Stresser, M., Ziemer, F., Horstmann, J., Wu, L. C., 2014. Coherent microwave radar backscatter from shoaling and breaking sea surface waves. Oceans 2014 - Taipei.

Senechal, N., Abadie, S., Gallagher, E., MacMahan, J., Masselink, G., Michallet, H., Reniers, A., Ruessink, G., Russell, P., Sous, D., Turner, I., Ardhuin, F., Bonneton, P., Bujan, S., Capo, S., Certain, R., Pedreros, R., Garlan, T., 2011. The ECORS-Truc Vert'08 nearshore field experiment: Presentation of a three-dimensional morphologic system in a macro-tidal environment during consecutive extreme storm conditions. Ocean Dynamics 61 (12), 2073–2098.

Sénéchal, N., Dupuis, H., Bonneton, P., Howa, H., Pedreros, R., 2001. Observation of wave transformation in the surf zone over a gently sloping beach. Oceanologica Acta 24 (6), 545–546.

Senet, C. M., Seemann, J., Flampouris, S., Ziemer, F., aug 2008. Determination of bathymetric and current maps by the method DiSC based on the analysis of nautical X-band radar image sequences of the sea surface (November 2007). IEEE Transactions on Geoscience and Remote Sensing 46 (8), 2267–2279.

Senet, C. M., Seemann, J., Ziemer, F., 2001. The near-surface current velocity determined from image sequences of the sea surface. IEEE Transactions on Geoscience and Remote Sensing 39 (3), 492–505.

Shao, S., may 2006. Simulation of breaking wave by SPH method coupled with k -âĹŁ model. Journal of Hydraulic Research 44 (3), 338–349.
URL https://doi.org/10.1080/00221686.2006.9521686

Shao, S., Ji, C., 2006. SPH computation of plunging waves using a 2-D sub-particle scale (SPS) turbulence model. International Journal for Numerical Methods in Fluids 51 (8), 913–936.

Shemdin, O. O. H., 1972. Wind-Generated Current and Phase Speed of Wind Waves.
URL http://journals.ametsoc.org/doi/abs/10.1175/1520-0485{%}281972{%}29002{%}3C0411{%}3AWGCAPS{%}3E2.0.CO{%}3B2

Skolnik, M., 2008. Radar Handbook, 3rd Edition. McGraw-Hill.

Sletten, M. A., Wu, J., jan 1996. Ultrawideband, polarimetric radar studies of breaking waves at low grazing angles. Radio Science 31 (1), 181–192.
URL http://doi.wiley.com/10.1029/95RS01762

Smagorinski, J., mar 1963. GENERAL CIRCULATION EXPERIMENTS WITH THE PRIMITIVE EQUATIONS. Monthly Weather Review 91 (3), 99–164.
URL http://journals.ametsoc.org/doi/abs/10.1175/1520-0493{%}281963{%}29091{%}3C0099{%}3AGCEWTP{%}3E2.3.CO{%}3B2

Smit, P., Zijlema, M., Stelling, G., 2013. Depth-induced wave breaking in a non-hydrostatic, near-shore wave model. Coastal Engineering 76, 1–16.
URL http://dx.doi.org/10.1016/j.coastaleng.2013.01.008

Song, C., Sirviente, A. I., 2004. A numerical study of breaking waves. Physics of Fluids 16 (7), 2649–2667.

Soulsby, R. L., 1998. Coastal Sediment Transport: The COAST3D Project. pp. 2548–2558.
URL https://ascelibrary.org/doi/abs/10.1061/9780784404119.192

Stoker, J. J., 1948. The formation of breakers and bores the theory of nonlinear wave propagation in shallow water and open channels. Communications on Pure and Applied Mathematics 1 (1), 1–87.

Stokes, G., 1847. On the Theory of Oscillatory Waves. Transactions of the Cambridge Philosophical Society 8, 441 ff.

Stokes, G. G., 1880. Considerations relative to the greatest height of oscillatory irrotational waves which can be propagated without change of form., Appendix B to "On the Theory of Oscillatory Waves". In: Mathematical and Physical Papers, vol. 1 Edition. Cambridge University Press, pp. 225–229.

Stokes, M. D., Deane, G. B., Latz, M. I., Rohr, J., 2004. Bioluminescence imaging of wave-induced turbulence 109 (September 2003), 1–8.

Støle-Hentschel, S., Seemann, J., Borge, J. C. N., Trulsen, K., 2018. Consistency between sea surface reconstructions from nautical X-band radar Doppler and amplitude measurements. Journal of Atmospheric and Oceanic Technology 35 (6), 1201–1220.

Streßer, M., 2014. Erfassung der Dynamik des Wellenbrechens mit einem dopplerisierten Mikrowellenradar (Diploma Thesis in German), Leibniz Universität Hannover.

Suhayda, J. N., Pettigrew, N. R., 1977. Observations of wave height and wave celerity in the surf zone. Journal of Geophysical Research 82 (9), 1419–1424.

Sutherland, P., Melville, W. K., 2013. Field measurements and scaling of ocean surface wave-breaking statistics. Geophysical Research Letters.

Sutherland, P., Melville, W. K., apr 2015a. Field Measurements of Surface and Near-Surface Turbulence in the Presence of Breaking Waves. Journal of Physical Oceanography 45 (4), 943–965.
URL http://journals.ametsoc.org/doi/10.1175/JPO-D-14-0133.1

Sutherland, P., Melville, W. K., 2015b. Measuring turbulent kinetic energy dissipation at a Wavy sea surface. Journal of Atmospheric and Oceanic Technology 32 (8), 1498–1514.

Svendsen, I. A., 1984. Wave heights and set-up in a surf zone. Coastal Engineering 8, 303—-329.

Svendsen, I. A., 2006. Introduction to Nearshore Hydrodynamics.

Terray, E., Brumley, B., Strong, B., 2008. Measuring waves and currents with an upward-looking ADCP, 66–71.

Thomson, J., 2012. Wave breaking dissipation observed with "swift" drifters. Journal of Atmospheric and Oceanic Technology 29 (12), 1866–1882.

Thornton, E. B., Guza, R. T., 1983. Transformation of wave height distribution. Journal of Geophysical Research 88 (C10), 5925.
URL http://doi.wiley.com/10.1029/JC088iC10p05925

Thornton, E. B., Kraphol, R. F., 1974. Wave particle velocity measured under ocean waves. J. Geophys. Res. 79 (6), 847–852.

Tissier, M., Bonneton, P., Almar, R., Castelle, B., Bonneton, N., Nahon, A., 2011. Field measurements and non-linear prediction of wave celerity in the surf zone. European Journal of Mechanics, B/Fluids 30 (6), 635–641.
URL http://dx.doi.org/10.1016/j.euromechflu.2010.11.003

Torres-Freyermuth, A., Losada, I. J., Lara, J. L., 2007. Modeling of surf zone processes on a natural beach using Reynolds-Averaged Navier-Stokes equations. Journal of Geophysical Research: Oceans 112 (9), 1–20.

Trizna, D. B., Carlson, D. J., 1996. Studies of dual polarized low grazing angle radar sea scatter in nearshore regions. IEEE Transactions on Geoscience and Remote Sensing 34 (3), 747–757.

Tucker, M. J., 1991. Waves in ocean engineering. Ellis Horwood series in marine science. Ellis Horwood Limited.

Valenzuela, G. R., 1978. Theories for the interaction of electromagnetic and oceanic waves - A review. Boundary-Layer Meteorology 13 (1-4), 61–85.

Van Der Vlugt, T., Van Der Vlugt, R., 2014. Comparison of Directional WaveGuide Radar with Directional WaveRider Buoy. Tech. rep.
URL https://radac.nl/docs/Comparison{_}directionradar{_}buoy.pdf

Van Der Westhuysen, A. J., jan 2010. Modeling of depth-induced wave breaking under finite depth wave growth conditions. Journal of Geophysical Research: Oceans 115 (1), C01008.
URL http://doi.wiley.com/10.1029/2009JC005433

Voulgaris, G., Collins, M. B., 2000. Sediment resuspension on beaches: Response to breaking waves. Marine Geology 167 (1-2), 167–187.

Voulgaris, G., Trowbridge, J. H., 1998. Evaluation of the Acoustic Doppler Velocimeter (ADV) for Turbulence Measurements. Journal of Atmospheric and Oceanic Technology 15, 272–289.

Wetzel, L., 1986. On Microwave Scattering by Breaking Waves. In: Wave Dynamics and Radio Probing of the Ocean Surface.

Whitford, D. J., 1988. Wind Wave Forcing of Longshore Currents Across a Barred Beach. Ph.D. thesis, Naval Postgraduate School.

Wright, J. W., 1968. A New Model for Sea Clutter. IEEE Transactions on Antennas and Propagation AP-16 (2), 217–223.

Wright, J. W., Keller, W. C., 1971. Doppler spectra in microwave scattering from wind waves. Phys. Fl. 14 (3), 466.

Wright, L. D., Short, A. D., 1984. Morphodynamic variability of surf zones and beaches: A synthesis. Marine Geology 56 (1-4), 93–118.

Wu, C. H., Nepf, H. M., 2002. Breaking criteria and energy losses for three-dimensional wave breaking. Journal of Geophysical Research C: Oceans 107 (10), 41–1.

WW3DG, 2019. User Manual and System Documentation of WAVEWATCH III version 6.07, The WAVEWATCH III Development Group. Tech. Note 326 pp. + Appendices, NOAA/NWS/NCEP/MMAB.

Young, I. R., Rosenthal, W., Ziemer, F., 1985. A three-dimensional analysis of marine radar images for the determination of ocean wave directionality and surface currents. Journal of Geophysical Research: Oceans 90 (C1), 1049–1059.

Zijlema, M., Stelling, G., Smit, P., 2011. SWASH: an operational public domain code for simulating wave fields and rapidly varied flows in coastal waters. Coastal Engineering 58 (10), 992–1012.

Zijlema, M., Stelling, G. S., 2005. Further experiences with computing non-hydrostatic free-surface flows involving water waves. International Journal for Numerical Methods in Fluids 48 (2), 169–197.

Appendix A

Radar Pulse Shape

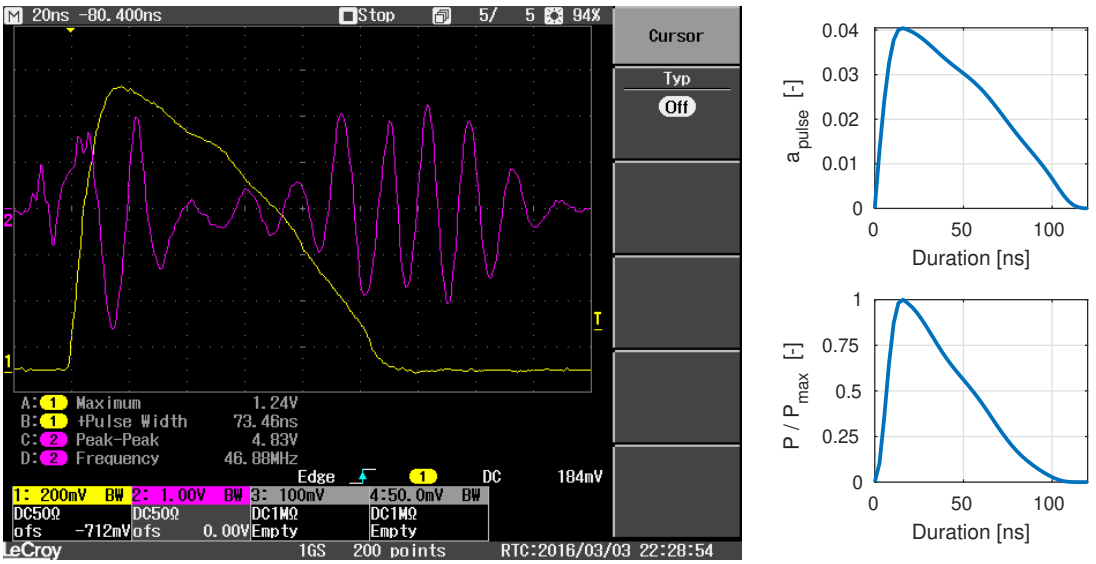

Figure A.1: Radar pulse measured in the laboratory on March 3, 2016 (left) and spline representation (right) of the measured pulse. The upper right panel shows the pulse amplitude a_{pulse} which is normalized such that $\int a_{pulse} = 1$. The lower right plot shows the power ($P = a_{pulse}^2$) normalized by its maximum value P_{max}.

Appendix B

Phase-Resolving Simulation

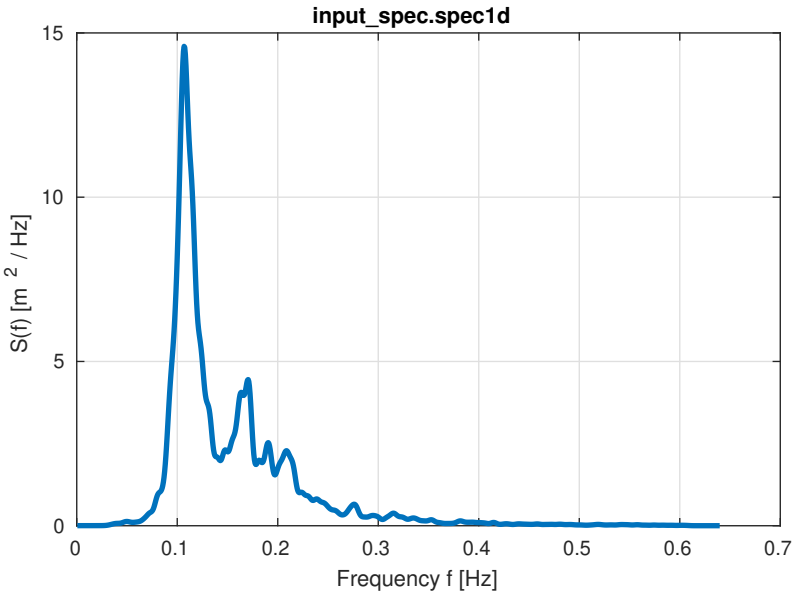

Figure B.1: One-dimensional wave spectrum imposed at the offshore boundary of the NH20 model run (computed from the buoy measured surface elevation time series at Sep 29, 2016 22:20 UTC).

Appendix C

Forward Model

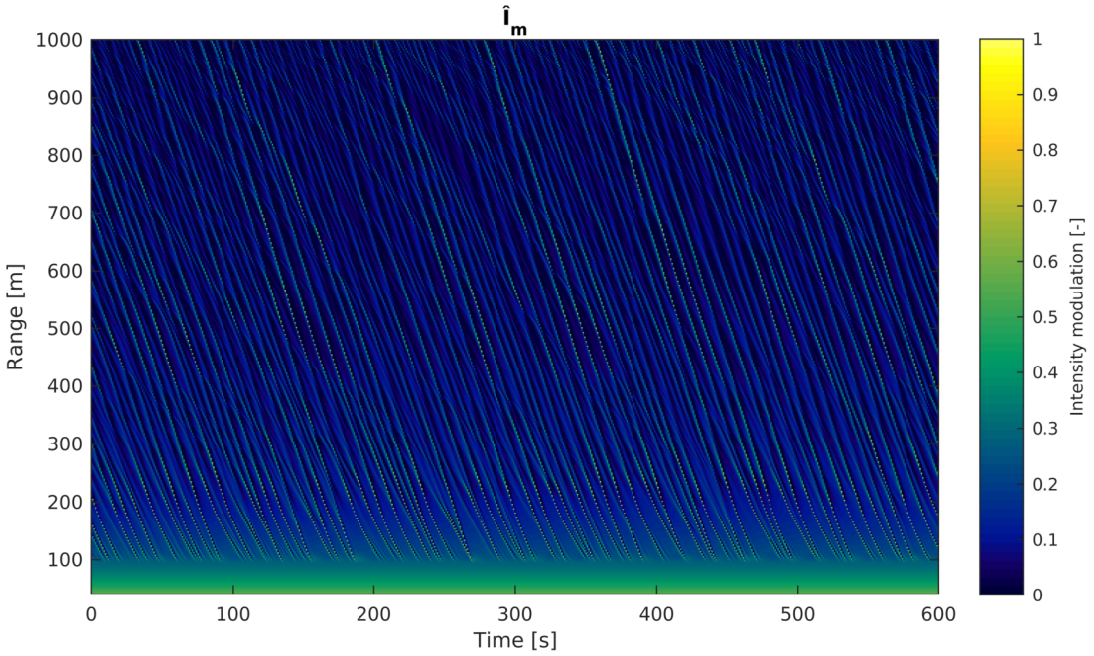

Figure C.1: Time-range diagram of the simulated intensity modulation resulting from surface tilt.

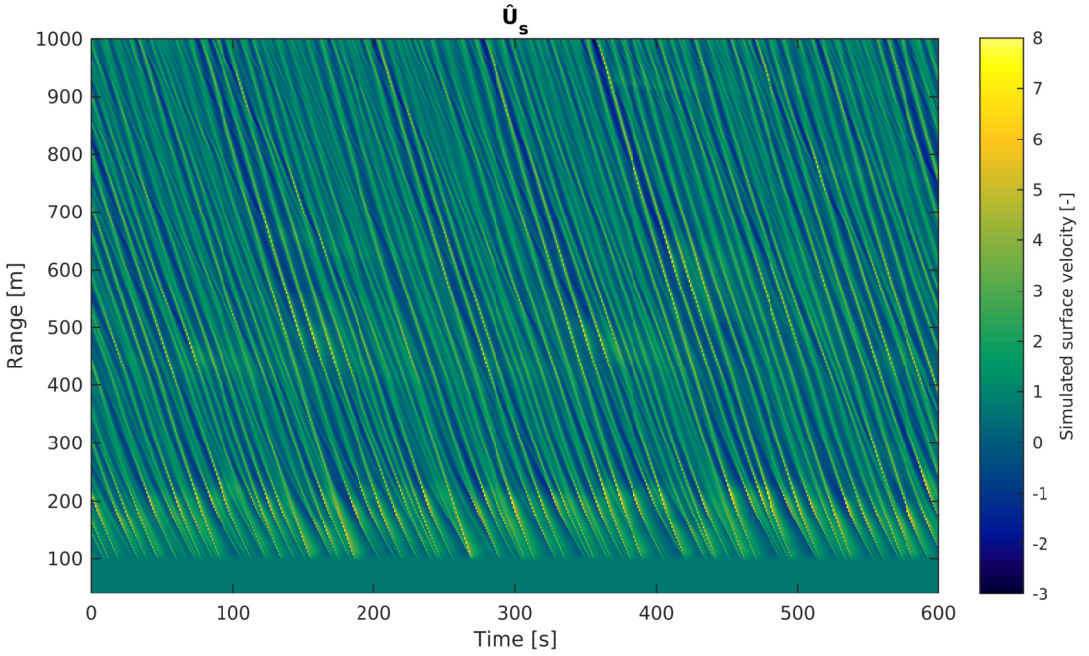

Figure C.2: Time-range diagram of the surface simulated velocity $\hat{U}_s$.

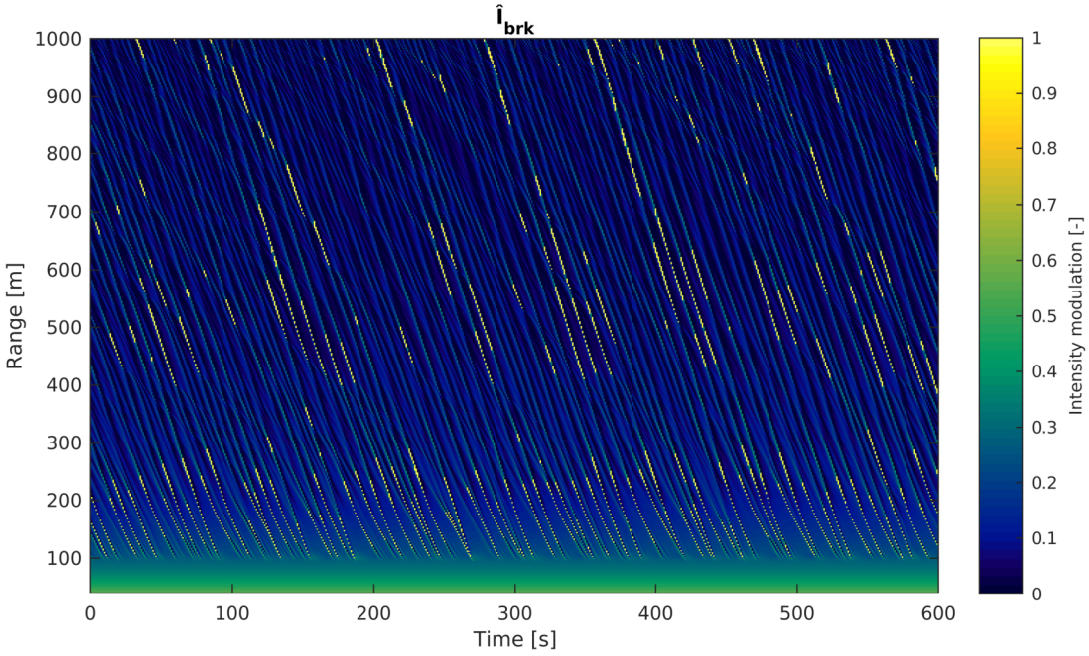

Figure C.3: Time-range diagram of the simulated intensity modulation resulting from surface tilt and wave breaking.

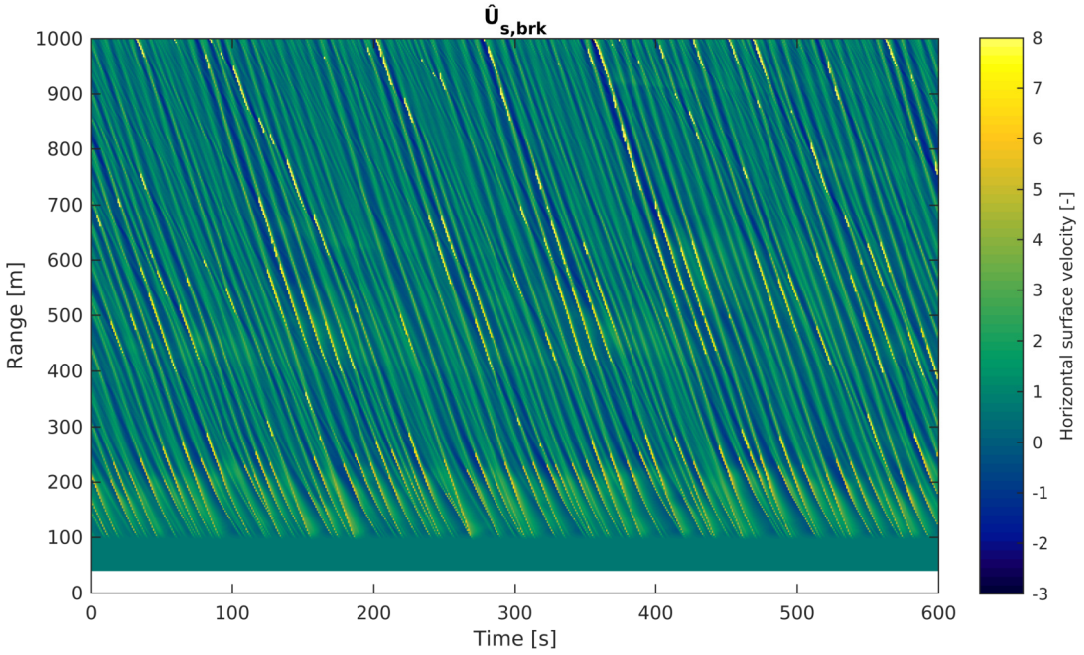

Figure C.4: Time-range diagram of the simulated surface velocity accounting for breaking $\hat{U}_{s,brk}$.

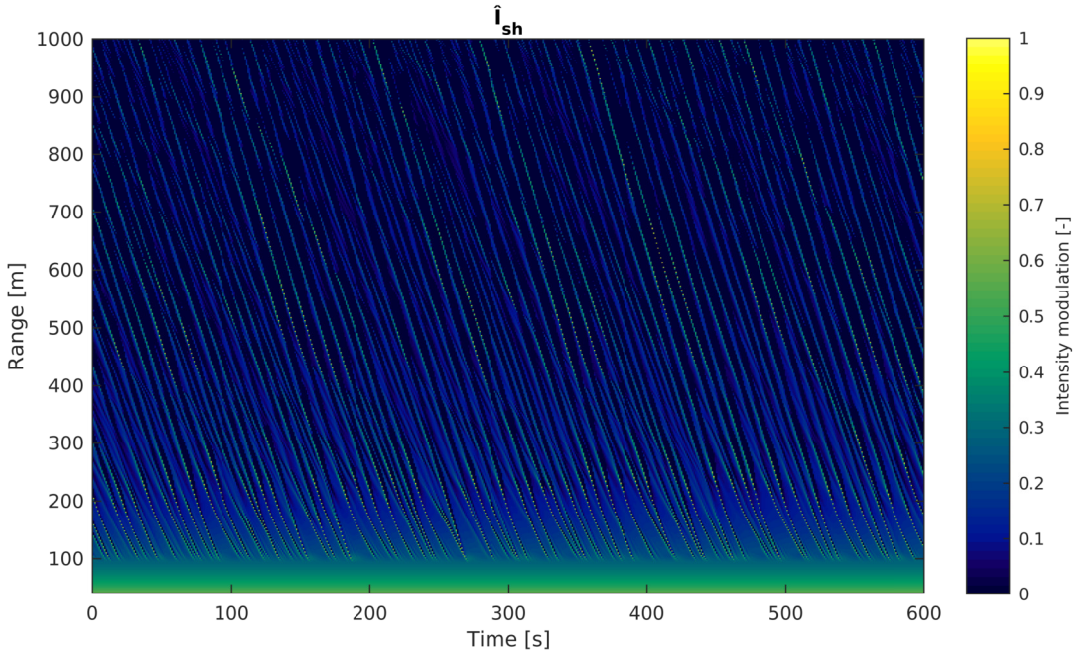

Figure C.5: Time-range diagram of the simulated intensity modulation resulting from surface tilt and shadowing.

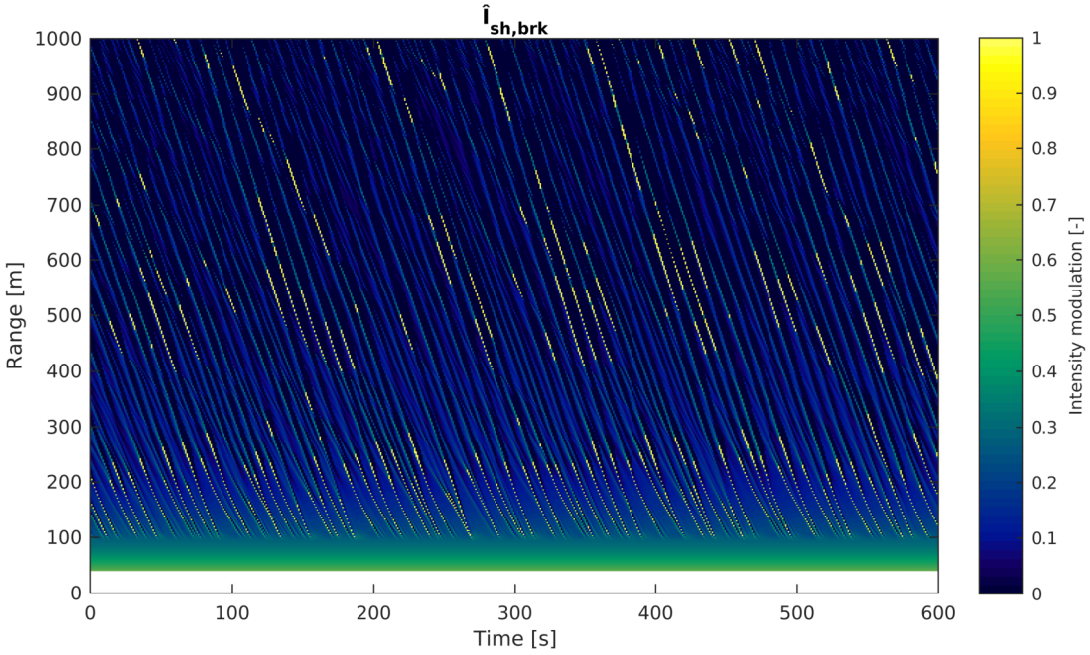

Figure C.6: Time-range diagram of the simulated intensity modulation resulting from surface tilt, wave breaking and shadowing.

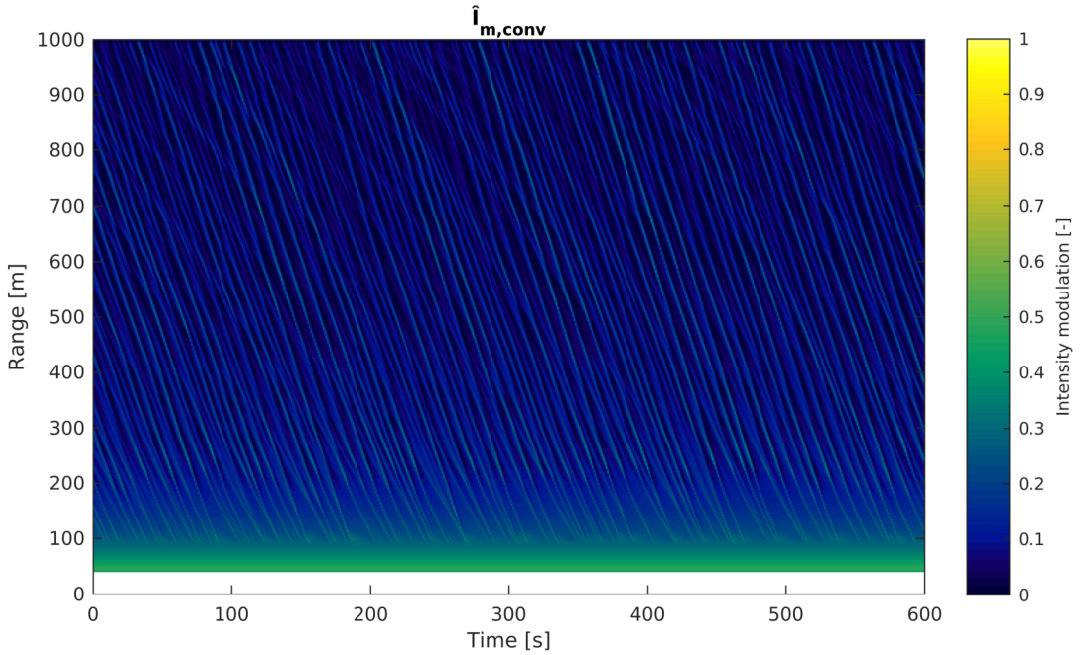

Figure C.7: Time-range diagram of the simulated intensity modulation resulting from surface tilt and convolution by the radar pulse.

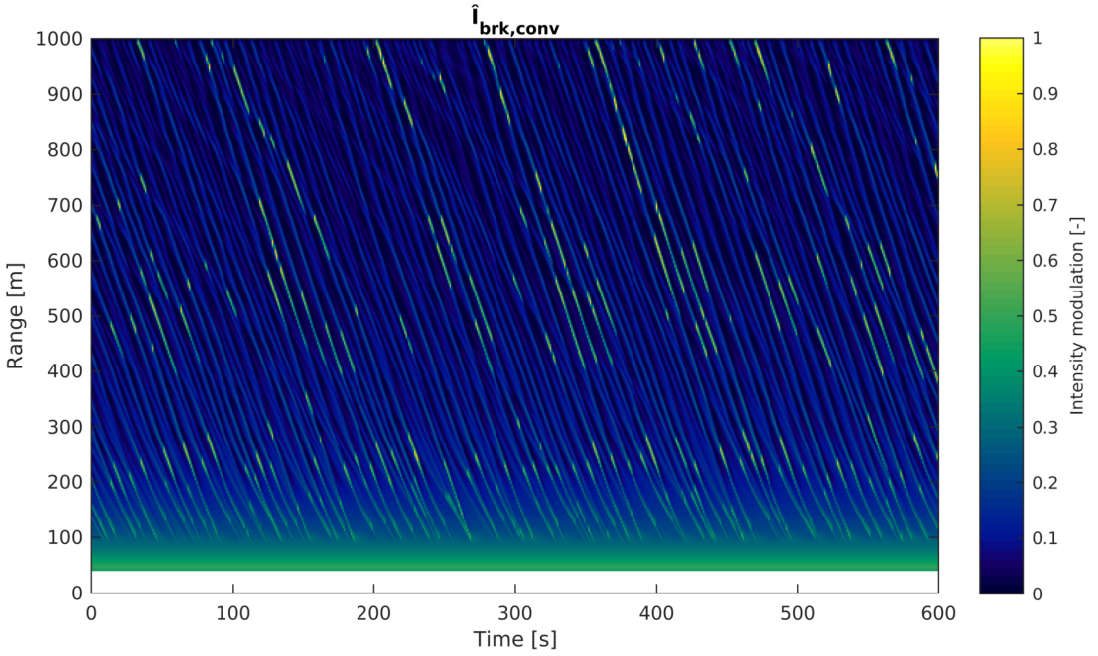

Figure C.8: Time-range diagram of the simulated intensity modulation resulting from surface tilt, wave breaking and convolution by the radar pulse.

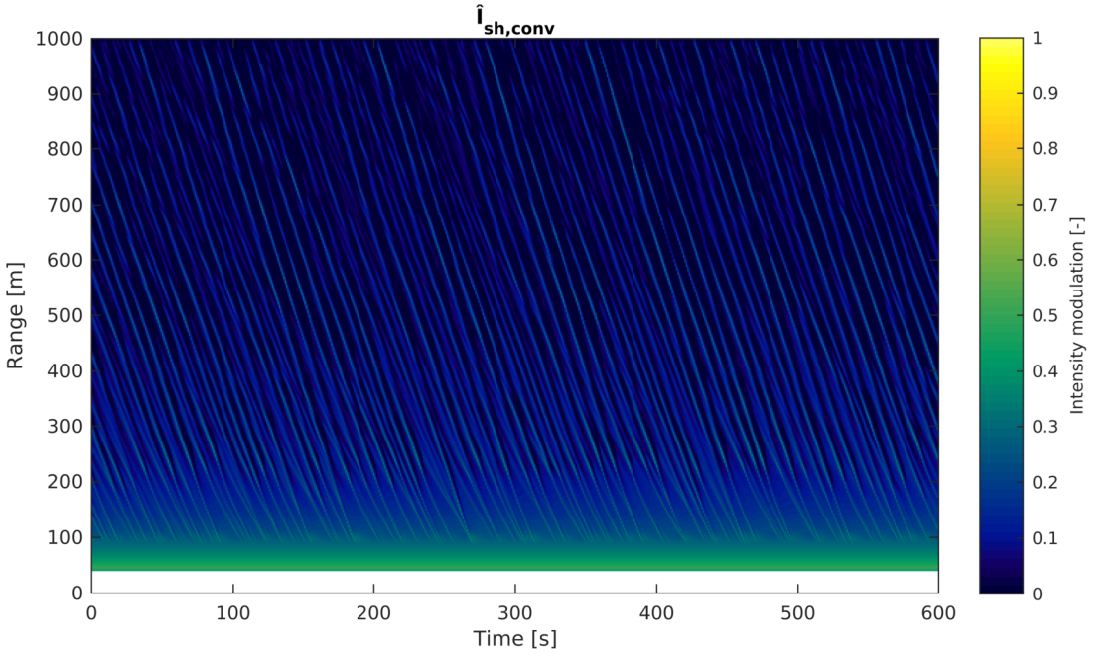

Figure C.9: Time-range diagram of the simulated intensity modulation resulting from surface tilt, shadowing and convolution by the radar pulse.

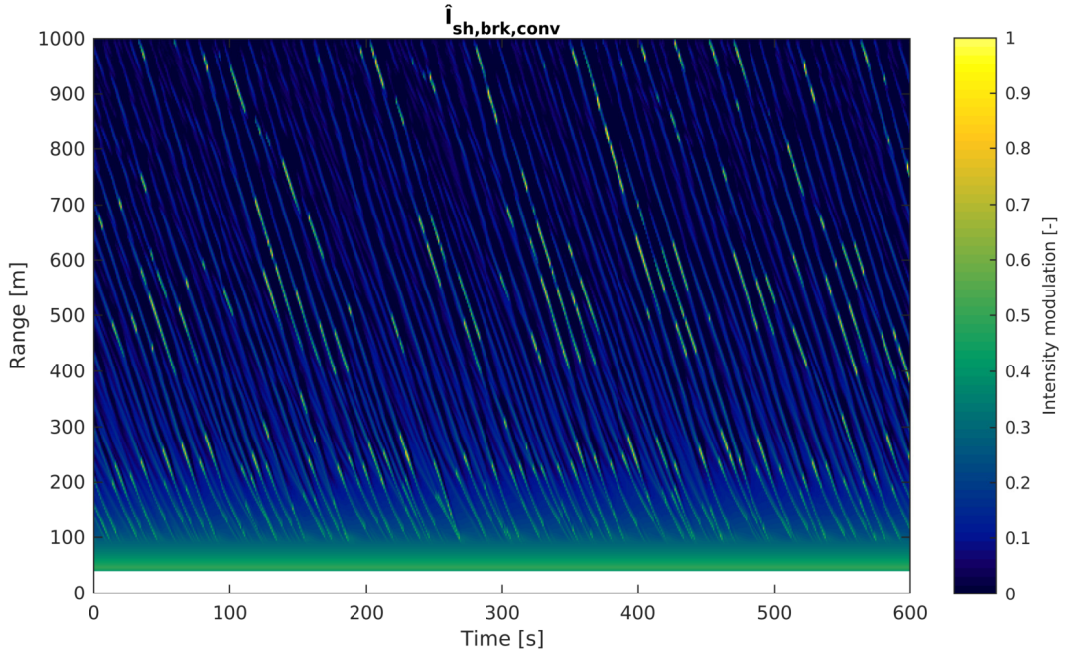

Figure C.10: Time-range diagram of the simulated intensity modulation resulting from surface tilt, wave breaking, shadowing and convolution by the radar pulse.

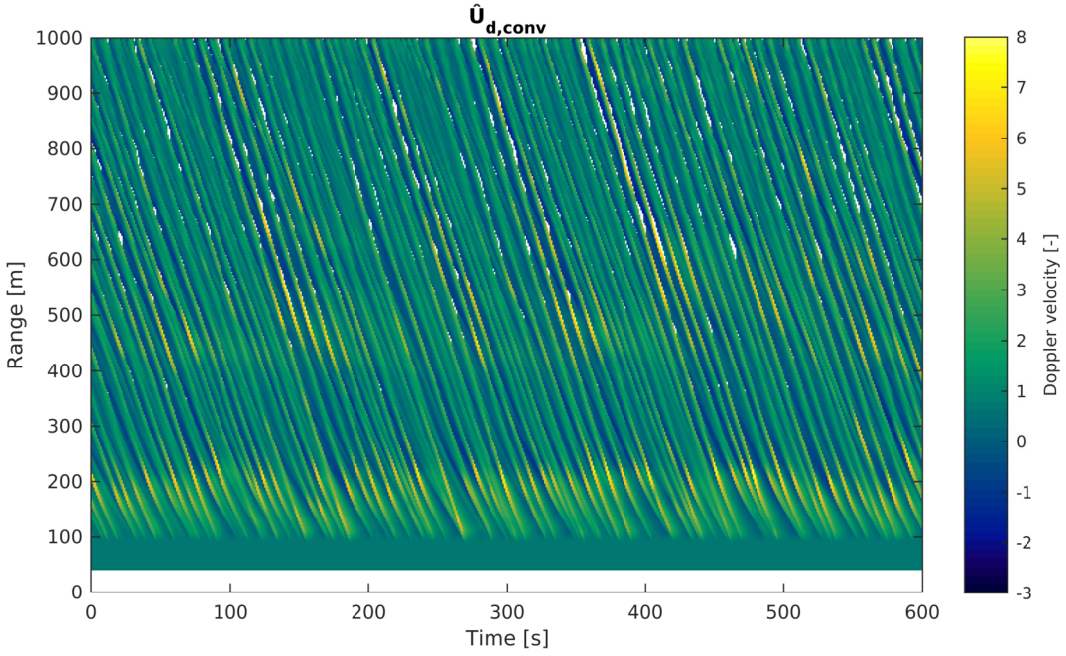

Figure C.11: Time-range diagram of the simulated Doppler velocity $\hat{U}_d$.

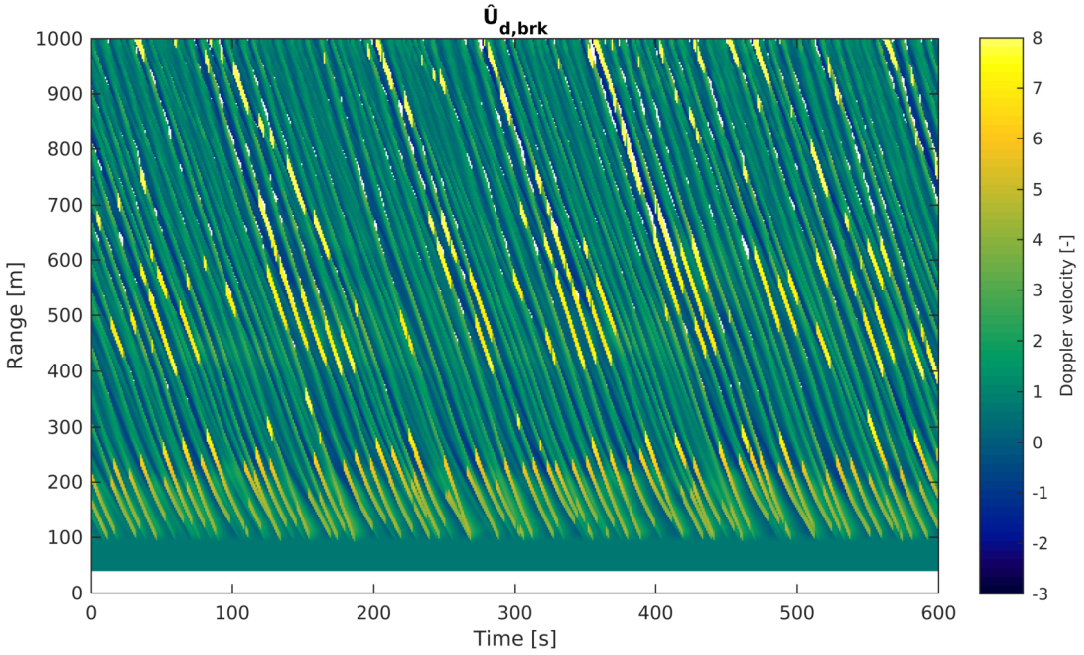

Figure C.12: Time-range diagram of the simulated Doppler velocity accounting for wave breaking $\hat{U}_{d,brk}$.

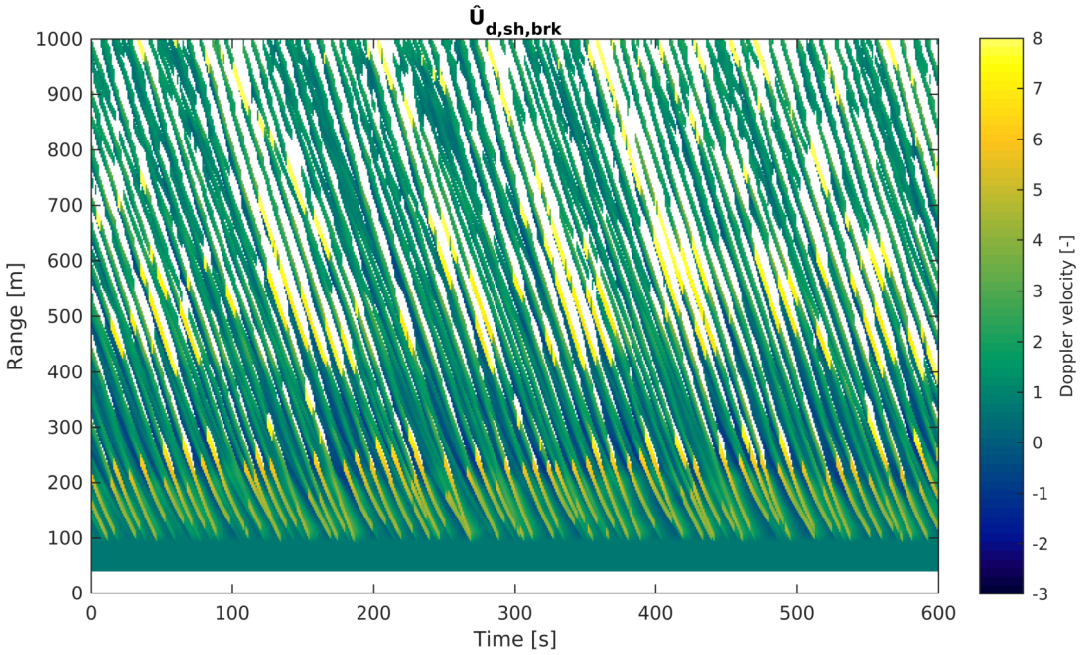

Figure C.13: Time-range diagram of the simulated Doppler velocity accounting for wave breaking and shadowing $\hat{U}_{d,sh,brk}$.

Symbols

α	angle between the target movement and antenna line-of-sight
α_b	calibration coefficient for wave breaking in the two-layer non-hydrostatic siumlation
α_{ad}	amplitude dispersion factor
$\tilde{\beta}$	breaking probability scaling parameter
β_b	calibration coefficient for wave breaking in the two-layer non-hydrostatic siumlation
β_s	slope coefficient in the Roller model
β_ρ	proportion of water with respect to air inside the roller
β_d	Doppler velocity difference to phase speed conversion factor
β_{emp}	exponent in empirical method to estimate H_s
γ	breaker parameter
Δ	difference operator
$\varepsilon(c)$	scale dependent dissipation rate
ε_r	relative dielectric constant of the ocean
ζ	tidal elevation
η	surface elevation
θ_r	roller angle of inclination
λ_{beam}	beam opening angle
θ_{crit}	critical slope as breaking treshold
$\theta_{crit,toe}$	critical slope at the toa of a breakingf front
θ_g	grazing angle
θ_i	incidence angle

θ_l	local incidence angle
θ_s	local surface slope angle
θ_w	wave direction
κ	proportionality constant to scale roller area
λ_{el}	electromagnetic wave length
$\Lambda(c)$	Phillip's Lambda-Function
Λ_{peak}	value at the peak of the Lambda-Function
ν	kinematic viscosity of water
ν_t	eddy viscosity
ξ_0	Iribarren number (or surf similarity parameter)
ρ	fluid density
ρ_w	density of (sea) water
ρ'	bulk roller density
σ	radar cross-section
σ_D	standard deviation of the Doppler velocity
σ_s	radar cross-section of the sea surface
τ	Reynolds stress
ϕ	wave phase
ϕ_{el}	phase of the radar signal
Ω	Doppler shifted radial frequency
ω (ω_p)	radial frequency (at spectral peak)
∇	nabla operator
a	wave amplitude
a_{down}	downward acceleration
α_s	beach slope angle
A_e	effective area
A_{el}	amplitude of the radar signal
A_r	roller area
b	breaking strength parameter
B	bore dissipation scaling factor
B_{cp}	binary mask indicating Doppler ensembles affected by dominant breakers
B_{nobrk}	binary mask indicating Doppler ensembles not affected by dominant breakers

$B_{cp,out}$	binary mask indicating pulse smearing artifacts related to dominant breakers
B_{trail}	binary mask indicating possible other pulse smearing artifacts
B_{dom}	binary mask indicating valid dominant breakers
B_{small}	binary mask indicating valid smaller breakers
B_r	scaling factor for the radar based estimation of the roller energy
c (c_p)	wave phase velocity (at spectral peak)
c_g	wave group velocity
C_{el}	complex radar signal
c_{Bragg}	phase speed of the Bragg-resonant waves
c_0	speed of the most frequent whitecaps
d	water depth
D	dissipation rate per unit surface area
$\langle D \rangle$	bulk dissipation per wave
D_{hj}	dissipation of an hydraulic jump (or bore) scaling factor
D_τ	dissipation of roller energy
D_w	dissipation of organized wave energy
D_{rec}	total record duration
dU	positive increase of the Doppler velocity at the toe of the roller
E_w	organized wave energy
F	convolution kernel function
f_d	Doppler shift frequency
f_{el}	electromagnetic frequency
F_w	organized wave energy flux
f_{rep}	representative frequency of the wave field
g	gravitational accelaration of the Earth
g_{HH}, g_{VV}	scattering coefficients for horizontally (HH) and vertically (VV) polarized radar radiation
H	wave height
H_{rms}	Root-mean-square wave height

H_s	significant wave height
H_b	breaking wave height
I_1, I_2, I_3	Intensity corresponding to first, second and third peak in the Doppler spectrum
$\hat{I}_m$	simulated intensity modulation
$\hat{I}_{brk}$	simulated intensity modulation affected by breaking
$\hat{I}_{sh,brk}$	simulated intensity modulation affected by shadowing and breaking
$\hat{I}_{sh}$	simulated intensity modulation affected by shadowing
$\hat{I}_{m,conv}$	simulated intensity modulation affected by the sensor impulse response
$\hat{I}_{brk,conv}$	simulated intensity modulation affected by breaking andthe sensor impulse response
$\hat{I}_{sh,brk,conv}$	simulated intensity modulation affected by shadowing, breaking and the sensor impulse response
$I_{max,ADC}$	maximum intensity value given by the ADC
k (k_p)	wave number (at spectral peak)
K	hardware dependent factor in the radar equation
L	wave length
L_k	Kolmogorov length scale
L_r	roller length
N_w	total number of waves
N_b	number of breaking waves
N_{wc}	number of whitecaps (small breakers)
p	pressure
$P_r(H)$	Rayleigh distribution of wave heights
P_{trans}	transmitted power
P_{rec}	received power
PRF	Pulse repetition frequency
$P_b(H)$	wave breaking probability distribution
P_1, P_2, P_3	Power corresponding to first, second and third peak in the Doppler spectrum
$\hat{P}$	simulated received radar power

P_{thresh}	power level threshold for the classification algorithm
Q_b	overall breaking probability or fraction of breaking waves
R_b	whitecap passage rate
r	range, i.e. distance to radar antenna
S_η, $S_{\eta\eta}$	surface elevation (power) spectrum
S_0	offshore wave steepness
t	time
T	wave period
u, v, w	horizontal (x y) and vertical (z) fluid velocity
U_x, U_y	x- and y-component of the depth avaraged ambient current
U_d	Doppler velocity of the ocean surface (many targets)
$U_{d,pp}$	Doppler velocity from pulse-pairs
$U_{d,fft}$	Doppler velocity from first moment of the Doppler spectrum
$U_{d,1}$, $U_{d,2}$, $U_{d,3}$	Doppler velocity corresponding to first, second and third peak in the Doppler spectrum
U_{10}	the 10-m wind speed
$\hat{U}$	simulated velocity in the upper uppermost 5% of the water column
$\hat{U}_s$	simulated surface velocity
$\hat{U}_{s,brk}$	simulated surface velocity affected by breaking
$\hat{U}_d$	simulated Doppler velocity
$\hat{U}_{sh}$	simulated Doppler velocity affected by shadowing
$\hat{U}_{d,brk}$	simulated Doppler velocity affected by breaking
$\hat{U}_{d,sh,brk}$	simulated Doppler velocityaffected by shadowing and breaking
u_r, w_r	bulk horizontal and vertical roller propagation speed
$\mathbf{v}$	three dimensional of the fuid velocity
v_d	Doppler speed of a single target
$W(H)$	empirical probability weighting function

Acronyms

ADC analog-to-digital converter

ADCP acoustic Doppler current profiler

ADU analog-to-digital unit

ADV acoustic Doppler velocimeter

B98 Breaking parameterization by Baldock et al. (1998)

BJ78 Breaking parameterization by Battjes and Janssen (1978)

BWHD breaking wave height distribution

BSH Federal Hydrographic and Maritime Traffic Agency of Germany

CK02 Breaking parameterization by Chawla and Kirby (2002)

COSYNA Coastal Observing System for Northern and Arctic Seas

DNS direct numerical simulation

EM electromagnetic current meter

FA12 Breaking parameterization by Filipot and Ardhuin (2012)

FFT fast Fourier transform

FRF United States Army Corps of Engineers Field Research Facility

GPS Global Positioning System

HFA hydrostatic front approximation

HH radar radiation that is horizontally polarized in transmit and receive

HORS Hazaki Oceanographical Research Station

HZG Helmholtz-Zentrum Geesthacht

JB07 Breaking parameterization by Janssen and Battjes (2007)

JPD joint probability distribution

laser light amplification by stimulated emission of radiation, used here as a noun for the instrument

LES large eddy simulation

LGA low grazing angle

MSL Mean Sea Level

NH20 non-hydrostatic simulation with 20 vertical layers

NH2 non-hydrostatic simulation with 2 vertical layers

NLSWE non-linear shallow water equations

PG Pressure gauge

PIV particle imaging velocimetry

PRF pulse repetition frequency

PUV directional wave gauge that uses pressure and velocity

PVC polyvinyl chloride

radar radio detection and ranging, used here as a noun for the instrument

RANS Reynolds averaged Navier-Stokes Simulation

RTK Real-time kinematics

sonar sound navigation and ranging, used here as a noun for the instrument

SPH smoothed-particle hydrodynamics

SW The SimpleWaves1D model

SWAN The Simulating WAves Near shore model

SWASH The Simulating WAves till SHore model

TG83 Breaking parameterization by Thornton and Guza (1983)

UAV unmanned aerial vehicle

UTC Coordinated Universal Time

VV radar radiation that is vertically polarized in transmit and receive

W88 Breaking parameterization by Whitford (1988)

WR Wave rider

Acknowledgments

First, I like to express my gratitude to my supervisor Burkard Baschek for giving me the opportunity to conduct this research at the Helmholtz-Zentrum Geesthacht (HZG). He was always available when I needed consultation and gave me enough freedom to "explore the side roads" - as he formulated it - while staying on course during this journey. Many thanks also to Grant Deane, from Scripps Institution of Oceanography, for his support as a member of my PhD committee. Every conversation I had with Grant was extremely inspiring and always sourced new ideas. Also part of the committee was Torsten Schlurmann from the Ludwig-Franzius Institute in Hannover, where my curiosity for coastal research definitely has its roots. As a student assistant there I worked with many great people, most of them have become good friends. Therefore, I am grateful that Torsten continued to support me also on this next part of my career and that he added the view point of a coastal engineer to the committee.

Also gratefully acknowledged here is the support of Yaron Toledo from the Marine Engineering and Physics Lab at Tel Aviv University. With his help I was able to acquire a Minerva short term research grant to visit his research group in Israel. Yaron also enabled me to attend the WISE Meeting in Tel Aviv, where I had the chance to establish new contacts among the wave modelling community.

Moreover, I like to thank Peter Fröhle and Jens Winkelbauer from the Technical University Hamburg Harburg for sharing the design of the pressure wave gauges that I used for this work.

Another important bunch of people who provided essential support for the success of this project (and many nice barbecues) are my colleagues from the Department of Radar Hydrography (KOR) here at HZG. First and foremost my daily advisor Jochen Horstmann. The confidence he placed in me from the beginning convinced me not only to start this work in his research group. He also pushed me towards the right decisions to apply for grants and awards and brought me in contact with the international ocean radar community during the SOMaR Meetings. Jochen's enthusiasm in conducting field research and building custom measurement solutions made me learn a lot. It was always great fun to spent time with him in the field, the workshop or traveling. Also, I want to thank all other colleagues at HZG, who provided support in various fields. Jörg Seemann helped me many times in understanding maths and physics and often pointed me to the right literature. Marius Cysewski shared his vast experience in acquiring and

post-processing hydrographic and geodetic data as well as his sound skills in organizing a field campaign. Ruben Carrasco added his experience in processing radar data or coding in general. I enjoyed every hour we spent together coding and the competitions we had about who writes more efficient code (which he always won). Thanks also to Marc Buckley, who was always willing to enter into a stimulating debate about the essence of ocean waves. Furthermore, I appreciate the essential technical support of Jan Bödewadt and Jurij Stell, who - with their Mc Gyver-like skills - made sure that all the equipment is up and running whenever it was needed.

I want to thank also my peers and good friends Lea Lange and Gian Bremm. Lea was not only a talented and helpful student but also a nice roommate when she wrote her master's thesis at HZG. Thank you Lea for many long philosophical conversations about science and life in general. Similarly, the hundreds of stimulating discussions I had with Gian about the pleasures of studying waves (while surfing) always pushed forward my motivation. The lunch breaks at the beach of Norderney certainly provided a better environment for such kind of conversations, however, I am happy that we continued this tradition remotely on the phone.

Last but not least, I am sincerely grateful to my family. My mother Wilma, my father Edmund and my sister Anke always endorsed my plans and dreams, but - more important - always guaranteed me a save haven back at home. Many heartfelt thanks also to Hannah for her love, patience and support particularly during the past year, which was also a year of change regarding her own career.

Michael Streßer, Geesthacht, January 13, 2020

Erklärung

Hiermit erkläre ich, dass ich die vorliegende Dissertation selbstständig angefertigt, dabei keine anderen als die angegebenen Quellen und Hilfsmittel benutzt und die den benutzten Quellen wörtlich oder inhaltlich entnommenen Stellen als solche kenntlich gemacht habe. Diese Arbeit ist in gleicher oder ähnlicher Form weder ganz noch teilweise veröffentlicht worden und hat noch keiner anderen Prüfungsbehörde vorgelegen. Sie ist unter Einhaltung der Regeln guter wissenschaftlicher Praxis der Deutschen Forschungsgemeinschaft entstanden. Mir wurde bis zum jetzigen Zeitpunkt noch kein akademischer Grad entzogen.

Hamburg, 17.1.2020

Michael Streßer